LIQUID AIR BASED ENERGY CONVERSION AND STORAGE: SYSTEM CONFIGURATION, SIMULATION AND OPTIMIZATION

By

TONGTONG ZHANG

A thesis submitted to the University of Birmingham for the

Degree of Doctor of Philosophy

School of Chemical Engineering

College of Engineering and physical Sciences

University of Birmingham

January 2022

The candidate confirms that the work submitted is her own and that appropriate credit has been given where reference has been made to the work of others.

Abstract

The past decade has seen a significant growth in renewable energy installations driven by a global effort to combat climate change. The non-dispatchable nature of most renewable energy generation and the less predictable end-user demand imply a highly challenging supply-demand management for energy networks. Energy storage technologies provide an avenue to meet the energy supply and demand through the chain of generation, transmission, distribution, and end use. Liquid Air Energy Storage (LAES) is one of the most promising energy storage technologies, which have started large-scale commercial deployment.

There has been an increased number of studies on the LAES technology, especially since 2010. These studies include the basic characteristics and performance of the standalone LAES in the early stage of development, and the improvement of the round trip efficiency of the standalone LAES through configuration optimization in most of the subsequent publications. These studies also explored the integration of the LAES with external cold/heat sources or industrial processes for performance improvement. However, the range of applications of the LAES is still very limited, mainly focusing on the decarbonization of the power sector, especially for the large-scale power grid. This Ph.D. work aims to extend the application fields of the LAES technology, including the provision of green multi-energy-vector products, decarbonizing the industrial sector and building sector at different scales.

First, a power plant for recovering cryogenic waste energy from LNG regasification and compression heat from the LAES is proposed and the thermodynamic analyses are carried out. The results show that the power plant could achieve a thermal efficiency of 27% and an exergy efficiency of 40%. An economic analysis of the plant shows a payback period of only 2.2 years, due to the use of the excess heat from a 5MW/40MWh LAES system.

Second, apart from the use of excess compression for power generation, it can also be utilized for the provision of multi-energy-vector services. Therefore, a standalone LAES system is

proposed for combined cooling, heating, hot water, and power supply. The results show that such a standalone LAES can achieve a high nominal-electrical round trip efficiency between 52% and 76%, with the maximum at a charging pressure of 5 MPa, a new finding that has not reported before.

Third, decoupled LAES provides a route to transport energy from renewable energy-rich areas to end-use sites. A new cryogenic thermoelectric generation (Cryo-TEG) method is therefore proposed to recover the cryogenic energy of the decoupled LAES during the discharging process. The results show that the Cryo-TEG has a thermal efficiency of ~9%, which is lower than that of a Rankine cycle operated over the same temperature range. However, the Cryo-TEG gives a levelized cost of electricity of 0.0218 $/kWh for small-scall applications, which is ~4 times cheaper than that of the Rankine cycle system. With the Cryo-TEG, the decoupled LAES systems could achieve an electrical round trip efficiency of ~29% and a combined cooling and power efficiency of ~50%.

Fourth, the ammonia synthesis process requires the feed gas of nitrogen, one of the ingredients of the storage mediums for the LAES system. Two new integrated methods between the LAES system and the ammonia synthesis system are therefore proposed: LAES-NH_3 and LAES-AS-NH_3. The LAES-NH_3 is found to be more suitable for the existing ammonia production plant. The LAES is used as a nitrogen buffer to transfer the peak load of the air separation unit to off-peak time. In this way, the air separation unit used for nitrogen supply to the ammonia synthesis process can realize an operation cost decrease by ~38%. On the contrary, the LAES-AS-NH_3 is more suggested for a new ammonia production plant. In such a configuration, a single distillation column is added to the LAES (denoted as LAES-AS) for air separation. Both liquid nitrogen and liquid air can be obtained during the charging process, for use as the feed gas for ammonia synthesis and the working fluid for the LAES discharging process. The nominal round trip efficiency of the LAES-AS side is shown to reach 69%, and the electricity consumption of the ammonia synthesis process can be reduced

by ~31.6%. As a result, the LAES-AS-NH_3 system could achieve an overall round trip efficiency of 30%, which is 13% higher than that of the standalone ammonia synthesis system.

Acknowledgements

I would like to extend my deepest gratitude to my supervisor, Professor Yulong Ding, who guided me during the course of my Ph.D. degree. He is the man opening the doors for me to the fields of energy storage. His research enthusiasm and immense knowledge have encouraged me in all the time of my academic research and daily life. Without his support, encouragement and patience, I would not have been able to complete my Ph.D. research.

I am also grateful to my co-supervisor Professor Yongliang Li, for all his help and advice with this Ph.D.

Special thanks to Dr. Xiaohui She. He has always been willing to impart his knowledge to me selflessly which has been a great help to me during my Ph.D. study.

I would like to thank all the members in Birmingham Centre for Energy Storage (BCES), Dr. Boyang Zou, Dr. Zhu Jiang, Dr. Binjian Nie, Dr. Lin Cong, Dr. Yanqi Zhao, Dr. Abdalqader Ahmad, Dr. Helena Navarro, Ms. Jie Chen, Mr. Yunren Li, Mr. Yuanye Meng, Ms Ting Liang, Ms Hongkun Ma, Mr Siyuan Dai, Mr Xuefeng Lin and everyone in BCES. It is their kind help and support that have made my study and life in the UK a wonderful time.

In particular, I am grateful to my supervisor for my master's degree, Professor Yufeng Guo, enlightening me the first glance of research and encouraging me to start my Ph.D. study.

Besides, it is grateful for the financial support provided by China Scholarship Council (CSC) during my PhD study.

Finally, my appreciation also goes out to my family: my parents Jianxin Zhang and Shuying Ma, and my sister Bin Zhang, for supporting me spiritually throughout my life.

Table of Contents

List of Figures

List of Tables

Abbreviations

ASU	Air Separation Unit
CAES	Compressed Air Energy Storage
CEPCI	Chemical Engineering Plant Cost Index
CNG	Compressed Natural Gas
CCP	Combined Cooling and Power
CCHP	Combined Cooling, Heating, and Power
CCHHP	Combined Cooling, Heating, Hot water and Power
Cryo-TEG	Cryogenic Thermoelectric Generation/Generator
Cryo-RC	Cryogenic Rankine Cycle
eRTE	Electrical Round Trip Efficiency
HPG	High-Pressure Generator
LCOE	Levelized Cost of Electricity
LAES	Liquid Air Energy Storage
LNG	Liquefied Natural Gas
LPG	Low-Pressure Generator
MAT	Minimum Approach Temperature
NG	Natural Gas
NPV	Net Present Value
neRTE	Nominal-Electrical Round Trip Efficiency
O&M	Operating and Maintenance expenditure
ORC	Organic Rankine Cycle
PNG	Piped Natural Gas
P2A2P	Power-to-Ammonia-to-Power
PH	Power and Hot water
PHC	Power, Hot water and Cooling
PHH	Power, Hot water and Heating
PTES	Pumped Thermal Energy Storage
PHS	Pumped Hydro Storage

RC	Rankine Cycle
RTE	Round Trip Efficiency
SIR	Saving to Investment Ratio
SPP	Simple Payback Period
TEG	Thermoelectric Generator
TOU	Time-Of-Use
TES	Thermal Energy Storage

Nomenclature

$C/CAPEX$	Capital cost (USD or GBP)
C_{NCI}	Net cash inflow (USD or GBP)
$C_{O\&M}$	Operating and maintenance cost (USD or GBP)
COP	Cooling or heating performance
$Cost$	Operation cost (USD or GPB)
$Cost^{0}_{H2}$	Cost to produce 1kg hydrogen production (GPB/kg)
$C_{revenue}$	Revenue (USD or GBP)
D_{LN2}	Net power consumption to produce per unit liquid nitrogen (kJ/kg)
E_{PES}	Primary energy savings (MWh)
ex	Specific exergy (kJ/kg)
Ex	Exergy flow rate (kJ/s)
Ex_{d}	Exergy destruction (kJ)
h	Specific enthalpy (kJ/kg)
I_0	Electric current (A)
$I_{\mathrm{solar/m}^2}$	Investment cost of solar collector per square meter (USD/m^2)
K_{LNG}	Ratio of the mass flow rate of LNG to working fluid
K_{oil}	Ratio of the mass flow rate of thermal oil to working fluid
$lifetime$	Lifespan (year)
m	Mass flow rate (kg/s)
M_{CO2}	Avoided carbon dioxide emissions (ton)
P	Pressure (MPa)
$payback\_period$	Payback period (year)
Q	Heat flux, heating capacity, cooling capacity, electricity (kJ)
q^{N2}_{ASU}	Electricity consumption of ASU to produce 1kg pure nitrogen (kWh/kg)
$q_{\mathrm{solar/m}^2}$	Annual heat production by solar collector (MWh/(m^2·year))
R_0	Internal resistance (Ω)
s	Specific entropy (kJ/(kg K))
S	Seebeck coefficient (VK^{-1})

T	Temperature (K)
t	Time (hour)
tariff	Electricity tariff (USD/kWh or GPB/kWh)
W	Work (kJ/s)
w_{net}	Specific power generation (kJ/kg)
Y	Liquid yield or product yield
η	Isentropic efficiency
h_{th}	Thermal efficiency
η_{ex}	Exergy efficiency
η_{loss}	Thermal loss
$\eta_{gas,ther}$	Thermal efficiency of gas boiler
$\eta_{gas,ele}$	Thermal-to-electricity efficiency of gas turbine
η_{E_RTE}	Electrical round trip efficiency
η_{NE_RTE}	Nominal-electrical round trip efficiency
η_{CCP}	Combined cooling and power (CCP) efficiency
η_{TE}	Thermal efficiency of the Cryo-TEG
$\eta_{TE,ex}$	Exergy efficiency of the Cryo-TEG
$\eta_{combustion}$	Combustion efficiency of ammonia

Subscripts/superscripts

abs	Absorber
air	Air
air	Air
ambient	Ambient environment
ASU	ASU
ave	Average
ch	Charging process
com	Compressor
cool	Cooling

cryo-pump	Cryo-pump
cryo-tur	Cryo-turbine
dis	Discharging process
eva	Evaporator
flat	Flat time
gas	Gas boiler
H_2	Hydrogen or hydrogen production process
HB	Haber–Bosch process
heat	Heating
hp	Heat pump
h-water	Hot water
in	Inlet
LAES	LAES system
LAES-AS	LAES-AS system
LN_2	Liquid nitrogen
LNG	LNG
methanol	Methanol stream
N_2	Nitrogen
NH_3	Ammonia or ammonia synthesis system
off	Off-peak time
oil	Thermal oil
out	Outlet
peak	Peak time
PG1	Power generation#1
PG2	Power generation#2
pre	Pre-purification unit
propane	Propane stream
s	Isentropic compression or expansion process
solar	Solar collector
Standalone-NH_3	Standalone ammonia synthesis system

steam	Steam turbine or steam
TE	Cryo-TEG
TEG-FH	Cryo-TEG with free waste heat
TEG-solar	Cryo-TEG with solar energy
turb	Turbine
w	Water
WF	Working fluid

Chapter 1 Introduction

1.1 Background

To achieve the aim of maintaining the global average temperature rise of 1.5 ℃, all sectors across the economy will need to be decarbonised by the early second half of this century [1]. Renewables (wind, solar, hydropower, biomass, tide) will undoubtedly play a major and critical role not only for the power sector, but also the thermal (heating and cooling) and transportation sectors. The intermittency of the renewable requires the use of energy storage technologies, the key focus of this Ph.D. study.

1.1.1 Energy storage in the power sector

In the power sector, the past decade has seen significant growth in renewable energy installations. In 2019, renewables experienced record-high increases in newly installed capacity, reaching more than 200 GW and dominating new power installations [2]. Overall, the power capacity of renewable energy accounted for 27.3% of the global power supply by the end of 2019 [2]. With the technological progress and policy support across many countries, shares of renewables in electricity expect a further increase worldwide. Figure 1.1 shows the assessment of the world net electricity generation projection provided by different resources from 2010 to 2040 [3]. One can see that the renewables are the fastest-growing source of power generation over the next 20 years, with an average growth rate of 2.8% per year. However, the non-dispatchable nature of most renewable energy generation and the less predictable end-use demand imply a highly challenging supply-demand management for power networks. For example, in case of no extra reserve capacity to ensure electricity quality, renewable penetration is not recommended to exceed 20% of the total load [4,5].

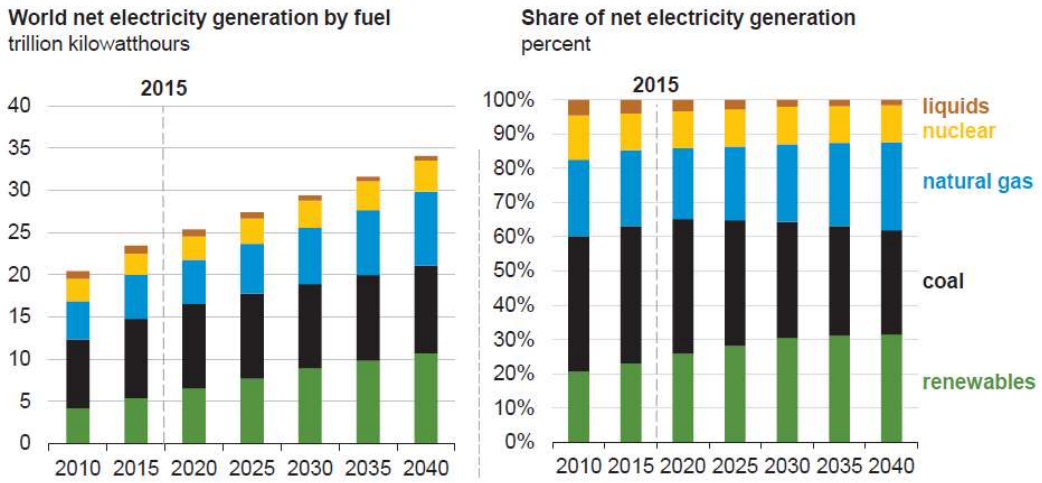

Figure 1.1 Share of world net electricity generation by types from 2010 to 2040 [3].

Clearly, more effort is needed to increase the penetration of renewable energy in the power sector, for which, as mentioned above, energy storage technology is one of the most effective measures to facilitate this transition. Energy storage systems can provide numerous and various energy services, as shown in Figure 1.2 [6], from generation and transmission to distribution and customer/end-users. On the one side, these services are able to increase the flexibility and reliability of power networks, improving the uptake capacity of the grid for renewable electricity [7]. On the other side, energy storage systems can smooth the power and voltage outputs from renewable energy directly, improving the renewable electricity quality and reducing its impact on the power grid [8]. Furthermore, energy storage can also provide off-grid electricity services, making renewable energy utilization in off-grid areas more effective and efficient [9].

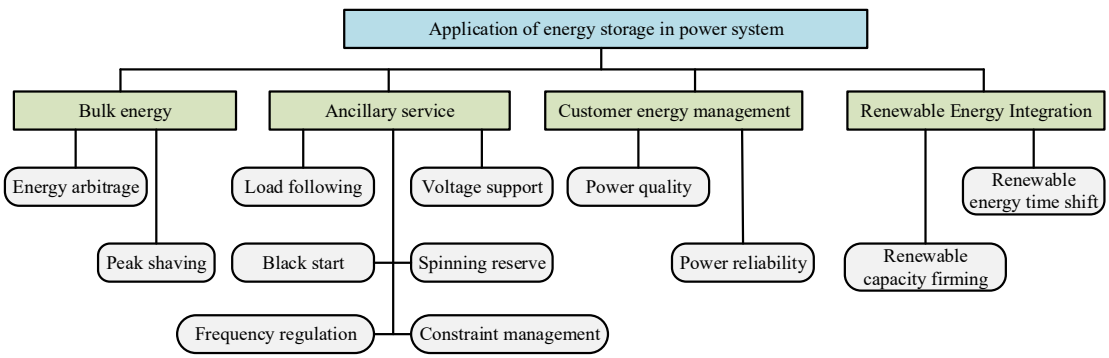

Figure 1.2 Application overview of energy storage systems in the power sector [6].

1.1.2 Energy storage in thermal and transport sectors

Thermal (heating and cooling) energy and transportation are also extremely important sectors that have been regarded as the most challenging for decarbonization. Figure 1.3 illustrates the split of total final energy consumption by different sectors in 2017 [10]. It can be seen that the thermal (heating and cooling) sector is the largest end use energy consumer, making up about 51% of total final energy consumption, followed by transport sector (32%) and power sector (17%). However, although renewable energy takes a considerable portion in power supply, its use in thermal and transport sectors lag significantly. As shown in Figure 1.3, only 10.1% of thermal energy and 3.3% of transport energy are from renewable sources. Thus, an accelerated phase-out of fossil fuels in the thermal and transport sectors is critical to achieving the net zero targets.

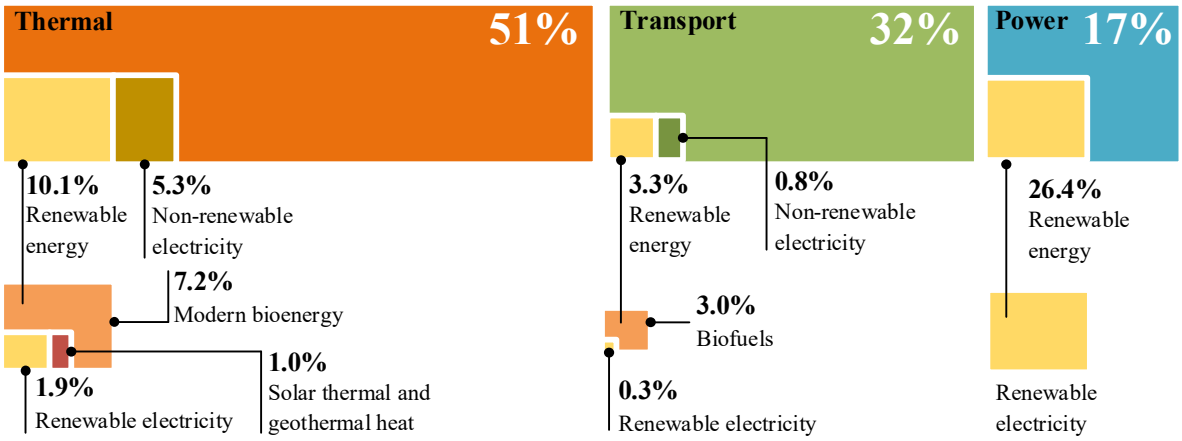

Figure 1.3 The end-use energy consumption structure in 2017 [10].

To promote the uptake of renewable energy in the thermal sector, energy storage has a big role to play. First, electricity is one of the main energy sources to supply cooling and heating in the thermal sector. The utilization of energy storage is capable of facilitating a high penetration of renewable energy for electricity generation which can be used for heat and cold energy generation and hence increase the contribution of renewables in heating and cooling provision. Second, energy storage can shift the peak thermal demand, benefiting the whole thermal systems. This can be achieved by charging thermal stores during lower-cost periods

with renewable energy and discharging at peak thermal loads, leading to a better utilization of renewables in the thermal sector. Third, energy storage provides a solution to deal with seasonal thermal demand-and-supply mismatches. For example, the surplus renewable heat in summer can be stored in thermal energy farms for use in winter [11].

In the transport sector, transportation electrification is regarded as one of the most effective ways towards decarbonization. This includes the use of battery-electric, hybrid, or fuel cell (based on renewable hydrogen) vehicles [2], which are all based on the development of different energy storage technologies (e.g., battery and hydrogen storage). Also, the above-mentioned approaches are based on the principle that the electricity itself is generated by renewables, which cannot be achieved without energy storage.

1.1.3 Classification of energy storage technologies

As briefly mentioned above, the development of energy storage technologies is essential for the transition to net-zero energy future with high penetration of renewable energy. Energy storage can be defined as a process or a device which stores energy generated (charge), keeps the stored energy (storage), and uses the stored energy (discharge) [12]. One can classify the energy storage technologies according to the form of energy stored and the storage duration (long, medium, or short term). Various parameters such as cycle efficiency, technical maturity, response time, cost of investment, storage capacity, energy density, and influence on the environment, etc. have been used to assess the storage performance [7,13]. Figure 1.4 shows the classification of energy storage technologies according to the form of energy stored [13,14].

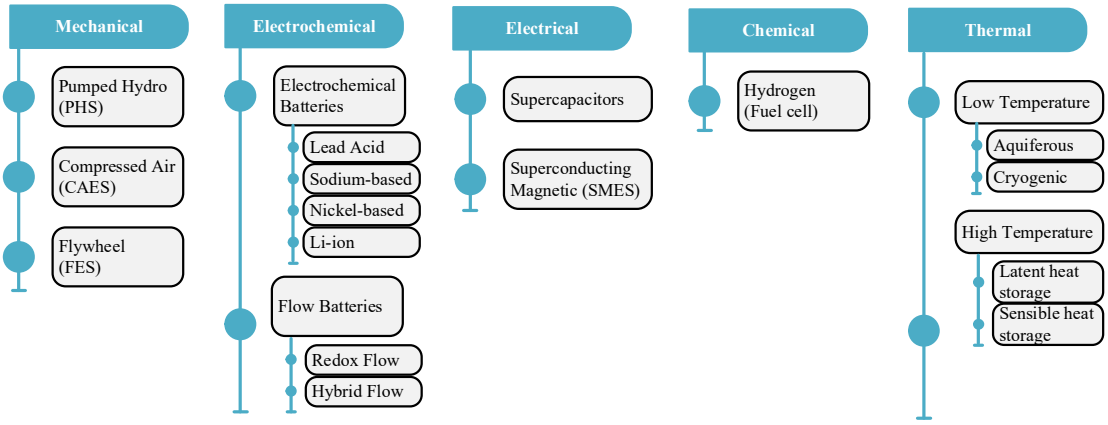

Figure 1.4 Categories of energy storage technologies by the form of energy stored [13,14].

This Ph.D. work focuses on Liquid Air Energy Storage (LAES) which is a Thermal Energy Storage (TES) method fundamentally, which stores the majority of energy at very low temperatures (cryogenic). The LAES uses liquefied air or nitrogen as the main storage medium [15]. Compared with other energy storage technologies, the LAES shows the following advantages [15,16]:

- LAES can reach both multiple GWs and GWhs scales. So far, only Pumped Hydro Storage (PHS), Compressed Air Energy Storage (CAES) and natural gas can be at such a level.
- LAES plants have no geographical constraints.
- LAES is safe and reliable because the storage tank works at or close to the atmospheric pressure.
- LAES uses off-the-shelf components, so the capital cost is competitive.

In addition, LAES has a lifetime of more than 30 years. Its maintenance and operation costs are low. Cost reduction and revenue improvement of LAES are possible with scale. Finally, LAES gives zero emissions and actually, it can help clean the air by taking CO_2 out [17]. These outstanding features make the LAES one of the most attractive large-scale energy storage technologies.

1.2 Aims, Objectives and Methodologies

This research aims to explore various application scenarios that the LAES technology could be used through integration and optimization. So far, the LAES system has been mainly considered for use at large scales in the in the power sector, especially in large power grids. This work also explores the use of LAES for the decarbonization of the industries and buildings across both small and large scales.

The main tasks and methods of this work include:

- To identify research gaps related to the LAES through an extensive literature review.
- To develop a method to utilize the excess compression heat of the LAES, and create values for the heat through the provision of additional electricity with a power generation cycle along with waste cold energy sources e.g., the LNG regasification process, and the thermal products (combined cooling, heating, and hot water) with a multifunctional LAES system.
- To develop a decoupled LAES system for the building sector through the integration of thermoelectric generators for cryogenic energy recovery.
- To develop a process to integrate the LAES with an ammonia synthesis system, and understand the characteristics of the integrated LAES system with the ammonia synthesis.

1.3 Novelties

There have been increased number LAES studies in the recent years. The present work differs significantly from these published studies:

- This work considers a power plant operated over a wide working temperature range between a cold source (-160 ℃) and a heat source (~200 ℃), specifically for recovering both LNG waste cold and industrial waste heat in one integrated system.

- This work proposed a multifunctional LAES system for combined cooling, heating, hot water, and electricity supply, specifically for applications in local decentralized micro energy networks, and the decarbonization of the thermal sector.
- This work proposed the use of a thermoelectric generator for the first time to recover the cryogenic energy in a decoupled LAES, as a more cost-effective way than the traditional method of using a Rankine cycle in a small-scale application scenario. This opens an avenue for the decoupled LAES to provide green electricity to the remote areas that are not connected with the power grid in an economical way.
- This work proposed for the first time, integration of a LAES system with an ammonia synthesis system, for better thermodynamic and economic performances. This opens a scenario for the use of LAES system in industrial sector decarbonization.

1.4 Layout of this thesis

This thesis consists of 8 Chapters. Chapter 2 summarizes the relevant literature covering standalone LAES, integrated LAES, and decoupled LAES.

Chapter 3 introduces the thermodynamic modelling and optimization methods for complex power/thermal systems, including a generalized method using energy analysis, exergy analysis, and pinch analysis for process and system optimization.

Chapter 4 optimizes a waste thermal energy based power generation plant, in which the compression heat from a LAES plant and the cryogenic energy from a LNG regasification plant are used as the heat and cold sources, respectively.

Chapter 5 analyses the thermodynamic performance of a standalone LAES system for combined cooling, heating, hot water, and electricity supply over a wide charging pressure range.

Chapter 6 analyses both the thermodynamic and economic performances of a thermoelectric generator integrated to a LAES system for cryogenic energy recovery.

Chapter 7 studies the integration of a LAES system with an ammonia synthesis system. Two configurations of the LAES are considered with and without an air separation function.

Chapter 8 summarizes the main conclusions of this study with recommendations provided for future work.

Chapter 2 Literature Review

This Chapter briefly explains the characteristics of the LAES technologies first (Section 2.1). The focus is then on relevant studies on the development of the LAES technologies, which can be divided into three parts: thermodynamic analysis and configuration optimization of standalone LAES systems (Section 2.2); integration methods of LAES systems with external thermal sources and other industrial processes (Section 2.3); and development of decoupled LAES systems (Section 2.4). Finally, a summary of the literature review is given (Section 2.5).

2.1 Liquid Air Energy Storage (LAES) characteristics

2.1.1 Brief history and development of LAES

The concept of using liquid air or liquid nitrogen as an energy storage medium can be dated back to the 19th century, while the use of liquid air or liquid nitrogen for the provision of peak-shaving in a power grid first proposed by the University of Newcastle upon Tyne (UK) in 1977 [18]. These led subsequent research by Mitsubishi Heavy Industries [19] and Hitachi [20] on the area. However, turning the concept to the LAES technology took over 40 years with the world's first LAES pilot plant (350kW/2.5 MWh) designed, built, and trialled over 2005-2013 by Highview Power in collaboration with the University of Leeds [21]. This pilot plant was donated to the University of Birmingham for further research in 2013, as shown in Figure 2.1(a). In 2018, Highview Power commissioned its first pre-commercial plant of the LAES (5MW/15MWh) in Manchester, United Kingdom [22] (Figure 2.1(b)). These efforts have led to the first large-scale commercial plant (50MW/300MWh) currently under construction at a decommissioned thermal power station in North of England [23].

(a) (b)

Figure 2.1 The LAES plants: (a) 350 kW/2.5 MWh at University of Birmingham and (b) 5 MW/15 MWh at Manchester.

2.1.2 Basic principle and configuration of LAES

The working principle of the baseline coupled LAES (standalone) includes an air liquefaction unit for charging at off-peak hours and a power recovery unit for discharging at peak hours, as shown schematically in Figure 2.2 (a).

- In the charging process: purified air is first compressed to a high pressure, then cooled down to a low temperature, and finally expands to produce liquid air, with heat generated during air compression harvested and stored for later utilization in the discharging process.
- In the discharging process: the stored liquid air is pumped to a high pressure first, evaporated with ambient heat and then superheated to a high temperature by the stored compression heat, and finally expands in the air turbine to generate electricity.
- Cold and heat recycle: the heat generated during air compression in the charging process is harvested and stored for later utilization in the discharging process; the cold released during liquid air evaporation in the discharging process is recovered and stored for reuse in the liquefaction process to enhance the liquid yield and hence the round efficiency.

In the coupled LAES, the charging and discharging processes are closely coupled through the cold energy and heat recovery and storage to enhance the system performance. There is

another case that liquid air is produced on site with offshore or onshore renewable energy [24], and then transported to end users for electricity supply [25], in which the air charging and discharging processes operate in different places. This is defined as decoupled LAES (see Figure 2.2 (b)).

Clearly, in either coupled or decoupled LAES, air liquefaction (charging process) and power recovery (discharging process) are two major processes that affect the overall system performance.

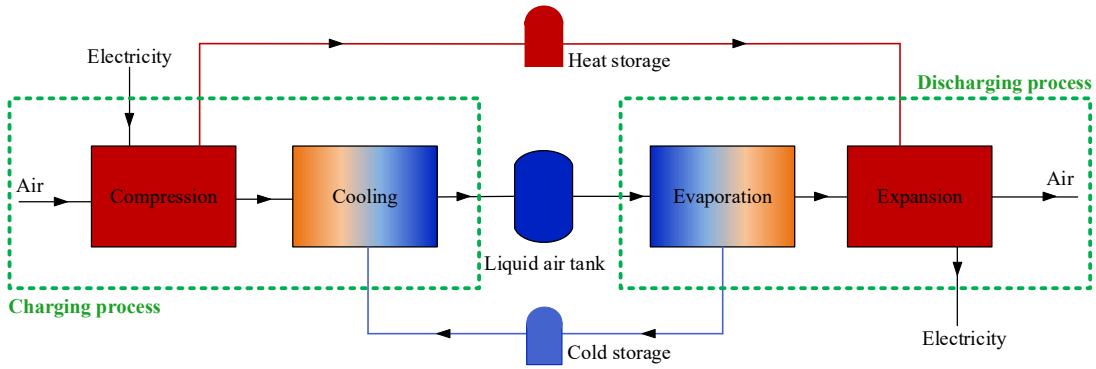

(a)

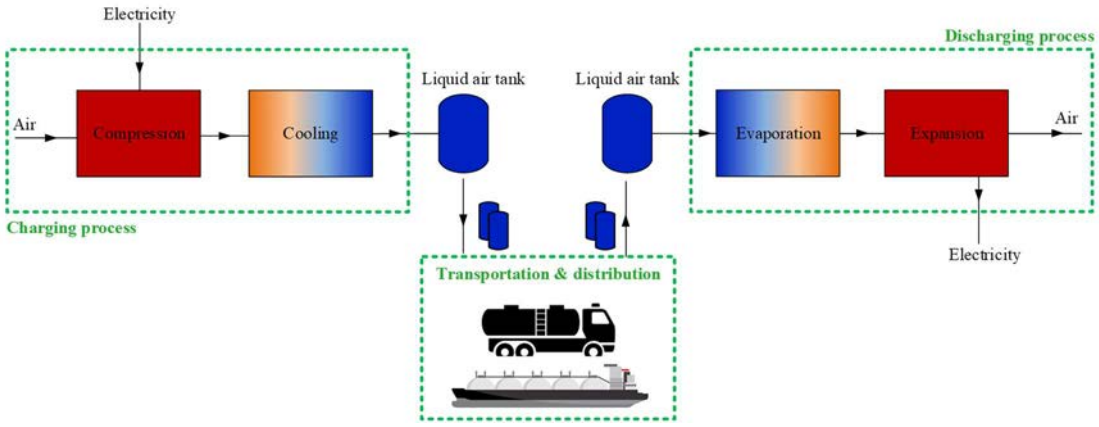

(b)

Figure 2.2 (a) Basic principle of coupled LAES and (b) decoupled LAES.

2.1.2.1 Air liquefaction (charging process)

Air liquefaction is a process in which the purified air is refrigerated to a temperature below its boiling point (-194.35 ˚C, 78.8 K) to form a liquid phase at a suitable pressure, leading to a

significant reduction in volume (by ~700 times) and hence an energy-dense storage medium. Many methods can create such a low temperature for gas liquefication, almost all of which are based on the same principle illustrated in Figure 2.3. First, the feed gas, a mix of the fresh gas and the return gas, is compressed to a high pressure through a compressor. Then, the pressurized feed gas is cooled down to as low temperature as possible through heat exchange with the return gas and other refrigerants in a countercurrent heat exchanger (also termed a cold box). The cooled feed gas from the cold box enters a decompressor (typically a Joule-Thomson valve), expanding to a low pressure, through which cooling occurs with some liquid product produced in the reservoir. The low-temperature, low-pressure vapor portion of the feed gas returns to the compressor inlet after releasing the cold energy in the cold box to repeat the cycle. According to whether the refrigeration unit is employed and the specific configuration of the refrigeration unit, the gas liquefication method can be divided into Linde-Hampson cycle, cascade refrigeration cycle, mixed refrigeration cycle, and expander cycle [26–28].

The cascade refrigeration cycle and the mixed refrigeration cycle are two most widely used processes for large-scale gas liquefaction, especially in the field of the Liquefied Natural Gas (LNG) production due to their high exergy efficiency. However, the cascade refrigeration cycle and the mixed refrigeration cycle have to deal with the distribution of the vapor and liquid phases of the refrigerants, making them less suitable for intermittent operations. Therefore, these two cycles are not commonly used in the LAES system [29,30]. In most studies, the air liquefaction unit of the LAES system is based on the Linde-Hampson cycle and the expander cycle [31].

Linde-Hampson cycle is known as the most straightforward gas liquefaction process in which the low-temperature return gas is the only cooling load in the cold box, as shown in Figure 2.4 (a). The advantages of the Linde-Hampson cycle are its simple configuration, long lifespan, and low cost since there are no moving parts and extra refrigeration units. However, the

exergy loss of the irreversible throttling process and the mismatch of the temperature profile in the cold box lead to its exergy efficiency below 10% [32,33].

One of the most commonly used expander cycles for air liquefaction is the Claude cycle. The basic Claude cycle uses a two-stage expansion process with an expander and a Joule-Thomson valve (JT valve), as shown in Figure 2.4 (b). Thus, there are two cold sources to provide cooling load in the cold box: one is the low-temperature air in the gaseous phase after expanding in the JT valve, which is the same as the Linde-Hampson cycle; the other one is a stream of air out of the expander, which increases the exergy efficiency further. There are two additional (modified) Claude cycles, termed as Kapitza cycle and Heylandt cycle (see Figure 2.4 (c) and (d)), which are generally utilized for low-pressure and high-pressure (up to 20 MPa) air liquefaction, respectively [31,34]. As a modification or an extension to the Claude cycle, the Collins cycle (Figure 2.4 (e)), which uses multiple expanders instead of a single expander has also been proposed for the performance enhancement. However, the Collins cycle is not yet economically feasible due to its complex configuration [35].

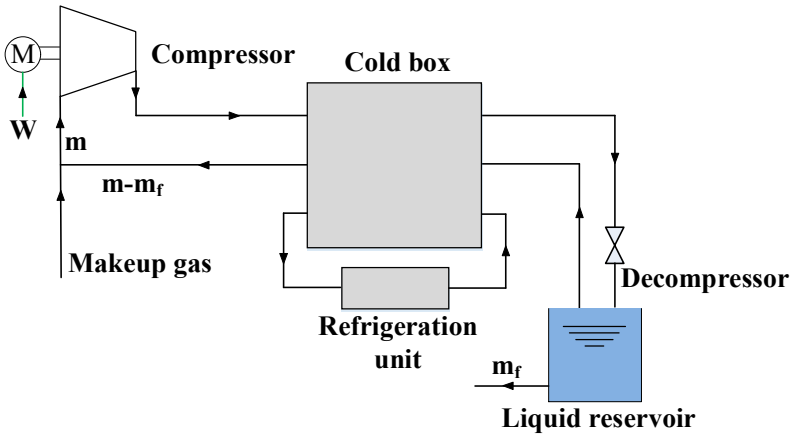

Figure 2.3 Basic configuration of gas liquefaction.

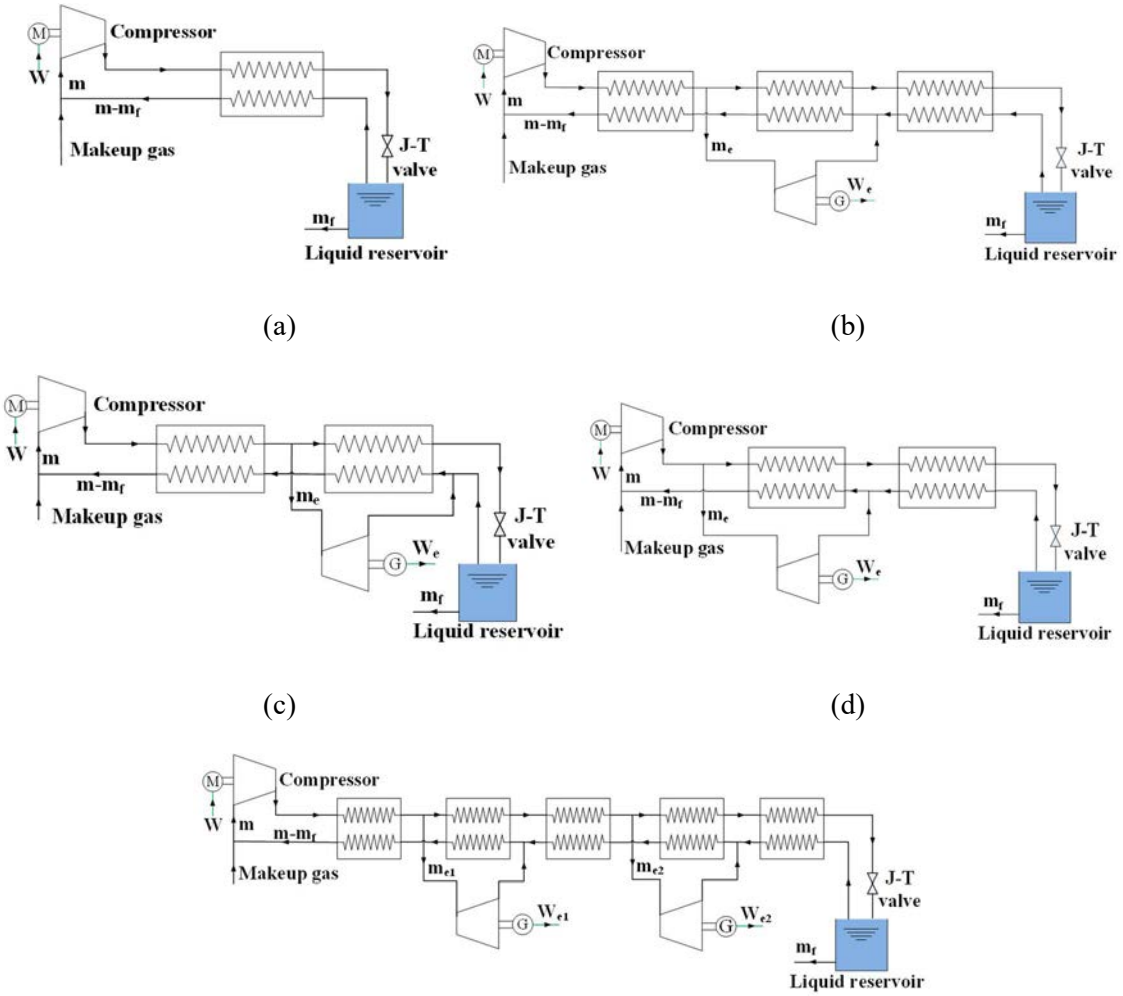

Figure 2.4 Common used air liquefaction cycles: (a) Linde-Hampson cycle; (b) Claude cycle; (c) Kapitza cycle; (d) Heylandt cycle; and (e) Collins cycle.

To improve the thermodynamic performance of the whole LAES system, the configurations of these air liquefaction cycles usually need to be refined. A typical configuration of the Linde-Hampson cycle-based liquefaction process of a standalone LAES is given in Figure 2.5 as an example. Comparing with the conventional air liquefaction cycles, the main changes in the refined air liquefication process are discussed as follow:

- The inclusion of a more efficient expansion process: the cryo-turbine is usually adopted to replace the JT valve, reducing the big exergy loss caused by the irreversible throttling process.

- The use of a high-grade cold recovery: the cold energy released from the liquid air evaporation during discharging is captured and stored in a high-grade cold storage unit. The high-grade cold storage unit contains one or multiple stages (a two-stage cold storage unit is illustrated in Figure 2.5), each of which is filled with latent or sensible thermal energy storage materials for corresponding working temperatures. In this way, the exergy loss caused by the mix of different grades of cold can be reduced. During charging, the cold energy stored in the high-grade cold storage unit is recovered and introduced into the cold box for cooling supply. The heat transfer fluids of the high-grade cold storage unit could be pressurized air, pressurized nitrogen, propane, and methanol, and so forth.
- Compression heat recovery: the heat generated during the air compression is recovered and stored in a compression heat storage unit. The heat storage unit also contains one or multiple stages filled with latent or sensible thermal energy storage materials for different storage temperature ranges (a one-stage compression heat storage unit is shown in Figure 2.5). The stored compression heat is usually reused in the discharging process for power generation enhancement.

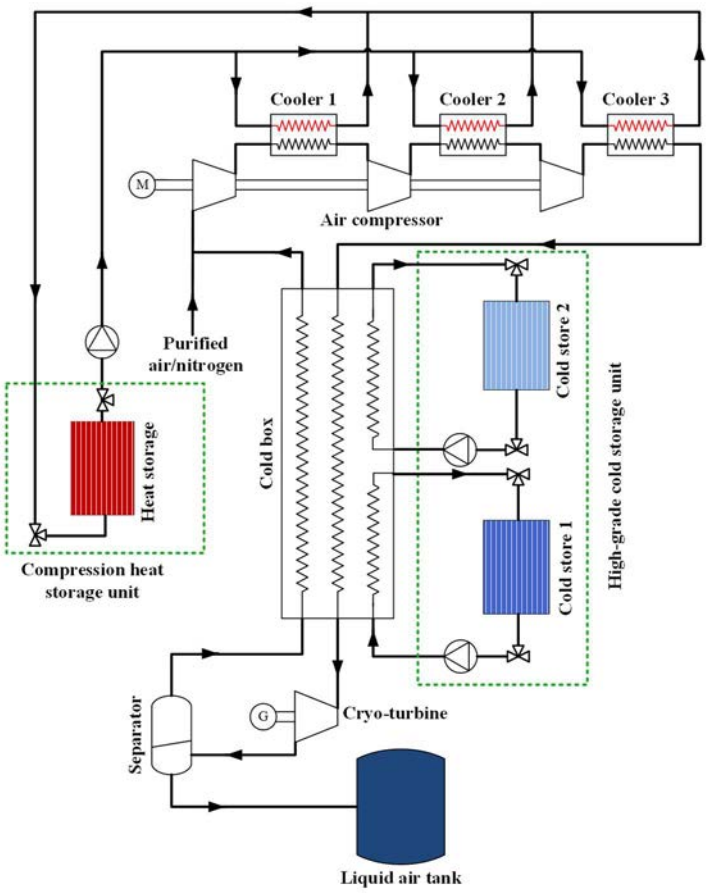

Figure 2.5 A typical Linde-based air liquefication process in the standalone LAES system.

2.1.2.2 Power recovery (discharging process)

The power recovery process of a LAES system refers to the process that the stored cryogenic exergy in the liquid air is extracted and converted back to electrical energy. This process could be realized by one or more of the following four basic cycles of direct expansion cycle, Rankine Cycle, Brayton cycle, and combined cycle [30], as summarized in Figure 2.6:

In the direct expansion cycle (Figure 2.6 (a)), the cryogen is pumped up to over its critical pressure and then heated to approximately atmospheric temperature by using ambient heat, or to a higher temperature by waste heat or combustion with fuel, before expansion to generate power. The Rankine cycle (Figure 2.6 (b)) uses the cryogen as a heat sink to condense the working fluid (e.g., propane, methane, ethane, and carbon dioxide), and the atmosphere or waste heat, if available, as the heat source to generate power. In the Brayton cycle (Figure 2.6

(c)), a compressor is employed to bring the working fluid to a high pressure for expansion to produce electricity, whereas the cryogen is used to cool down the working fluid before entering the compressor to reduce compression work and increase efficiency. The combined cycle (Figure 2.6 (d)) integrates the direct expansion cycle with either the Rankine cycle or the Brayton cycle to enhance the overall performance.

The direct expansion cycle has the lowest cryogenic exergy utilization efficiency among the four cycles discussed above, as it only uses the mechanical (pressure) part of the cryogenic exergy and discards the thermal part into the environment. The combined cycle uses both the mechanical part and the thermal part of the cryogenic exergy, and hence has the highest exergy efficiency.

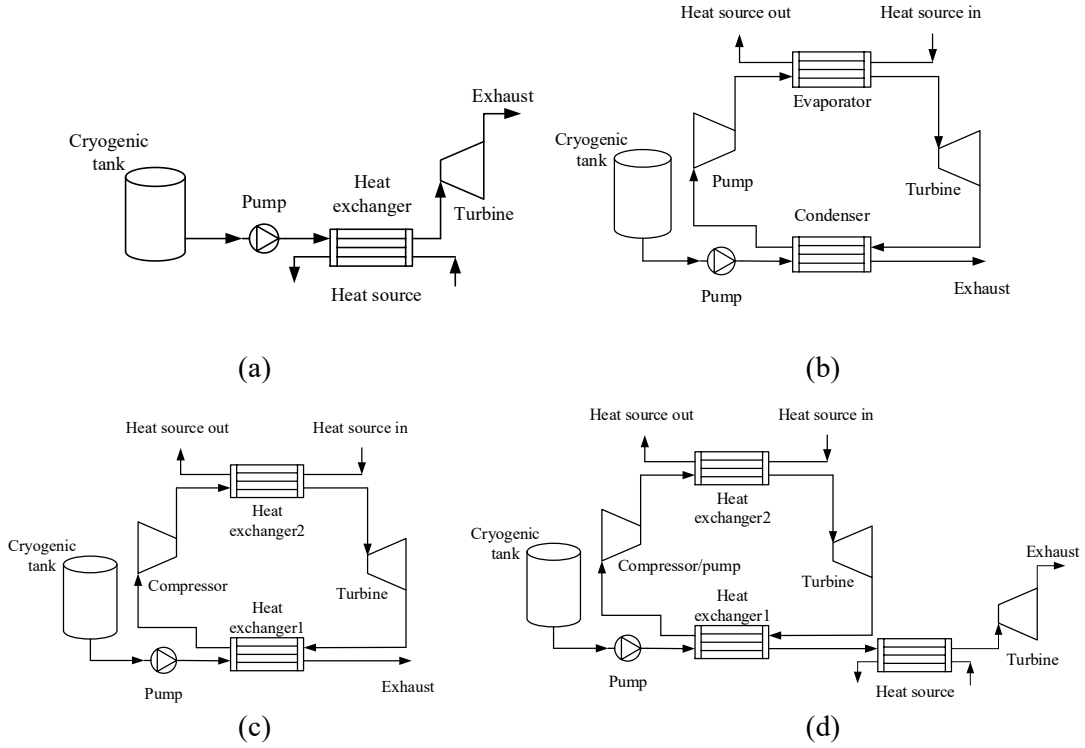

Figure 2.6 Common cycles for power generation from cryogenic exergy: (a) direct expansion cycle; (b) Rankine cycle; (c) closed Brayton cycle; and (d) Combined cycle.

A typical configuration of the power recovery process in a standalone LAES is given in Figure 2.7. One can see that in the standalone LAES system, the thermal part of the cryogenic exergy of the liquid air is recovered and stored in the high-grade cold storage unit for use in

the liquefaction process. Therefore, only the mechanical part is exploited to generate electricity, making the direct expansion cycle the most suitable power recovery process.

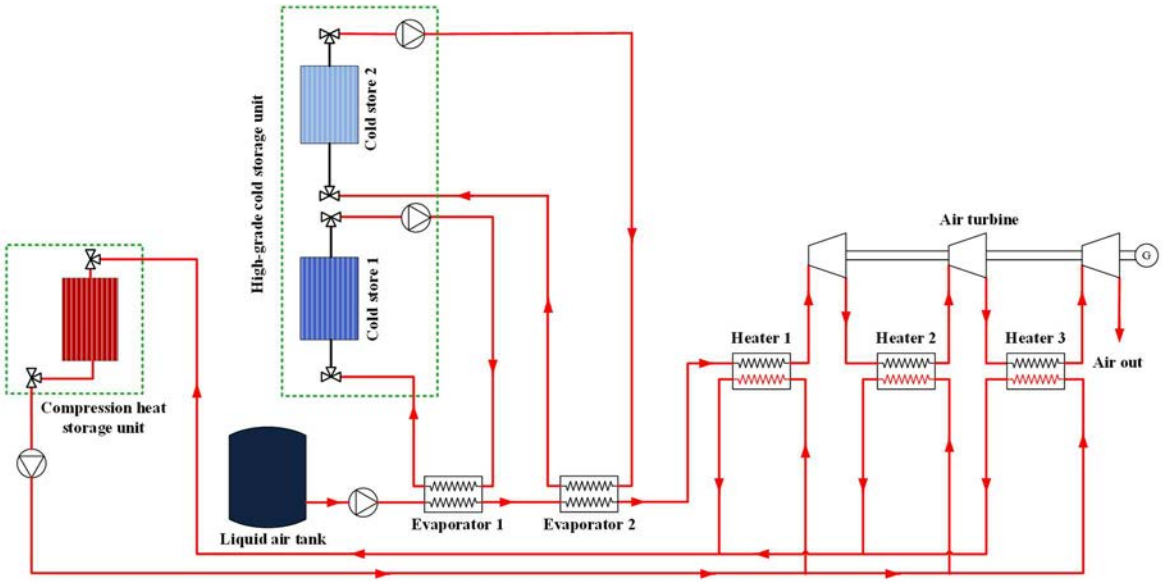

Figure 2.7 A typical power recovery process in the standalone LAES system.

2.1.3 Comparison with other energy storage technologies

As shown in Figure 2.8, the functions that energy storage can provide can be classified by energy, power, and discharge duration [7,13]. Based on this, LAES belongs to the medium-to-long-term energy storage technology for large-scale applications (energy management and some of the grid support functions). Pumped Hydro Storage (PHS), Compressed Air Energy Storage (CAES), flow batteries, and hydrogen storage coupled with fuel cell are capable of providing equivalent or similar functions to the LAES. On the contrary, supercapacitor, flywheel, Li-ion batteries, etc. are usually utilized for power quality and reliability enhancement applications, which the LAES cannot cover without specific measures, e.g., Spin-Gen (i.e., keeping the turboexpander-generator pre-synchronised to the grid and motoring during periods when a dispatch is expected).

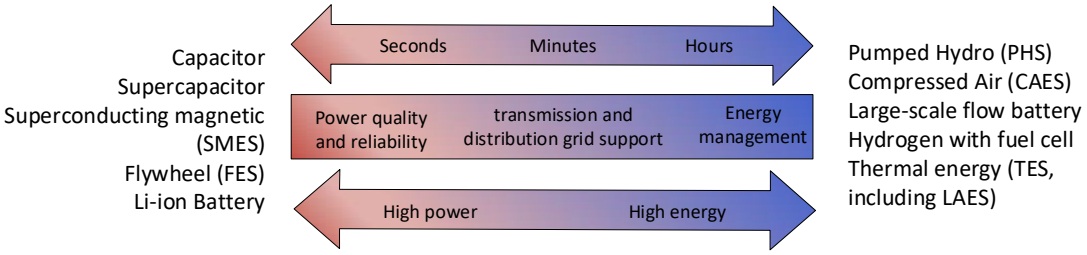

Figure 2.8 Energy Storage functions by the needs in energy, power, and discharge duration.

Some critical technical performances of the LAES, PHS, CAES, large-scale battery (flow battery), and hydrogen storage are summarized in Table 2.1 for comparison purpose. It can be seen that flow battery and hydrogen storage coupled with fuel cell have power rating and storage capacity within 200 MW and hundred MWh, respectively. They are far less than those of the LAES, PHS, and CAES (GW/GWh). Among the GWh-scale energy storage technologies, the LAES shows a lower round trip efficiency and a lower level of technical maturity than PHS and CAES. Nevertheless, the potential of the LAES is huge due to no geographical constraints and high energy density. In addition, LAES has features that CAES and PHS do not have, e.g., combined heating, cooling and power.

Table 2.1 Comparison of technical characteristics of energy storage systems for large-scale application.

Storage method	Energy storage density (Wh/L)	Power rating	Discharge time	Round trip efficiency	Lifetime (year)	Response time	Daily self-discharge	Geological conditions	Maturity
LAES	97 [36] 120-200 [7] 60-120 [37]	100kW-300MW [7] Up to GW [17]	Hours-days [36]	50-70% [36]	20-60 [37] > 30 [17]	min [38,39]	~0.5-1% [7]	No	Demonstration – pre-commercialized
PHS	0.5-1.5 [7] 0.5-1.33 [40] 0.2-2 [41]	100-5000MW [7,36]	Hours-days [7,13]	60-80%	40-60 [7] 30-50 [42]	min [41]	~0 [43]	Strict	Matured
CAES	3-6 [7] 0.4-20 [40] 2-6 [41]	5-300MW [7,13]	Hours-days [7,13]	70% [13] 41-75% [41] 70-73% [42]	20-40 [7] 30-40 [42]	min [41]	~0 [43]	Strict	Commercialized
Flow battery (Vanadium redox)	16-33[7] 10-33 [40] 20-70 [41]	0-20MW [40] Up to 200MW [44]	Seconds-10h [13,36]	75-85% [13] 60-75% [41] 85-90% [36]	5-10 [36] 5-20 [13]	<sec [41]	0.15%[13] 0.2% [45]	No	Commercialized
Hydrogen storage coupled with fuel cell	500-3000 [7] 600 (20 MPa) [41]	0.1-50MW [36,42]	Seconds-days [7,36] Hours-weeks [41]	35-42% [42] 20-50% [46]	10-30 [41] 5-20 [13]	< sec [13] sec-min [41]	~0 [43]	No	Developing

2.2 Standalone LAES system

2.2.1 Thermodynamic analysis of standalone LAES systems

A standalone LAES system operates independently without energy inputs from external sources. It is, therefore, more flexible in terms of site selection, but further round trip efficiency improvement is difficult without a deep understanding of the system. Thus, along with the LAES technology proposed and developed, the thermodynamic performance of the standalone LAES system has been extensively researched to understand optimal operation conditions and ways to enhance the round trip efficiency.

To obtain the highest theoretical round trip efficiency of the standalone LAES system, Morgan et al. [39] studied an ideal LAES cycle (Figure 2.9) without considering the second law losses in the heat transfer processes. An increase in the charging pressure was found to give a higher liquid yield, and an increase in the discharging pressure contributed to a higher power generation. Both can enhance the round trip efficiency. However, the increasing discharging pressure had a negative influence on the cold recycle, and hence beyond 12 MPa, the theoretical round trip efficiency of this ideal LAES cycle could reach a maximum of ~86%.

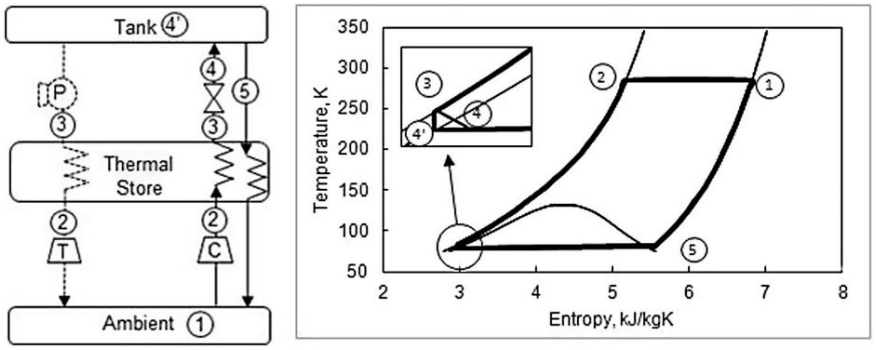

Figure 2.9 Ideal LAES cycle without accounting for second law losses [39].

Most thermodynamic analysis is based on a more technically feasible LAES configuration instead of the ideal LAES cycle. The study of the thermodynamic performance of the

standalone LAES can be divided into three aspects: system configuration, design/operating parameter, and component/material in the system.

2.2.1.1 System configuration

Several studies have been performed to understand the impact of different basic configurations (either different air liquefaction or different power recovery configurations) on the thermodynamic performance of the standalone LAES system. A summary is given in Table 2.2.

Air liquefaction Borri et al. [47] compared simple Linde, simple Claude and Kapitza cycles for a small-scale LAES system without considering the high-grade cold recovery. The results showed that the LAES configuration with a two-stage compression Kapitza cycle gave the best result with a performance enhancement of 25%. Abdo et al. [35] compared the simple Linde-based, the Kapitza-based and the Collins-based LAES systems without the high-grade cold recovery process. The Kapitza-based and the Collins-based LAES systems were found to have very similar thermodynamic performance, which were better than the Linde-based system. As is known, the high-grade cold recovery can improve the performance of the liquefaction cycle of the standalone LAES further. Based on this, Hamdy et al. [31] considered six different air liquefaction cycles (the simple Linde, the precooled Linde, the dual pressure Linde, the simple Claude, the Kapitza cycle and the Heylandt cycle) in a 'liquefaction block' of a standalone LAES system equipped with a cold storage unit, analysed and compared their thermodynamic performances, see Figure 2.10. Their results showed that although the precooled Linde liquefaction cycle performed the best among the three Linde-based LAES configurations, its exergy efficiency was still far below the other three Claude-based LAES configurations. Among the three Claude-based liquefaction cycles, the Heylandt process could achieve a higher exergy efficiency and lower specific power consumption at a higher charging pressure (≥12 MPa). However, the simple Claude process and the Kapitza process presented approximately the same thermodynamic performances and showed a better

performance in the standalone LAES system at a lower charging pressure. Morgan et al. [39,48] refined the layout of the liquefaction cycle in the LAES system further, utilizing four refrigeration expanders and arranging them in series as well as parallel in the cold box (Figure 2.11). They found an improved utilization efficiency of the available cold up to 91%, leading to a round trip efficiency of 57%.

The above discussion shows that the standalone LAES system with Claude or modified Claude liquefaction cycles gives a better thermodynamic performance (low specific power consumption for charging and high round trip efficiency) than that with Linde liquefaction cycles. However, the Claude-based LAES systems incur a higher initial investment and maintenance cost than the Linde-based LAES systems. Besides, the introduction of expanders can increase system control difficulties and decrease operation flexibility. Therefore, a balance needs to be stricken between the improvement of the round trip efficiency, the cost effectiveness, and the complexity of the system.

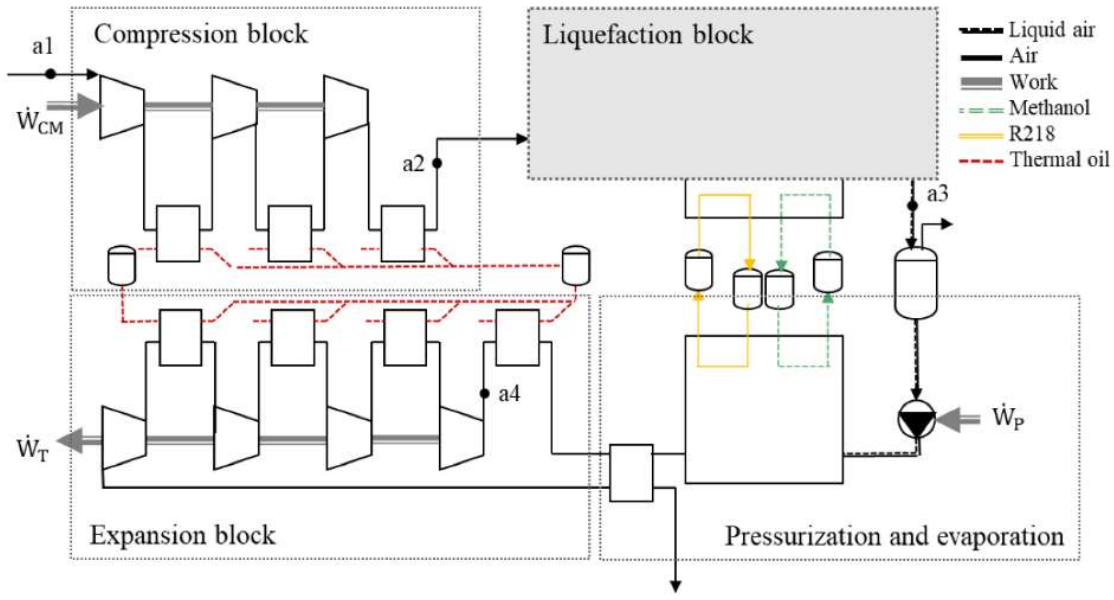

Figure 2.10 Overall configuration of standalone LAES with “black box” liquefaction block [31].

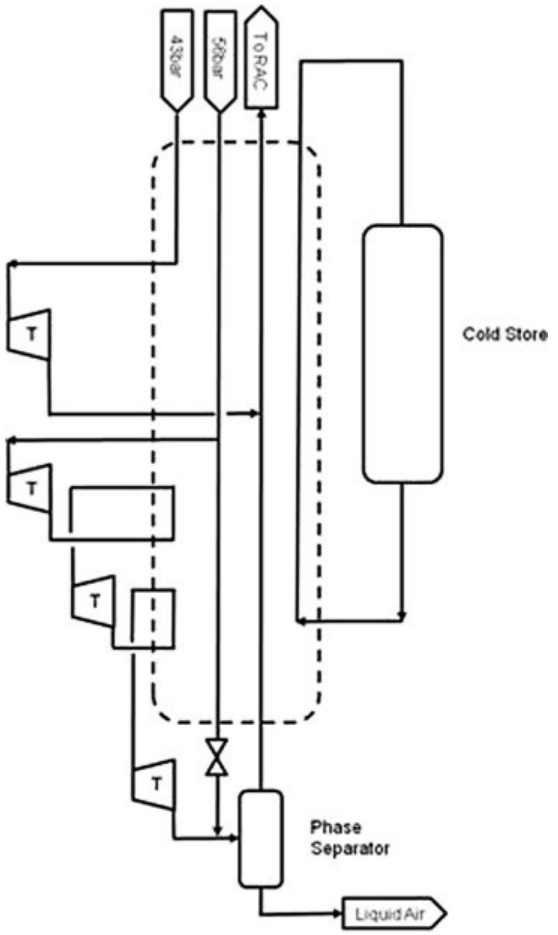

Figure 2.11 Layout of the cold box with four expanders [39].

Power recovery There are also studies focusing on the impact of power recovery unit configurations on the thermodynamic performance of the LAES. Hamdy et al. [49] analysed the performance of the LAES system with two different power recovery processes (i.e., cold exergy extracting methods). One is the direct expansion of the liquid air for power generation with the high-grade cold recycle for further air liquefaction use. The other one is the combination of an indirect Rankine cycle driven by the high-grade cold of the liquid air and a direct expansion cycle. The additional Rankine cycle could increase the specific power output by 24% during discharging but decrease the liquid yield from 0.603 to 0.204 during charging. As a result, the round trip efficiency of the LAES system with the Rankine cycle could only reach ~16-32%, much lower than the direct expansion with the cold recovery process (40%). A discharging process of the LAES system integrated with two fuel combustion chambers was proposed by Antonelli et al. [50], as shown in Figure 2.12. Compared with the direct air

expansion discharging process under ambient temperature, the equivalent round trip efficiency could be increased from 18% to 76%. Antonelli et al. [50] also refined the configuration of the discharging process to capture and utilize the cold energy released from the liquid air evaporation process to drive an Organic Rankine Cycle (ORC) or an open Brayton cycle. They found that the equivalent round trip efficiency could be increased to 77% and 90%, respectively. Chino et al. [51] also proposed the use of fuel combustion to increase the air inlet temperature of the gas turbine. The difference is that the high-temperature air at the gas turbine outlet generates steam for additional power generation through a steam turbine. In this way, the round trip efficiency of the LAES could exceed 70%. However, despite the improvement of the round trip efficiency, the use of fuel combustion in the LAES system increases the operation cost (additional fuel cost) as well as carbon emissions.

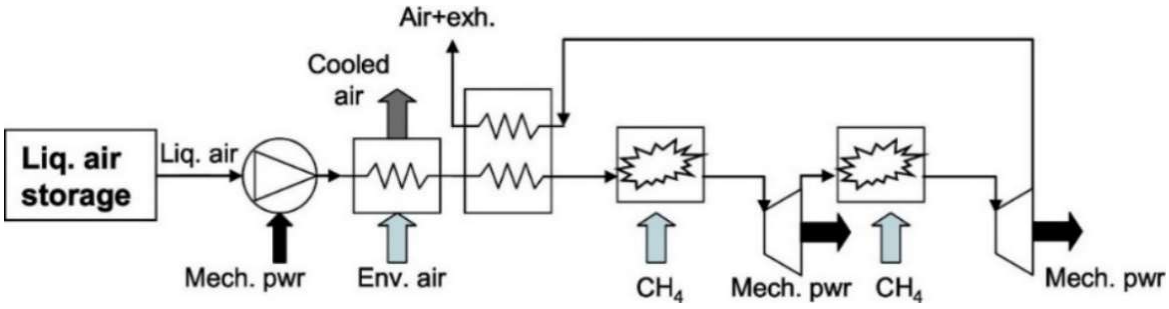

Figure 2.12 Discharging process of LAES with fuel combustion process [50].

.

Table 2.2 Summary of thermodynamic analysis of the standalone LAES - system configuration.

Focus	Ref.	Air liquefaction cycle /charging pressure/cold recovery	Specific power consumption/liquid yield/storage pressure	Power recovery /discharging pressure/heat source	Specific power generation	Round trip efficiency
Air liquefaction	[47]	Simple Linde, simple Claude, Kapitza cycle/ 240-260bar, 38-45bar /without cold recovery	2.5-2.6, 0.72-0.73, 0.71-0.72 kWh/kg / -- /1.0 bar	--	--	--
	[35]	Kapitza, Collins cycle/ 40 bar / with cold recovery	~70% of Linde cycle / -- / --	Direct expansion/200 bar/ compression heat	~120% of Linde cycle	--
	[31]	Simple, Pre-cooled, dual-press Linde cycle/ 200 bar / with cold recovery	0.56, 0.42, 0.53 kWh/kg / 0.337, 0.453, 0.288/ 1.03 bar	Direct expansion/150 bar/ compression heat	0.13 kWh/kg	23.37%, 30.98%, 24.8%
	[31]	Simple Claude, Kapitza, Heylandt cycle/ 95 bar, 95 bar, 130 bar/ with cold recovery	0.264, 0.264, 0.2633 kWh/kg / 0.54, 0.54, 0.59/ 1.03 bar	Direct expansion/150 bar/ compression heat	0.13 kWh/kg	46.9%, 46.9%, 49.0%
	[39,48]	4-expander Collins cycle/ 56.8 bar/ with cold recovery	~0.23 kWh/kg / -- / 9 bar	Direct expansion/190 bar/ compression heat	--	57%
Power recovery	[49]	Heylandt cycle/ 180 bar/ with and without cold recovery	-- /0.603 with cold recovery and 0.204-0.305 without cold recovery/1.0 bar	Direct expansion, combined cycle (direct expansion+Rankine cycle) /150 bar, 33 bar/ compression heat	0.119 kWh/kg, 0.136 kWh/kg	40.4%, 16.4-32.1%
	[50]	--	0.35 kWh/kg /-- /--	Direct expansion with fuel combustion/ 200 bar/ fuel combustion	0.472 kWh/kg	76%
	[50]	--	0.35 kWh/kg /-- /--	Combined direct expansion with fuel combustion and Rankine cycle or Brayton cycle / 200 bar / fuel combustion	0.479, 0.864 kWh/kg	77%, 90%
	[51]	Linde cycle/ 40 bar/ with cold recovery	-- /-- / 1.0 bar	Direct expansion with fuel combustion + steam turbine /40 bar / fuel combustion	--	73-87%

2.2.1.2 Operating parameters

The thermodynamic performance of a standalone LAES system is also affected by the design and operating parameters (e.g., charging pressure, discharging pressure, and storage pressure) for a given system configuration.

Guizzi et al. [52] studied the effects of the charging pressure on the system performance based on a standalone Linde-based LAES. Their results showed that increasing the charging pressure within a certain range increased the liquid yield, the round trip efficiency and the exergy efficiency. However, a maximum liquid yield existed with increasing charging pressure, beyond which the liquid yield kept almost constant, and the round trip efficiency started to reduce. In other words, when the discharging pressure is fixed, there is an optimal charging pressure at which the round trip efficiency is maximum for the standalone LAES system (54-55% at 18 MPa). Sciacovelli et al. arrived at the same conclusion regarding the charging pressure based on a standalone Collins-based LAES (~50% at 18.5 MPa) [53].

The influence of the discharging pressure on the round trip efficiency was also analysed by Sciacovelli et al. [53]. They showed that a higher discharging pressure gave a higher specific power generation and a lower cold recovery from liquid air during discharging. The increase in the power generation was found to be more important than that of the decrease in the cold recovery, leading to an improved round trip efficiency. However, the benefit obtained from the discharging pressure increase became very limited when the discharging pressure was higher than a threshold value. Morgan et al. [39] obtained similar results for a standalone Collins-based LAES, suggesting an optimal discharging pressure between 15-20MPa, beyond which the round trip efficiency of the LAES remained almost unchanged. However, the standalone Linde-based LAES system appears to give a different result. A reduction of the round trip efficiency with an increase in the discharging pressure occurred when the discharging pressure was higher than a certain level [54–56].

The liquid air storage pressure is also an important parameter for the LAES system. Increasing the liquid air storage pressure could reduce the specific power consumption of the charging process significantly [47,57] and improve the round trip efficiency [58,59]. With a storage pressure of 4 MPa, the round trip efficiency could reach 64.7%, which is about 9% higher than the LAES under the ambient storage pressure [59]. Furthermore, Peng et al. [60] studied the effect of the temperature of the compressed air at the inlet of the cold box, showing that the increase of the inlet temperature from 293K to 310K gave a decrease in the liquid yield from 83% to 79%, and a reduced round trip efficiency.

One should note that all the thermodynamic analyses reviewed above were carried out under the design conditions. Vecchi et al. [61] compared the thermodynamic performance of the LAES under both design and off-design conditions, with the latter caused by part-load discharging operations. Their results showed that a part-load operation had a strong effect on the specific power output. When the load decreased from 100% of the rated power to 90% and 50%, the specific power output decreased from 473 kJ/kg to 451 kJ/kg and 301 kJ/kg, respectively, leading to the decrease of the instantaneous round trip efficiency of the LAES from 48% to 44% and 31%, respectively.

2.2.1.3 Component/material

The performance of components (including turbomachinery, heat exchange equipment, and storage) plays an essential role in the LAES system. The distribution of the exergy loss of the components for a standalone Kapitza-based LAES system was studied by Lin et al. [58], and the result is reproduced in Figure 2.13. It can be seen that the highest exergy loss is due to compressor and turbine, followed by that of heat transfer in the condenser (cold box) and evaporator, and the lowest exergy loss are from the cryo-pump and cryo-expander. Thus, a high LAES system performance is linked to high efficiencies of compressors/turbines, and low heat transfer exergy loss in air liquefaction and evaporation processes. Guo et al. [62] compared the impacts of the efficiencies of compressors and turbines, and found that the

electrical round trip efficiency of the LAES was more sensitive to the isentropic efficiency of the turbine. Guizzi et al. [52] studied the effects of pressure drop in heat exchangers and the pinch-point temperature difference on the LAES performance, and their results showed that a 1% increase in pressure drop and a 5K increase in the pinch-point temperature difference could lead to a reduction of the round trip efficiency by 0.9% and 2.2%, respectively.

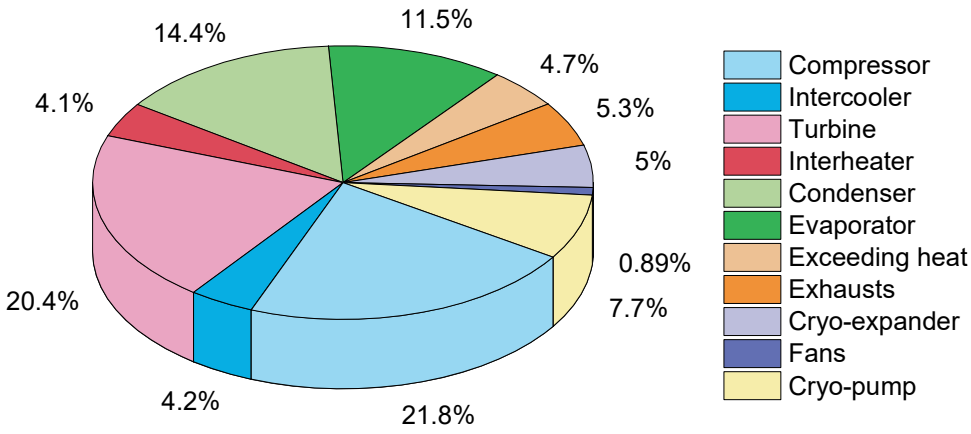

Figure 2.13 Distribution of exergy loss in the standalone LAES [58].

She et al. [63] investigated the influences of the storage exergy efficiency (liquid air storage, cold storage and compression heat storage) on the round trip efficiency of the standalone LAES equipped with the cold energy storage unit. Their results showed that the storage exergy efficiencies of the liquid air tank and the high-grade cold energy storage played a critical role in the round trip efficiency, and the thermal insulation for these two components must be taken seriously.

The high-grade cold storage performance is crucial to the overall LAES system performance, which has been studied in the literature. Packed bed is one of the most studied cold storage methods due to low cost and high reliability for practical applications (see Figure 2.14). Such packed-bed storage unit is charged and discharged periodically and synchronous to the overall storage system operation. Because the heat exchange process (both charging and discharging) in the packed bed presents very strong time-dependent behaviour, which deeply affects the

overall LAES system performance, dynamic analysis is needed to understand the dynamic characteristics.

Based on heat transfer governing equations derived from energy conservation and Fourier's law, a one-dimensional differential energy balances can be established (Equation (2.1) and (2.2)). They can be solved for temperature distribution of air (gas phase, T_f) and packed bed (solid phase, T_s) through coupling with mass and momentum balance equations [53,64,65]:

$$\varepsilon\rho_f C_{pf}\frac{\partial T_f}{\partial t}+\varepsilon\rho_f C_{pf}v\frac{\partial T_f}{\partial z}=\frac{\partial}{\partial z}\left(\lambda_f\frac{\partial T_f}{\partial z}\right)+h_{sf,v}\left(T_s-T_f\right) \tag{2.1}$$

$$\left\{\left(1-\varepsilon\right)\rho_s C_{ps}\right\}\frac{\partial T_s}{\partial t}=\frac{\partial}{\partial z}\left(\lambda_s\frac{\partial T_s}{\partial z}\right)+h_{sf,v}\left(T_f-T_s\right)-\beta_v\left(T_s-T_0\right) \tag{2.2}$$

In Equation (2.1) and (2.2), the subscripts f and s represent respectively the gas (air) and solid phases; ρ is the density; C_p is the specific heat capacity; ε is the void fraction; λ is the thermal conductivity; $h_{sf,v}$ is the volumetric convective heat transfer coefficient; β_v is the overall volumetric convective heat between vessel and environment; and v is the axial air velocity inside packed bed.

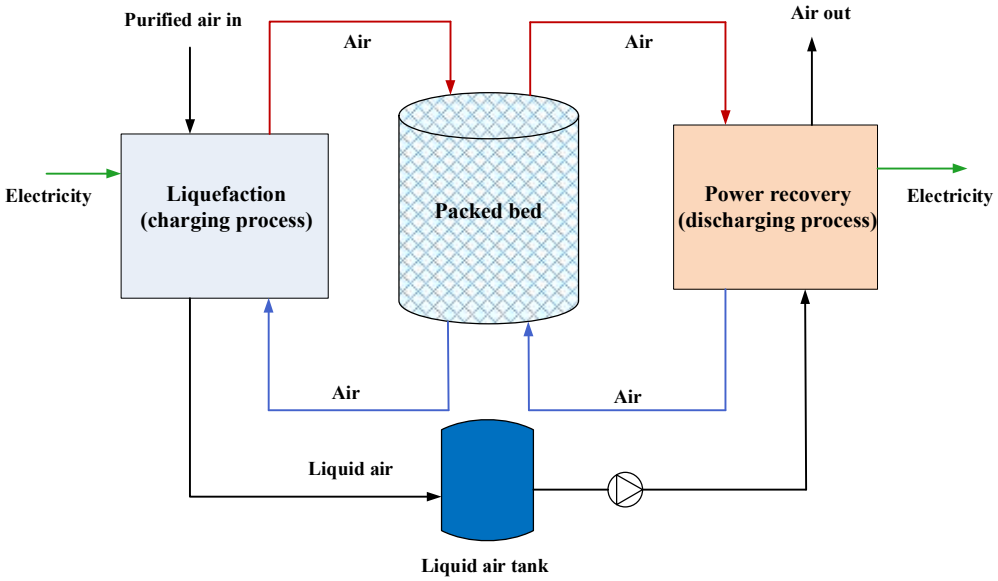

(a)

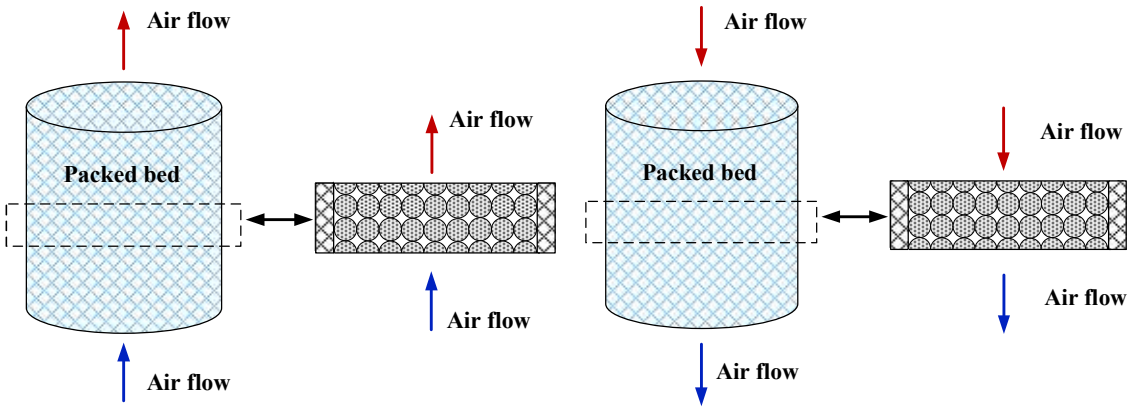

(b) (c)

Figure 2.14 Schematic diagrams of (a) a LAES system integrated with a packed bed cold store; (b) discharging cycle; (c) charging cycle.

The cycle performance of the packed bed and its impact on the overall LAES system were studied, and the temperature profiles along the packed bed over 30 discharge and charging cycles of a standalone LAES system obtained by Sciacovelli et al. [53] are shown in Figure 2.15. It can be seen that the temperature stratification rapidly degenerates over cycles because the axial conduction (and dispersion) expands along the bed length with the charging/discharging cycles of the LAES system. The degeneration of the temperature stratification results in the decline of the specific power consumption for the charging process and the rise of the round trip efficiency from cycle to cycle, which finally stabilizes after about 20 cycles due to the establishment of the steady-state temperature profile in the packed bed. After 20-30 cycles, the packed bed storage unit reaches steady periodic behaviour, all charging and discharging processes run almost identically. Legrand et al. [66] investigated the dynamic behaviour of a packed bed in a LAES under periodic conditions, and they indicated that within one stabilized charging cycle, approximately 75% of the charging process could work under the design condition, beyond which the stored cold has been almost used up, leading to a dramatical decrease in the liquid yield. Lin et al. [58] proposed the use of a cascaded packed bed cryogenic storage, one for low to ambient temperature and the other for low to middle temperature, to reduce the exergy loss. Their results showed an optimal middle temperature between -80 ℃ and -60 ℃, which could maximize the round trip efficiency of

the standalone LAES. Hüttermann et al. [67] defined a storage efficiency representing the usable share of the total thermal capacity of the packed bed storage. Nine different storage materials for the high-grade cold storage packed bed were compared by computational simulations. Polypropylene, polyethylene, sodium chloride and quartz were found to give the high storage efficiency, good feasibility, and low costs, and were therefore recommended.

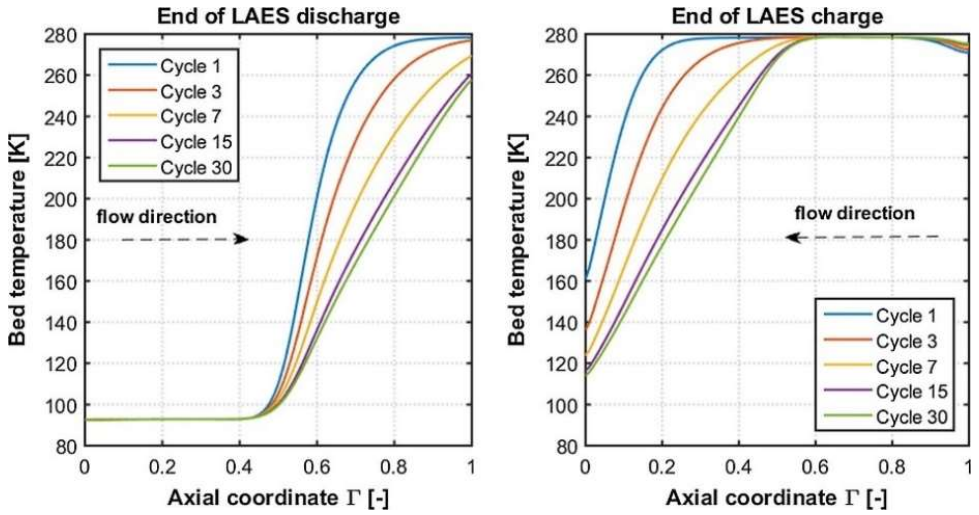

(a) (b)

Figure 2.15 Packed bed temperature profiles after (a) LAES discharging and (b) LAES charging for different cycles [53].

2.2.2 Configuration and optimization of the standalone LAES system

Based on the baseline LAES system (basic air liquefaction cycle + basic power recovery cycle from cryogenic exergy), efforts have been made to improve the round trip efficiency and to develop more functions through optimizing the system configuration.

2.2.2.1 Utilization of surplus compression heat for additional power generation

She et al. [54] studied the efficiency enhancement of the LAES and found as much as 40% of the excess compression heat at ~180 ℃ when a three-stage expansion process is employed. This part of excess heat can be fully utilized if the stages of the expansion are increased to five, which could give an enhancement of the round trip efficiency by about 5-7%. This is clearly not very attractive due to costs. As a result, the excess heat was proposed to generate

additional electricity by driving an ORC (as shown in Figure 2.16), which could improve the round trip efficiency by ~12%.

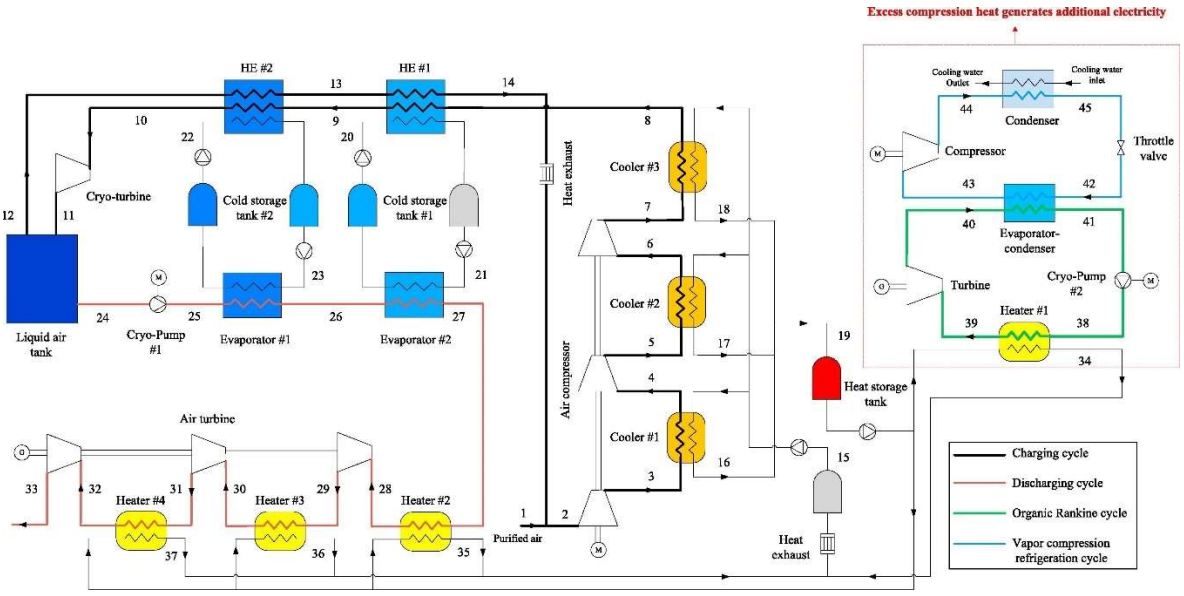

Figure 2.16 A schematic diagram of the standalone LAES system with ORC for excess heat utilization [54].

Since then, several studies were published on the use of excess compression heat for power generation and efficiency enhancement. Peng et al. [55] proposed the use of the excess compression heat to produce cold energy by an absorption refrigeration cycle for use as a low-temperature cold source for improving power generation efficiency of ORC (denoted as LAES-ORC-ARC, as shown in Figure 2.17 (a)). In this way, an increment of 13% in the round trip efficiency could be achieved, which is lower than 18% achieved by the ORC with the cooling water as the cold source (denoted as LAES-ORC, as shown in Figure 2.17 (b)). Zhang et al. [68,69] compared ORC and Kalina Cycle in the standalone LAES for surplus compression heat utilization. The subcritical ORC with dry fluid as the working fluid was recommended due to higher round trip efficiency (~57%), simpler configuration, and lower operating pressure. Liu et al. [70] proposed a configuration of the LAES, with thermoelectric generators (TEG) installed for power generation using the excess compression heat as the hot source. Their round trip efficiency of the LAES system integrated with TEG could be

improved by about 1%-4.5%. Compared with Kalian cycle or ORC, the TEG showed a lower power generation but a shorter payback period of 3 years.

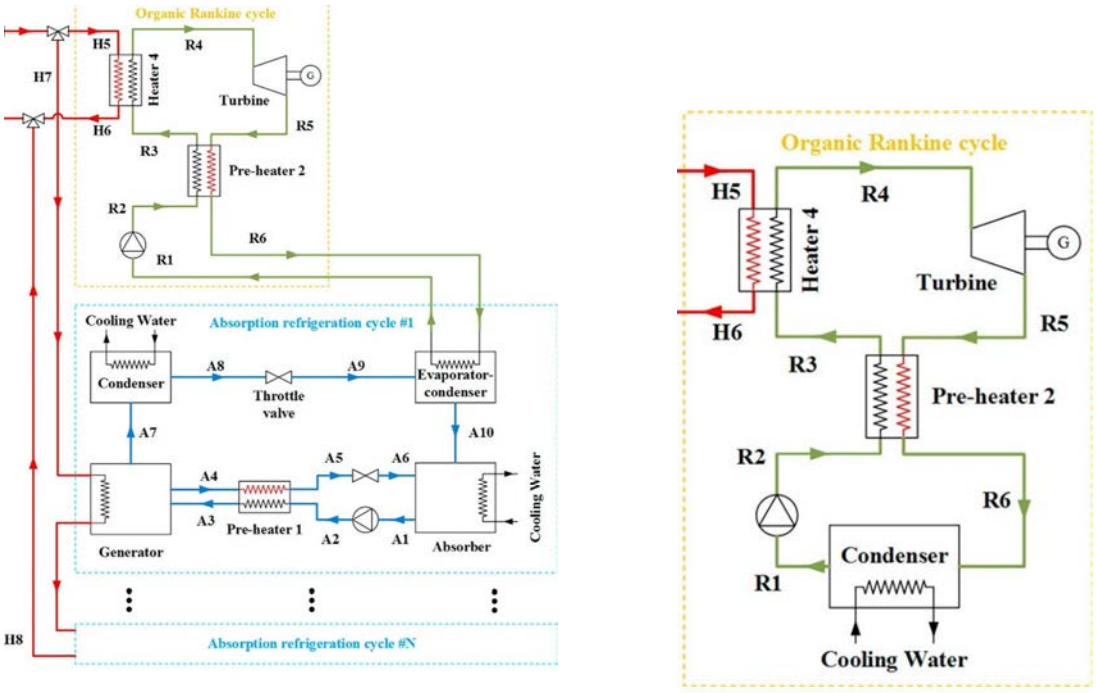

(a) (b)

Figure 2.17 Schematic diagrams of the ORC with (a) absorption refrigeration cycle, and (b) cooling water as low-temperature cold sources in the LAES [55].

2.2.2.2 Multi-functional LAES (combined power, heat, and cooling supply)

The other optimization based on the baseline LAES has mainly focused on developing multi-energy-vector services using the standalone LAES: the provision of by-products (heat and/or cold) to users. In this way, an equivalent electricity production of different commodities needs to be taken into account for the round trip efficiency (η_{RTE}) calculation [71]:

$$\eta_{RTE} = \frac{W_{\mathrm{dis}} + \frac{Q_{\mathrm{cooling}}}{COP_{\mathrm{c}}} + \frac{Q_{\mathrm{heat}}}{COP_{\mathrm{h}}}}{W_{\mathrm{ch}}} \tag{2.3}$$

where W_{ch} is the electricity consumption during charging; W_{dis} is the electricity generation during discharging; Q_{cooling} and Q_{cooling} are the cooling capacity and heating capacity that the

LAES can produce, respectively; COP_c and COP_h are the cooling and heating performances of the general ways to obtain cooling and heating, respectively.

Combined heat and power supply Guo et al. [62] found that the thermal oil temperature (compression heat storage medium) is still high enough to produce domestic hot water after superheating the air at the inlet of the turbine. In this way, the round trip efficiency of the standalone LAES could be improved from about 46% to 60%.

Combined cooling and power supply Tafone et al. [72–74] proposed a cogenerative configuration of the LAES system by controlling the turbine outlet temperature at 5 ℃ for cooling supply, giving a round trip efficiency of ~40%. The round trip efficiency could be further improved to about 48% if an ORC is adopted to recover the excess compression heat for power generation (as shown in Figure 2.18 (a)).

Combined heating, cooling and power supply Tafone et al. [75] further improved the standalone LAES to a trigenerative configuration, as shown in Figure 2.18 (b), in which the excess compression heat is utilized in series to drive an ORC as well as an absorption chiller for additional power and cooling output. Besides, the remaining low-grade waste heat is further used for the provision of domestic hot water. In this way, the overall round trip efficiency could reach 55.72%. Al-Zareer et al. [76] investigated the integration of the LAES with a solid-gas sorption cycle driven by the compression heat for cooling supply. The remaining compression heat is used for heating supply directly. They found an overall exergy efficiency of 53.7% when the cooling product was provided at 0°C. Gao et al. [77] also proposed a trigeneration LAES system for combined cooling, hot water, and power supply, as shown in Figure 2.19. The compression heat is used both in series and parallel to drive an absorption refrigeration unit, superheat the air at the inlet of turbines, and produce hot water in a heater. This system could regulate the output of power, cooling, and hot water to adapt to different energy demands in different seasons by the flexible distribution of the compression

heat. They obtained a round trip efficiency as high as 55.4% and 54.7% in the winter and summer mode, respectively.

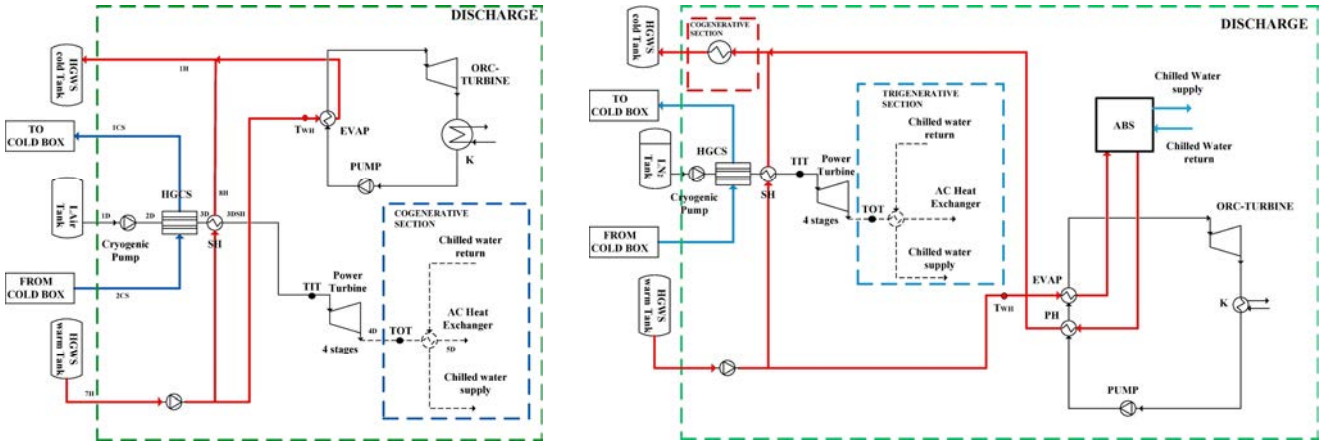

(a) (b)

Figure 2.18 Schematic diagrams of (a) cogenerative and (b) trigenerative configurations of the discharging cycle of the standalone LAES [74,75].

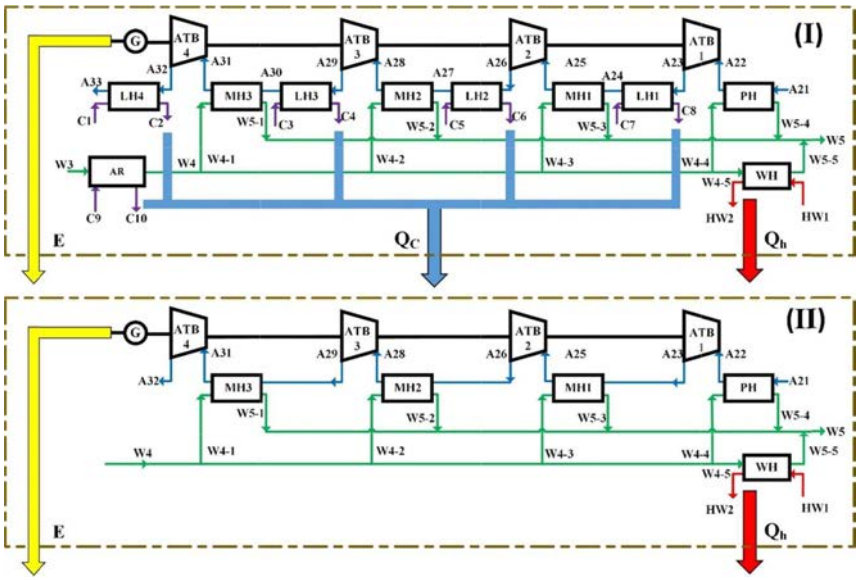

Figure 2.19 Schematic diagrams of the discharging cycle of the standalone LAES for trigeneration: (I) in summer, and (II) in winter, spring, and autumn [77].

Summary The above review of the multi-functional LAES systems indicates that the provision of heating can always be realized by the use of compression heat. However, the provision of cooling uses two common methods: one by regulating the air temperature before expansion to obtain a low-temperature air at the outlet of the turbine for cooling supply; the

other by using the excess compression heat to drive an absorption refrigeration unit for cooling supply. The second way is more flexible than the first one because the cooling supply part is relatively independent of the power supply part, making the cooling capacity more easily adjustable and controllable.

Besides, from the review one can also see that little work has been done so far on the performance of the standalone LAES over a wide range of charging pressures across both subcritical and supercritical regions. This is because the standalone LAES for power supply only performs better at a high charging pressure. However, the standalone LAES produces a large amount of excess heat, especially at low charging pressures. The excess heat can be valuable for the multi-functional LAES to supply thermal products. In such a scenario, the comprehensive performance of the multi-functional LAES, especially at low charging pressures, needs to be assessed. Part of this Ph.D. work is to fill this gap.

2.3 Integrated LAES system

The LAES is a very flexible energy storage system that can be integrated with external thermal energy sources (either or both of heat and cold energy sources) and other industrial processes, e.g., Air Separation Unit (ASU), for performance enhancement.

2.3.1 LAES integrated with external cold sources

The charging process of the LAES can use external cold energy to improve the liquid air yield, which, as a result, has been widely studied.

Liquefying Natural Gas (NG) is the most energy-intensive step in the Liquefied Natural Gas (LNG) production chain [78]. The process consumes electricity to drive a refrigeration cycle for liquifying NG. When LNG is used, it needs to be heated by a heat source, such as seawater and/or via burning NG, for the regasification. This leads to a large amount of cold energy in LNG wasted if no recovery step is used during the regasification process. This calls for a cost-effective way to recover and reuse such high-grade cold energy. Thus, great efforts

have been made on using the LAES for cold energy recovery of LNG in recent years, as summarized in Table 2.3.

2.3.1.1 LNG for performance improvement of the air liquefaction process in LAES

LNG for refrigeration in LAES cold box Zhang et al. [79] studied the recovery of cold energy of LNG to cool down the compressed air directly. External heat was also introduced for power generation enhancement. These gave a round trip efficiency of ~70.5%. A similar method to recover the cold energy of LNG for the LAES system but without any external heat was studied by Li et al. [80], who obtained a round trip efficiency of ~60%.

Peng et al. [81] proposed a more flexible system design, denoted as LAES-LNG-CS, with the cold energy released during the regasification process of LNG captured and stored in the cryogenic energy storage unit of the LAES. Such additional stored cold energy could be reutilized in the LAES charging process to produce more cooling load in the cold box, leading to an increased liquid yield. The advantage of this LAES-LNG-CS system is that a cold storage is used to link the LAES side and the LNG side, making the LNG regasification process independent of the LAES system. In this way, the round trip efficiency of the LAES-LNG-CS system could reach ~88%. Kim et al. [82] also used a cryogenic energy storage tank to recover and store the cold energy of LNG for air liquefaction use. After such a cold recovery process, the ambient-temperature NG is used as the fuel in the LAES discharging process to combust with air for power generation, achieving a round trip efficiency of 64.2%.

Park et al. [83] proposed an integration method (denoted as MCES), which can be regarded as a combination of the systems proposed in [79] and [81]. The cold energy released from the LNG evaporation process is stored in a cryogenic storage unit, but only during the peak time. In the off-peak time, the compressed air is liquified by two cold sources: one is the stored cold energy at peak time, and the other is the direct heat exchange with LNG. They showed that the proposed MCES could obtain a round trip efficiency of 85.1%. Park et al. [84,85] proposed further to integrate the LAES system with the LNG regasification power plant

(called LPCES). The LPCES system has three different working modes corresponding to different working hours, as shown in Figure 2.20. During the off-peak period, the LAES is charged, whilst the LNG is introduced to the cold box of the LAES system to cool down and liquify the compressed air directly. During the peak period, the LNG is introduced to a standard regasification power unit for power generation, and the LAES is discharged. During the flat period, the LAES system is switched off, and the LNG is used to drive the standard regasification power unit. A very high round trip efficiency of 95.2% was achieved, although the regasification power unit needs to start and stop frequently, which is difficult for practical operations.

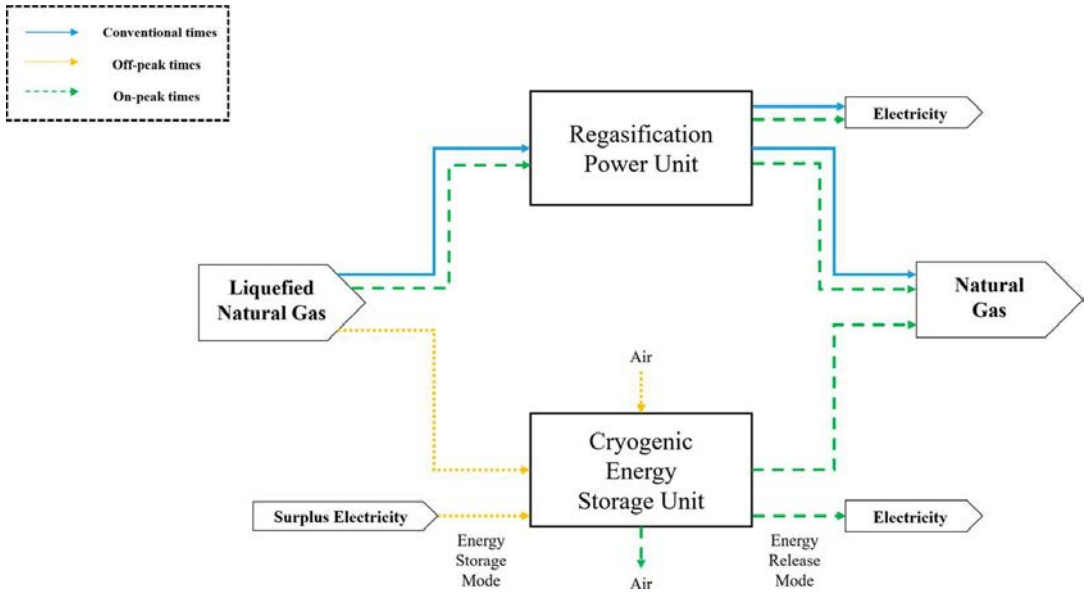

Figure 2.20 Working principle of LPCES system [84,85].

LNG for refrigeration in LAES interstage coolers In the methods reviewed above [79–85], the cold energy recovered from the LNG regasification process is finally used to cool down and liquify the air that has been already compressed to a high pressure by multi-stage compressors (i.e., providing the cooling load for the cold box in the air liquefaction cycle). Such LNG cold energy can also be used in a different way. Park et al. [86] proposed a new method to utilize the cold energy of LNG in LAES system. In their method, the cold energy of LNG is used as a cooling load for interstage coolers of multi-stage compressors. This was shown to reduce the power consumption for air compression significantly (as shown in Figure

2.21). A cascade utilization method of the cryogenic energy of the LNG was proposed by Qi et al., which uses the LNG cold energy as both the cooling load in the cold box and interstage coolers in series [87]. In this way, the round trip efficiency of the LAES could reach 129.2% (assuming LNG cold is free).

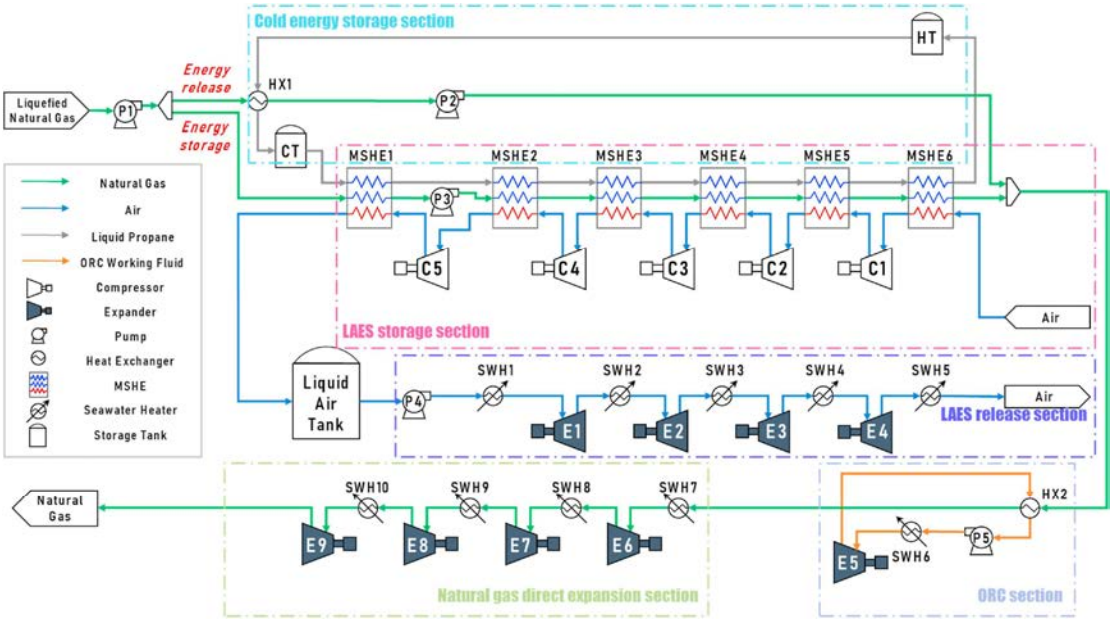

Figure 2.21 Schematic diagram of using LNG to provide interstage cooling for multi-stage compressors in the LAES [86].

LNG for refrigeration and compression in LAES In all the methods mentioned above to integrate the LAES with LNG, only the thermal component for the LNG cold energy is recovered and reused in the LAES, providing cooling load for the air liquefaction process. The mechanical (pressure) component for the LNG cold energy is usually used for power generation through direct expansion. A novel system design (denoted as LNG-CES, as shown in Figure 2.22 (a)) was proposed by Lee et al. [88], in which both the thermal component and the mechanical component [89] of the LNG cold energy were considered for driving the charging process of the LAES system for liquid air production. In this way, no more external electricity would be needed for the air compression process. Because the temperature of the LNG after heat exchange with air would be still very low in the LNG-CES system, an ORC was proposed for recovering the remaining cold energy from LNG, as shown in Figure 2.22

(b) (called as LNG-ORC-LAES) [90]. The overall round trip efficiencies of the LNG-CES and the LNG-ORC-LAES were found to be as high as 105.64% and 122.82%, respectively. To make this conceptual design of LNG-CES more industrially feasible, Lee et al. [91] applied more practical components in the LNG-CES system, such as the expansion valve and vapour-liquid separator, which improved the practicability of the proposed systems. He et al. [92] used a similar method to recovery the cold energy of LNG by LAES termed as LNG-ORC-LAES in [90]. The difference lied in that an additional ORC was proposed in the LAES discharging process to obtain high power generation, leading to an increase in the round trip efficiency to 141.88%.

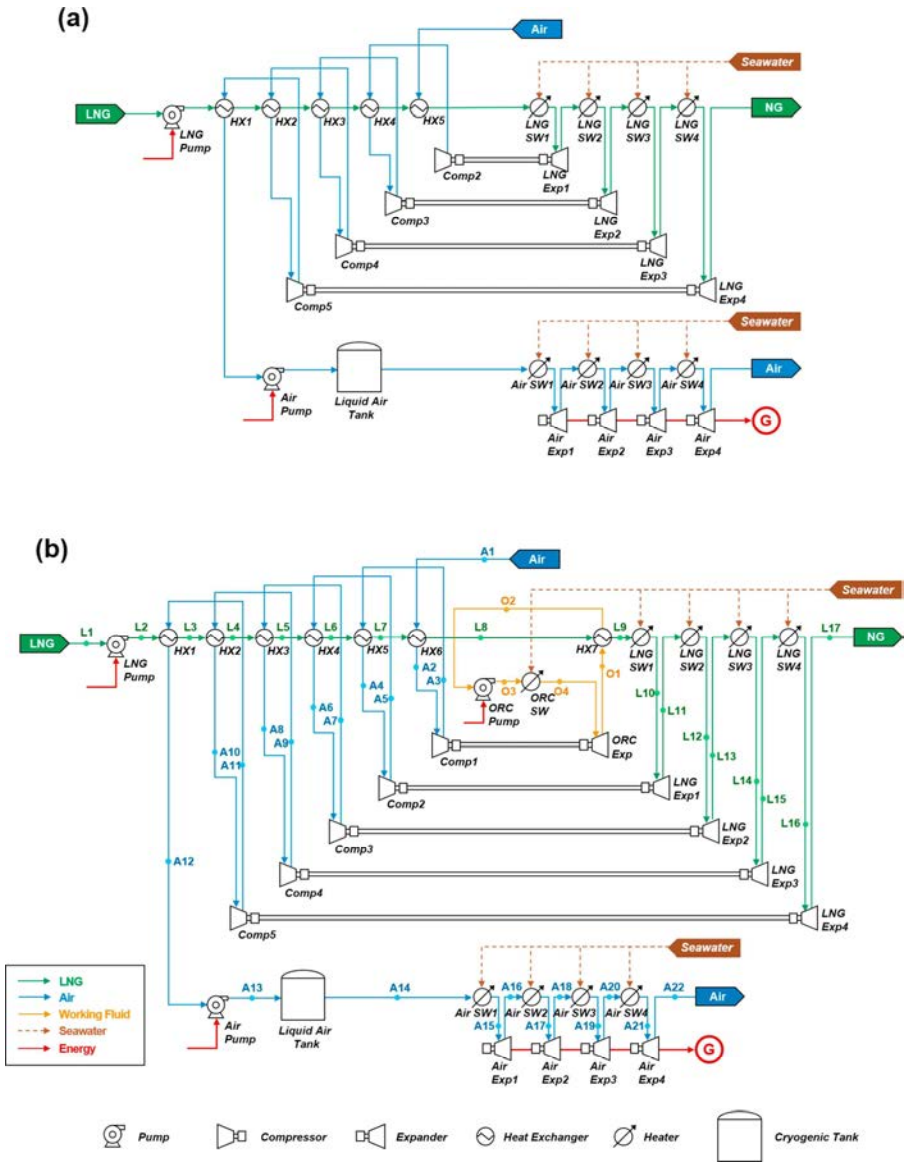

Figure 2.22 Conceptual design for (a) LNG-CES and (b) LNG-ORC-LAES [90].

Summary The literature review above (summarized in Table 2.3) shows that all the research on the utilization of LNG for the performance improvement of the air liquefaction process of the LAES can be divided into four sub-groups, as illustrated in Figure 2.23.

In Group I, the high-grade cold energy of the liquid air released from the LAES discharging process still needs to be captured, stored, and reused to provide the cooling load for air liquefaction. The thermal component of the LNG cold energy only provides some extra cooling load to the LAES charging process, leading to improved liquid yield and reduced power consumption of the air compression, and hence an increased round trip efficiency. The mechanical component of the LNG is used for direct power generation or goes to waste. Thus, most of the configurations of the LAES system in Group I keep the baseline LAES design (basic air liquefaction cycle + basic power recovery cycles from cryogenic exergy), with minor modifications to the layout of the cold box.

For Groups II and IV, the thermal component of the LNG cold energy is the only cooling load in the LAES to liquify the air liquefaction, which means there is no recycling process of the high-grade cold energy of the liquid air in the LAES. To ensure the liquid yield as high as possible, the liquid air storage pressure in these integrated systems is set to be higher than 1.8 MPa, at which the liquefaction temperature of the air (>116 K) is higher than the LNG temperature. The difference between Group II and IV lies in the way the mechanical component of the LNG cold energy is used: Group II uses the same way as Group I, while Group IV transfers the shaft work generated by the mechanical component of the LNG to the compressors of the LAES. Therefore, the configurations of the air liquefaction cycles in Groups II and IV need to be redesigned according to their respective situations, most of which are quite different from the baseline LAES.

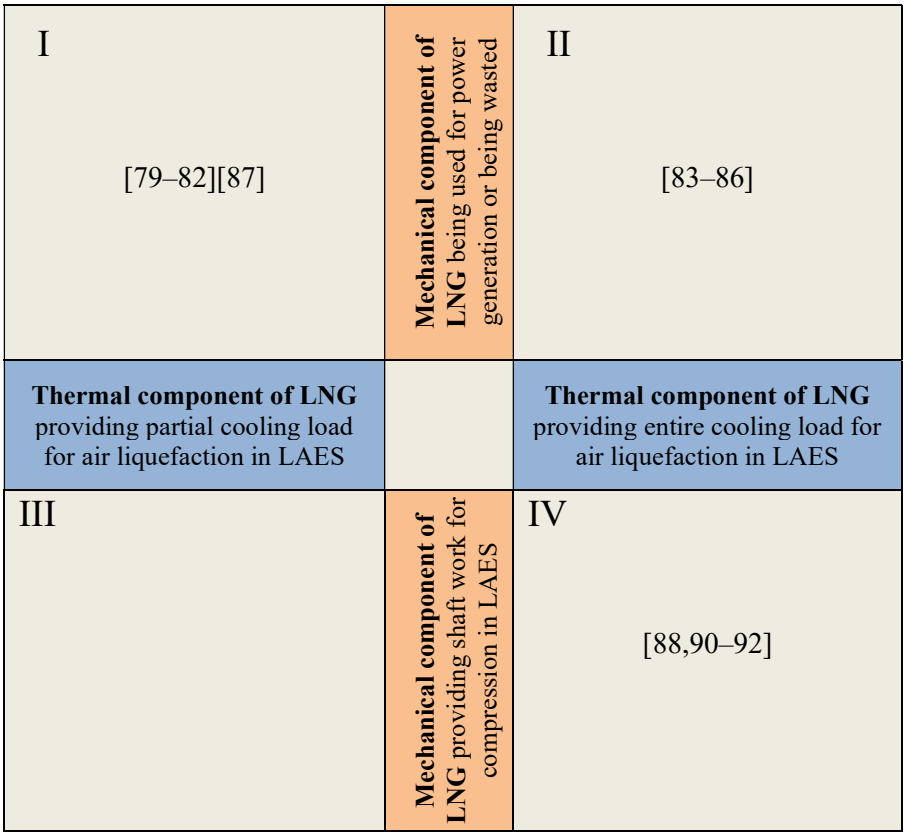

Figure 2.23 Categorization of the methods to integrate the LNG regasification process with the air liquefaction process of the LAES.

2.3.1.2 LNG for performance improvement of the power recovery process in LAES

As mentioned in Section 2.2.2, up to ~40% of the compression heat at ~180 ℃ is not be effectively used in the discharging process when a three-stage expansion process is employed [54]. She et al. [93] proposed a Brayton Cycle for power generation, using nitrogen as the working fluid, the excess compression heat as the hot source and the LNG as the cold source (denoted as LAES-Brayton-LNG). In this way, the total amount of power generation of the LAES can be significantly enhanced, and the round-trip efficiency can be further improved to 72%, which is much better than that using the excess compression heat alone for power generation as introduced in Section 2.2.2. The most significant advantage of the LAES-Brayton-LNG system is that there is no change of the current configurations of the baseline LAES system and the LNG regasification process, making it technically feasible and easily applied widely. The research [93], however, mainly focused on the thermodynamic analysis

of the overall system, with little work on optimizing the newly proposed Brayton Cycle, the core of this LAES-Brayton-LNG system.

Table 2.3 Summary of the integration methods between the LNG regasification process and the LAES.

Focus/Ref.	LNG regasification working mode	LAES working mode	Liquid air storage pressure	Round trip efficiency (η_{RTE}) (definition and result)	Exergy efficiency (η_{ex}) (definition and result)
Air liquefaction-Group I [79]	Off-peak: LNG for direct refrigeration in LAES cold box Peak+flat: no description	Off-peak: air liquefaction (charging) with LNG and CES as cold load Peak: power recovery (discharging) with TES and external heat for air heating + CES	0.2 MPa	$\eta_{RTE}=\frac{W_{\mathrm{dis}}}{W_{\mathrm{ch}}}$ 70.5%	$\eta_{\mathrm{ex}}=\frac{W_{\mathrm{dis}}}{W_{\mathrm{ch}}+(Ex_{in}-Ex_{out})}$ 50.73%
Air liquefaction-Group I [80]	Off-peak: LNG for direct refrigeration in LAES cold box +power generation Peak+flat: no description	Off-peak: air liquefaction (charging) with LNG and CES as cold load Peak: power recovery (discharging) with TES for air heating + CES	0.1-0.2 MPa	$\eta_{RTE}=\frac{W_{\mathrm{dis}}}{W_{\mathrm{ch}}-W_{\mathrm{LNG,off}}}$ 60.1%	/
Air liquefaction-Group I [81]	Off-peak: LNG with CES + power generation Peak: LNG with CES + power generation	Off-peak: air liquefaction (charging) with CES as cold load Peak: power recovery (discharging) with TES for air heating + CES	0.1 MPa	$\eta_{RTE}=\frac{W_{\mathrm{dis}}+W_{\mathrm{LNG,peak}}}{W_{\mathrm{ch}}-W_{\mathrm{LNG,off}}}$ 88%	$\eta_{\mathrm{ex}}=\frac{W_{\mathrm{dis}}}{W_{\mathrm{ch}}+(Ex_{in}-Ex_{out})}$ 64%
Air liquefaction-Group I [82]	Off-peak: not working Peak-time: LNG with CES + power generation	Off-peak: air liquefaction (charging) with CES as cold load Peak: power recovery (discharging) with fuel combustion + CES	0.2 MPa	$\eta_{RTE}=\frac{W_{\mathrm{dis}}}{W_{\mathrm{ch}}+LHV_{\mathrm{LNG}}}$ 64.2%	$\eta_{\mathrm{ex}}=\frac{W_{\mathrm{dis}}}{W_{\mathrm{ch}}+(Ex_{in}-Ex_{out})}$ 62.1%

Air liquefaction-Group II [83]	Off-peak: LNG for direct refrigeration in LAES cold box Peak: LNG with CES	Off-peak: air liquefaction (charging) with LNG and CES as cold load Peak: power recovery (discharging) with external heat for air heating	3.7 MPa	$\eta_{RTE}=\frac{W_{dis}}{W_{ch}}$ 85.1%	$\eta_{ex}=\frac{W_{dis}}{W_{ch}+(Ex_{in}-Ex_{out})}$ 56.7% (~)
Air liquefaction-Group II [84,85]	Off-peak: LNG for direct refrigeration in LAES cold box Peak+flat: LNG without being integrated with LAES + power generation	Off-peak: air liquefaction (charging) with LNG as cold load Peak: power recovery (discharging) with external heat for air heating	~2.5 MPa	$\eta_{RTE}=\frac{W_{dis}+W_{LNG,peak}-W_{LNG,flat}}{W_{ch}}$ 95.2%	/
Air liquefaction-Group II [86]	Off-peak: LNG for direct refrigeration in LAES interstage coolers + power generation Peak: LNG with CES + power generation	Off-peak: air liquefaction (charging) with LNG and CES as cold load Peak: power recovery (discharging) at ambient temperature	3.7 MPa	$\eta_{RTE}=\frac{W_{dis}+W_{LNG,peak}}{W_{ch}-W_{LNG,off}}$ 187.4%	$\eta_{ex}=\frac{W_{dis}+W_{LNG}+Ex_{out}}{W_{ch}+Ex_{in}}$ 75.1% $\eta_{ex}=\frac{W_{dis}}{W_{ch}+(Ex_{in}-Ex_{out})}$ 57.8% (~)
Air liquefaction-Group I [87]	Off-peak: LNG for direct refrigeration in LAES interstage coolers and cold box + power generation Peak: LNG without being integrated with LAES + power generation	Off-peak: air liquefaction (charging) with LNG as cold load Peak: power recovery (discharging) at ambient temperature + CES	0.15 MPa	$\eta_{RTE}=\frac{W_{dis}}{W_{ch}}$ 129.2%	$\eta_{ex}=\frac{W_{dis}}{W_{ch}+(Ex_{in}-Ex_{out})}$ 35% (~)

Air liquefaction-Group IV [88,90,91]	Off-peak: LNG for direct refrigeration in LAES interstage coolers + shaft work for compression in LAES Peak: not working	Off-peak: air liquefaction (charging) with LNG as cold load and shaft work for compression Peak: power recovery (discharging) at ambient temperature	4.4 →21 MPa [88,90] 3.6 → 1.8 MPa [91]	$\eta_{RTE}=\frac{W_{dis}-W_{LNG,off}}{W_{ch}}$ 105.64% [88], 122.82% [90] 135.98 [91]	$\eta_{ex}=\frac{W_{dis}+Ex_{out}}{W_{ch}+Ex_{in}}$ 68.6% [88], 70.3% [90], 68.12% [91] $\eta_{ex}=\frac{W_{dis}}{W_{ch}+(Ex_{in}-Ex_{out})}$ 38% [88] (~), 43% [90] (~)
Air liquefaction-Group IV [92]	Off-peak: LNG for direct refrigeration in LAES interstage coolers + shaft work for compression in LAES Peak: not working	Off-peak: air liquefaction (charging) with LNG as cold load and shaft work for compression Peak: power recovery (discharging with additional ORC) at ambient temperature	4.4 →21 MPa	$\eta_{RTE}=\frac{W_{dis}-W_{LNG,off}}{W_{ch}}$ 141.88%	$\eta_{ex}=\frac{W_{dis}+Ex_{out}}{W_{ch}+Ex_{in}}$ 73.9% $\eta_{ex}=\frac{W_{dis}}{W_{ch}+(Ex_{in}-Ex_{out})}$ 47% (~)
Power recovery [93]	Off-peak: LNG with CES + power generation Peak: LNG with CES + power generation	Off-peak: air liquefaction (charging) with CES as cold load Peak: power recovery (discharging) with TES for air heating + Brayton cycle driven by TES and CES + CES	0.1 MPa	$\eta_{RTE}=\frac{W_{dis}+W_{Brayton}}{W_{ch}}$ 72%	$\eta_{ex}=\frac{W_{dis}+W_{Brayton}}{W_{ch}+(Ex_{in}-Ex_{out})}$ 57%

*CES - cryogenic energy storage; TES - heat energy storage (compression heat storage); (~) - recalculated by author.
*Equations: *Ex* - external cold and heat sources exergy; *LHV* - low heating value; W_{LNG} - Power generation by LNG; *W* - Power consumption or generation;
*Subscripts: ch - charging process; dis - discharging process; off - off peak time; peak - peak time; flat - flat time;

2.3.2 LAES integrated with external heat sources

The discharging process of the LAES can be enhanced by using heat input. Consequently, the integration of standalone LAES with different external heat sources has been studied extensively.

Heat from power plants To increase the capacity of nuclear power plants for load shifting, the integration of the LAES with the nuclear power plant (denoted as NPP-CES) was proposed by Li et al. [94]. It has three working modes corresponding to different periods. During the flat time, the nuclear power plant works at its rated power. During the off-peak time, although the electricity demand is lower than the rated power of the nuclear power plant, the nuclear power plant still works as normal with part of the power output used to drive the charging process of the LAES. Then, during peak time, the nuclear power plant and the discharging process of the LAES work together for power supply to meet the peak electricity demand. Apart from the electrical integrated, the secondary loop from the nuclear power plant is integrated with the LAES for superheating the air before expansion, providing an avenue to increase the power output of the LAES. As a result, the round trip efficiency of the LAES could be improved to 71%. The power generation of the NPP-CES at the peak time was found to be as high as 2.7 times that of the nuclear power plant rated power. Analogously, Cetin et al. [95] proposed to use the LAES to help single flash geothermal power plants with load shifting. In return, the waste geothermal water is utilized to increase the air temperature in the LAES discharging process, resulting in a round trip efficiency of 46.7%. Cetin et al. [96] further proposed to integrate the LAES with binary geothermal power plants, in which the high-grade cold energy storage is removed from the LAES. Thus, during LAES discharging process, the cryogenic energy released from the liquid evaporation is recovered and used for power generation through a cryogenic ORC with the waste geothermal water as the heat source. The ORC has a thermal efficiency of 35.5%, whereas the LAES system gives a round trip efficiency of 28.4%.

Heat from solar thermal collectors Ji et al. [97] the use of the heat collected from a solar thermal collector as the heat source for air superheating during the LAES discharging process. The compression heat recovered from the LAES charging process was proposed for the hot water supply. Their round trip efficiency (without considering hot water) was 45.7%. Additionally, some 205-ton hot water (60 °C) could be provided by this integrated LAES (storage capacity: 3.9 MWh) per day. Ebrahimi et al. [98] proposed the use of thermal oil to store the heat from a parabolic trough collector, which is then used as the heat source in the LAES discharging process. The compression heat generated during the LAES charging process was proposed to store in a phase change material. The stored heat was used to drive a Kalina-based cogeneration cycle for combined power and cooling supply during peak times. The electrical round trip efficiency of this integrated system was found to be as high as ~58%.

Heat from Joule heating Nabat et al. [99] proposed an integration of a high-temperature thermal energy storage (by means of concrete) with the LAES system to store the heat produced by electrical coils with off-peak electricity. The stored Joule heat (1300 °C) was proposed for use in the LAES discharging process to superheat air before expansion. The heat from the turbine exhaust air (still at high temperature), together with the compression heat was used to drive an additional ORC for power generation. The remaining compression heat from the system was further utilized for additional electricity supply through a thermoelectric generator (TEG). These gave a round trip efficiency of 61%. Wu et al. [100] suggested the use of a thermochemical energy storage (Co_3O_4/CoO, 850-950 °C) for Joule heat storage. During peak times, the stored heat was used in the LAES discharging process for air superheating. They obtained a round trip efficiency of 47% without the use of compression heat.

2.3.3 LAES integrated with other industrial processes

Integrated with Air Separation Unit (ASU) Li et al. [101,102] considered the use of ASU to produce gaseous/liquid oxygen and liquid nitrogen during the off-peak time. For the oxygen

flow, the gaseous oxygen combusted with a fuel gas to drive a gas turbine [101], or the liquid oxygen was pressurized, heated and expanded to drive a high-pressure turbine, after which, it combusted with a fuel gas to drive a gas turbine [102]. As for the nitrogen flow, the liquid nitrogen was pumped and heated first and then expanded in a two-stage turbine for power generation. In the meantime, the carbon dioxide in the exhaust of the gas turbine is separated and condensed by the cold recovered from the liquid nitrogen, realizing carbon capture without additional energy input. The principle diagram is shown in Figure 2.24, and the overall exergy efficiency of this proposed system is about 64-70%.

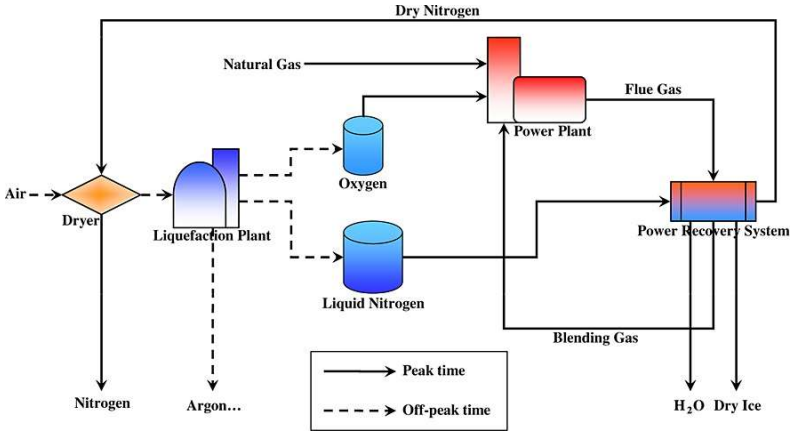

Figure 2.24 Principle diagram of the overall system of LAES integrated with ASU [102].

Pacheco et al. [103] proposed a very similar method to Li et al. [101,102]: oxygen and liquid nitrogen produced by the ASU are utilized for power generation through coal combustion and direct expansion, respectively. Pacheco et al. [103] built a complete model instead of a black box model in [101,102] to simulate the whole air separation process, as shown in Figure 2.25. Thus, the working process of the ASU to produce liquid nitrogen could be studied: the gaseous nitrogen product from the ASU needs to consume extra electricity for compression to a high pressure, before feeding to the main heat exchangers of ASU for liquefaction to give the liquid nitrogen. This process is regarded as the charging process of the LAES. As a result, their round trip efficiency of the LAES in this integrated system is only about 19.22%.

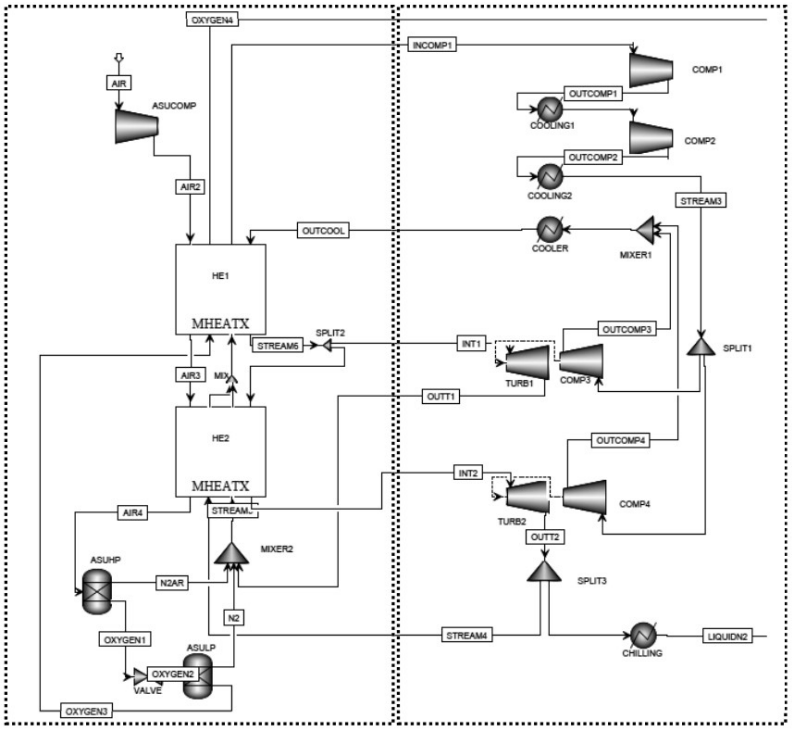

Figure 2.25 Integration of ASU with LAES charging process [103].

Wang et al. [104] investigated another way to integrate the ASU with the LAES, as illustrated in Figure 2.26. The conventional/baseline configurations of ASU and LAES are employed, and only the nitrogen flow was used as a bridge for their integration. The ASU side was suggested to work for the whole day to produce high-purity oxygen (99.99 mol%) and gaseous crude nitrogen (95.45 mol%). For the LAES side, the charging process of the LAES was proposed to work only at off-peak time, using the gaseous nitrogen from ASU as the working medium. During peak time, the discharging process of the LAES operates, as usual, generating electricity and releasing the gaseous nitrogen. This part of exhaust nitrogen is heated by the compression heat before introduced back to the ASU for the adsorber (air cleaning unit) regeneration. The round trip efficiency of this hybrid system was found to be around 39%, considerably lower than that of the baseline LAES. However, the payback period of this hybrid system (10 MW/80 MWh, including ASU) could be as short as three years, due to the additional revenue from the pure oxygen supply (as commodity) and heating supply (excess compression heat).

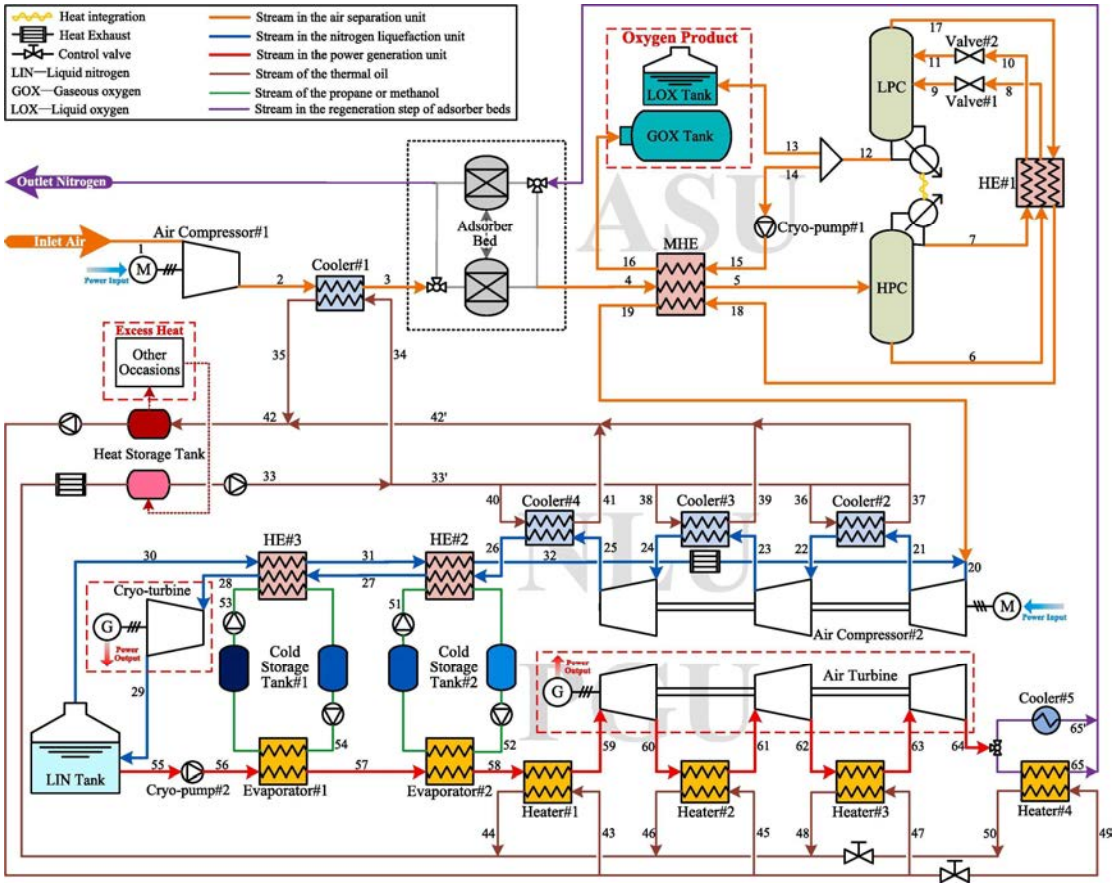

Figure 2.26 Schematic diagram of the LAES system integrated with ASU [104].

He et al. [105] proposed another way to integrate the ASU with the LAES system (denoted as ASU-ESG), in which the working capacity of the compression, cooling, purification equipment in the ASU side is shared with the LAES system without affecting the normal operation of the ASU, as illustrated in Figure 2.27. The ASU always works within 70-105% of the design load. Thus, when the gas load demand of the ASU is lower than 105%, the remaining load of the air compressors and cooling is occupied by the LAES for the charging process. During the LAES discharging process, the evaporation process of the liquid air occurs in the main heat exchanger of the ASU, providing additional cooling load to the ASU. Their results showed that the round trip efficiency of this combined system could increase from 46% to 65% when the gas load demand of the ASU increases from 70%-100%. The payback period of this LAES system (excluding ASU) was shown to be around 3-4 years.

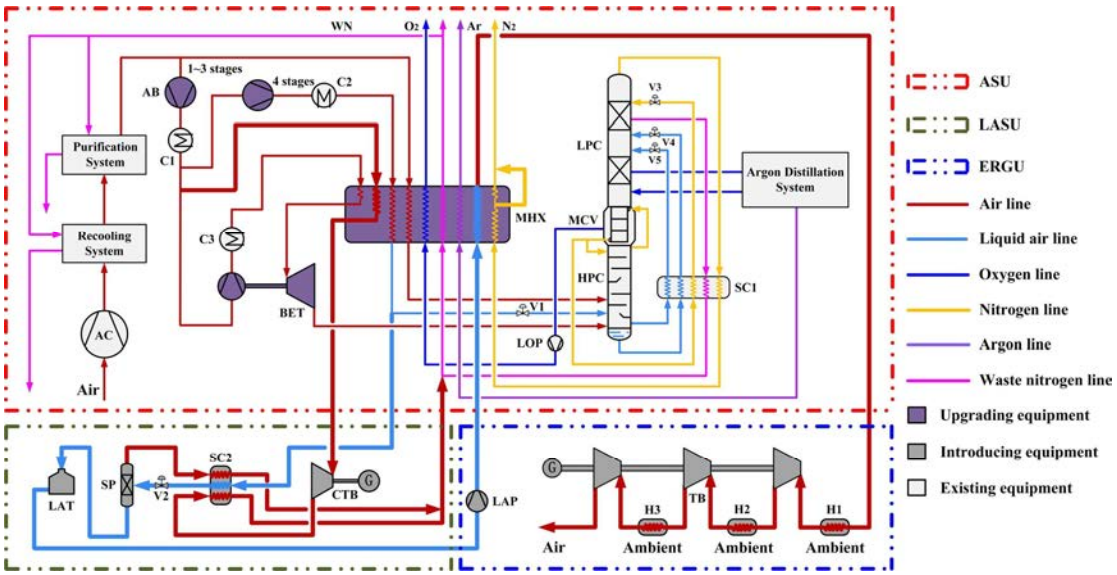

Figure 2.27 Flowsheet of the ASU-ESG system [105].

Integrated with other energy storage systems Kantharaj [106,107] explored the integration of a LAES system with a Compressed Air Energy Storage (CAES) system, with the liquid air as a backup of the CAES to save the storage space for high-pressure air. When the compressed air tank is almost full, some stored compressed air is liquefied. During peak time, the liquid air converts back to compressed air. The efficiencies of the forward and reverse conversions are 63% and 67%, respectively. Farres-Antunez [108] investigated the integration of LAES and a Pumped Thermal Energy Storage (PTES) system, as shown in Figure 2.28. The PTES provides the cooling load to the LAES for air liquefaction during the charging process. In return, the cold energy released from liquid air evaporation during the discharging process is used as the cooling load for PTES. The round trip efficiency of this hybrid storage system (~60%) is very close to that of the standalone LAES and PTES, but the energy density is improved significantly because the high-grade cold energy storage unit could be removed from this hybrid storage system.

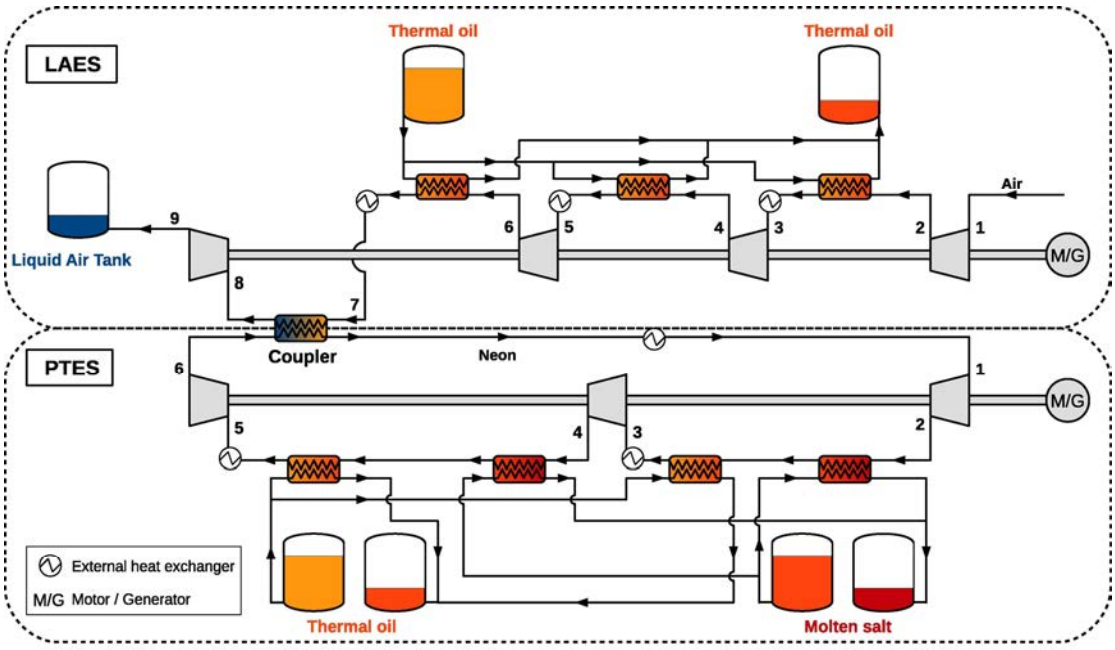

Figure 2.28 Layout of the combined system of LAES and PTES [108].

2.4 Decoupled LAES system

The volumetric energy density of liquid air is around 60-120 Wh/L which is much higher than that of the compressed air (0.5-1.5 Wh/L) [37]. Although it has an order of magnitude lower energy density than hydrogen (500–3000 Wh/L depending on the storage methods [37]), the liquid air can be stored at ambient pressure without the risk of flammability. Besides, liquid air can be transported easily with the current infrastructure. As a result, one can produce liquid air on site with offshore or onshore renewable energy [24,109], and transport the liquid air to end-user sites for electricity and cooling supply [25,110]. As the air charging and discharging processes operate in different locations, it is often referred to decoupled LAES. The decoupled LAES system has a good prospect because of its environmental friendliness and high flexibility. It is especially attractive when the end users have no access to the national grid infrastructures. The literature work on the decoupled LAES system is very limited, and the reported studies can be divided according to three application areas. The first is the use of liquid air as a fuel for transport (i.e., cryogenic engines); the second is to provide cooling and electricity for buildings; and the third is to integrate with other industrial

processes. A brief literature survey on the decoupled LAES is given in the following; see also Table 2.4 for a summary.

The decoupled LAES for transport Liquid air/nitrogen is able to provide power for vehicles through a cryogenic engine, thus the potential for contributing to zero-emission transport [111]. The first of such an attempt can be dated back to 1900 when Tripler Liquid Air Company developed the first prototype [112]. A more efficient cryogenic engine with isothermal expansion was built and fitted to a small car around 2001 by Peter Dearman, who claimed that the car ran at a speed of around 30 mph on a non-public road. The engine is often referred to as Dearman Engine and the technology development of the cryogenic engine was initially done by Highview Enterprises Ltd in collaboration with university of Leeds [113–115]. This led to the establishment of Dearman Engine Company around 2012. The company made a considerable effort to commercialise the technology, particularly for transport refrigeration applications [116,117]. However, there is a long way to go for the liquid air/nitrogen vehicles to be applied due to both technical and economic issues. This is mainly because of the small scale operations and ineffective cryogenic energy recovery from liquid air/nitrogen.

The decoupled LAES for buildings The decoupled LAES system considered to be more promising for applications in the building sector than the transport sector, mainly due to the system scale. It is very common to recover the cryogenic energy during liquid air/nitrogen evaporation through either direct cooling or power generation with Rankine/Brayton cycles [118,119]. The direct cooling is an exergy destructive process as the heat transfer temperature difference is huge (around 200 ^{o}C), while the power generation with Rankine/Brayton cycles incurs a high capital cost. These call for a more efficient way to recover the cryogenic energy and hence presents a research gap.

The integration of decoupled LAES with industrial processes Several studies on the integration of decoupled LAES with industrial processes, aimed to make better use of the

cryogenic energy in the decoupled LAES. Li et al. [120] proposed the integration of the discharging process of the decoupled LAES with a solar thermal power plant. The closed Brayton cycle in the solar thermal power plant and the direct expansion cycle in the LAES are combined to improve the efficiency: the cryogenic energy of the liquid air is used to cool down the gas before compression in the closed Brayton cycle, and the solar heat energy is used to heat up the gas before expansion in both the direct expansion and closed Brayton cycles. The integrated system could deliver 30% more power output than the sum of two separate systems. Park et al. [121] proposed the use of liquid air as a cold energy carrier in a complete LNG supply chain. In the LNG regasification stage, the air liquefaction process of the LAES works to produce liquid air by utilizing the cold energy of LNG. The liquid air is then shipped back to the Natural Gas (NG) liquefaction site, providing cooling load to liquify the NG and generating electricity. Besides LNG, Rehman et al. [122] proposed the recovery of the cryogenic energy of the decouple LAES for biomethane liquefaction and power generation in a liquefied biomethane plant.

Table 2.4 Main developments of the decoupled LAES systems

System types	Main features	Main conclusions	Ref.
Decoupled Transportation	Liquid nitrogen as energy carrier to drive cryogenic engines for both mechanical power and cooling supply on vehicles	The liquid nitrogen truck can obtain positive income when the liquid nitrogen utilization factor and diesel price are higher than 83% and 1.08 USD/kg, respectively.	[117]
Decoupled Building	Liquid air as energy carrier to drive direct expansion cycle for electricity and cooling supply to cold storage room (-29 ℃)	COP and recovery efficiency of this supply chain are 0.56 and 32%, respectively.	[118]
Decoupled Building	Liquid air/nitrogen as energy carrier to drive various cryogenic cycles with different configurations for electricity and cooling supply to commercial buildings	Combined cycle (cascade Rankine cycles + direct expansion) is suggested, and the overall thermal efficiency is 74%. However, the capital cost is high.	[110,119]
Decoupled Integration	Liquid nitrogen as energy carrier integrated with solar thermal power system to drive direct expansion cycle as well as closed Brayton cycle	Solar thermal power system provides heat for superheating before expansion; liquid nitrogen provides cold for cooling before compression; Overall exergy efficiency was 27.55; power generation is 30% higher than the sum of two separate systems.	[120]
Decoupled Integration	Liquid air as energy carrier in the complete LNG supply chain: air liquefaction in LNG regasification stage; power recovery in NG liquefaction stage for electricity and additional cooling supply.	Energy requirement for NG liquefaction is reduced by 26-30%.	[121]
Decoupled Integration	Liquid air as energy carrier to drive direct expansion cycle (with fuel combustion) for electricity and additional cooling supply in biomethane liquefaction stage	Overall exergy efficiency of this integrated system is 72.3%.	[122]

2.5 Summary of the literature review

The LAES is one of the most promising large-scale energy storage technologies, which have started large scale commercial deployment. The key advantages of such a technology include high energy density, no geographical constraints, sustainable storage material (mainly air), direct capture of CO_2 from air as part of the process, transportability, and ability to provide multi-energy-vector services.

Standalone LAES A significant amount of research work has been conducted on the thermodynamic performance of the standalone LAES system in terms of the system configuration, the optimal operating parameters, and the component/material. The Linde based and Claude/modified Claude based liquefaction cycles are commonly used for air liquefaction (charging) process considering their efficiency, capital cost/maintenance cost, and system flexibility. The direct expansion cycle without combustion is more popular for power recovery (discharging) process due to its comprehensive environmental, economic and efficiency benefits. The standalone LAES is often equipped with high-grade cold and compression heat storage units for enhancing the round trip efficiency. For a standalone LAES system with the baseline configuration, the optimization of the operating parameters (e.g., charging and discharging pressures) and the increase of the component efficiency can improve the round trip efficiency to a certain extent. Further enhancement of the round trip efficiency of the standalone LAES system would require the use of the surplus compression heat for additional power generation or combined cooling and heating supply. There is a lack of comprehensive studies on the utilization of the surplus compression heat, especially for the cases at low charging pressures.

Integrated LAES Many studies in the literature have been focused on the LAES integration with external thermal sources. Among them, the integration of the LAES with the LNG regasification process has attracted most of the attentions. Most of the studies only considered the thermal component of the LNG cold energy as the cooling load for the LAES for

increasing the liquid yield. If the cold energy of the LNG is used as a supplement of cooling in the air liquefaction process of the LAES, the cryogenic cold energy of the liquid air still needs to be recycled within the LAES. The advantage of this is that the configuration of the LAES charging process is usually close to the baseline LAES, which presents little doubt on the technical feasibility. If the LNG is used as the only cooling load for the air liquefaction process, the configuration of the LAES charging process would need to be redesigned according to different scenarios, and the liquid air storage pressure would need to be set to ~2 MPa or higher for temperature match. The advantage of the new design is that the liquid yield of the LAES could be improved to 100%, and hence a significant contribution to the round trip efficiency enhancement. Another method to use the thermal component of the LNG cold energy is to take the LNG as the cold source to drive an additional power generation cycle, along with the excess compression heat from the LAES as the heat source. In this way, both the LAES system and the LNG regasification plant can keep their original layouts. As for the integration of the LAES with external heat sources, almost all the heat sources discussed in the literature are utilized to superheat the air in the LAES discharging process.

The ASU is another focus for LAES integration studies. These studies can be broadly split into two: one is the use of the low-purity gaseous product (e.g., crude nitrogen) of the ASU as both the working and storage medium for the LAES; the other shares the load capacity of the ASU (compressors and heat exchange equipment) with the LAES for saving the initial equipment investment of the LAES. Although much work has been done on the integrated LAES, the scope of the processes for LAES integration are still very limited. More integration scenarios are needed to be considered to improve the adaptability and flexibility of the LAES and broaden the application scope of the LAES.

Decoupled LAES Decoupled LAES systems have a great potential but very little has been investigated compared with the coupled LAES systems. The development gaps for the decoupled LAES system, especially in the transport and building sectors, can be identified in the following: (1) it is a common challenge to recover the cryogenic energy and compression

heat of the decoupled LAES system; (2) the traditional method to recover the cryogenic energy through Rankine/Brayton cycles faces a very high capital cost. Therefore, new ways are needed to address these challenges for decoupled LAES to play any significant role in the future.

The present Ph.D. work covers the standalone LAES, integrated LAES, and decoupled LAES, aimed to bridge the gaps as summarised above. For the integrated LAES, a waste-energy based power generation system is proposed and optimized to recover the excess compression heat from the LAES and the cryogenic energy from the LNG. A multi-functional standalone LAES is proposed to supply multi-energy-vector services for decentralized micro-energy networks. An economically feasible decoupled LAES integrated with a cryogenic thermoelectric generator is proposed to deal with cryogenic energy recovery and high capital cost problems. Finally, two hybrid LAES systems integrated with the ammonia synthesis process are proposed and analysed to extend the application scope of the LAES, as well as addressing the high energy consumption of the ammonia product. This latter has significance as ammonia is regarded as a potential hydrogen carrier for net zero energy future.

Chapter 3 Methodologies

This chapter explains the general methods used in this Ph.D. study, including first and second thermodynamic analysis, thermodynamic properties, modelling and optimization, and pinch analysis. Detailed mathematical models and detailed methods are given in the subsequent chapters and will not be discussed in this chapter.

3.1 Thermodynamic analysis

3.1.1 Energy and exergy analyses

The LAES system and other thermal energy systems are often made up of several thermodynamic cycles. As shown in Figure 3.1, a basic thermodynamic cycle consists of a sequence of thermodynamic processes realized by the transfer of heat and work, which result in the variation in state properties (pressure, temperature, enthalpy, entropy). The work transfer processes involve compression and expansion processes. Usually, a compression process is realized by compressors or pumps, and an expansion process is realized by gas turbines, liquid expanders, or other expansion engines. The analyses of these thermodynamic processes are established based on the first and the second laws of thermodynamics.

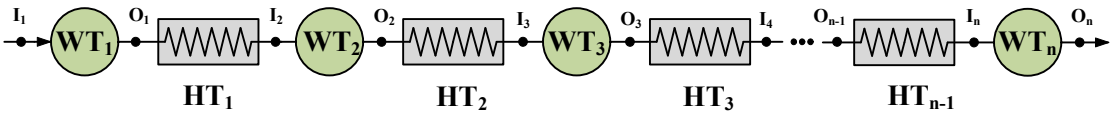

Figure 3.1 Diagram of a generalized thermodynamic cycle (I-Inlet; O-Outlet; WT-Work transfer process; HT-Heat transfer process).

Energy Analyses The energy analyses are based on the first law of thermodynamics. For example, for an adiabatic compression process, its isentropic efficiency is defined as:

$$\eta_{\mathrm{C,s}} = \frac{h_{\mathrm{O,s}} - h_{\mathrm{I}}}{h_{\mathrm{O}} - h_{\mathrm{I}}} \tag{3.1}$$

where $\eta_{C,s}$ is the isentropic efficiency of a compressor or a pump; h represents the specific enthalpy; subscripts O and I represent the outlet and inlet states of the compression process, respectively; subscript s represent the isentropic process. In this way, the actual specific power consumption of the compression process (w_C) and the actual specific enthalpy at the outlet of the compression process (h_O) can be given respectively as follows:

$$w_C = \frac{h_I - h_{O,s}}{\eta_{C,s}} \tag{3.2}$$

$$h_O = h_I - \frac{h_I - h_{O,s}}{\eta_{C,s}} \tag{3.3}$$

For an adiabatic expansion process, the isentropic efficiency is given as:

$$\eta_{E,s} = \frac{h_O - h_I}{h_{O,s} - h_I} \tag{3.4}$$

where $\eta_{E,s}$ is the isentropic efficiency of a turbine or an expander. Thus, the real specific power generation of the expansion process (w_E) and the real specific enthalpy at the outlet of the expansion process (h_O) are expressed as below:

$$w_E = (h_I - h_{O,s}) \cdot \eta_{E,s} \tag{3.5}$$

$$h_O = h_I - (h_I - h_{O,s}) \cdot \eta_{E,s} \tag{3.6}$$

For the heat transfer process, the specific heat flux can be defined as the specific enthalpy difference of the working fluid at the outlet and inlet of the heat transfer unit:

$$q_{HT_i} = h_{I_{i+1}} - h_{O_i} \tag{3.7}$$

where the q_{HTi} represents the specific heat flux of the i^{th} heat transfer process; subscripts I_{i+1} and O_i represent the states in Figure 3.1. See Section 3.2 for a detailed introduction to the analysis and optimization methods of the heat transfer process.

Exergy Analyses The energy analyses can only give the energy flow but fail to quantify different types (grades) of energy in a thermodynamic cycle. Hence, the exergy analyses based on the second law of thermodynamics are essential.

In this study, the kinetic and potential exergies are not considered for the specific exergy flow calculations as they are usually negligible:

$$ex_{\mathrm{I/O}} = (h_{\mathrm{I/O}} - h_{\mathrm{ambient}}) - T_{\mathrm{ambient}} \cdot (s_{\mathrm{I/O}} - s_{\mathrm{ambient}}) \tag{3.8}$$

where ex is the specific exergy flow; s represents specific entropy; T represents the temperature; subscript I/O represents the inlet (I) or outlet (O) states of the compression and expansion process; and the subscript ambient represents the ambient state.

The exergy destruction of a thermodynamic cycle is the sum of the exergy destruction of the processes that compose this cycle. The exergy destruction of a process is defined as the exergy difference between the inlet and outlet of the process. The exergy destructions of the compression and expansion processes are given respectively:

$$D_{\mathrm{C}} = ex_{\mathrm{I}} - ex_{\mathrm{O}} - w_{\mathrm{C}} \tag{3.9}$$

$$D_{\mathrm{E}} = ex_{\mathrm{I}} - ex_{\mathrm{O}} - w_{\mathrm{E}} \tag{3.10}$$

where D is the specific exergy destruction of a process; subscripts C and E represent the compression and expansion processes, respectively; w_{C} and w_{E} are respectively the real specific power consumption and generation through the compression and expansion processes. Note that w_{C} is a negative value according to the Equation (3.2).

3.1.2 Thermodynamic properties

Thermodynamic properties are not all independent. The so-called equation of state gives the linkage of these properties. The ideal gas law is the simplest equation of state for a gas:

$$PV = nRT \tag{3.11}$$

where P is the absolute pressure; V is volume; T is the absolute temperature; n is the number of moles; R is the universal gas constant. The ideal gas state equation assumes zero size and zero interaction between molecules of the gas, and is therefore roughly accurate to predict the behaviour of gases at high temperatures and low pressures. However, it deviates for an environment with low temperatures and/or high pressures, especially a gas condensation process, leading to an inaccurate or even wrong estimation of the gas properties. This environment and condition are very common in this study, making the ideal gas law is not applicable.

To ensure the accurate results of the thermodynamic analyses, more realistic models are used. This is done through the use of a commercial software called REFPROP.

This REFPROP is a computer program, distributed through the Standard Reference Data program of the National Institute of Standards and Technology (NIST) [123]. It provides thermophysical properties of industrially important pure fluids and mixtures over a wide range of fluid conditions including liquid, gas, and supercritical phases. The program is based on the most accurate pure fluid and mixture models currently available. Three models are implemented for pure fluid calculations in REFPROP: equations of state which is explicit in Helmholtz energy, the modified Benedict-Webb-Rubin equation of state, and an extended corresponding states (ECS) model. For mixtures, the REFPROP implements a model that applies mixing rules to the Helmholtz energy and a departure function to account for the departure from ideal mixing. Viscosity and thermal conductivity are modelled with either fluid-specific correlations, an ECS method, or in some cases, the friction theory method. These models are implemented in a suite of FORTRAN subroutines. They are written in a structured format, are internally documented with extensive comments, and have been tested on a variety of compilers. [123,124]

The property models in the REFPROP can be accessed by a wide range of platforms and programming environments (e.g., Excel, LabVIEW, and MATLAB) through the use of a

dynamic link library (DLL) [125]. In the present work, the thermodynamic simulation is carried out in the MATLAB environment. Both pure fluids and mixtures (including predefined and user-defined mixtures) can be called and calculated in the MATLAB environment by the following calling sequences:

$$\text{result=refpropm}(\text{prop\_req, spec1, value1, spec2, value2, substance1}) \tag{3.12}$$

$$\text{result=refpropm}(\text{prop\_req, spec1, value1, spec2, value2, mixture1}) \tag{3.13}$$

$$\text{result=refpropm(prop\_req, spec1, value1, spec2, value2, substance1, substance2, ...substanceN, x)} \tag{3.14}$$

Equation (3.12), Equation (3.13) and Equation (3.14) are used for calling pure substances, predefined mixtures and user-defined mixtures, respectively. In Equation (3.12)-(3.14), prop_req is the requested properties; spec1 and spec2 are the first and second input properties (know properties), and value1 and value2 are their corresponding values; substance1 is the name of the pure fluid or the first component of the user-defined mixture; mixture1 is the name of the predefined fluid mixture; substance2 and substanceN are the names of the second and N^{th} component of the user-defined mixture; x is a vector with mass fractions of each component in the user-defined mixture. Each property is represented by a character, as given in Table 3.1.

Table 3.1 Characters standing for the properties in REFPROP calling sequence.

prop_req/ spec	Property	Unit	prop_req/ spec	Property	Unit
A	Speed of sound	m/s	V	Dynamic viscosity	Pa·s
B	Volumetric expansivity	K^{-1}	W	d(rho)/dT (constant P)	$kg/(m^3 K)$
C	Cp	J/(kg K)	X	Liquid phase & gas phase composition (mass fraction)	
D	Density	kg/m^3	Y	Heat of Vaporization	J/kg
E	dP/dT (along the saturation line)	kPa/K	Z	Compressibility factor	
F	Fugacity	kPa	$	Kinematic viscosity	cm^2/s
G	Gross heating value	J/kg	%	Thermal diffusivity	cm^2/s
H	Enthalpy	J/kg	^	Prandtl number	
I	Surface tension	N/m	)	Adiabatic bulk modulus	kPa
J	Isenthalpic Joule-Thompson coefficient	K/kPa	|	Isothermal bulk modulus	kPa
K	Ratio of specific heats (Cp/Cv)		=	Isothermal compressibility	kPa^{-1}
L	Thermal conductivity	W/(m K)	+	Liquid density of equilibrium phase	
M	Molar mass	g/mol	-	Vapor density of equilibrium phase	

N	Net heating value	J/kg	{	Dielectric constant	
O	Cv	J/(kg K)	#	dP/dT (constant rho)	kPa/K
P	Pressure	kPa	!	dH/d(rho) (constant T)	(J/kg)/(kg/m^3)
Q	Quality (vapor fraction)	kg/kg	&	dH/d(rho) (constant P)	(J/kg)/(kg/m^3)
R	d(rho)/dP (constant T)	kg/(m^3 kPa)	(	dH/dT (constant P)	J/(kg K)
S	Entropy	J/(kg K)	@	dH/dT (constant rho)	J/(kg K)
T	Temperature	K	*	dH/dP (constant T)	J/(kg kPa)
U	Internal energy	J/kg	`	Throat mass flux	kg/(m^2 s)

3.2 Optimization method

3.2.1 Pinch analysis

Introduction to the pinch analysis Pinch analysis is a method aimed at the energy saving of industrial processes by optimizing the process heat integration, maximising the heat recovery and minimising the external energy requirement with the help of thermodynamic principles [126]. This method was first devised and introduced by Linnhoff in 1978 for a systematic analysis of the overall plant [127–129] and was further developed for the heat exchanger network design by Linnhoff and Hindmarsh [130].

Pinch analysis plays a significant role in the overall process design. Figure 3.2 shows the "Onion Diagram" of hierarchy in process design [131]. The design basically proceeds from the inside to the outside of the onion. The reactors design (the core of the "Onion Diagram") is the first to be determined for extracting the feeds, products, recycle concentrations and flowrates, after which the separators and power systems (the second and third layer of the "Onion Diagram") can be designed. Then the basic material and heat balance is established, and the heat exchanger network (the fourth layer of the "Onion Diagram") can be designed with pinch analysis. Finally, the remaining heating and cooling duties are settled by the utilities (the fifth layer of the "Onion Diagram"), including the process utility and site-wide utility systems. Using the pinch analysis to describe and analyse the heat exchanger network can contribute to every layer of the process design: for the first three layers, the pinch analysis helps to identify the impact of their changes on the energy saving of the process, which will guide the core process design; for the fourth and fifth layers, the pinch analysis is used to optimize the heat exchanger network to achieve the energy-saving target of the utility system [132].

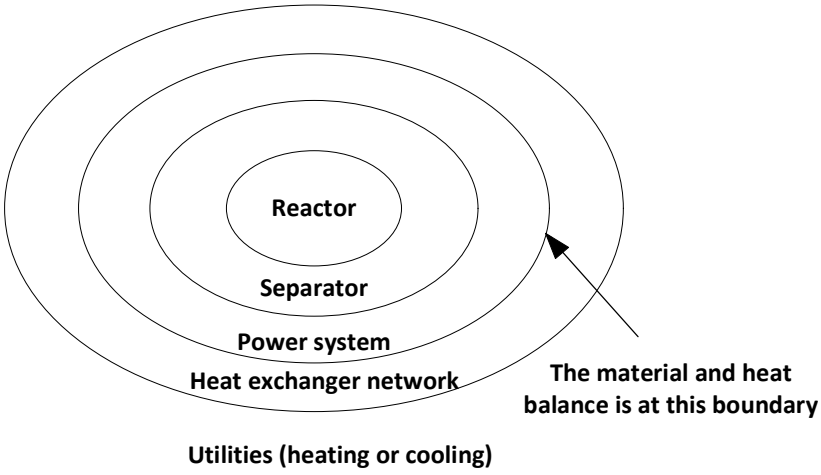

Figure 3.2 "Onion Diagram" for process design [131].

Principle of the pinch analysis Using pinch analysis to analyse and optimize the heat exchanger network is based on the first and second laws of thermodynamics. The first law of thermodynamics provides the energy equation for calculating the enthalpy changes in the streams passing through a heat exchanger. The second law of thermodynamics determines the direction of heat flow (without work input, heat energy may only flow in the direction of hot to cold). In a practical process, a Minimum Approach Temperature (MAT) determines how closely the hot and cold streams can be pinched without violating the second law of thermodynamics (none of the heat exchangers can have a temperature crossover), and hence, this MAT must be maintained in the heat exchanger network.

The pinch analysis can construct composite curves in the heat exchanger network, which refer to temperature and enthalpy profiles of heat availability (the hot composite curve) and heat demands (the cold composite curve) together. The composite curves can be used to predict the minimum energy (both hot and cold utility) required in the heat exchange process and the maximum heat recovery, as shown in Figure 3.3 (a). The position of the closest temperature approach between hot and cold composite curves is defined as the process pinch point at which the temperature difference must be higher than MAT. The pinch point is recognized to be the most constrained part that limits the overall performance of this process. It has been reported that any change in process parameters caused by debottlenecking will change the

pinch position and further affect the cooling and heating utilities, as illustrated in Figure 3.3 (b).

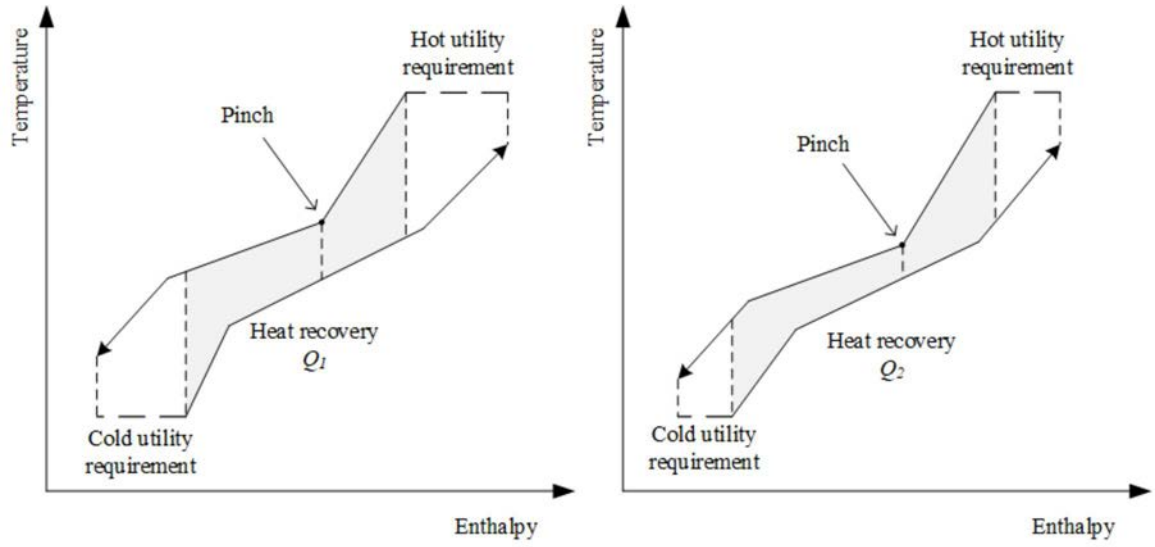

(a) (b)

Figure 3.3 Composite curves of the hot and cold streams in heat exchanger network: (a) original composite curves; (b) optimized composite curves [30].

3.2.2 Heat exchanger optimization using the Pinch analysis

The use of the pinch analysis ***in this work*** In the LAES system, heat transfer usually occurs between high-pressure air and cold/heat storage media. The high-pressure air experiences significant changes in the specific heat capacity, especially during the cooling processes, as shown in Figure 3.4. Thus, the temperature distribution of high-pressure air in the heat exchangers is non-linear. This makes it challenging for an efficient design of heat exchangers. This can be overcome by the employment of the pinch analysis, through which the performance of heat exchangers in the LAES (including general heat exchangers and the cold box) can be optimized for a high exergy efficiency.

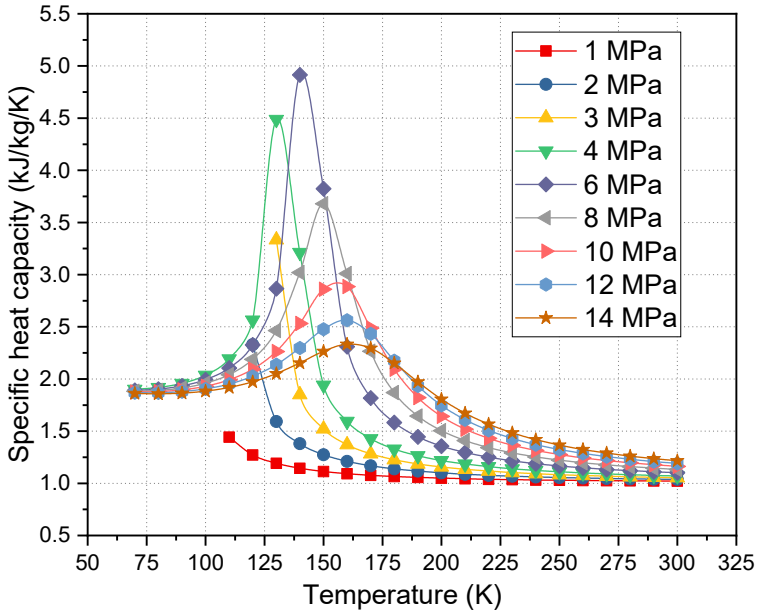

Figure 3.4 Specific heat capacity of air at different temperatures and pressures.

Key steps in the pinch analysis ***for process optimization*** Applying the pinch analysis to a process design and optimization is usually done in several steps as follows [133]:

(1) Establishment of the mass and energy balances;

(2) Extract the stream data from the mass and energy balances;

(3) Select an appropriate MAT value, construct the composite curves of the heat exchange network, and then calculate the energy targets (minimum heating and cooling utility requirements) and the pinch point;

(4) Modify the process, and then update the stream data to obtain the new energy targets;

(5) Once decided whether to implement process modifications and what utility levels are used, design a heat exchanger network within the process;

(6) Design the utility systems to supply the remaining heating and cooling utility requirements, and modify the heat exchanger network if necessary;

(7) Reproduce the process based on the above modifications, return to step (2) to study if a

further improvement is possible.

Figure 3.5 gives an example of using the pinch analysis in the LAES for an optimal design of the cold box (multi-stream heat exchanger). The way to calculate the stream data (temperatures, pressures, enthalpies, and entropies) of the cold and hot streams is based on the thermodynamic modelling method introduced in Section 3.1. The pinch analysis is used to analyse and examine the efficiency and feasibility of the overall heat exchange process, providing strategies to guide the process optmization. This optimization procedure is essential for realizing an efficient heat exchange process and an efficient overall system, although it is a very time-consuming part in the system simulation process.

Figure 3.5 Optimization procedure for the cold box in the LAES.

Chapter 4 Waste energy recovery through integration of liquid air energy storage and liquefied natural gas regasification

4.1 Introduction

LNG regasification is a very important industrial process and there are many LNG regasification plants across the world today. Most such regasification plants discard the valuable cold energy. On the other hand, the commercial deployment of the LAES technology is ongoing after a pilot scale LAES plant (350 kW/2.5 MWh) and a grid-scale LAES commercial demonstrator plant (5 MW/15 MWh) were built and tested successfully. The LAES plant need cold energy: it would therefore an attractive approach to integrate two technologies to reduce energy loss of LNG and enhance the LAES efficiency. As the LAES power plants mostly use the 'off-the-shelf' components, and the existing LNG regasification terminal can use the current layout with little modification, this integrated system should have good technical and commercial feasibilities. Some work has been performed on this. For example, LAES-Brayton-LNG system was proposed [93], which uses an additional Brayton cycle to recover the waste cold energy from LNG regasification process and excess compression heat from the LAES (The temperature and proportion of the excess compression heat of a standalone LAES are shown in Figure 4.1). However, this piece of research [93] mainly focused on the thermodynamic analysis of the overall integrated system, with very little on the optimization of the proposed power plant (Brayton cycle).

This chapter explains one aspect of this Ph.D. work, aimed to bridge the above gap by performance optimization of the proposed power plant based on waste energy recovery. Nitrogen and argon are selected as the working fluids to address the challenge. Both energy analysis and exergy analysis are carried out on the use of the two working fluids under different working conditions. An economic analysis is also performed on the proposed power plant.

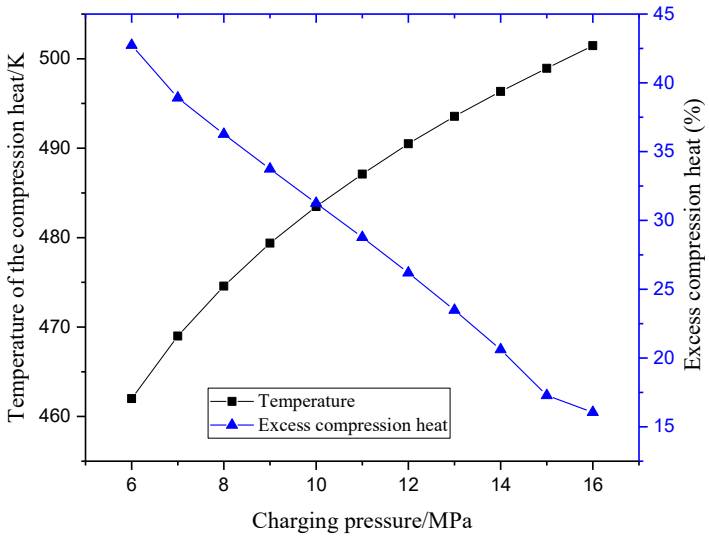

Figure 4.1 Excess compression heat (hot thermal oil) in the standalone LAES at different charging pressure.

4.2 System description and modelling

4.2.1 System description

In the LAES system, the compression heat is high grade, and assumed to be stored in thermal oil. As is introduced in Section 4.1, the compression heat is often surplus in a standalone LAES system. Thus, this part of heat is used together with cold energy in the pressurized LNG, to drive a power generation cycle, producing additional electricity. Figure 4.2 (a) shows the proposed power generation system, consisting of two power generation cycles: Power generation#1 and Power generation #2. In Power generation#1, the compression heat from the LAES system and the cold energy from the LNG system are recovered, working as the heat source and cold source, respectively. The Power generation#2 is a traditional LNG direct expansion cycle.

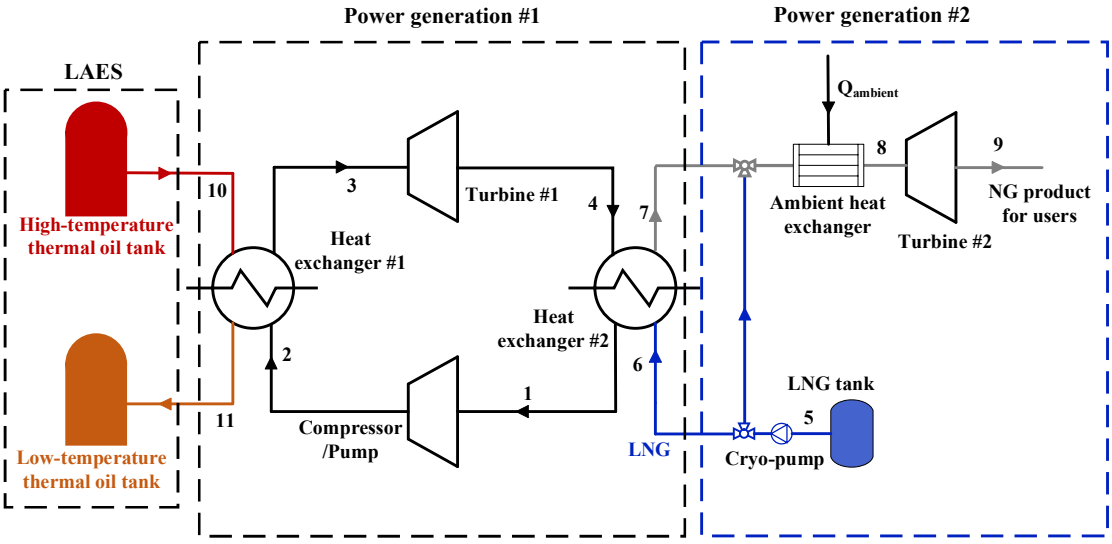

(a)

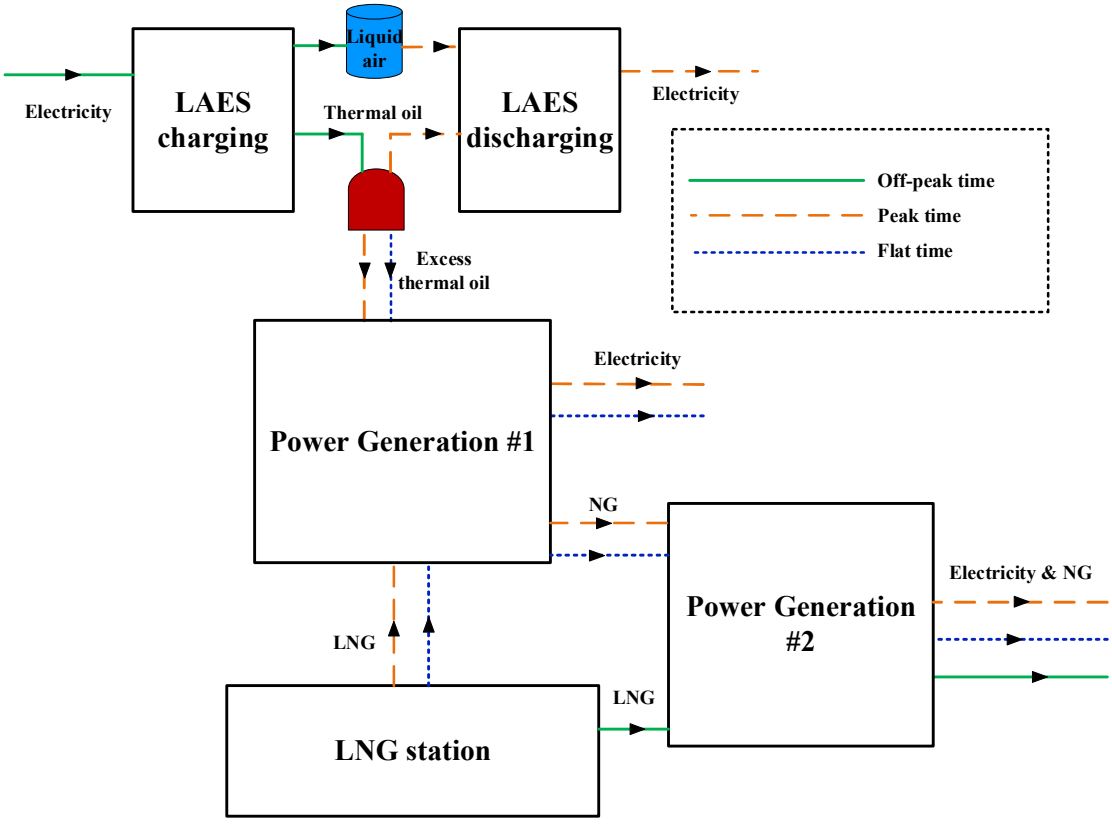

(b)

Figure 4.2 (a) Flowsheet of the proposed power generation system, and (b) working modes of the proposed power generation system.

The excess compression heat from the LAES can be utilized in a very flexible way, as shown in Figure 4.2 (b), depending on the user demand of natural gas (NG) and the working time of the LAES:

During off-peak time, the LAES system is charged, which produces not only liquid air, but also high-temperature thermal oil. In this period, if NG is in demand, only Power generation#2 operates, which is the same as a conventional LNG regasification terminal. The required pressure of the NG product for users depends on the purpose, as illustrated in Table 4.1. In this work, the NG product is assumed to be used for long-distance transmission.

During peak time, the LAES system is discharged for power generation. If NG is in demand during this period, both Power generation#1 and Power generation#2 operate. In Power generation#1, the working fluid is compressed by the compressor firstly (status 2). Then it is heated up through the heat exchange with a stream of the high-temperature thermal oil from the LAES (status 3). The high-temperature compressed working fluid is then expanded in turbine#1 for power generation (status 4), after which the working fluid is cooled down (status 1) through the heat exchange with the pressurized LNG. Finally, the working fluid is compressed to a high pressure (status 2) to complete the whole closed cycle. Meanwhile, the pressurized LNG completes the first regasification process in the heat exchanger#2 (from Status 6 to Status 7). In Power generation#2, the pressurized NG enters the ambient heat exchanger for further regasification (status 8), after which the high-pressure NG is expanded in turbine#2 to the gas-supplying pressure (status 9).

During flat time, the LAES system operation stops. If there is still excess thermal oil left in the high-temperature thermal oil storage tank, Power generation#1 and Power generation#2 can operate in the same way as that at the peak time until the stored heat in the thermal oil is used up. After that, Power generation#1 stops, and Power generation#2 keeps running for LNG regasification.

Table 4.1 Required pressure of NG for several purposes [134].

Purpose	Pressure (MPa)
Steam power stations	0.6
Combined cycle stations	2.5
Local distribution	3
Long-distance transmission	7

4.2.2 System model development

4.2.2.1 Thermodynamic model for energy analysis

In Power generation#1, the working fluid is compressed to a high pressure, and the outlet enthalpy of the working fluid after the compression process can be calculated as follows:

$$h_2 = h_1 + \frac{(h_{2,s} - h_1)}{\eta_{com}} \tag{4.1}$$

where h_i represents the specific enthalpy at status i; subscript s represents an isentropic process; and η_{com} represents the isentropic efficiency of the compressor.

Then the pressurized working fluid (status 2) is heated up by the high-temperature thermal oil in heat exchanger#1. The outlet state (status 3) can be calculated according to the law of energy conservation subject to the limitation of the pinch point:

$$m_{WF} \cdot (h_3 - h_2) = K_{oil} \cdot m_{WF} \cdot (h_{10} - h_{11}) \tag{4.2}$$

$$K_{oil} = \frac{m_{oil}}{m_{WF}} \tag{4.3}$$

where m_{WF} and m_{oil} are the mass flow rates of the working fluid and the thermal oil in the power generation cycle, respectively; K_{oil} is the ratio of the mass flow rate of the thermal oil to that of the working fluid.

The high-temperature pressurized working fluid (status 3) then expands in turbine#1 to low pressure (status 4), and the outlet condition can be obtained by:

$$h_4 = h_3 - \eta_{turb1} \times (h_3 - h_{4,s}) \tag{4.4}$$

where η_{turb1} represents the isentropic efficiency of turbine#1.

The pressurized LNG cools down the working fluid out of turbine#1 in heat exchanger#2. The outlet state of the working fluid (status 1) can be calculated by using the law of energy conservation subject to the limitation of the pinch point:

$$m_{WF} \cdot (h_4 - h_1) = K_{LNG} \cdot m_{WF} \cdot (h_7 - h_6) \tag{4.5}$$

$$K_{LNG} = \frac{m_{LNG}}{m_{WF}} \tag{4.6}$$

where m_{LNG} is the mass flow rate of LNG in the power generation system; K_{LNG} is the ratio of the mass flow rate of LNG to that of the working fluid.

In Power generation#2, the ambient-pressure LNG (status 5) stored in the LNG tank is pumped to high pressure (status 6) by the cryo-pump. The cryo-pump outlet condition can be calculated as follows:

$$h_6 = h_5 + \frac{(h_{6,s} - h_5)}{\eta_{cryo-pump}} \tag{4.7}$$

in which $\eta_{cryo-pump}$ is the isentropic efficiency of the cryo-pump.

The pressurized LNG is heated to ambient temperature in the ambient heat exchanger after finishing the first regasification process in Power generation#1:

$$T_8 = T_{ambient} \tag{4.8}$$

$$Q_{ambient} = m_{LNG} \cdot (h_8 - h_7) \tag{4.9}$$

where T_i represents the temperature at status i; $T_{ambient}$ represents the ambient temperature; $Q_{ambient}$ represents the heat flux in ambient heat exchanger.

The ambient-temperature pressurized NG (status 8) then expands in turbine#2 to gas-supplying pressure (status 9). The outlet condition can be obtained by:

$$h_9 = h_8 - \eta_{turb2} \cdot (h_8 - h_{9,s}) \tag{4.10}$$

where η_{turb2} represents the isentropic efficiency of the turbine#2.

The specific power generation of this proposed power generation system, w_{net}, is defined as the net energy output produced by per unit mass flow of the working fluid, which is the sum of the specific power generation of Power generation#1 ($w_{net,PG1}$) and Power generation #2 ($w_{net,PG2}$):

$$w_{net} = w_{net,PG1} + w_{net,PG2} = \frac{(W_{turb1} - W_{com}) + (W_{turb2} - W_{cryo\text{-}pump})}{m_{WF}} \tag{4.11}$$

$$W_{com} = m_{WF} \cdot (h_2 - h_1) \tag{4.12}$$

$$W_{turb1} = m_{WF} \times (h_3 - h_4) \tag{4.13}$$

$$W_{cryo\text{-}pump} = m_{LNG} \cdot (h_6 - h_5) \tag{4.14}$$

$$W_{turb2} = m_{LNG} \cdot (h_8 - h_9) \tag{4.15}$$

To study the effects of the amount of LNG and thermal oil on the system performance, the power generation per unit mass flow rate of the LNG (w_{net}^{LNG}) and per unit mass flow rate of the thermal oil (w_{net}^{oil}) are proposed and defined respectively as:

$$w_{net}^{LNG} = w_{net,PG1}^{LNG} + w_{net,PG2}^{LNG} = \frac{W_{turb1} - W_{com}}{m_{LNG}} + \frac{W_{turb2} - W_{cryo\text{-}pump}}{m_{LNG}} \tag{4.16}$$

$$w_{net}^{oil} = w_{net,PG1}^{oil} + w_{net,PG2}^{oil} = \frac{W_{turb1} - W_{com}}{m_{oil}} + \frac{W_{turb2} - W_{cryo\text{-}pump}}{m_{oil}} \tag{4.17}$$

The thermal efficiency of this proposed system, η_{th}, is defined as the ratio of the net energy output of this system to the total heat input at the high temperature of this system:

$$\eta_{th} = \frac{(W_{turb1} - W_{com}) + (W_{turb2} - W_{cryo\text{-}pump})}{Q_{hot,PG1} + Q_{hot,PG2}} \tag{4.18}$$

$$\eta_{th,PG1} = \frac{(W_{turb1} - W_{com})}{Q_{hot,PG1}} \tag{4.19}$$

$$Q_{hot,PG1} = m_{oil} \cdot (h_{10} - h_{11}) \tag{4.20}$$

$$Q_{hot,PG2} = Q_{ambient} = m_{LNG} \cdot (h_8 - h_7) \tag{4.21}$$

4.2.2.2 Thermodynamic model for exergy analysis

In this study, the exergy flow rate (*Ex*) is defined as the product of the mass flow rate and the specific exergy (assuming negligible kinetic and potential exergy), which is illustrated mathematically by:

$$Ex_i = m_i \cdot ex_i = m_i \cdot [(h_i - h_{ambient}) - T_{ambient} \cdot (s_i - s_{ambient})] \tag{4.22}$$

The exergy input by the LNG to the whole system (Ex_{in}^{LNG}) and to Power generation#1 ($Ex_{in,PG1}^{LNG}$) are respectively given by:

$$Ex_{in}^{LNG} = Ex_5 - Ex_9 \tag{4.23}$$

$$Ex_{in,PG1}^{LNG} = Ex_6 - Ex_7 \tag{4.24}$$

The exergy input by the thermal oil to the system (Ex_{in}^{oil}) is given:

$$Ex_{in}^{oil} = Ex_{10} - Ex_{11} \tag{4.25}$$

Thus, the total exergy input to the whole system (Ex_{in}) and Power generation#1 ($Ex_{in,PG1}$) are:

$$Ex_{in} = Ex_{in}^{LNG} + Ex_{in}^{oil} \tag{4.26}$$

$$Ex_{in,PG1} = Ex_{in,PG1}^{LNG} + Ex_{in}^{oil} \tag{4.27}$$

There are several different definitions of exergy efficiency proposed by different researchers [135,136]. The exergy efficiency of the system (η_{ex}) is defined as the ratio of the total useful exergy output from the system to the total exergy input into the system, with the net power

output of the system considered as the useful exergy output, and the physical exergy changes of the natural gas and the thermal oil considered as the exergy input. This exergy efficiency definition is very common and has been used in many studies about the LNG-based power generation system [137–139].

$$\eta_{ex}=(m_{\mathrm{WF}}\cdot w_{\mathrm{net}})/Ex_{\mathrm{in}}=（Ex_{\mathrm{in}}\text{-}Ex_{\mathrm{d}})/Ex_{\mathrm{in}} \tag{4.28}$$

$$\eta_{ex,PG1}=(m_{WF}\cdot w_{net,PG1})/Ex_{in,PG1}=（Ex_{in,PG1}\text{-}Ex_{\mathrm{d},PG1})/Ex_{in,PG1} \tag{4.29}$$

In Equations (4.28) and (4.29), Ex_{d} and $Ex_{\mathrm{d},PG1}$ represent the total exergy destruction of the whole system and Power generation#1, respectively. The total exergy destruction is the sum of the exergy destruction of each system component:

$$Ex_{\mathrm{d}}=Ex_{\mathrm{d}}^{com}+Ex_{\mathrm{d}}^{HEX1}+Ex_{\mathrm{d}}^{turb1}+Ex_{\mathrm{d}}^{HEX2}+Ex_{\mathrm{d}}^{cryo-pump}+Ex_{\mathrm{d}}^{AHEX}+Ex_{\mathrm{d}}^{turb2} \tag{4.30}$$

For Power generation#1:

$$Ex_{\mathrm{d},PG1}=Ex_{\mathrm{d}}^{com}+Ex_{\mathrm{d}}^{HEX1}+Ex_{\mathrm{d}}^{turb1}+Ex_{\mathrm{d}}^{HEX2} \tag{4.31}$$

The terms in Equations (4.30) and (4.31) are given by:

$$Ex_{\mathrm{d}}^{com}=Ex_1-Ex_2+W_{com} \tag{4.32}$$

$$Ex_{\mathrm{d}}^{HEX1}=Ex_2-Ex_3+Ex_{10}-Ex_{11} \tag{4.33}$$

$$Ex_{\mathrm{d}}^{turb1}=Ex_3-Ex_4-W_{turb1} \tag{4.34}$$

$$Ex_{\mathrm{d}}^{HEX2}=Ex_4-Ex_1+Ex_6-Ex_7 \tag{4.35}$$

$$Ex_{\mathrm{d}}^{cryo-pump}=Ex_5-Ex_6+W_{cryo-pump} \tag{4.36}$$

$$Ex_{\mathrm{d}}^{AHEX}=Ex_7-Ex_8 \tag{4.37}$$

$$Ex_{\mathrm{d}}^{turb2}=Ex_8-Ex_9-W_{turb2} \tag{4.38}$$

4.2.2.3 Economic performance indexes

To evaluate the economic benefit of the proposed system, an economic analysis was also performed. The net present value (*NPV*) and saving to investment ratio (*SIR*) are used to show the investors whether the investment of such a power plant is cash-flow-positive. *NPV* is defined as the difference between the present value of revenue and the present value of cost. *SIR* is calculated by dividing the present value of revenue by the present value of cost. *NPV*>0 and *SIR*>1 indicate that the investment has a potential economic benefit. Otherwise, they suggest an economic loss. The *NPV* and *SIR* are given mathematically in the following:

$$NPV = \sum_{i=1}^{lifetime} \frac{C_{NCI}}{(1+r)^i} - C \tag{4.39}$$

with

$$C_{NCI} = C_{revenue} - C_{O\&M} \tag{4.40}$$

$$SIR = \frac{\sum_{i=1}^{lifetime} \frac{C_{NCI}}{(1+r)^i}}{C} \tag{4.41}$$

where C_{NCI} represents the net cash inflow, C represents the capital cost, $C_{revenue}$ represents the revenue obtained, $C_{O\&M}$ represents the operating and maintenance cost, *lifetime* represents the lifespan, and r refers to the discount rate. In this study, the daily revenue for this proposed system only considered the electricity generation of the Power generation#1. The Power generation#1 is assumed to operate 16 hours per day (8 hours each during peak and off-peak periods) for electricity supply using the waste thermal energy from the LAES and LNG plants. Besides, the operating and maintenance costs (O&M) typically amount to 1.5-3% of the capital cost of the whole system per annum [140]. In this study, the O&M cost is assumed to account for 2% of the capital cost per annum in this study. The details about the calculation of the capital cost of the Power generation#1 and the industrial electricity tariffs are given in Section 4.4.

Besides, the payback period (*payback_period*) is also an important index to evaluate the economic value of an investment, which is defined as below:

$$payback\_period = \frac{C}{C_{NCI}} \tag{4.42}$$

4.3 Results and discussion

Many factors could influence the performance of this power generation system, among which, the expansion ratio of the turbine, the temperatures of the cold and heat sources, and the ratio of the mass flow rates among the working fluid, cold fluid, and hot fluid are the most critical parameters. Thus, analyses were done on how these factors affect the thermodynamic performance of the proposed power generation system based on waste energy recovery. MATLAB was used to calculate the system performance. The thermal properties of nitrogen, argon, and LNG (assumed to be pure methane) were obtained from REFPROP 9.0, and the thermal properties of thermal oil (Dowtherm G) are extracted from ASPEN plus 8.8 software package. Table 4.2 lists the default operating conditions for this power generation system. The calculation results and a comprehensive discussion of these results will be present in this section.

Table 4.2 Default design conditions for the power generation system

Parameters	Value
Thermal oil temperature (K)	473.15
LNG temperature (K)	111.51
LNG pressure in tank (MPa)	0.1
Cryo-pump outlet temperature of LNG (K)	116.94
Cryo-pump outlet pressure of LNG (MPa)	10
Turbine#2 outlet pressure of NG (MPa)	7
Turbine outlet pressure of argon (MPa)	1.44
Turbine outlet pressure of nitrogen (MPa)	2.93

Minimum Approach Temperature of heat exchanger#1 (K)	2
Minimum Approach Temperature of heat exchanger#2 (K)	2
Isentropic efficiency of compressor [141]	70%
Isentropic efficiency of cryo-pump/pump [55]	70%
Isentropic efficiency of turbine#1&2 [137]	90%
Mass flow rate of working fluid (nitrogen/argon) (kg/s)	1

4.3.1 Selection of working fluid

First, due to suitable temperature range, the Dowtherm G thermal oil was used as the heat transfer medium of the heat source in heat exchanger#1.

Second, LNG needs to be pressurized before regasification to ensure long-distance and high-efficiency NG pipeline transportation. Thus, LNG is pumped to a high pressure (10 MPa) in this proposed power generation system before entering heat exchanger#2. The pressurized LNG is used to cool down the working fluid during the regasification process in heat exchanger#2, which is followed by a further heating process to the ambient temperature before expansion in turbine#2 to 7 MPa for long-distance transmission.

For the cryogenic power generation cycle, nitrogen and argon are considered, which have widely studied as the working fluid because of their low triple point, nonflammability, and non-pollution. [142]. In order to utilize the high-grade cold energy of LNG more effectively, nitrogen and argon are working under different outlet pressures of turbine#1 (P_4). At their respective design pressures, the liquefaction temperatures of nitrogen and argon (nitrogen: 123.13 K at 2.93 MPa, argon: 123.15 K at 1.44 MPa) can be very close to the LNG temperature.

4.3.2 Constant heat and cold sources

To analyse the influence of the expansion ratio of turbine#1 (P_3/P_4) on this power generation system performance, the heat source and cold source are assumed to be at a constant

temperature first. This can avoid the influences of the temperatures and mass flows of the cold and heat sources on the system performance.

4.3.2.1 Effect of the turbine expansion ratio

Figure 4.3 shows the effect of the expansion ratio of the turbine (P_3/P_4) on the specific power of Power generation#1 ($w_{net,PG1}$). With the increase of the turbine expansion ratio (P_3/P_4) from 2 to 40, the specific power of Power generation#1 ($w_{net,PG1}$) increases first and then decreases, giving a maximum for both argon and nitrogen. This is mainly because the increase of the turbine expansion ratio (P_3/P_4) contributes to the increased power generation of turbine#1. However, it also implies the increase of the compression ratio (P_2/P_1), which finally leads to the increase of the power consumption of the compressor. With increasing turbine expansion ratio (P_3/P_4), the amount of the power generation increases more steeply than the power consumption, leading to the increase in the specific power generation ($w_{net,PG1}$) first. However, with the continuous increase of the turbine expansion ratio (P_3/P_4), the rate of the power consumption due to compression accelerates and finally catches up with the rate of the power generation, which makes the specific power generation ($w_{net,PG1}$) reach the peak. A further increase in the turbine expansion ratio (P_3/P_4) gives the rate of the power consumption overtaking the rate of the power generation, leading eventually to the observed decline of the specific power generation ($w_{net,PG1}$).

From Figure 4.3, it can also be seen that with the increase of the LNG outlet pressure of the cryo-pump (P_6), the specific power generation ($w_{net,PG1}$) for both the nitrogen and argon reduces. This is mainly because the increase of the outlet pressure of the cryo-pump leads to an increase of the temperature of the LNG (T_6). Therefore, the compressor inlet temperature for both the nitrogen and argon (T_1) increases as well, resulting in an increased power consumption of the compressor.

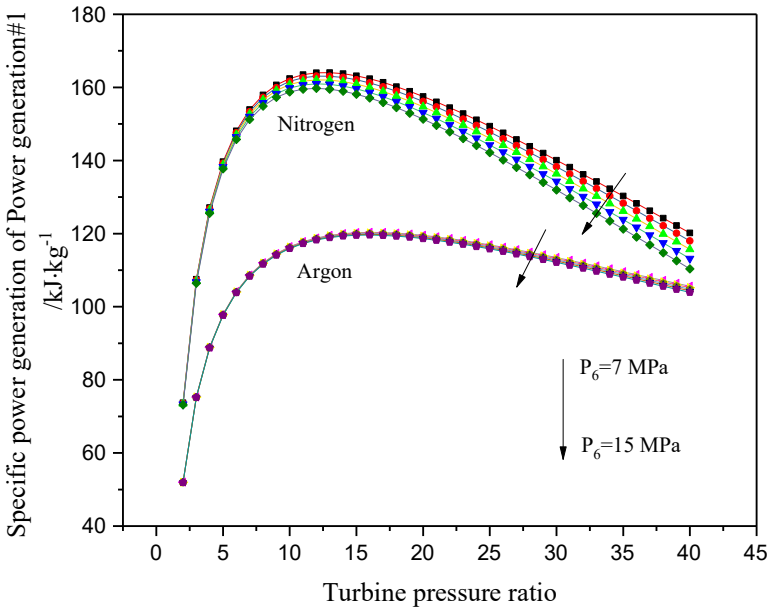

Figure 4.3 Effect of the turbine expansion ratio on the specific power generation of nitrogen/argon at different LNG pressures (Power generation#1).

4.3.2.2 Effect of the temperatures of heat and cold sources

Under a fixed turbine expansion ratio of 8 (P_3/P_4=8), the effects of the temperatures of the constant heat and cold sources on the specific power generation ($w_{net,PG1}$) have been investigated. The temperature variation ranges of the cold and heat sources are 113.15 K - 120.15 K and 413.15K - 473.15 K, respectively. Figure 4.4 (a) and (b) show the variations of the specific power of Power generation#1 ($w_{net,PG1}$) at different cold source and heat source temperatures, with nitrogen and argon as the working fluids respectively. The results illustrate that a lower cold source temperature and/or a higher heat source temperature would increase the specific power generation of Power generation#1.

However, the extents of the influence of the cold and heat source temperatures are different. According to Figure 4.4 (a), as the cold source temperature (T_6) increases from 113.15K to 120.15K, the specific power generation of nitrogen shows a decrease of 0.66kJ/(kg·K). A decrease of the heat source temperature from 473.15K to 413.15K leads to a decrease of 0.48 kJ/(kg·K) in the specific power generation of nitrogen. As a result, the change of the specific

power generation of the nitrogen caused by the change of the cold source temperature is ~1.38 times that caused by the change of the heat source temperature. However, the result is opposite when argon is used as the working fluid, as shown in Figure 4.4 (b). The temperature increase of the cold source and the temperature decrease of the heat source lead to a specific power generation decrease of 0.08 kJ/(kg·K) and 0.29kJ/(kg·K) for argon, respectively. The decrease of the specific power generation of argon caused by the heat exergy loss is ~3.63 times that caused by the cold exergy loss.

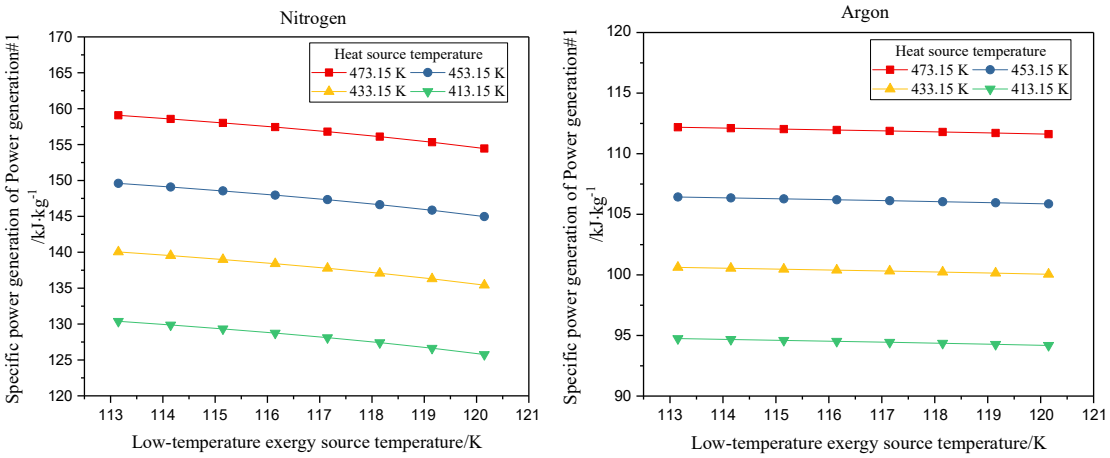

(a) (b)

Figure 4.4 Effects of the heat source and cold source temperatures on the specific power generation of nitrogen (a) and argon (b) (Power generation#1).

4.3.3 Limited cold source and constant heat source

4.3.3.1 Effect of the mass flow rate of LNG: energy analysis

To analyse the effect of the mass flow rate of the cold fluid (LNG) on the system performance, the heat source is assumed to be constant, whereas the effect of real mass flow rate of LNG is considered during the simulation process. The expansion ratio of the turbine is selected as 8 ($P_3/P_4 = 8$), and the LNG outlet pressure of the cryo-pump is fixed at 10 MPa (P_6=10 MPa). Figure 4.5 shows the variations of the specific power generations of the whole system (w_{net}) and Power generation#1($w_{net,PG1}$) as a function of the mass flow rate of LNG. Figure 4.6 (a)

and (b) show the temperature-entropy diagrams (T-S diagrams) of Power generation#1 with nitrogen and argon as the working fluids, respectively. Since the heat source is assumed to be constant, the outlet state of heat exchanger#1 (status 3) is independent of the mass flow rate of LNG. Thus, the positions of status 3 and status 4 in the temperature-entropy diagram are fixed. However, the mass flow rate of LNG can impact the positions of status 1 and status 2 very much.

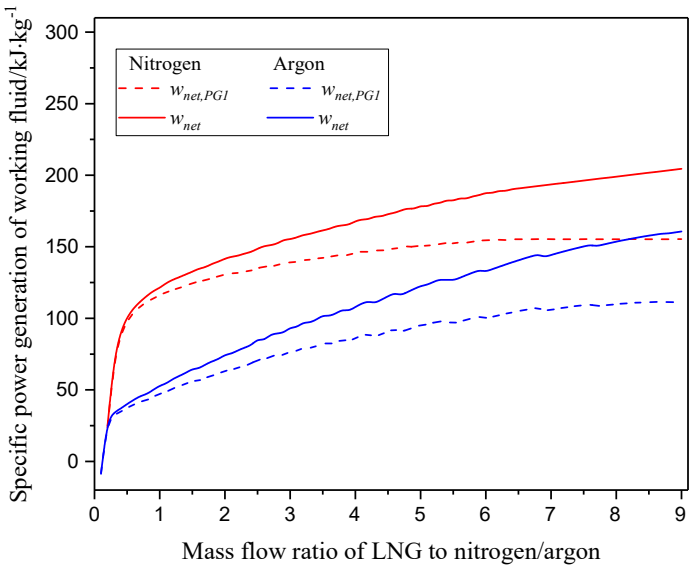

Figure 4.5 Specific power generation variation with the mass flow ratio of LNG to working fluid (Power generation#1 and whole system).

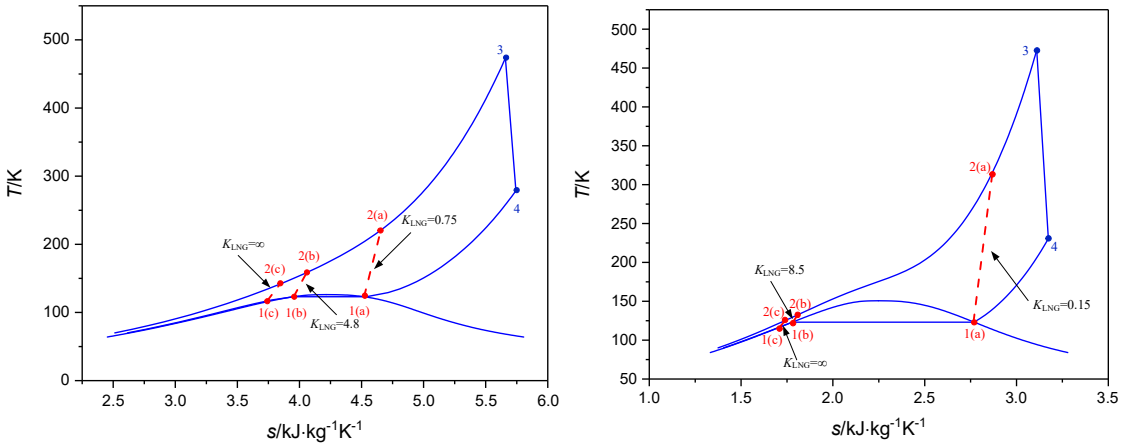

(a) (b)

Figure 4.6 T-S diagrams for nitrogen (a) and argon (b) in Power generation#1.

From the nitrogen curves (red curves) shown in Figure 4.5, one can observe that with the increasing mass flow ratio of LNG to the nitrogen (K_{LNG}), the specific power generation of Power generation#1 ($w_{net,PG1}$) increases when the ratio is smaller than 0.75 (K_{LNG} <0.75), beyond which (K_{LNG} >0.75), the increasing trend levels off. The maximum specific power generation of Power generation#1 ($w_{net,PG1}$) approaches the value obtained when both the cold and heat sources are assumed to be constant. That is because when the mass flow ratio of LNG to nitrogen is below 0.75 (K_{LNG} <0.75), the cooling capacity is insufficient to condense nitrogen in heat exchanger#2. In this case, nitrogen in this power generation system can only finish the Brayton Cycle. In this study, this value of 0.75 (K_{LNG} =0.75) is defined as the cut off value of the Brayton Cycle for nitrogen. When the mass flow ratio is equal to the cut off value (K_{LNG} = 0.75), nitrogen could complete the maximum-range Brayton Cycle, as shown in Figure 4.6 (a): 1(a)-2(a)-3-4-1(a). When the mass flow ratio of LNG to nitrogen is over the cut off value (K_{LNG} > 0.75), nitrogen in this power generation system enters the transition stage from the Brayton Cycle to Rankine Cycle, with an increased portion of the nitrogen condensed in heat exchanger#2. This continues until the mass flow ratio reaches 4.8 (K_{LNG} = 4.8), beyond which this power generation system can operate under the Rankine Cycle fully, as shown in Figure 4.6 (a): 1(b)-2(b)-3-4-1(b). When the mass flow ratio is beyond 4.8 (K_{LNG} > 4.8), the specific power generation of nitrogen in Power generation#1 ($w_{net,PG1}$) can only be close to but not exceed the result calculated under the condition of the constant cold source because of the pinch point constraint, as shown in Figure 4.6 (a): 1(c)-2(c)-3-4-1(c). Table 4.3 shows the calculated results at each state of the Power generation#1 with nitrogen as working fluid at different mass flow ratios of LNG to nitrogen (K_{LNG}). The effect of the mass flow ratio of LNG to nitrogen can be more clearly understood from Table 4.3. Firstly, the change of K_{LNG} does not affect the expansion process of Power generation#1 (status 3 to status 4), and hence the specific power generation of the turbine#1 remain constant. Secondly, with the increase of K_{LNG}, more cooling energy is released from LNG to cool down the nitrogen in Power generation#1 (status 4 to status 1) which lead to the temperature decrease in the nitrogen before compression (status 1). Lastly, the decrease of the temperature at status 1 can reduce

the specific power consumption of the compression process (status 1 to status 2), especially for nitrogen in the gaseous form. Therefore, as the K_{LNG} increases, the unchanged power generation of the expansion process and the decreased power consumption of the compression process ultimately result in the trend of the net specific power generation of Power generation#1 shown in Figure 4.5.

The similar result is also obtained when argon is used as the working fluid. The argon curves (blue curves) illustrated in Figure 4.5 show that the cut off value of the Brayton Cycle for argon in this power generation system is 0.15 (K_{LNG} = 0.15). When the mass flow ratio of LNG to the argon is lower or equal to 0.15 ($K_{LNG} \leqslant 0.15$), Power generation#1 can only work under the Brayton Cycle. When the ratio is between 0.15 and 8.50 ($0.15 < K_{LNG} < 8.50$), an increasing portion of argon completes the transition from the Brayton Cycle to the Rankine Cycle, as present in Figure 4.6 (b): from 1(a)-2(a)-3-4-1(a) to 1(b)-2(b)-3-4-1(b). When the ratio is over 8.50 ($K_{LNG} \geqslant 8.50$), argon in this power generation system can complete the full Rankine Cycle, as illustrated in Figure 4.6 (b): from 1(b)-2(b)-3-4-1(b) to 1(c)-2(c)-3-4-1(c). Table 4.3 shows the calculated results at each state of the Power generation#1 with argon as working fluid at different mass flow ratios of LNG to nitrogen (K_{LNG}).

Table 4.3 Stream data of Power generation#1

State	Nitrogen				Argon			
	T (K)	P (MPa)	h (kJ/kg)	s (kJ/(kg·K))	T (K)	P (MPa)	h (kJ/kg)	s (kJ/(kg·K))
1(a)	123.13	2.93	65.09	4.52	123.18	1.44	47.77	2.77
2(a)	220.84	23.44	161.23	4.66	315.98	11.52	145.94	2.87
3	473.15	23.44	486.22	5.66	473.15	11.52	239.31	3.11
4	278.56	2.93	281.72	5.74	230.46	1.44	115.49	3.17
1(b)	123.13	2.93	-4.71	3.95	123.18	1.44	-74.03	1.78
2(b)	158.55	23.44	49.38	4.06	132.60	11.52	-61.51	1.81
3	473.15	23.44	486.22	5.66	473.15	11.52	239.31	3.11
4	278.56	2.93	281.72	5.74	230.46	1.44	115.49	3.17
1(c)	116.94	2.93	-30.37	3.74	116.94	1.44	-82.32	1.71
2(c)	141.68	23.44	17.15	3.84	125.21	11.52	-70.36	1.74

3	473.15	23.44	486.22	5.66	473.15	11.52	239.31	3.11
4	278.56	2.93	281.72	5.74	230.46	1.44	115.49	3.17

Furthermore, the power generation per unit mass flow of LNG for Power generation#1 ($w_{net,PG1}^{LNG}$) and the whole system (w_{net}^{LNG}) are studied and the results are presented in Figure 4.7. The power generation per unit mass flow of LNG is peaked at a mass flow ratio of 0.30 and 0.20 (K_{LNG} = 0.30 and 0.20) for nitrogen and argon, respectively. The specific power generation with respect to the mass flow of LNG for Power generation#1 ($w_{net,PG1}^{LNG}$) and the whole system (w_{net}^{LNG}) then drops sharply firstly, followed by a slow gradual decrease. Thus, in terms of the utilization efficiency of the cold energy of LNG, there is an optimal mass flow rate of LNG in this power generation system. The Brayton Cycle is the most efficient option for this power generation system (K_{LNG} = 0.30) when nitrogen is selected as the working fluid. As for argon, the combination of the Brayton Cycle and Rankine Cycle (argon has a vapour fraction of 97.10% at the outlet of the heat exchanger#2) shows the optimum (peak) at K_{LNG} = 0.20. The composite curves of heat exchanger#2 with nitrogen and argon as working fluids at their respective optimal LNG mass flow are shown in Figure 4.8 (a) and (b), respectively.

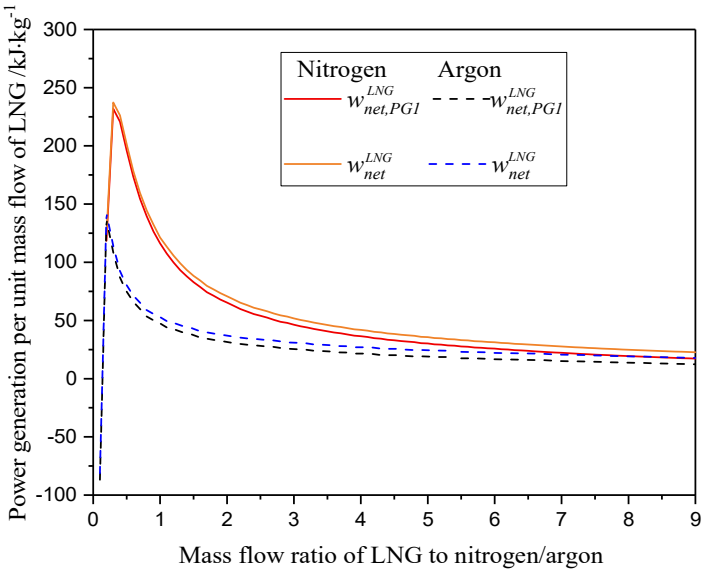

Figure 4.7 Effect of the mass flow ratio of LNG to working fluid on power generation per unit mass flow of LNG (Power generation#1 and whole system).

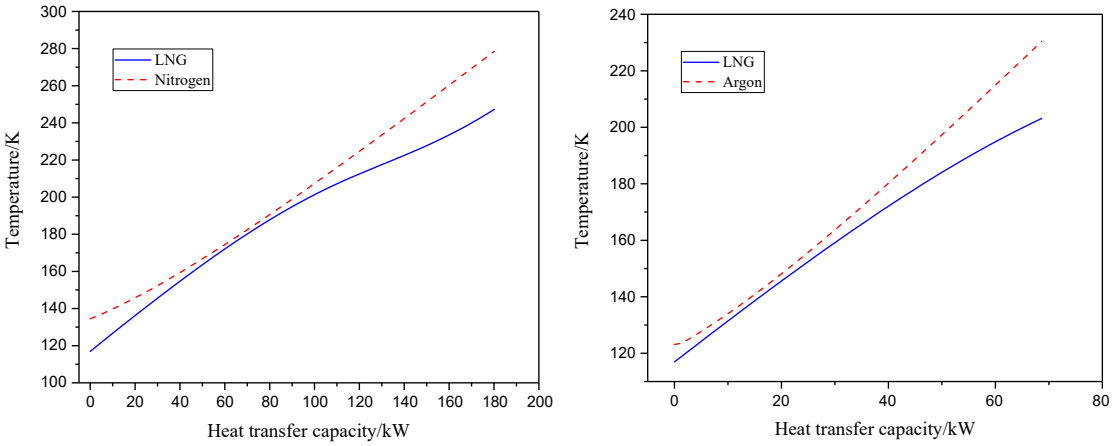

(a) (b)

Figure 4.8 Composite curves of heat exchanger#2 with nitrogen (a) and argon (b) as working fluids.

4.3.3.2 Effect of the mass flow rate of LNG: exergy analysis

The influence of the mass flow rate of LNG on the total system exergy destruction and the exergy destruction per unit mass flow rate of LNG are also studied and are illustrated in Figure 4.9. The total exergy destruction (Ex_d, blue curves) shows an almost linear dependence on the mass flow ratio of LNG to the working fluid at K_{LNG} > 0.30 and K_{LNG} >0.20 for nitrogen and argon, respectively. Under the optimal values of K_{LNG} = 0.30 and 0.20 for nitrogen and argon, respectively, the exergy destruction is almost constant. As a result, the exergy destruction per unit mass flow rate of LNG (Ex_d^{LNG}, red curves) shows a minimum value at the optimal mass flow ratios of 0.30 and 0.20 for nitrogen and argon, respectively. Figure 4.10 shows the respective exergy destruction occurred in Power generation#1 and Power generation #2, demonstrating that the sharp decrease of the total exergy destruction per unit mass flow rate of LNG at the very beginning of the increase of LNG input is caused mainly by the sharp decrease of the exergy destruction of Power generation#1.

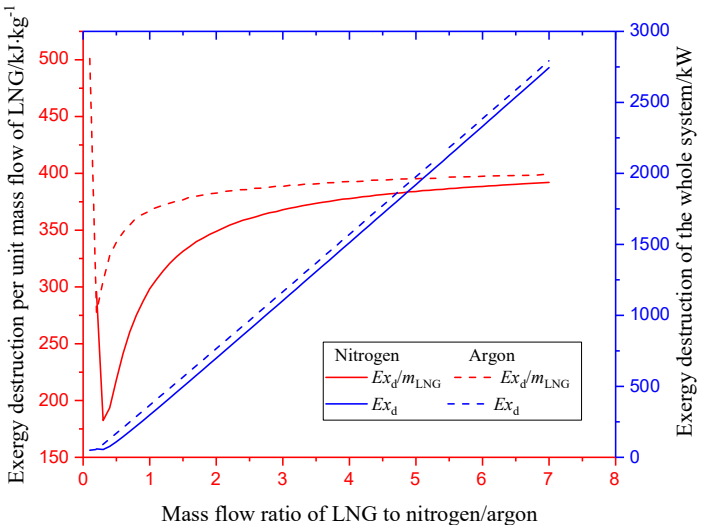

Figure 4.9 Effect of the mass flow ratio of LNG to working fluid on exergy destruction.

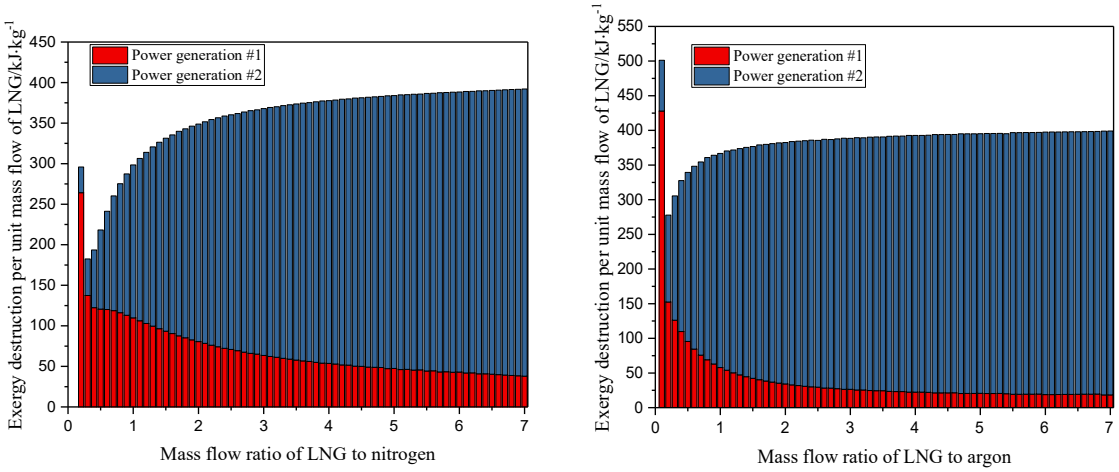

(a) (b)

Figure 4.10 Exergy destruction distribution in power generation#1 and #2 with nitrogen (a) and argon (b) as working fluids.

4.3.4 Limited heat and cold sources

4.3.4.1 Effect of the mass flow rate of thermal oil: energy analysis

The effects of the mass flow rate of the heat source on the specific power generation (w_{net}) and power generation per unit thermal oil (w_{net}^{oil}) are analysed, and the results are presented in Figure 4.11 and Figure 4.12. The best optimal flow ratios of LNG to nitrogen/argon obtained in Section 4.3.3 (K_{LNG}=0.30 and 0.20) are employed in the analyses of this section.

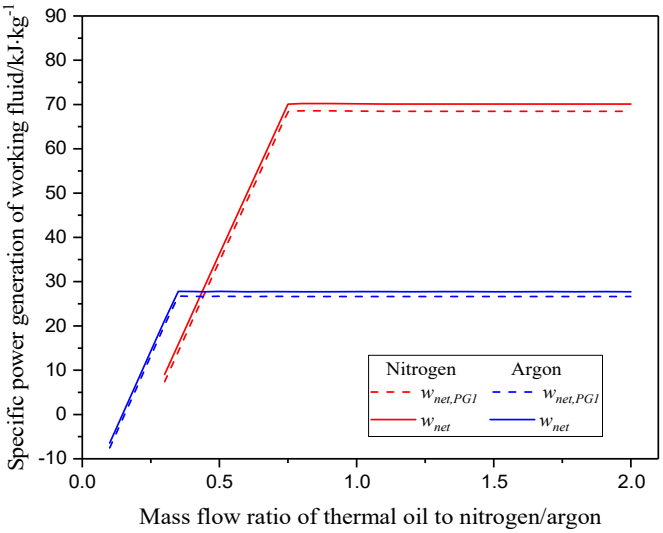

Figure 4.11 Specific power generation variation with the mass flow ratio of thermal oil to working fluid (Power generation#1 and whole system).

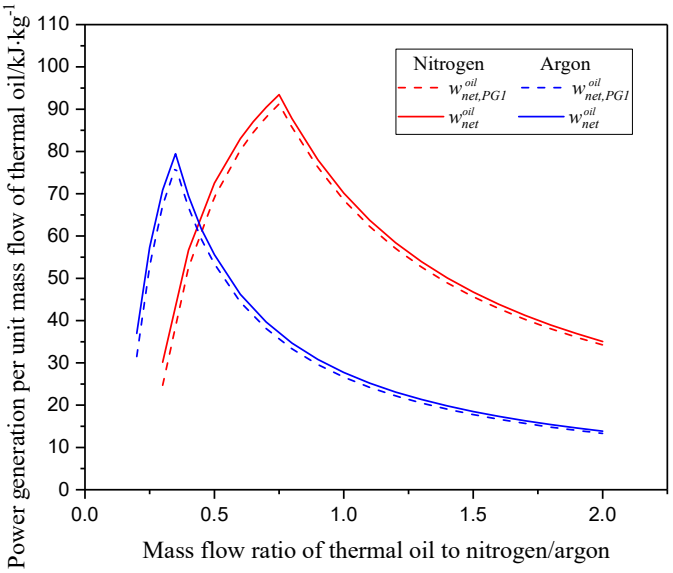

Figure 4.12 Effect of the mass flow ratio of thermal oil to working fluid on power generation per unit mass flow of thermal oil (Power generation#1 and whole system).

One can see from Figure 4.11 that, with increasing mass ratio of the thermal oil to nitrogen/argon (K_{oil}), the specific power generation of Power generation#1 ($w_{net,PG1}$) increases linearly, reaches maximum and then stays constant at the maximum. The turning points from the linear increase part to the maximum are 0.75 and 0.35 for nitrogen and argon, respectively. This is because there is an upper limit on the outlet temperature of heat exchanger#1, which is

determined by the heat source temperature and the pinch point of the heat exchanger. The initial increase of the mass flow of thermal oil can increase the working fluid temperature at the outlet of heat exchanger#1, resulting in an improved specific power generation ($w_{net,PG1}$). However, once the outlet temperature reaches the upper limit, the continuous increase of the mass flow of the thermal oil no longer affects the temperature of the working fluid at the outlet of heat exchanger#1. As a result, there is no change in the specific power generation ($w_{net,PG1}$) anymore. The power generation per unit mass flow of the thermal oil in Power generation#1 ($w^{oil}_{net,PG1}$) has a peak value at the turning point (K_{oil} = 0.75 for nitrogen and K_{oil} = 0.35 for argon), as shown in Figure 4.12.

Furthermore, as shown in Figure 4.13, the trend of the thermal efficiency of Power generation#1 and that of the whole system are similar to the dependence of the specific power generation on the mass flow ratio. Therefore, there is an optimal mass flow rate of the heat source for this power generation system (K_{oil} = 0.75 for nitrogen and K_{oil} = 0.35 for argon), which can maximize the thermal efficiency, the specific power generation, and the power generation per unit mass flow of the thermal oil. Figure 4.14 shows the composite curves for heat exchanger#1 under the condition of the highest thermal efficiency.

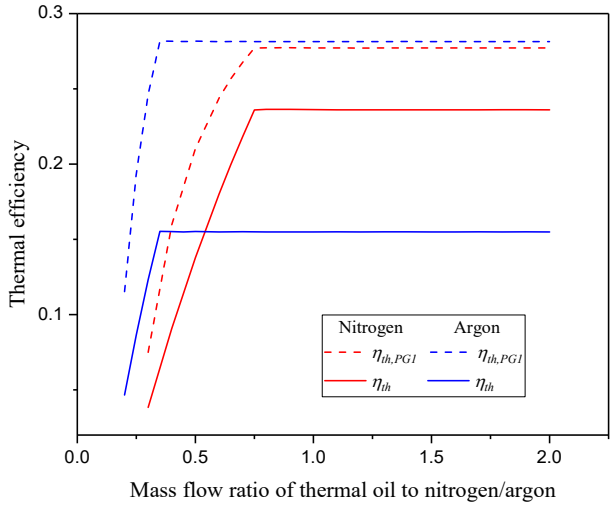

Figure 4.13 Effect of the mass flow ratio of thermal oil to working fluid on thermal efficiency (Power generation#1 and whole system).

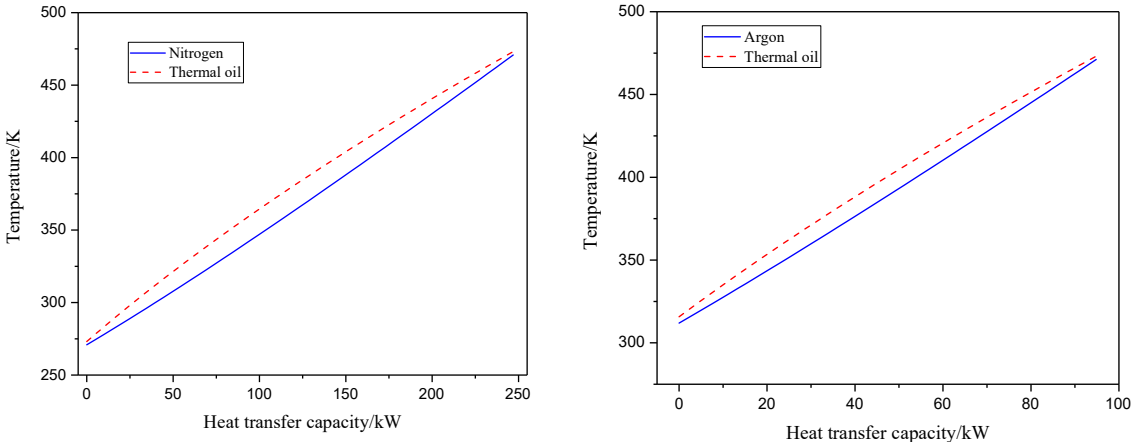

(a) (b)

Figure 4.14 Composite curves of heat exchanger#1 with nitrogen (a) and argon (b) as working fluids.

4.3.4.2 Effect of the mass flow rate of thermal oil: exergy analysis

Figure 4.15 and Figure 4.16 show the effects of the mass flow rate of the thermal oil on the exergy efficiency (η_{ex}) and the exergy destruction distribution, respectively. The highest exergy efficiency occurs at the same point where the thermal efficiency is at the maximum (K_{oil} = 0.75 for nitrogen and K_{oil} = 0.35 for argon), as illustrated in Figure 4.15. Figure 4.15 also shows that the exergy efficiency of the nitrogen system is much higher than that of the argon system, suggesting that the use of nitrogen as a working fluid be a better option to recover the waste compression heat of LAES and the cryogenic energy of LNG. From Figure 4.16, one can see that, with the increase of the mass flow rate of the thermal oil, the total exergy destruction of the whole system decreases first due to a clear decrease of the exergy destruction in the ambient heat exchanger. The total exergy destruction of the whole system is seen to reach a minimum, after which the total exergy destruction increases mainly due to the exergy destruction increase in heat exchanger#1.

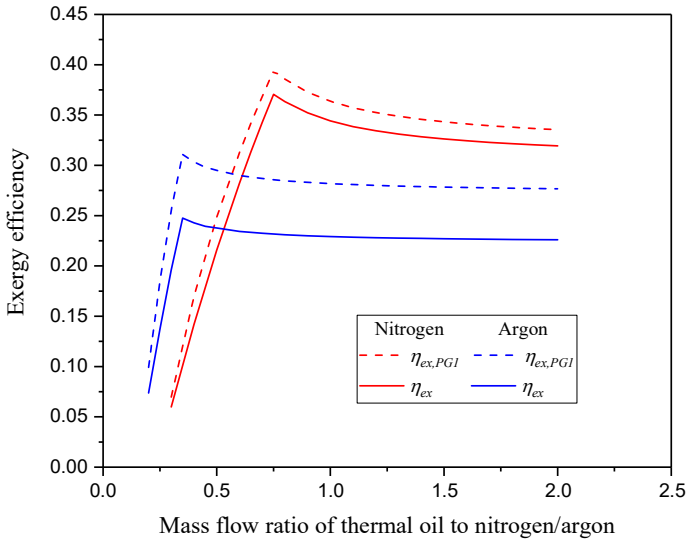

Figure 4.15 Effect of the mass flow ratio of thermal oil to working fluid on exergy efficiency (Power generation#1 and whole system).

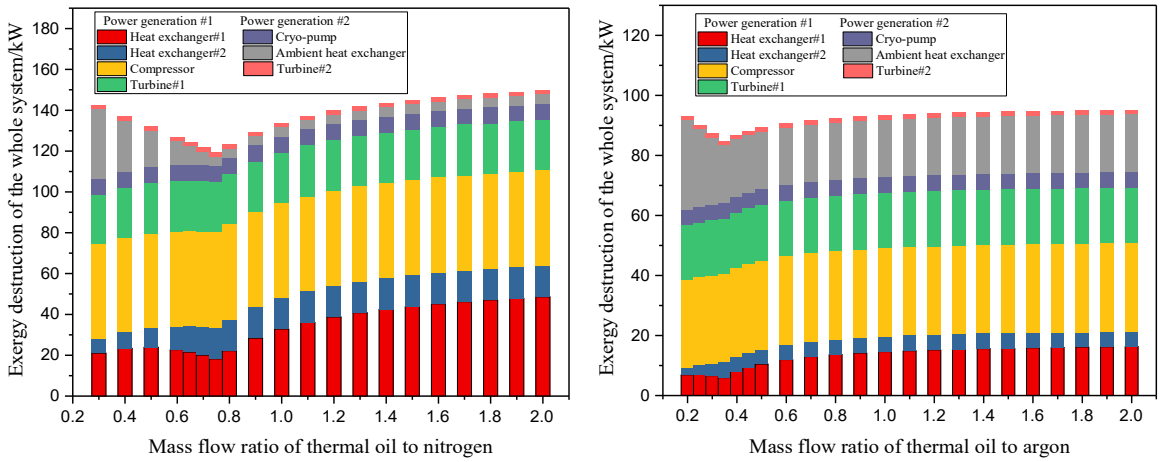

(a) (b)

Figure 4.16 Exergy destruction distribution in each component of the whole system with nitrogen (a) and argon (b) as working fluids.

4.3.4.3 Effect of the pressure drop of heat exchangers

The results discussed above carry an assumption that the pressure drops in all heat exchangers are negligible. However, the pressure drop of heat exchangers may be a very important factor that influences the system performance. Thus, in this section, the mass flow rates of both thermal oil and LNG (nitrogen: K_{LNG}=0.30 and K_{oil} = 0.75; argon: K_{LNG}= 0.20 and K_{oil} = 0.35)

are assumed to be fixed to study the effect of the pressure drop, as illustrated in Figure 4.17. It can be seen that as the pressure drop increases from 0% to 2.0%, the total exergy input of the whole system keeps almost constant, while the total exergy destruction of the whole system increases, leading to a reduced total net energy output and the exergy efficiency of the whole system. These results illustrate that the increase of every 1% in the pressure drop gives a decrease of ~3.5% and ~7% in the exergy efficiency for nitrogen and argon as working fluids, respectively.

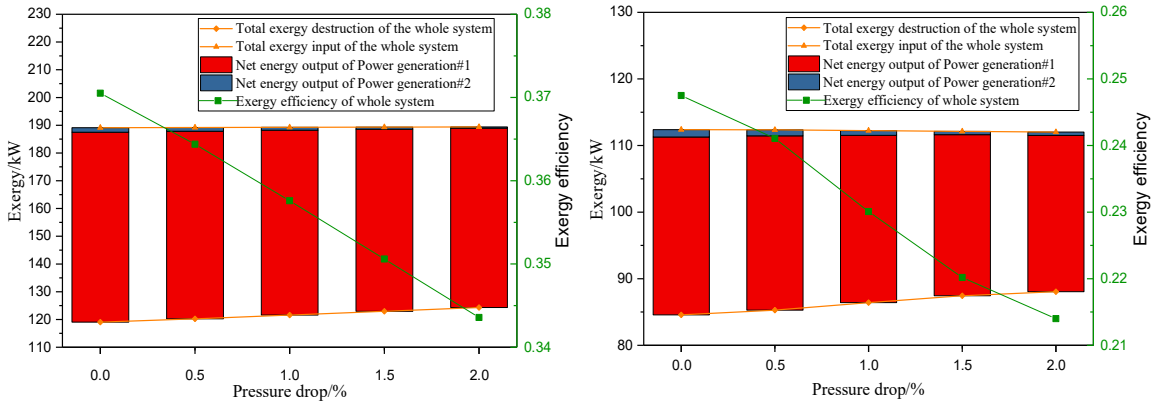

Figure 4.17 Effect of the pressure drop in heat exchangers on system performance with nitrogen (a) and argon (b) as working fluids.

4.4 Economic evaluation

The economic benefit to invest such a power generation system with nitrogen as the working fluid is analysed. Since all configurations in Power generation#2 stay the same as the original LNG regasification configurations in the LNG terminal, the economic analysis only considers the electricity output and the capital cost of Power generation#1. The cost functions for all the components in Power generation#1 are shown in Table 4.4. These cost functions are adopted in this study because they have been very commonly used in the economic analysis of power generation systems using LNG cold energy (-160 ℃) [143,144] and other industrial waste heat (100-200 ℃) [145,146], and this temperature range can match the designed operating temperature of Power generation#2 (-160℃ - 200℃).In Table 4.4, P_{in} and P_{out} represent the

inlet and outlet pressures of the working fluid, respectively; T_{in} represent the inlet temperature of the working fluid; q_{HX} is total exchanged heat flux of the heat exchanger; htc_c and htc_h are convective heat transfer coefficients of the cold and hot side of the heat exchanger, respectively; Δt_{in} and Δt_{out} are the temperature differences between the two streams at two ends of the heat exchanger, respectively. Besides, cost indices are required to convert purchased equipment cost into one that is accurate for the present time. In this work, the Chemical Engineering Plant Cost Index (CEPCI) is referred to adjust for the effects of inflation through time, where average annual value for 2018 of 603.1 is adopted [147].

Table 4.4 Cost functions for economic analysis.

System components	Capital cost function	Original year	CEPCI
Turbine [146]	$\frac{479.34 \cdot m}{0.92\text{-}\eta_{tur}} \cdot \ln(\frac{P_{\text{in}}}{P_{\text{out}}}) \cdot \left(1+e^{0.036T_{\text{in}}-54.4}\right)$	1996	381.7
Compressor [146]	$\frac{71.1 \cdot m}{0.9\text{-}\eta_{com}} \cdot \frac{P_{\text{out}}}{P_{\text{in}}} \cdot \ln(\frac{P_{\text{out}}}{P_{\text{in}}})$	1996	381.7
Heat exchanger [148]	$1650\left\{\frac{q_{HX}(1/htc_{\text{c}}+1/htc_{\text{h}})}{\left[\Delta t_{\text{in}}\Delta t_{\text{out}}(\frac{\Delta t_{\text{in}}+\Delta t_{\text{out}}}{2})\right]^{1/3}}\right\}^{0.65}$	2001	394.3

According to [54], there is about 395 ton/day excess thermal oil for a standalone LAES system (scale: 5MW/40MWh). In the study of [54], an ORC system with R32 as the working fluid was proposed to recover this part of excess heat (ambient-temperature cooling water is used as cold source). For comparison, a LAES system with the same scale is assumed to be integrated with the LNG regasification process through the way proposed in this chapter. All the excess thermal oil from the LAES side is utilized for power generation with nitrogen as the working fluid. In the analysis, the charging process of the LAES works for 8 hours per day (off-peak time) and 300 days per year. Hence, Power generation#1 can work for the rest of 16 hours at a rated power of 626 kW. The electricity rates of $291/MWh for peak time (8

hours) and $80.6/MWh for off-peak time (8 hours), the discount rate of 5%, and the project lifespan of 15 years are employed in the calculation, all of which keep the same as [54].

The results are shown in Table 4.5. It is clear that this proposed power generation system has a payback period of only 2.19 years and a saving to investment ratio of 4.73. This suggests that building a waste energy-based power plant co-located with the LNG terminal and LAES plant be more cost-effective than building a waste energy-based power plant located with the LAES plant alone. In addition, the specific investment cost of this waste energy-based power plant co-located with the LNG terminal and LAES plant is 1877 $/kW approximately.

Table 4.5 Economic analysis comparative results

Performance indexes	System in this chapter	System in [54]
Saving to investment ratio	4.73	2.78
Net present value ($)	4,379,880	2,690,991
Payback period (years)	2.19	3.1

Furthermore, the effect of the peak electricity tariff on the economic benefit has been considered when the off-peak time electricity tariff is fixed at $80.6/MWh, as illustrated in Figure 4.18. It can be seen that when there is no price difference between the peak and off-peak electricity, the payback period is around 5.3 years. A higher price difference between the peak and off-peak electricity can reduce the payback period significantly.

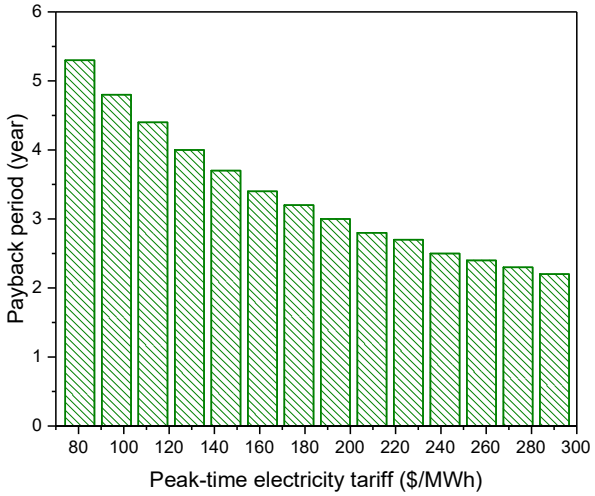

Figure 4.18 Effect of peak electricity tariff on the payback period.

4.5 Conclusions of Chapter 4

In this chapter, a power plant for recovering the high-grade cold energy from LNG (-160 ℃) and waste compression heat from the LAES system (200 ℃) is proposed. This provides a new way in the integration between the LAES system and the LNG regasification process. In this way, the LAES system keeps the baseline configuration, and requires little construction work to the existing LNG terminal, and hence make it more industrially feasible.

Nitrogen and argon are selected as the working fluids. Both energy analysis and exergy analysis are conducted on this power plant under different working conditions to optimize the working parameters, filling the gap in designing power plants working in a wide temperature range. Some conclusions have been obtained as follow:

- The optimal mass flow rate ratios of the working fluid to LNG to thermal oil are achieved, which are 1:0.3:0.75 and 1:0.2:0.3 for this power generation system with nitrogen and argon as working fluids, respectively. With the optimal mass flow ratio, the power generations per unit mass flow of LNG/thermal oil, thermal efficiency (nitrogen: ~27% and argon: ~28%), and exergy efficiency (nitrogen: ~40% and argon: ~32%) of this system could reach the maximum value.
- Nitrogen is more suitable to work in this proposed power generation system than argon, considering both the thermal efficiency and exergy efficiency of the whole system. However, argon has a higher thermal efficiency in Power generation#1.
- Every 1% increase in the pressure drop in heat exchangers could lead to ~3.5% and ~7% decrease in the whole system exergy efficiency for nitrogen and argon as working fluids, respectively.
- Under given circumstances, a waste energy-based power plant co-driven by the excess heat from a LAES power plant (5MW/40MWh) and the waste cold from an LNG terminal could achieve a payback period of 2.19 years and a saving to

investment ratio of 4.73, which is more profitable than a waste energy-based power plant only driven by the excess heat.

Chapter 5 Liquid air energy storage for multi-energy-vector services

5.1 Introduction

The excess compression heat of the LAES system for power generation was discussed in Chapter 4. This heat can also be used to provide the multi-energy-vector services. These include electricity, heat and/or cold energy, and the latter can be of high demand. The excess compression heat of ~200 ℃ can be used directly for heating or converted to cold energy for cooling. As a result, a standalone LAES system has the potential to provide trigeneration services.

As discussed in the previous chapters, the baseline LAES can produce a large amount of excess heat, especially at low charging pressures. The excess heat is valuable if the baseline LAES is used for a decentralized micro-energy network for residential communities and/or industrial/commercial centres. In those cases, the performance of the baseline LAES, especially at low charging pressures, is underestimated by only considering electrical energy in most of the previous studies. Here, in this chapter, a new configuration of the standalone LAES is proposed for combined cooling, heating, hot water and power (CCHHP) supply for decentralized micro-energy networks. As will be shown, a high performance could be achieved for such a newly proposed system even at low charging pressures.

5.2 The proposed standalone LAES for CCHHP supply

5.2.1 The baseline LAES for power supply

Figure 5.1 shows the conceptual and flow diagrams of the baseline LAES, which includes a charging cycle (air liquefaction) and a discharging cycle (power recovery). During off-peak hours, excess electricity is used to liquify air in the charging cycle: purified air (state 1) is compressed to a high pressure (state 8), and in the meantime heat generated during air compression is captured and stored in a thermal oil storage tank; the compressed air (state 8) is

first cooled by cold methanol (state 20) from a methanol storage tank to bring air to the state 13; the air is then cooled further by cold propane (state 22) from a propane storage tank to bring air to the state 12; the low temperature air (state 10) expands in a cryo-turbine with a portion of the air liquified and stored in the liquid air tank. During peak hours, the stored liquid air is used to generate electricity in the discharging cycle: the liquid air (state 24) is pumped to a high pressure (state 25) and then transfers cold energy to propane (state 23) and methanol (state 21) in turn, which are stored and used for air liquefaction in the charging cycle; the room temperature air (state 27) is further heated to a high temperature by the hot thermal oil in the thermal oil storage tank, before entering a multi-stage air turbine to generate electricity.

The round trip efficiency of a large-scale standalone baseline LAES is around 50-60%. This implies that the power recovered in the discharging process is only 50-60% of the power consumed in the charging process. An energy balance across the baseline LAES would mean a significant amount of excess heat stored in the thermal oil storage tank (see Section 5.3.1 for more details).

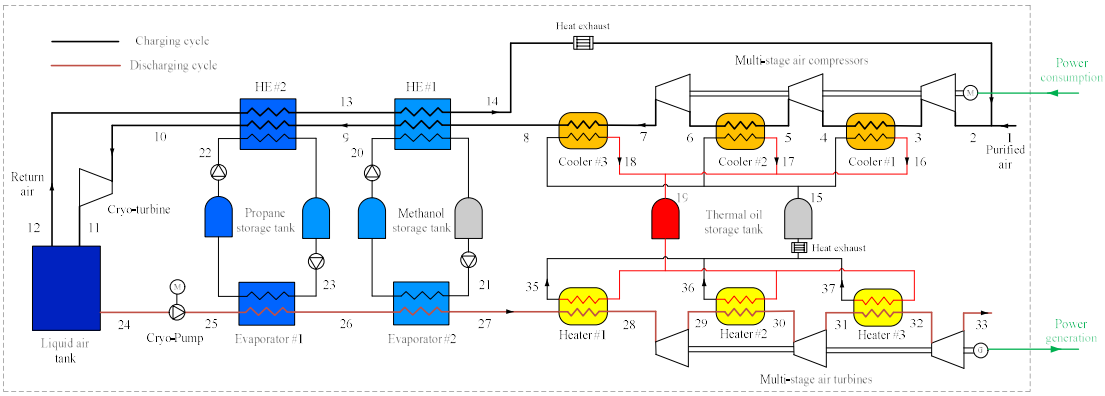

Figure 5.1 Flow diagram of the baseline LAES for peak load shifting (i.e. power supply).

5.2.2 The proposed LAES for CCHHP supply

To make full use of the excess heat, an option is to generate extra electricity through a power generation cycle. However, for cases where LAES plants are close to end users with demands on different forms of energy and/or integrated with local micro-energy grids, the use of the excess

heat for power generation is not necessarily the best option. This is because the end users not only require electricity, but also cooling, heating and hot water supplies. In addition, the conversion efficiency of low-grade heat (100-220 ºC) to electricity is very low around 20% and even lower in most cases [149], and the subsequent use of the electrical energy to produce cooling, heating and/or hot water is not an efficient process and requires more capital investment. Therefore, an LAES system for CCHHP supply is proposed that uses the compression heat to generate cold energy and provide heating and hot water; see Figure 5.2 for the conceptual and flow diagrams. This proposed system for CCHHP is more flexible, multi-functional, and applicable to small scale applications.

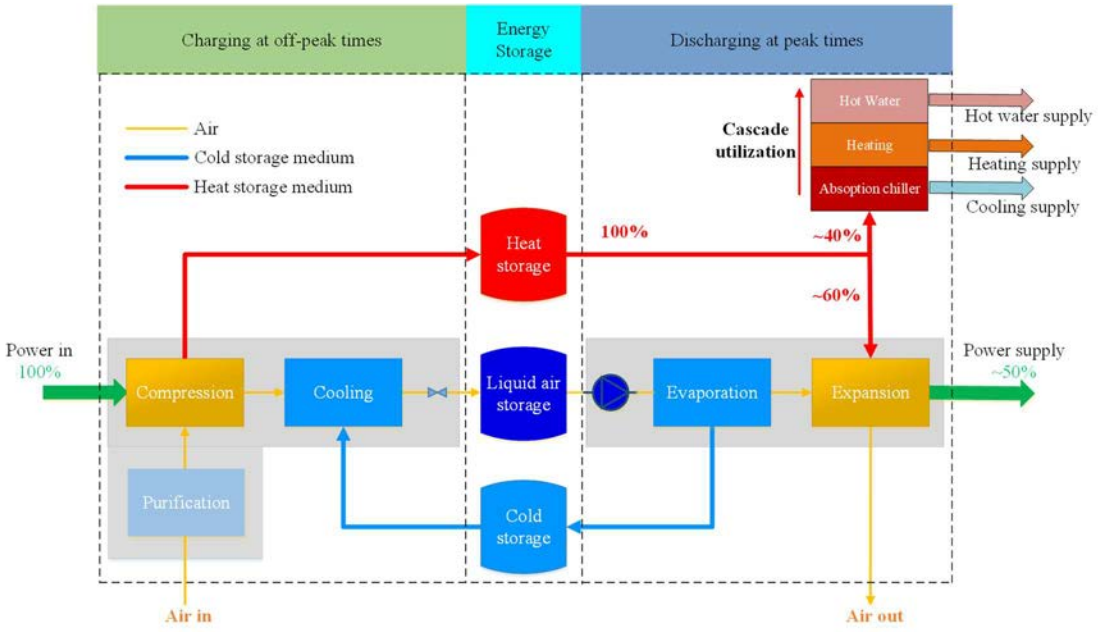

(a)

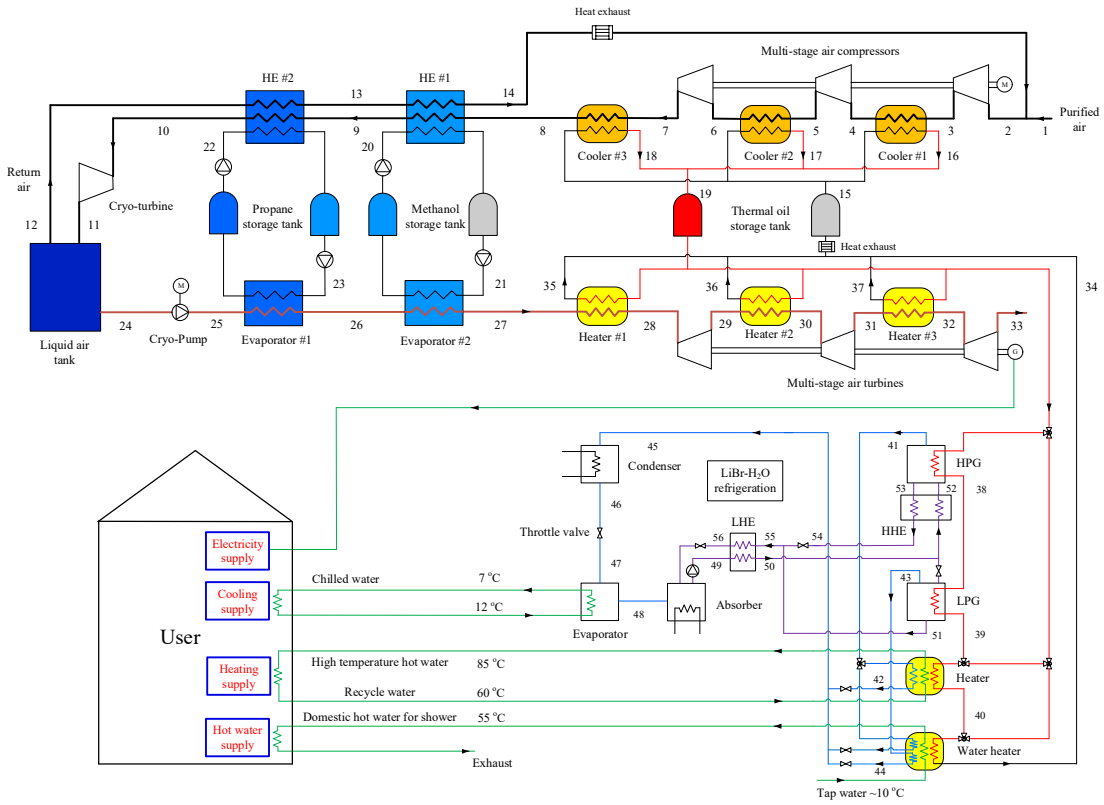

(b)

Figure 5.2 The proposed LAES for cooling, heating, hot water and power supply: (a) conceptual diagram and (b) flow diagram.

In the LAES for CCHHP, the cooling is achieved with a double-effect LiBr-H_2O refrigeration cycle which gives a cooling temperature of 7 °C; the heating is realized through a heater by heating inlet water at 60 to 85 °C; and the domestic hot water at 55 °C is obtained in a water heater by heating cold tap-water with an average annual temperature of 10 °C in the UK (These temperatures are taken based on practical applications). It should be noted that the high-pressure water vapour (state 41) leaving the high-pressure generator (HPG) flows into either the heater or the water heater through three-way valves to provide heating or domestic hot water, rather than goes to the low-pressure generator (LPG). This is because it has a lower condensing temperature (~90 °C), which is much lower than the thermal oil temperature (~180 °C). In addition, the low-pressure water vapour (state 43) leaving the LPG still carries low-grade heat and is used for domestic hot water.

Demands for hot water and power are inevitable for almost all end users, whereas heating and cooling requirements are optional in many cases. Therefore, to meet different end-user demands, the following three working modes for this proposed LAES are considered, as illustrated in Figure 5.3:

- Power, Hot water and Cooling supply in summer (PHC mode)
- Power, Hot water and Heating supply in winter (PHH mode)
- Power and Hot water supply in spring or autumn (PH mode)

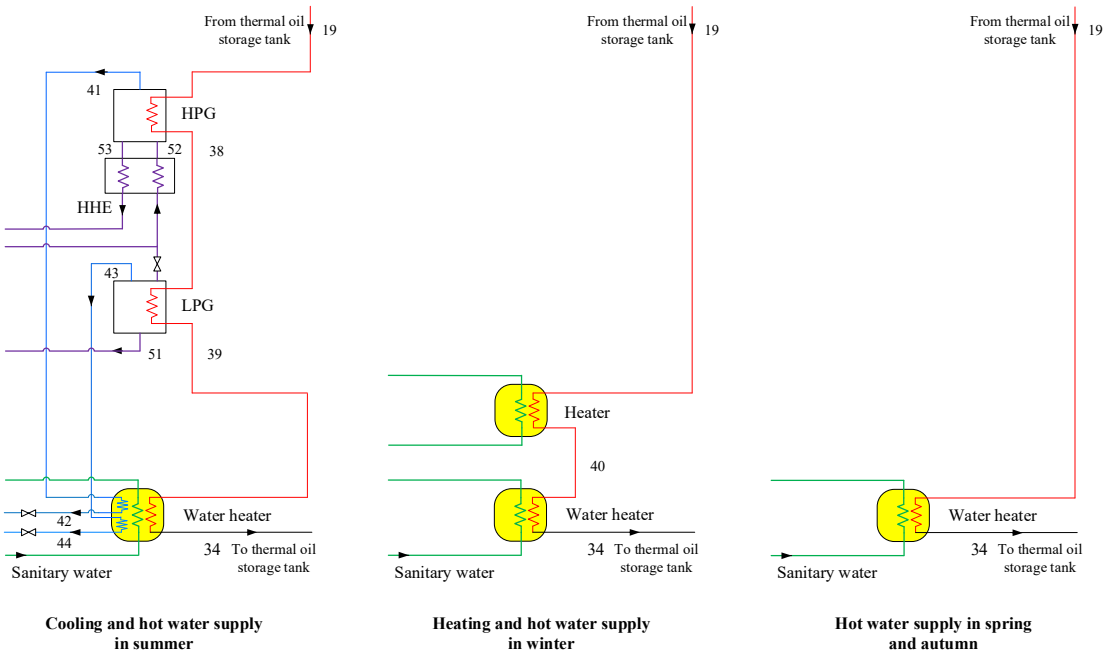

Figure 5.3 Three working modes of the proposed LAES for meeting end-user demand.

In the PHC mode, the excess heat is carried by the hot thermal oil (state 19) flowing in turn through the HPG, the LPG and the water heater. Both the high-pressure water vapour (state 41) generated in the HPG and the low-pressure water vapour (state 43) generated in the LPG transfer their heat to the tap water in the water heater (for domestic hot water supply) before being throttled to the same condensing pressure (state 45), and subsequently flowing through the condenser and the throttle valve, and finally arriving at the evaporator to produce chilled water (7 ºC) for cooling. The hot thermal oil (state 39) leaving the LPG enters the water heater, where it transfers the heat energy to the tap water to produce domestic hot water.

In the PHH mode, the excess heat is carried by the hot thermal oil (state 19) flowing through the heater first to heat the recirculating water (60 °C) for space heating, and then the water heater to heat the tap water for domestic hot water supply.

In the PH mode, the excess heat is carried by the hot thermal oil (state 19), which flows through the water heater to heat the tap water to produce domestic hot water.

5.2.3 Thermodynamic models

5.2.3.1 The charging and discharging processes

In the charging process of the LAES system for CCHHP supply, ambient air is purified first to remove moisture, carbon dioxide and particulate matters before compression by multi-stage air compressors. The power consumption of the air compressors, W_{com}, can be calculated by:

$$W_{com} = \frac{m_{air,ch} \cdot ((h_{3,s} - h_2) + (h_{5,s} - h_4) + (h_{7,s} - h_6))}{\eta_{com}} \tag{5.1}$$

where $m_{air,ch}$ is the air mass flow rate in the multi-stage air compressors in the charging process; h_i is the specific enthalpy with i corresponding to state i shown in Figure 5.2; η_{com} is the isentropic efficiency of air compressors; the subscript s represents an isentropic process.

For off-the-shelf products, screw compressors are widely used in industry for working pressures lower than ~2 MPa due to reliability and low maintenance costs, whereas piston compressors are for high pressure applications from ~3 to ~40 MPa [150]; see Figure 5.4. The screw compressors have an isentropic efficiency of 0.65-0.7 and the isentropic efficiency of piston compressors lies between 0.8 and 0.9 [151]. As a result, the selection of the compressors is shown in Table 5.1.

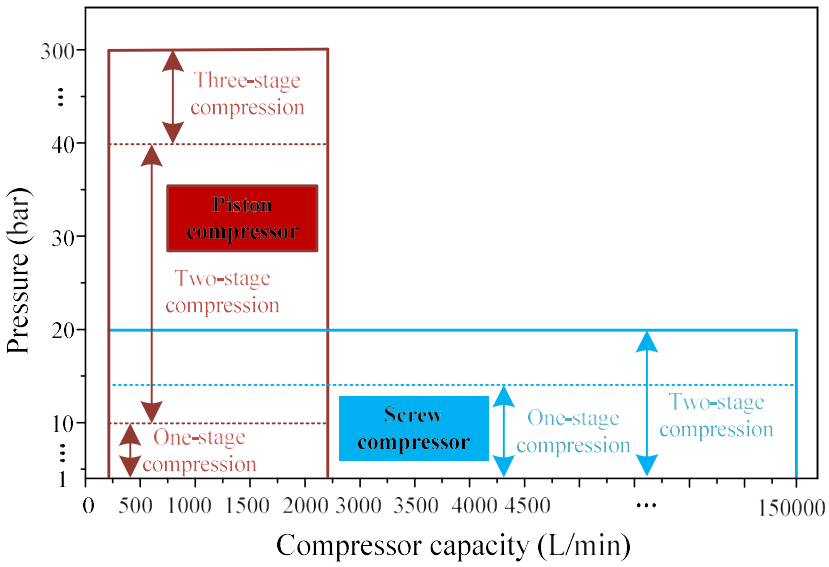

Figure 5.4 Screw and piston compressors: capacity and working pressure.

Table 5.1 Selections of air compressor type [150] and efficiency [151].

Charging pressure (MPa)	Compression stages	Compressor type	Isentropic efficiency
$P_{ch} \leqq 2$	2	Screw	0.68
$2 < P_{ch} \leqq 4$	2	Piston	0.89
$P_{ch} > 4$	3	Piston	0.89

The compressed air (state 8) is cooled in turn via heat exchangers HE #1 and HE #2. The air parameters at the outlet of the HE #1 and HE #2 are determined via energy conservation and pinch point constraints:

$$h_9 = h_8 - \frac{m_{methanol,ch} \cdot (h_{21} - h_{20}) + m_{12} \cdot (h_{14} - h_{13})}{m_{air,ch}} \tag{5.2}$$

$$h_{10} = h_9 - \frac{m_{propane,ch} \cdot (h_{23} - h_{22}) + m_{12} \cdot (h_{13} - h_{12})}{m_{air,ch}} \tag{5.3}$$

where $m_{methanol,ch}$ and $m_{propane,ch}$ are the mass flow rates of methanol and propane in the charging process, respectively.

The low-temperature compressed air (state 10) expands in the cryo-turbine with part of the air liquefied. The power generated by the cryo-turbine ($W_{cryo\text{-}tur}$) and the liquid air yield (Y) are given respectively by:

$$W_{cryo-tur} = m_{air,ch} \cdot \eta_{cryo-tur} \cdot (h_{10} - h_{11,s}) \tag{5.4}$$

$$Y = \frac{m_{air,ch} - m_{12}}{m_{air,ch}} \tag{5.5}$$

where $\eta_{cryo\text{-}tur}$ is the isentropic efficiency of the cryo-turbine.

During peak times, the stored liquid air is pumped to a high pressure by a cryo-pump. The power consumption of the cryo-pump, $W_{cryo\text{-}pump}$, is calculated by:

$$W_{cryo-pump} = \frac{m_{air,dis} \cdot (h_{25,s} - h_{24})}{\eta_{cryo-pump}} \tag{5.6}$$

where $\eta_{cryo\text{-}pump}$ is the isentropic efficiency of the cryo-pump; $m_{air,dis}$ is the mass flow rate of liquid air in the discharging cycle.

The low-temperature liquid air (state 25) transfers cold energy in turn to propane and methanol via the evaporator #1 and evaporator #2. The air outlet conditions can be determined by energy conservation and pinch point constraints:

$$h_{26} = h_{25} + \frac{m_{propane,dis} \cdot (h_{23} - h_{22})}{m_{air,dis}} \tag{5.7}$$

$$h_{27} = h_{26} + \frac{m_{methanol,dis} \cdot (h_{21} - h_{20})}{m_{air,dis}} \tag{5.8}$$

where $m_{methanol,dis}$ and $m_{propane,dis}$ are the mass flow rates of methanol and propane in the discharging process, respectively.

The high-pressure air (state 27) is preheated by the hot thermal oil stored during air compression in the charging process before entering the multi-stage air turbine to generate electricity. The power generated by the air turbines, W_{turb}, can be calculated by:

$$W_{turb} = m_{air,dis} \cdot \eta_{turb} \cdot ((h_{28} - h_{29,s}) + (h_{30} - h_{31,s}) + (h_{32} - h_{33,s})) \quad (5.9)$$

where η_{turb} is the isentropic efficiency of the air turbines.

5.2.3.2 The LiBr-H_2O refrigeration cycle

For the double-effect LiBr-H_2O refrigeration cycle, the following assumptions are made to analyse the cycle performance:

- Strong solutions (states 51 and 53) leaving the HPG and LPG are saturated; weak solution leaving the absorber is saturated
- The highest solution concentration leaving the HPG and LPG is set at 0.64 to avoid crystallization in pipelines; and the pump work is negligible in the cycle
- Refrigerant (water) is saturated at the outlet of the condenser and evaporator, and experiences an isenthalpic process in the throttle valve

For the HPG and LPG, the excess heat carried by the hot thermal oil is used to heat the weak solution for generating water vapour. The heat loads of the HPG (Q_{HPG}) and LPG (Q_{LPG}) are respectively calculated by the following energy conservation equations:

$$Q_{HPG} = m_{53} \cdot h_{53} + m_{41} \cdot h_{41} - m_{52} \cdot h_{52} \quad (5.10)$$

$$Q_{LPG} = m_{51} \cdot h_{51} + m_{43} \cdot h_{43} - (m_{50} - m_{52}) \cdot h_{50} \quad (5.11)$$

where m_{50}, m_{51}, m_{52} and m_{53} are the mass flow rates of the LiBr aqueous solution at different states; m_{41} and m_{43} are the mass flow rates of the water vapour generated in the HPG and LPG, respectively. Based on mass conservation in the HPG and LPG, one has:

$$m_{41} = m_{52} - m_{53} \quad (5.12)$$

$$m_{43} = (m_{50} - m_{52}) - m_{51} \quad (5.13)$$

The water vapour generated in the HPG and LPG is condensed and combined. The mass flow rates of the refrigerant (water), m_w, in the condenser, evaporator and the absorber are given by:

$$m_w = m_{41} + m_{43} \tag{5.14}$$

The saturated liquid water at the outlet of the condenser is throttled to the evaporating pressure before entering the evaporator to produce chilled water for cooling. The cooling capacity of the evaporator, Q_{eva}, is determined by:

$$Q_{eva} = m_w \cdot (h_{48} - h_{47}) \tag{5.15}$$

The saturated water vapour in the evaporator is absorbed by the strong solution in the absorber. The mass and energy conservation of the absorber gives:

$$m_{49} = m_w + m_{56} \tag{5.16}$$

$$Q_{abs} = m_{56} \cdot h_{56} + m_w \cdot h_{48} - m_{49} \cdot h_{49} \tag{5.17}$$

where Q_{abs} is the heat released in the absorber.

5.2.3.3 The district cooling, heating and hot water network

This proposed LAES system could supply cooling, heating and hot water for the decentralized energy network by consuming the excess heat as mentioned above. The thermal loss (η_{loss}) due to the district energy network is selected as 5% of the energy supplied by the proposed LAES system [152].

In the PHC mode, there is no heating. The hot water capacity ($Q_{h\text{-}water}$) and cooling capacity (Q_{cool}) are obtained as:

$$Q_{cool} = (1 - \eta_{loss}) \cdot Q_{eva} \tag{5.18}$$

$$Q_{h-water} = (1 - \eta_{loss}) \cdot (m_{41} \cdot (h_{41} - h_{42}) + m_{43} \cdot (h_{43} - h_{44}) + m_{oil} \cdot (h_{39} - h_{34})) \tag{5.19}$$

where m_{oil} is the mass flow rate of the excess heat carrying thermal oil.

In the PHH mode, heating capacity (Q_{heat}) and hot water capacity ($Q_{h\text{-}water}$) are required by end-users:

$$Q_{heat} = (1-\eta_{loss}) \cdot m_{oil} \cdot (h_{19} - h_{40}) \quad (5.20)$$

$$Q_{h-water} = (1-\eta_{loss}) \cdot m_{oil} \cdot (h_{40} - h_{34}) \quad (5.21)$$

In the PH mode, only hot water is in demand. Hence, the hot water capacity ($Q_{h\text{-}water}$) is determined by:

$$Q_{h-water} = (1-\eta_{loss}) \cdot m_{oil} \cdot (h_{19} - h_{34}) \quad (5.22)$$

5.2.3.4 Equivalent electricity production

As the excess heat in this proposed LAES system is used for providing different commodities (cooling, heating and hot water) for decentralized energy network, it is necessary to convert the different commodities into equivalent electricity production, for evaluating the nominal electrical round trip efficiency in the next section.

Figure 5.5 shows the general ways to obtain cooling, heating, and hot water in the UK. At the moment, cooling is usually achieved by mechanical chillers; hot water and heating are provided through gas boilers. However, UK is promoting the application of air-source heat pumps for heating or hot water as potential technologies for heat decarbonization by 2050. To evaluate the equivalent electrical consumed by the end-users with the above ways, several assumptions are made as follows:

- Gas boiler (condensing type) consumes natural gas to provide heating or hot water, which has a thermal efficiency ($\eta_{gas,ther}$) of 90% [153]. As the consumed natural gas is used for generating electricity in a combined gas turbine power plant, the thermal-to-electricity efficiency ($\eta_{gas,ele}$) is 50% [154]
- The reversible air-source heat pump produces cooling at 7 ºC in summer with R410A as the refrigerant and screw-type compressors; in winter, it works reversely to provide heating or hot water at 55 ºC; the cooling (COP_c) and heating (COP_h) performances of the reversible air-source heat pump are selected as 4.18 and 3.06, respectively (see discussions in the following)

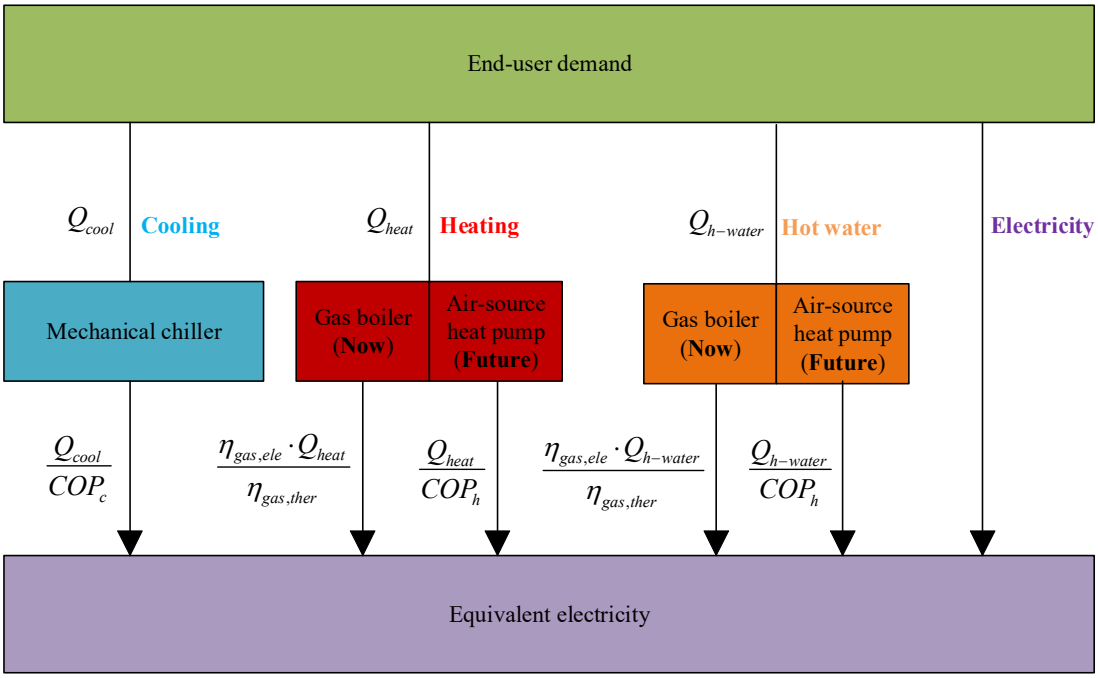

Figure 5.5 The general ways to obtain cooling, heating and hot water in the UK, and equivalent electricity calculations.

For the reversible air-source heat pump, the COP_c and COP_h are calculated as follows,

$$W_{ref,com} = m_{ref} \cdot \frac{(h_{com,out,s} - h_{com,in})}{\eta_{ref,com}} \tag{5.23}$$

$$\eta_{ref,com} = 0.07551 + 0.28995 \cdot r - 0.04521 \cdot r^2 + 0.00279 \cdot r^3 - 6.34 \times 10^{-5} \cdot r^4 \tag{5.24}$$

$$COP_c = \frac{Q_{cool}}{W_{ref,com}} \tag{5.25}$$

$$COP_h = \frac{Q_{heat}}{W_{ref,com}} \tag{5.26}$$

where m_{ref} is the mass flow rate of the refrigerant; $\eta_{ref,com}$ is the isentropic efficiency of the refrigeration compressor (screw type) and is calculated based on the pressure ratio (r) between the outlet and inlet of the refrigeration compressor [155].

Figure 5.6 shows the cooling and heating performance of the reversible air-source heat pump under the climate conditions of London, UK in 2018. It can be seen that the COP_c in summer is

at 4.18 and the COP_h in winter varies between 2.94 and 3.17 with an average at 3.06, which is mainly affected by the weather conditions.

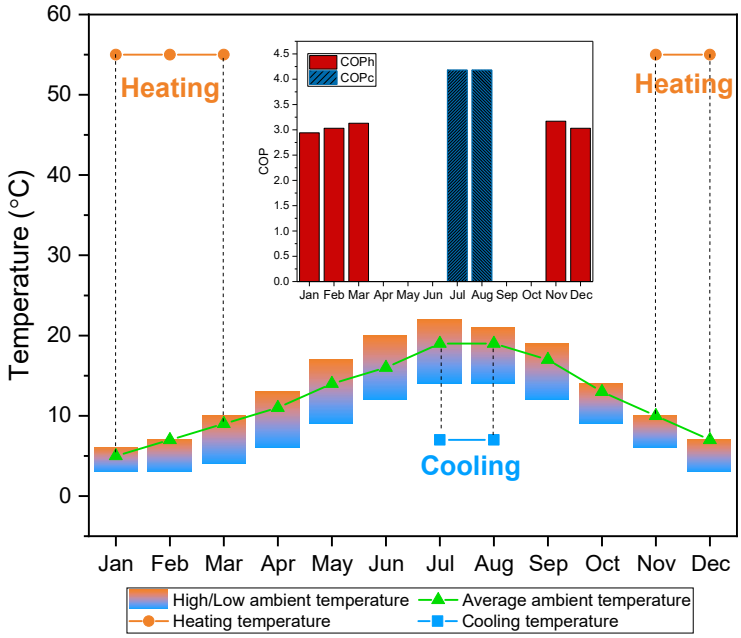

Figure 5.6 Cooling performance in summer and heating performance in winter of the reversible air-source heat pump in London, UK.

In the current case with gas boilers for heating or hot water, the equivalent electricity production of different commodities (cooling, heating and hot water) is defined as:

$$W_{eqv,gas} = \frac{Q_{cool}}{COP_c} + \frac{\eta_{gas,ele} \cdot Q_{heat}}{\eta_{gas,ther}} + \frac{\eta_{gas,ele} \cdot Q_{h-water}}{\eta_{gas,ther}} \tag{5.27}$$

As air source heat pumps are used for heating or hot water in the UK in the future, the equivalent electricity production of different commodities (heating and hot water) is calculated by:

$$W_{eqv,hp} = \frac{Q_{heat}}{COP_h} + \frac{Q_{h-water}}{COP_h} \tag{5.28}$$

5.2.4 Performance indexes

5.2.4.1 Electrical round trip efficiency

For the baseline LAES, electricity is stored in the form of liquid air at off-peak times, and the stored liquid air is used to generate electricity at peak times. Therefore, the electrical round trip efficiency of the baseline LAES, η_{E_RTE}, is defined as the ratio of net power generation at peak times to net power consumption at off-peak times:

$$\eta_{E\_RTE} = \frac{(W_{turb} - W_{cryo-pump}) \cdot t_{dis}}{(W_{com} - W_{cryo-tur}) \cdot t_{ch}} \tag{5.29}$$

where t_{ch} and t_{dis} are the charging and discharging time, respectively.

5.2.4.2 Maximum electrical round trip efficiency

The proposed LAES for CCHHP could generate not only electricity at peak times, but also excess heat (stored in thermal oil) that cannot be fully used for power generation. Therefore, considering the excess heat, the maximum electrical round trip efficiency (i.e., exergy efficiency) of this LAES system, $\eta_{E\_RTE\_max}$, is defined as:

$$\eta_{E\_RTE\_max} = \frac{(W_{turb} - W_{cryo-pump}) \cdot t_{dis} + m_{oil} \cdot ex_{heat} \cdot t_{dis}}{(W_{com} - W_{cryo-tur}) \cdot t_{ch}} \tag{5.30}$$

where ex_{heat} is the specific exergy of the excess heat, and can be calculated by:

$$ex_{heat} = (h_{19} - h_{ambient}) - T_{amb} \cdot (s_{19} - s_{ambient}) \tag{5.31}$$

5.2.4.3 Nominal electrical round trip efficiency

For the proposed LAES for CCHHP, the nominal-electrical round trip efficiency (neRTE) is defined as the ratio of the total power generation at peak times (net power generation by turbines plus equivalent electricity production by different commodities) to the net power consumption at off-peak times.

For the current case of end-users using gas boilers for heating or hot water in the UK, the neRTE of the LAES for CCHHP, η_{NE_RTE}, is defined as:

$$\eta_{NE\_RTE} = \frac{(W_{turb} - W_{cryo-pump}) \cdot t_{dis} + W_{eqv,gas} \cdot t_{dis}}{(W_{com} - W_{cryo-tur}) \cdot t_{ch}} \tag{5.32}$$

For the future case where end-users use air-source heat pumps for heating or hot water, the neRTE of the LAES for CCHHP is given as:

$$\eta_{NE\_RTE} = \frac{(W_{turb} - W_{cryo-pump}) \cdot t_{dis} + W_{eqv,hp} \cdot t_{dis}}{(W_{com} - W_{cryo-tur}) \cdot t_{ch}} \tag{5.33}$$

5.2.4.4 Primary energy savings

The proposed LAES system for CCHHP stores excess (off-peak) electricity from national grid, and then provides poly-generation for end-users at peak times, saving primary energy consumptions (natural gas is assumed as the primary energy here).

For the current case with gas boilers for heating or hot water in the UK, the primary energy savings of this proposed LAES system is defined as:

$$E_{PES} = \frac{((W_{tur} - W_{pump}) + W_{eqv,gas}) \cdot t_{dis}}{\eta_{gas-ele}} \tag{5.34}$$

For the future heating with air source heat pumps in winter, the primary energy savings of this proposed LAES system is calculated by:

$$E_{PES} = \frac{((W_{tur} - W_{pump}) + W_{eqv,hp}) \cdot t_{dis}}{\eta_{gas-ele}} \tag{5.35}$$

5.2.4.5 Avoided carbon dioxide emissions

The proposed LAES system for CCHHP contributes to primary energy savings as mentioned above, which avoids carbon dioxide emissions caused by the primary energy. For the current

case with gas boilers in the UK, the amount of avoided carbon dioxide emissions by this proposed LAES system is defined as:

$$M_{CO_2} = \xi \cdot ((W_{tur} - W_{pump}) + W_{eqv,gas}) \cdot t_{dis} \tag{5.36}$$

For the future heating in winter with air source heat pumps, the amount of avoided carbon dioxide emissions by this proposed LAES system is given as:

$$M_{CO_2} = \xi \cdot ((W_{tur} - W_{pump}) + W_{eqv,hp}) \cdot t_{dis} \tag{5.37}$$

where ξ is the emission factor, representing carbon dioxide emissions by a typical electricity mix, and is selected as 0.38 kg-CO_2/kWh [156].

5.3 Results and discussion

The default parameters used for the proposed LAES system for CCHHP supply are listed in Table 5.2. The charging time for air liquefaction at off-peak times is set as 8 hours/day and the liquid air is stored at 0.1 MPa; the discharging time for the power recovery process at peak times is set as 4 hours/day; and the discharging pressure is set at 12 MPa considering that a higher inlet pressure of air turbines would generate more power. The purified air in the charging process is assumed to consist of nitrogen (78.12%), oxygen (20.96%) and argon (0.92%). The Dowtherm G is chosen as the thermal oil and its properties are obtained from the ASPEN plus 8.8 software package. The properties of the purified air, propane and methanol are obtained from the REFPROP 9.0. The vapour pressure and enthalpy of the LiBr-H_2O solution are obtained from Pátek and Klomfar [157] and Talbi and Agnew [158], respectively. The models are solved in the MATLAB environment.

Table 5.2 Working parameters of the LAES system for CCHHP

Ambient pressure (MPa)	0.1
Ambient temperature (K)	293
Charging time t_{ch} (hour/day)	8

Liquid air storage pressure P_{24} (MPa)	0.1
Discharging pressure P_{25} (MPa)	12
Discharging time t_{dis} (hour/day)	4
Thermal oil storage temperature T_{15} (K)	293
Methanol storage temperature T_{21} (K)	293
Propane storage temperature T_{23} (K)	214
Minimum Approach Temperature of evaporators (K)	2
Minimum Approach Temperature of HEs, Heaters and Coolers (K)	5
Isentropic efficiency of air turbines	0.9
Isentropic efficiency of cryo-turbine	0.8
Isentropic efficiency of cryo-pump	0.7
Minimum usable temperature of hot thermal oil (K)	298
Evaporating temperature in the evaporator (K)	278
Condensing temperature in the condenser (K)	308
Absorbing temperature in the absorber (K)	308

Table 5.3 shows the representative performance of the proposed LAES system for CCHHP supply, where both the charging and discharging pressure are at 12 MPa. With a given power consumption of 8 MWh (1MW×8h) in the charging process at off-peak times, the proposed LAES system provides 4.4 MWh peak electricity and 2.64 MWh excess thermal energy available for heating and cooling applications; the maximum electrical round trip efficiency (i.e., exergy efficiency) reaches 0.64 with the contribution of the excess thermal energy.

Table 5.3 Representative performance of the proposed LAES system for CCHHP.

Results	PHC	PHH	PH
Electricity consumption during charging (MWh)	8	8	8
Electricity generation during discharging (MWh)	4.40	4.40	4.40
Electrical round trip efficiency	0.55	0.55	0.55
Cold energy stored (MWh)	3.73	3.73	3.73

Thermal energy stored (MWh)	5.86	5.86	5.86
Thermal energy available for other applications (MWh)	2.64	2.64	2.64
Maximum electrical round trip efficiency	0.64	0.64	0.64
Thermal energy available for heating (85 ˚C, MWh)	0	2.10	2.64
Thermal energy available for hot water (55 ˚C, MWh)	1.94	0.54	0
Thermal energy available for cooling (7 ˚C, MWh)	0.70	0	0

5.3.1 Performance of the baseline LAES over a wide range of charging pressure

In the charging process, the purified air is compressed to a high pressure (the charging pressure), and is then cooled down for air liquefaction. The compressed air requires different cooling capacities under different charging pressures, as shown in Figure 5.7. When the charging pressure is below the critical pressure of the air (3.85 MPa), there is a phase change as the air is cooled to its dew point, which requires more cold energy. Therefore, the performance of the baseline LAES at a charging pressure below the critical point will differ from that above the critical pressure.

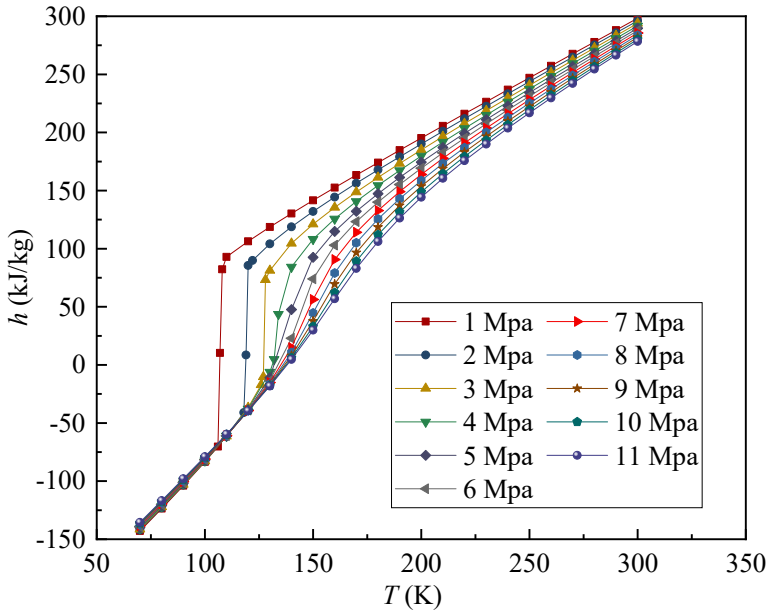

Figure 5.7 Properties of compressed air under different charging pressures.

Figure 5.8 shows the effect of the charging pressure on the liquid air yield for the baseline LAES system operated between 1 and 21 MPa. The liquid air yield is seen to increase significantly first from 0.214 to 0.432 as the charging pressure increases from 1 to 4 MPa mainly due to a significant decrease in the cooling capacity required for air liquefaction, as shown inFigure 5.7. It then increases gradually from 0.432 to 0.885 with the charging pressure increasing from 4 to 19 MPa due to a gradual decrease in the required cooling capacity (see Figure 5.7). Finally, the liquid air yield is seen to stabilize at 0.885 when the charging pressure goes above 19 MPa mainly because a further increase in the charging pressure has little effect on the cooling capacity required for air liquefaction.

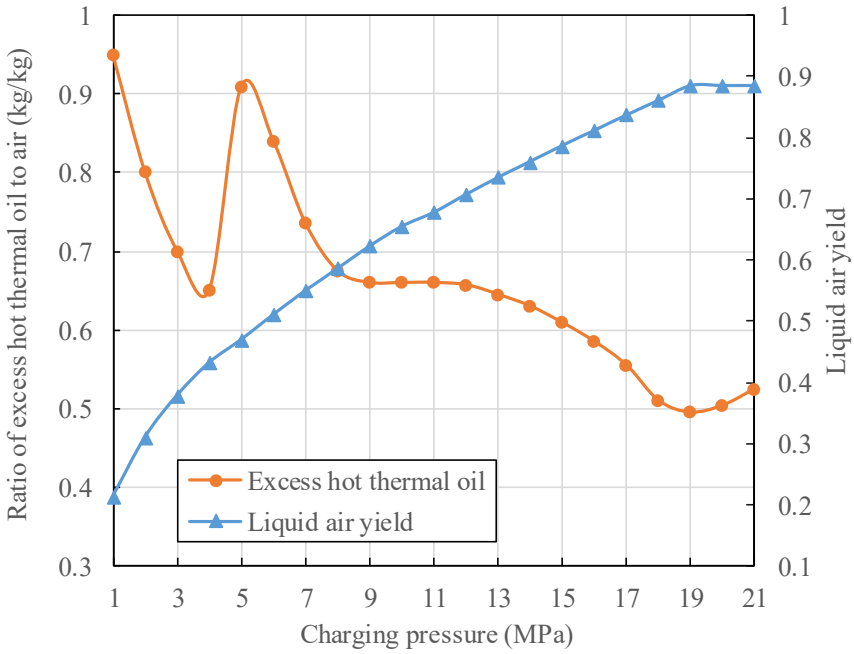

Figure 5.8 Effect of charging pressure on the excess compression heat (expressed as the ratio of the hot thermal oil mass to the air mass) and liquid air yield for the baseline LAES.

Figure 5.8 also shows the effect of the charging pressure on the production of excess compression heat, which is expressed as the mass ratio of the excess hot thermal oil to the compressed air in the charging process. The reason for using such a ratio is because the amount of hot thermal oil produced during air compression is proportional to the amount of compressed air. With a given compressed air mass flow rate in the charging process, a higher charging

pressure not only leads to more generation of compression heat (i.e. more hot thermal oil stored), but also produces more liquid air which consumes more compression heat to heat it up for generating power in the discharging process. Finally, the net stored compression heat (i.e. excess thermal oil) will fluctuate depending on the charging pressure. One can see that the excess hot thermal oil to compressed air mass ratio decreases dramatically from 0.95 to 0.65 when the charging pressure increases from 1 to 4 MPa. This is mainly due to the significant increase of liquid air yield, leading to the increasing consumption of hot thermal oil in the discharging process. The mass ratio increases significantly from 0.65 to 0.91 when the charging pressure increases from 4 to 5 MPa. This is mainly because a three-stage compression is used in this case (see Table 5.1), which produces more hot thermal oil in the charging process. When the charging pressure increases from 5 to 9 MPa, the mass ratio decreases dramatically from 0.91 to 0.66, mainly due to the significant increase in the liquid air yield. The mass ratio is stabilized at ~0.66 when the charging pressure increases from 9 to 12 MPa, which can be explained as a balance has been reached between the increasing hot thermal oil consumption in the discharging process and the increasing hot thermal oil generation in the charging process. The mass ratio is seen to decrease from 0.66 to 0.5 when the charging pressure increases from 12 to 19 MPa, due to an increased liquid air yield. As the charging pressure increases above 19 MPa, the mass ratio shows a gradual increase, which can be explained by the fact that the amount of hot thermal oil generated in the charging cycle increases but the liquid air yield remains stable. In summary, the baseline LAES has a lower liquid air yield, but produces more excess heat at low charging pressures of 1-7 MPa.

The effect of the charging pressure on the performance of the baseline LAES is shown in Figure 5.9 for an air mass flow rate in the charging process at 2 kg/s. Figure 5.9 (a) plots the power consumption of compressors, power generation of turbines, and the amount of excess heat generated under different charging pressures. Power consumption of air compressors in the charging process is seen increasing significantly from 4.93 to 7 MWh as the charging pressure increases from 1 to 2 MPa. There is a decrease in the power consumption to 6.18 MWh when a

further increase in the charging pressure from 2 to 3 MPa. This is because piston compressors with higher isentropic efficiency are selected for charging pressures above 2 MPa; see Table 5.1. When the charging pressure increases further from 4 to 5 MPa, the power consumption of air compressors decreases slightly from 7 to 6.83 MWh due to the three-stage compression process being chosen at a charging pressure above 4 MPa (see Table 5.1). At a charging pressure above 5 MPa, a gradual increase in the power consumption of air compressors occurs with increasing the charging pressure. Figure 5.9 (a) indicates the amount of power generation by air turbines increases significantly from 1.32 to 6.41 MWh when the charging pressure increases from 1 to 19 MPa. This is clearly due to the significant increase in the liquid air yield over the charging pressure range, as shown in Figure 5.8. There is a slight increase in the amount of power generation from 6.41 to 6.52 MWh with a further increase in the charging pressure from 19 to 21 MPa, which is mainly due to the increasing temperature of the hot thermal oil while the liquid air yield remains unchanged. Figure 5.9 (a) also shows that the excess compression heat carried by the hot thermal oil decreases from 4.94 to 2.34 MWh with the charging pressure increasing from 1 to 21 MPa.

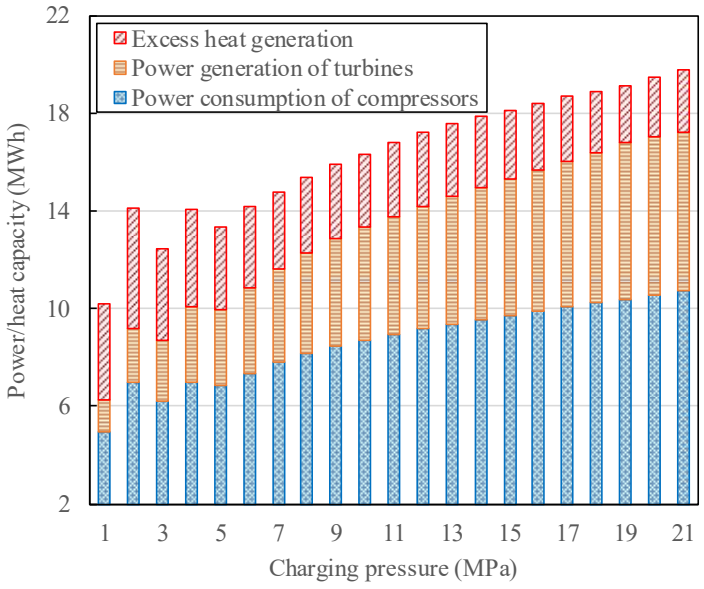

(a)

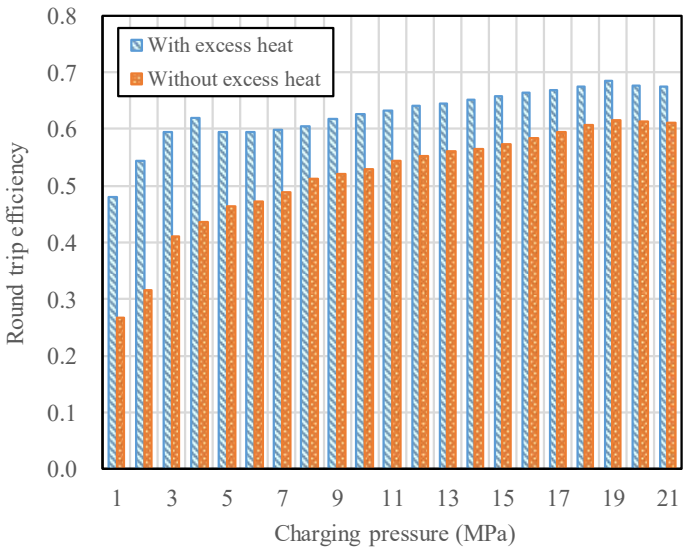

(b)

Figure 5.9 Effect of charging pressure on the performance of the baseline LAES.

Figure 5.9 (b) shows the effect of the charging pressure on the Electrical Round Trip Efficiency (eRTE) for the baseline LAES with and without the consideration of excess heat. For the case without excess heat, a dramatic increase occurs in the eRTE from 26.7% to 41.1% when the charging pressure increases from 1 to 3 MPa. This is clearly due to the significant increase in the liquid air yield over the pressure range. A slow rate of increase in the eRTE is seen with a further increase in the charging pressure from 3 to 19 MPa. The eRTE at 19 MPa reaches 61.7%. However, a further increase in the charging pressure from 19 to 21 MPa shows a decrease in the eRTE from 61.7% to 60.8%. This is mainly due to the increasing power consumption of air compressors in the charging process when the liquid air yield remains unchanged.

Figure 5.9 (b) suggests that the eRTE with excess heat (i.e., the maximum electrical round trip efficiency) lies between 48% and 69% and is much higher than that without excess heat. Importantly and somewhat unexpected, the baseline LAES with excess heat also has a high eRTE at lower charging pressures; a local maximum of 62% is achieved at a charging pressure of ~4 MPa. As a result, the performance of the baseline LAES, especially at low charging pressures has been somewhat underestimated in the past. The main reason for this is that the past research has only considered eRTE with the excess heat ignored, which can be highly valuable

for small scale applications such as the integration of the baseline LAES with decentralized local micro-energy networks where there are demands on heating, cooling and hot water on top of power.

The discussion above suggests the potential of a multi-functional LAES, namely the LAES system for CCHHP as described earlier in this chapter. The analyses in the following sub-sections will be on the proposed LAES system for CCHHP, where a direct comparison will be made on the supply capacities (cooling, heating, hot water, and power) in the discharging process with the same power consumption in the charging process (namely, the air flow rate varies with the charging pressure). As this multi-functional LAES is mainly applicable to decentralized local micro-grids, we shall consider the net power consumption in the charging process as 1 MW and the charging lasts for 8 hours (the total power consumption=8 MWh, ~20-40 tons/day of liquid air). This scale of LAES system (daily production ranging between few tons and a few tens of tons of liquid air) has been widely studied in recent years [47,82,159,160]. The working performance of air liquefaction processes (10 tons/day of liquid air), including Linde-Hampson process, Claude process and Kapitza process, were investigated by Borri et al. [47]. Their results showed a power consumption of 0.5-2.5 kWh to produce 1kg liquid air without cold recovery process which can demonstrate the industrial feasibility of the micro-grid scale air liquefiers.

5.3.2 The LAES for power, hot water and cooling supply in summer

A Sankey diagram of exergy flow in the proposed LAES system is shown in Figure 5.10 for providing power, hot water and cooling in summer (PHC mode), where both the discharging and charging pressure are at 12 MPa. The charging cycle and discharging cycle have a high exergy efficiency of 87% and 84%, respectively, while the conversion of excess heat to cooling and hot water has a low exergy efficiency of 20%.

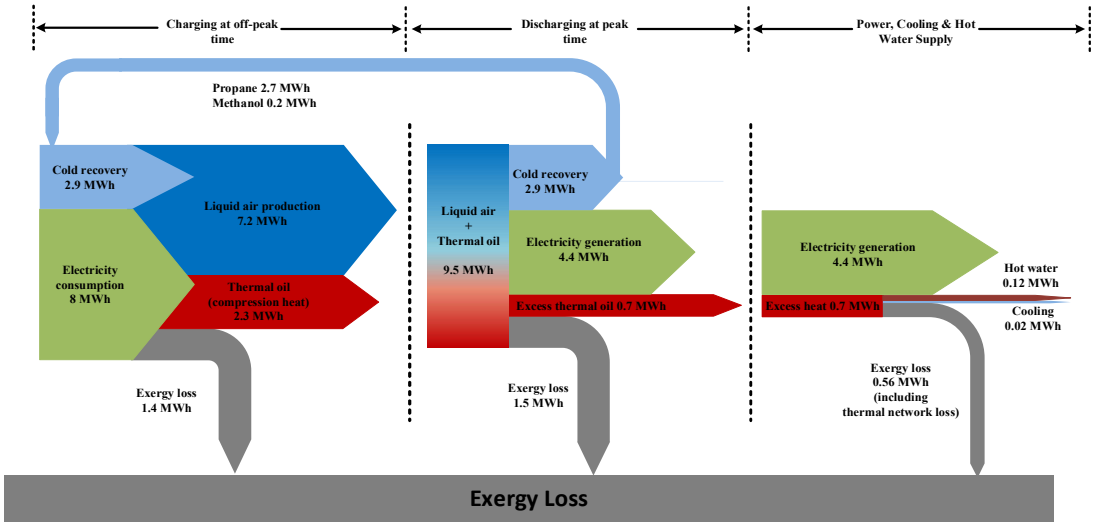

Figure 5.10 Sankey diagram of exergy flow in the proposed LAES system for providing power, hot water and cooling in summer (charging/discharging pressure at 12 MPa).

Figure 5.11 shows the supply capacity of the proposed LAES for power, hot water, and cooling (PHC) during discharging, for a given power consumption of 8 MWh (1MW×8h) in the charging process. The cooling supply capacity has an overall decreasing trend, changing from 1.36 to 0.28 MWh, as the charging pressure increases from 1 to 21 MPa. Fluctuations in the cooling supply capacity are observed between 1-7 MPa due to changes in the excess heat generation as a result of changes in the compressor type and/or compression stage, as explained earlier in this chapter. The hot water supply capacity decreases gradually from 5.72 to 1.4 MWh as the charging pressure increases from 1 to 21 MWh. The LAES in PHC mode is seen to give the largest power supply capacity of 4.94 MWh at a charging pressure of 19 MPa. However, at this charging pressure, the cooling and hot water supply capacities are at a low level. At a charging pressure of 1 MPa, the LAES in PHC mode has the lowest power supply capacity of 2.14 MWh, while the cooling and hot water supply capacities are at the largest, being respectively 1.36 and 5.72 MWh.

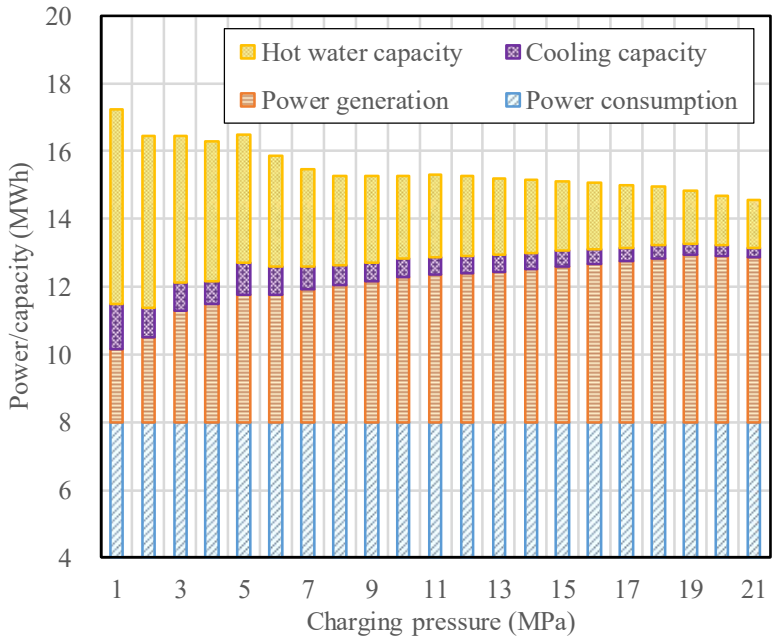

Figure 5.11 Supply capacity of the proposed LAES system for power, hot water and cooling in summer.

5.3.3 The LAES for power, hot water and heating supply in winter

Figure 5.12 shows the supply capacity of the proposed LAES for power, hot water and heating (PHH) during discharging for a given amount of power consumption of 8 MWh (1MW×8h) during charging. One can see that the heating supply capacity decreases gradually from 4.72 to 1.22 MWh as the charging pressure increases from 1 to 21 MPa. This gives the minimum heating supply capacity of 1.22 MWh at the charging pressure of 21 MPa. The hot water supply capacity varies between 0.27 and 1.36 MWh with the charging pressure increased from 1 to 21 MPa, and the maximum and minimum hot water capacities occur respectively at a charging pressure of 1 and 21 MPa. At the charging pressure of 1 MPa, the proposed LAES in PHH mode has the lowest power supply capacity, but provides the largest heating and hot water supply capacities. At the charging pressure of 19 MPa, the proposed LAES in PHH mode has the largest power supply capacity, but gives much lower heating and hot water supply capacities.

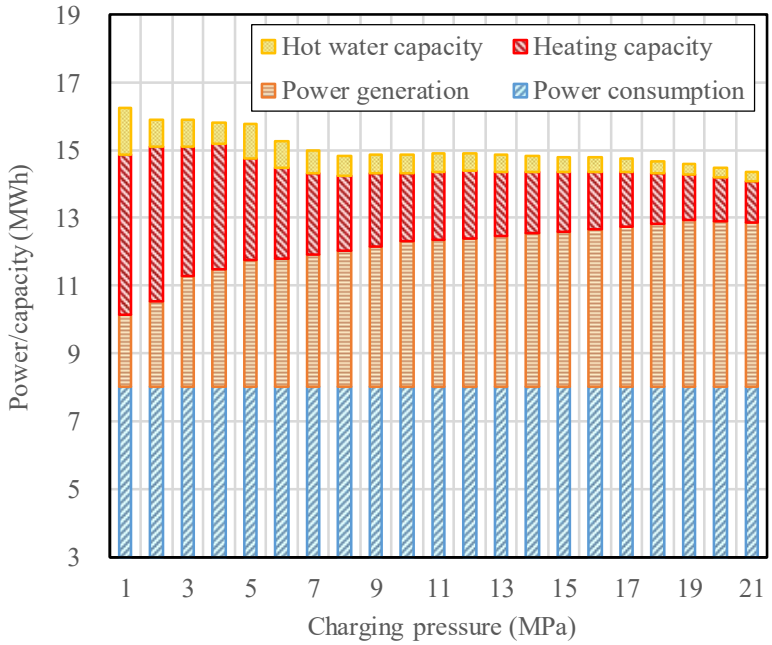

Figure 5.12 Supply capacity of the proposed LAES system for power, hot water and heating in winter.

5.3.4 The LAES for power and hot water supply in spring or autumn

Figure 5.13 shows the supply capacities of the proposed LAES for power and hot water (PH) during discharging, for a given amount of power consumption of 8 MWh (1MW×8h) in the charging process. The hot water supply capacity decreases quickly and considerably from 6.09 to 2.79 MWh as the charging pressure increases from 1 to 8 MPa; this is followed by a slow decrease from 2.79 to 1.49 MWh with a further increase in the charging pressure from 8 to 21 MPa. The LAES in PH mode has the highest hot water supply capacity of 6.09 MWh at the charging pressure of 1 MPa at which the power supply capacity is at the lowest of 2.14 MWh. As the charging pressure is at 19 MPa, the LAES in PH mode gives the maximum power supply capacity of 4.94 MWh but a much lower hot water supply capacity of 1.66 MWh.

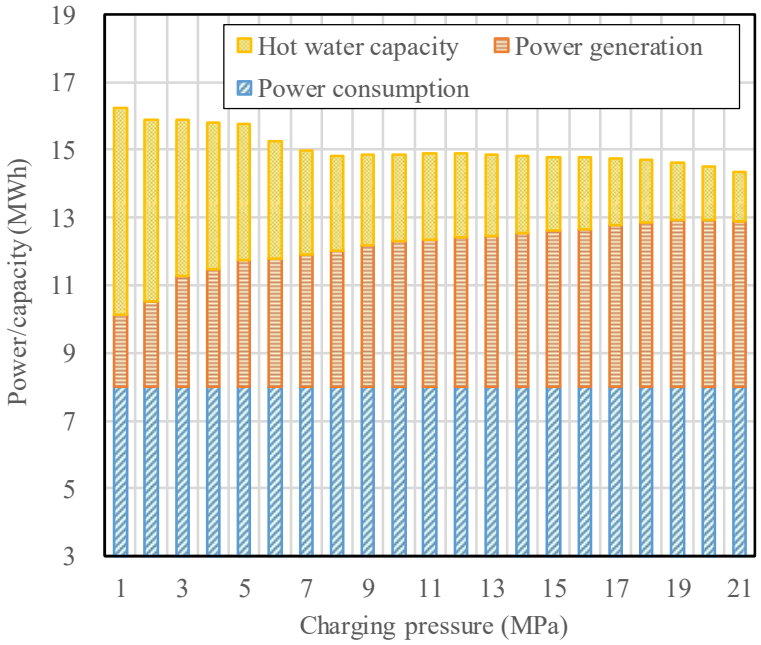

Figure 5.13 Supply capacity of the proposed LAES system for power and hot water in spring or autumn.

5.3.5 Nominal electrical round trip efficiency

The nominal-electrical round trip efficiency (neRTE) of the proposed LAES system for CCHHP is shown in Figure 5.14 with the three working modes of PHC in summer, PHH in winter, and PH in spring or autumn in the UK. The value of the neRTE is affected by the power consumption of air compressors, liquid air yield and the amount of excess heat. An increase of the charging pressure would increase the power consumption of air compressors, but the effect on the liquid air yield and the amount of excess heat is different (see Figure 5.8).

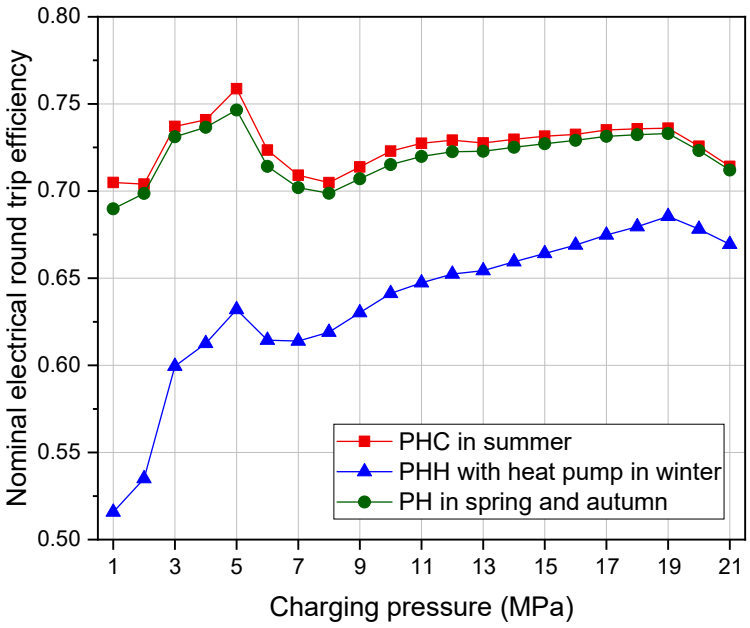

(a)

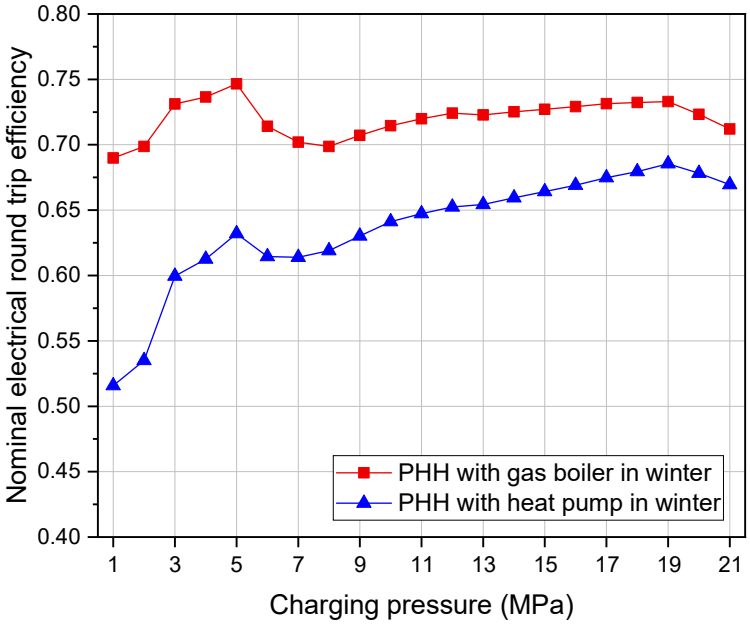

(b)

Figure 5.14 The nominal electrical round trip efficiency of the proposed LAES system for CCHHP supply.

The neRTE increases significantly as the charging pressure increases from 1 to 5 MPa, as shown in Figure 5.14 (a), which is mainly due to the dramatic increase of the liquid air yield. A further increase of the charging pressure to 7 MPa leads to a gradual decrease of the neRTE, resulting from the decrease of the amount of excess heat and the increase of power consumption of air

compressors. With the charging pressure increasing from 7 to 17 MPa, the neRTE increases gradually because of the gradual increase of the liquid air yield. A further increase of the charging pressure results in the decrease of the neRTE which is mainly affected by the increase of power consumption of air compressors. Overall, the proposed LAES for CCHHP supply has a high neRTE, ranging between 52% and 76% under the studied conditions. The highest neRTE of 76% is achieved as the charging pressure is ~5 MPa for summer conditions. A high neRTE is also observed with the charging pressure at 5 MPa for winter, spring and autumn conditions.

Figure 5.14 (b) compares the neRTE of the proposed LAES system for winter conditions (PHH mode) with gas boilers (the current case) and air-source heat pumps (the future case). For the current case using gas boilers for heating and hot water, the proposed LAES system in PHH mode has a high neRTE above 70%. As air-source heat pumps are used for heating and hot water in the future, the proposed LAES system in PHH mode has a lower neRTE, indicating air-source heat pumps are more energy-efficient than gas boilers. Finally, the proposed LAES system for CCHHP supply is suggested to work at the charging pressure of 5 MPa, which has the local maximum neRTE and contributes to a lower capital cost.

5.3.6 Primary energy savings and avoided carbon dioxide emissions

Figure 5.15 shows the potential of the proposed LAES system to reduce primary energy consumptions and carbon dioxide emissions with the charging pressure at 5 MPa, where power consumption is 8 MWh (1MW×8h) in the charging process. The primary energy savings of the proposed LAES system vary between 10.1 and 12.1 MWh, with the maximum achieved in the summer conditions (PHC mode). The avoided carbon dioxide emissions fluctuate between 1.9 and 2.3 ton, indicating that the proposed LAES system for CCHHP supply is promising to reduce carbon emissions and contribute to a low carbon future.

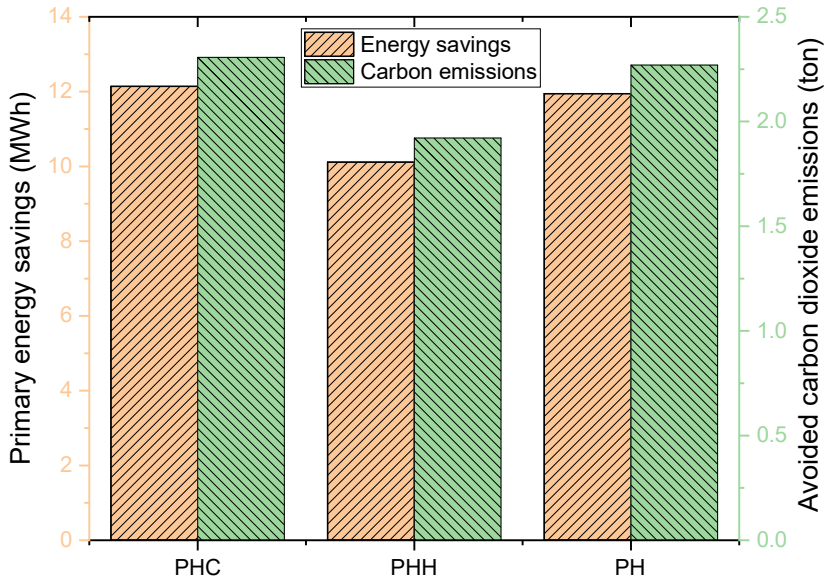

Figure 5.15 Primary energy savings and avoided carbon emissions by the proposed LAES system for CCHHP supply (charging pressure at 5 MPa)

5.4 Conclusions of Chapter 5

This chapter first investigates the performance of a standalone LAES (termed as a baseline LAES) over a range of charging pressure of 1-21 MPa, which is far wider than conventionally considered charging pressure of ~10 MPa. It is found that the baseline LAES could achieve a maximum eRTE above 60% at a charging pressure of 19 MPa. The baseline LAES, however, produces a large amount of excess heat, particularly at low charging pressures with the maximum at ~1 MPa. Such excess heat can be valuable if the baseline LAES is used for a decentralized micro-energy network for residential communities and/or industrial/commercial centres. In such cases, the performance of the baseline LAES, especially at low charging pressures, is underestimated by only considering electrical energy in the past.

By considering the excess heat, the eRTE of the baseline LAES is evaluated, which shows a high value even at lower charging pressures; the local maximum of 62% is obtained at ~4 MPa and the overall maximum of 69% is observed at 19 MPa. Therefore, the baseline LAES has the potential to achieve a high efficiency at low charging pressures by the effective use of the excess heat.

A new LAES system is then proposed by using the excess heat for combined cooling, heating, hot water and power (CCHHP) supplying for decentralized micro-energy networks. To evaluate the efficiency of the proposed LAES system for CCHHP use, the energy for supply cooling, heating and hot water is turned into equivalent electrical energy and a nominal-electrical round trip efficiency (neRTE) is proposed for the evaluation of this proposed LAES performance. What's more, the primary energy savings and avoided carbon dioxide emissions are also evaluated for the proposed LAES system for CCHHP supply. Three operation modes of the proposed system are studied to meet the end-user demands: Cooling, Hot water and Power supply in summer; Heating, Hot water and Power supply in winter; Hot water and Power supply in spring and autumn. Weather conditions of London in 2018 are selected to further analyse the working performance of this proposed system.

The results show that this proposed LAES for CCHHP can achieve a high neRTE between 52% and 76%, with the maximum achieved at a lower charging pressure of ~5 MPa. The primary energy savings and avoided carbon dioxide emissions are up to 12.1 MWh and 2.3 ton per day, respectively, with a given power consumption of 8 MWh (1MW×8h) in the charging process, indicating that this proposed LAES system is promising to contribute to a low carbon future. For the first time, these new findings suggest that small-scale LAES systems can be best operated at low charging pressures and that the technologies have a great potential for applications in local decentralized micro energy grids.

Chapter 6 Integration of decoupled liquid air energy storage with thermoelectric generator

6.1 Introduction

In the literature review (Chapter 2), it was shown that the coupled LAES systems have been extensively studied, whereas the decoupled LAES systems have a great potential but have been seldomly investigated. It is very common to recover the cryogenic energy during liquid air/nitrogen evaporation through direct cooling and power generation with some common power generation cycles (cryogenic engine for transport and Brayton/Rankine cycles for other sectors) [109,117–119]. However, for most of application scenarios, the direct cooling is usually exergy destructive as the heat transfer temperature difference is huge (around 200 °C), whereas power generation with Rankine/Brayton cycles incurs a high capital cost.

Thermoelectric generator (TEG) provides a solution, which has been widely investigated to recover waste heat for power generation through the so-called Seebeck effect [161]. Little has been done on the use of the TEG to recover the cryogenic energy for electricity generation (denoted as Cryo-TEG in this work). Lobunets et al. [162] built a Cryo-TEG prototype with a power output of 800W, where liquid nitrogen was selected as the working fluid. This prototype achieved a low Levelized Cost of Electricity (LCOE) of ~0.015 $/kWh, which was much lower than the Rankine/Brayton power plants (~0.04-0.05 $/kWh) [139]. These results suggest that the Cryo-TEG be a promising technology for cryogenic energy recovery in the decoupled LAES system in terms of the LCOE.

A cryogenic thermoelectric generation (Cryo-TEG) system is therefore proposed for cost-effectively recovering and utilising the cryogenic energy from the decoupled LAES system. Thermodynamic and economic analyses are performed on the Cryo-TEG using liquid nitrogen as the cold source. The results are compared with conventional cryogenic Rankine cycle (Cryo-

RC) based method. The use of Cryo-TEG in a decoupled LAES system is investigated for cooling and power supply in a decentralised energy network.

6.2 The proposed decoupled LAES system

6.2.1 System configuration

Figure 6.1 shows a schematic diagram of the decoupled LAES system integrated with Cryo-TEG for cooling and electricity supply for a distributed energy network. The whole system includes air liquefaction, transportation, distribution and power generation:

- The liquid nitrogen/air is produced by renewable energy in a charging cycle (i.e., air liquefaction) and then is transported to distributed energy networks, such as commercial buildings, domestic houses, and industrial parks etc.
- When energy is in demand, the liquid air/nitrogen is released to generate electricity in a discharging cycle (i.e., power generation): liquid air/nitrogen (state 1) is pumped to a high pressure (state 2), releases cryogenic energy to the Cryo-TEG to generate electricity (state 3), and then further releases the remaining cold energy to chilled water (7 ˚C) for cooling supply (state 4); finally, the high-pressure air is heated by a waste heat source (state 5) before expanding in a multi-stage turbine to generate electricity, where cold energy carried by the exhaust air/nitrogen at each stage is recovered for cooling supply. The waste heat source varies between 20 and 100 ^{o}C with a default temperature of 60 ^{o}C, which could be easily obtained from industrial waste heat or solar energy and hence is regarded as a free heat source.

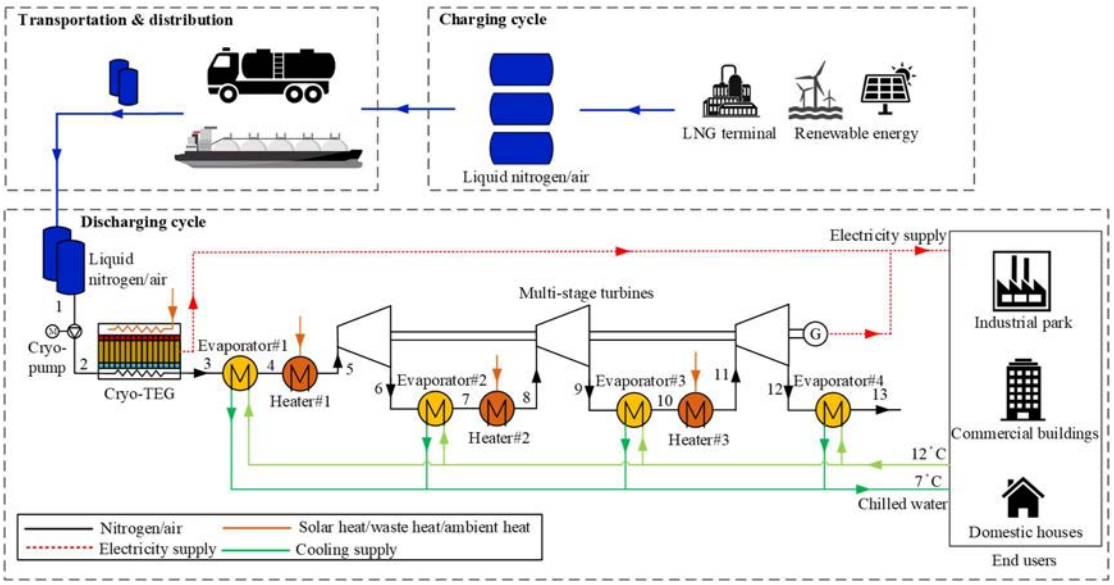

Figure 6.1 Schematic diagram of the decoupled LAES system integrated with Cryo-TEG

The general schematic structure of one typical Cryo-TEG is shown in Figure 6.2 (a), in which M (row) × N (column) thermoelectric modules are used for cryogenic energy recovery. A rectangular heat exchanger with counter flow is arranged for cold and hot streams separately. The distribution of thermoelectric modules in the Cryo-TEG system is simplified in Figure 6.2 (b): M rows and N columns thermoelectric modules are arranged in the system for power generation. The thermoelectric modules installed in the same row are connected both thermally and electrically in serial, and each row is connected thermally and electrically in parallel with each other. Thus, the thermoelectric modules in the same column could be considered to have the same temperature distribution, thermodynamic performance and power output.

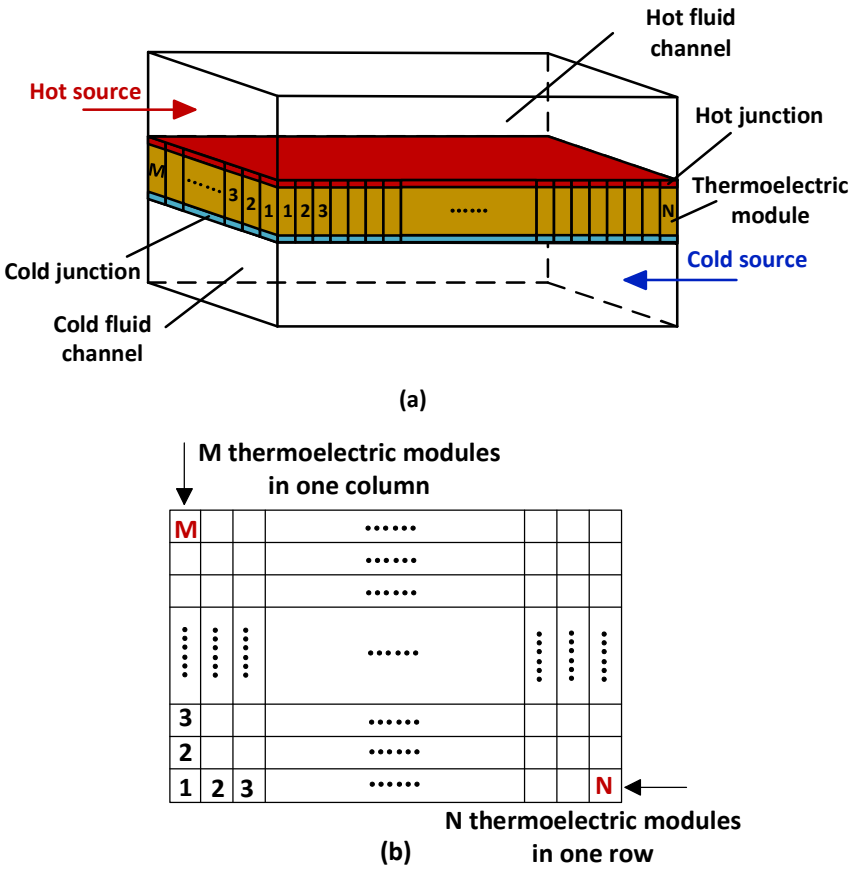

Figure 6.2 Schematic diagram of a cryogenic thermoelectric generator: (a) Overall structure; (b) A simplified layout.

6.2.2 Thermodynamic model

6.2.2.1 The discharging process

The cooling capacity ($Q_{LAES,cooling}$) and the electricity (W_{LAES}) provided by the decouple LAES system, as well as the external heat required ($Q_{LAES,heat}$) for air superheating before expansion can be calculate by:

$$Q_{LAES,\text{cooling}} = m_{LN_2} \cdot \left[(h_4 - h_3) + (h_7 - h_6) + (h_{10} - h_9) + (h_{13} - h_{12})\right] \tag{6.1}$$

$$W_{LAES} = (W_{turb} - W_{cryo-pump}) + W_{TE} \tag{6.2}$$

$$Q_{LAES,\text{heat}} = m_{LN_2} \cdot \left[(h_5 - h_4) + (h_8 - h_7) + (h_{11} - h_{10})\right] \tag{6.3}$$

$$W_{turb}=m_{LN_2}\cdot\eta_{turb}\cdot\left[(h_5-h_{6,s})+(h_8-h_{9,s})+(h_{11}-h_{12,s})\right] \tag{6.4}$$

$$W_{cryo-pump}=m_{LN_2}\cdot\frac{(h_{2,s}-h_1)}{\eta_{cryo-pump}} \tag{6.5}$$

where, m_{LN2} represents the mass flow rate of liquid nitrogen; h_i is the specific enthalpy of liquid nitrogen at state i; subscript s represents an isentropic compression or expansion process; $\eta_{cryo\text{-}pump}$ and η_{turb} are the isentropic efficiency of the cryo-pump and multi-stage turbine, respectively; W_{turb}, $W_{cryo\text{-}pump}$ and W_{TE} represent the electricity generated or consumed by the multi-stage turbine, cryo-pump and the Cryo-TEG, respectively.

The electrical round trip efficiency of the decoupled LAES system (η_{E_RTE}) is defined as the ratio of net power generation per unit liquid nitrogen during the discharging cycle to net power consumption to produce per unit liquid nitrogen during the charging cycle (D_{LN2}):

$$\eta_{E\_RTE}=\frac{W_{LAES}}{m_{LN_2}D_{LN_2}} \tag{6.6}$$

where, D_{LN2} is selected as 1350 kJ/kg [110].

Besides, the combined cooling and power (CCP) efficiency of the decoupled LAES system with the consideration of the cooling capacity could be obtained as:

$$\eta_{\mathrm{CCP}}=\frac{W_{LAES}+Q_{LAES,\mathrm{cooling}}}{m_{LN_2}D_{LN_2}} \tag{6.7}$$

6.2.2.2 The cryogenic thermoelectric generator (Cryo-TEG)

The thermoelectric modules arranged in the same column is considered having the same temperature distribution. Thus, a two-dimension model for one row of the thermoelectric modules is built to analyse the overall performance of the Cryo-TEG, as illustrated in Figure 6.3. The following assumptions are used in the modelling process, which are very common for TEG modelling [163,164]:

- Both the cold-side and hot-side of the Cryo-TEG are well insulated;

- The thermal resistances between the cold/hot surface and the thermoelectric module are neglected;
- The flow distributions of the cold and hot streams in the thermoelectric module are uniform;
- The temperature distributions of the hot and cold junctions in one thermoelectric module are uniform;
- The Seebeck coefficient, thermal conductivity and resistivity of the thermoelectric module are constant.

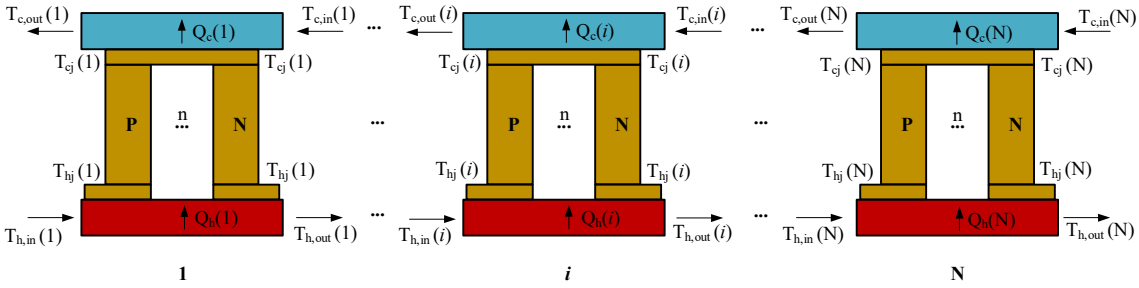

Figure 6.3 One representative row of the thermoelectric modules in the Cryo-TEG

Based on these assumptions, the heat balance in the hot side of the module *i* could be expressed as:

$$Q_h(i) = K_1 F_1 (T_{h,ave}(i) - T_{hj}(i)) = \frac{m_h}{M}(h_{h,in}(i) - h_{h,out}(i)) \tag{6.8}$$

$$T_{h,ave}(i) = \frac{T_{h,in}(i) + T_{h,out}(i)}{2} \tag{6.9}$$

where $Q_h(i)$ represents the heat released from the heat source to the module *i*; $T_{hj}(i)$ represents the hot junction temperature at the module *i*; $T_{h,in}(i)$, $T_{h,out}(i)$ and $T_{h,ave}(i)$ are the inlet temperature, outlet temperature and average temperature of the hot stream at the module *i*, respectively; m_h/M is the mass flow rate of the hot stream in each module; $h_{h,in}(i)$ and $h_{h,out}(i)$ represent the inlet and outlet enthalpy of the hot stream at the module *i*, respectively; K_1 and F_1 are the heat transfer coefficient and the heat transfer surface area of the hot side of the module *i*, respectively. K_1F_1 could be affected and optimized by the heat exchanger geometry and structure

[165,166]. In the following analysis, *K1F1* is fixed at 5.5 W/K, where the heat transfer surface (F_1) for one typical module is 50×50 mm^2 and the heat transfer coefficient (K_1) is 2200 W/(m^2·K) which can be easily achieved by turbulent flow [167].

In the same way, the heat balance in the cold side of the module *i* could be expressed as:

$$Q_c(i) = K_2 F_2 (T_{cj}(i) - T_{c,ave}(i)) = \frac{m_c}{M}(h_{c,out}(i) - h_{c,in}(i)) \tag{6.10}$$

$$T_{c,ave}(i) = \frac{T_{c,in}(i) + T_{c,out}(i)}{2} \tag{6.11}$$

where $Q_c(i)$ represents the heat released from the module *i* to the cold source; $T_{cj}(i)$ represents the cold junction temperature at the module *i*; $T_{c,in}(i)$, $T_{c,out}(i)$ and $T_{c,ave}(i)$ are the inlet temperature, outlet temperature and average temperature of the cold stream in the module *i*, respectively; m_c/M represents the mass flow rate of the cold stream in each module; $h_{c,in}(i)$ and $h_{c,out}(i)$ represent the inlet and outlet enthalpy of the cold stream in the module *i*, respectively. K_2 and F_2 represent the heat transfer coefficient and the heat transfer surface area of the cold side of the module *i*, respectively. K_2F_2 is fixed at 5.5, where the heat transfer surface (F_2) for one typical module is 50×50 mm^2 and the heat transfer coefficient (K_2) is 2200 W/(m^2·K) which can be easily achieved by liquid nitrogen or liquid air [162,168].

The heat released by the heat source, $Q_h(i)$, is split into three parts which are caused by Seebeck effect $Q_{hp}(i)$, thermal conductance $Q_k(i)$, and Joule heating $Q_j(i)$ [169], as shown in Figure 6.4:

$$Q_h(i) = Q_{hp}(i) + Q_k(i) - 0.5Q_j(i) \tag{6.12}$$

$$Q_{hp}(i) = SI_0 T_{hj}(i) \tag{6.13}$$

$$Q_k(i) = K_0 (T_{hj}(i) - T_{cj}(i)) \tag{6.14}$$

$$Q_j(i) = I_0^2 R_0 \tag{6.15}$$

where S is the Seebeck coefficient; I_0 is the electric current; K_0 represents the thermal conductance of the thermoelectric module; R_0 represents the internal resistance of the thermoelectric module.

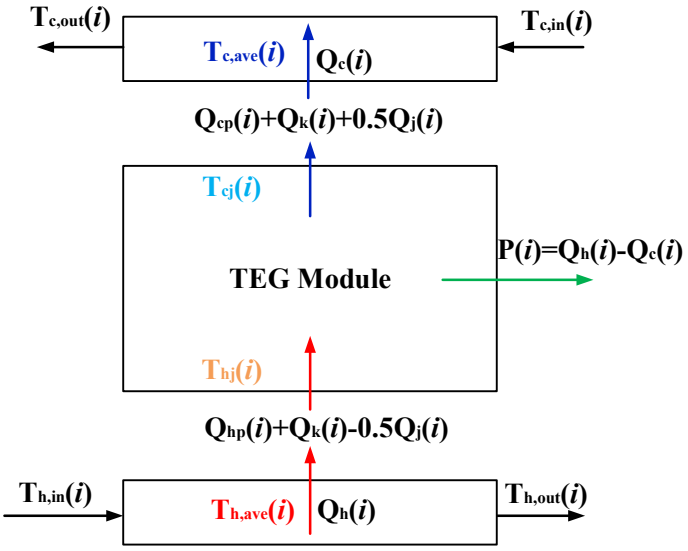

Figure 6.4 Transfer of heat flux through the TEG module

Similarly, the heat received by the cold source, $Q_c(i)$, is split into three parts which are caused by Seebeck effect $Q_{cp}(i)$, thermal conductance $Q_k(i)$, and Joule heating $Q_j(i)$ [169], as shown in Figure 6.4:

$$Q_c(i) = Q_{cp}(i) + Q_k(i) + 0.5Q_j(i) \tag{6.16}$$

$$Q_{cp}(i) = SI_0T_{cj}(i) \tag{6.17}$$

The power generation of the Cryo-TEG, W_{TE}, could be calculated as [169,170]:

$$W_{TE} = \sum_{i=1}^{N} M(Q_h(i) - Q_c(i)) \tag{6.18}$$

The power generation per unit mass flow of the cold stream ($w_{TE,c}$) and the hot stream ($w_{TE,h}$) in the Cryo-TEG system are defined as:

$$w_{TE,c} = \frac{W_{TE}}{m_c} \tag{6.19}$$

$$w_{TE,h} = \frac{W_{TE}}{m_h} \tag{6.20}$$

The thermal efficiency of the Cryo-TEG, η_{TE}, could be calculated as:

$$\eta_{TE} = \frac{W_{TE}}{\sum_{i=1}^{N} MQ_h(i)} \tag{6.21}$$

The exergy efficiency of the Cryo-TEG, $\eta_{TE,ex}$, is defined as the ratio of the total useful exergy output to the total exergy input:

$$\eta_{TE,ex} = \frac{W_{TE}}{Ex_{\text{in}}} = \frac{W_{TE}}{(Ex_{c,in}(N) - Ex_{c,out}(1)) + (Ex_{h,in}(1) - Ex_{h,out}(N))} \tag{6.22}$$

where Ex is the exergy of cold and hot streams, which could be calculated by:

$$Ex = m \cdot ex = m \cdot [(h - h_{\text{ambient}}) - T_{\text{ambient}} \cdot (s - s_{\text{ambient}})] \tag{6.23}$$

where s is the specific entropy.

In the above model, the inlet temperatures of the hot stream $T_{h,in}(1)$ and cold stream $T_{c,in}(N)$ are known (input values). To obtain the accurate outlet parameters, iteration method and trial method are used to solve the model, as shown in Figure 6.5. In the Cryo-TEG modelling process, $T_{h,in}(1)$ is the given condition to solve the Equations (6.8)-(6.17), and $T_{c,in}(N)$ is the given condition to verify the results. Two iteration loops are employed to get the final output parameters of every single TEG module and the overall Cryo-TEG system, respectively.

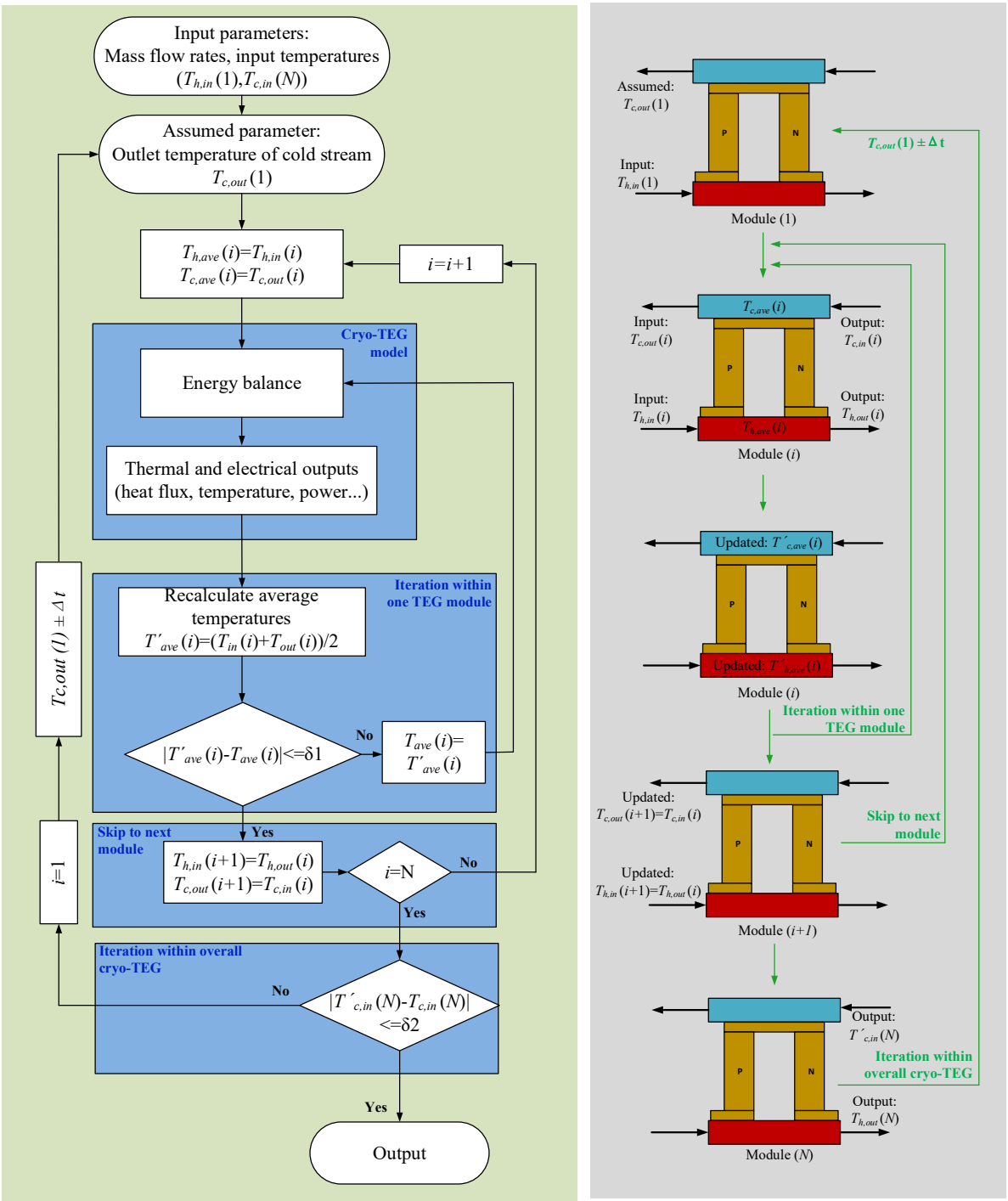

Figure 6.5 Flow chart of the iteration procedure for the Cryo-TEG model

6.2.3 Economic model of the Cryo-TEG system

In order to evaluate the economic benefit of the Cryo-TEG, an economic model is built. The investment expenditures of the thermoelectric modules in the Cryo-TEG are calculated with the price of \$1.67/W [171]. Besides, all the thermoelectric modules are mounted on a heat

exchanger, and the investment cost of the heat exchanger is estimated with the following equation [148]:

$$I_{HX}=1650\left\{\frac{q_{HX}\left(\frac{1}{K_2}+\frac{1}{K_1}\right)}{\left[\Delta t_{\text{in}}\Delta t_{\text{out}}\left(\frac{\Delta t_{\text{in}}+\Delta t_{\text{out}}}{2}\right)\right]^{1/3}}\right\}^{0.65}\frac{CEPCI_{2019}}{CEPCI_{2001}} \tag{6.24}$$

where q_{HX} is total exchanged heat flux of the heat exchanger; K_1 and K_2 are convective heat transfer coefficients of the cold and hot side of the heat exchanger, respectively; Δt_{in} and Δt_{out} are the temperature differences between the two streams at two ends of the heat exchanger, respectively. Cost indices are required to convert purchased equipment cost into one that is accurate for the present time. In this work, the chemical engineering plant cost index (*CEPCI*) is referred to adjust for the effects of inflation through time, where average annual value for 2001 and 2019 are 394.3 and 607.5, respectively [147]. Thus, the capital cost of the Cryo-TEG, $CAPEX_{TEG\text{-}FH}$, can be calculated by:

$$CAPEX_{TEG\text{-}FH}=I_{TE}+I_{HX}=1.67W_{TE}+I_{HX} \tag{6.25}$$

Formula (6.25) is applied to the situation that the ambient heat or free waste heat is used as the heat source in the Cryo-TEG system for power generation. If the heat source used in the Cryo-TEG is produced by the solar collector, the investment of the heating equipment (solar collector) needs to be considered in the initial investment, which is given as:

$$CAPEX_{TEG\text{-}solar}=I_{TE}+I_{HX}+I_{\text{solar}}=1.67W_{TE}+I_{HX}+I_{\text{solar}} \tag{6.26}$$

$$I_{\text{solar}}=\frac{Q_{\text{solar}}}{q_{\text{solar}/m^2}}\times I_{\text{solar}/m^2}=\frac{W_{TE}\times(hours/year)/\eta_{TE}}{q_{\text{solar}/m^2}}\times I_{\text{solar}/m^2} \tag{6.27}$$

where Q_{solar} is the heat required from the solar collect for Cryo-TEG use per year; $q_{\text{solar/m}^2}$ is the estimated annual heat production per square meter by solar collector, which normally could reach about 0.5-1 MWh/m^2 per year in different areas [172], and $q_{\text{solar/m}^2}$=0.7 MWh/m^2 is adopted in this study; $I_{\text{solar/m}^2}$ is investment cost of the installed solar collector per square meter, which is

reported in the range of \$250-1100/m^2 for large-scale to small-scale application [173]; hours/year is the operation hours of the Cryo-TEG system per year.

The Levelized Cost of Electricity (LCOE) is regarded as the average minimum price at which electricity must be sold in order to be break-even over the lifetime of the project. The LCOE of the Cryo-TEG could be calculated as follows:

$$LCOE = \frac{CAPEX + \sum_{t=1}^{n} \frac{M_t + F_t}{(1+r)^t}}{\sum_{t=1}^{n} \frac{E_t}{(1+r)^t}} = \frac{CAPEX + \sum_{t=1}^{n} \frac{M_t + F_t}{(1+r)^t}}{\sum_{t=1}^{n} \frac{W_{TE} \cdot (hours/year)}{(1+r)^t}} \tag{6.28}$$

where M_t and F_t represent the operating and maintenance expenditures (*O&M*) and fuel expenditures in year *t*, respectively; E_t represents the electricity generation in year *t*, which equals to the product of the output power (W_{TE}) and operation hours (*hours/year*); *r* and *n* represent the discount rate and expected lifetime of the system, respectively.

Simple payback period (*SPP*) refers to the amount of time that it takes for a project to recover the cost of its initial investment.

$$SPP = \frac{CAPEX}{\text{Net income/year}} = \frac{CAPEX}{W_{TE} \cdot (hours/year) \cdot tariff - (M_t + F_t)} \tag{6.29}$$

where *tariff* represents the on-grid tariff of the generated electricity of the Cryo-TEG.

6.3 Model validation

The reasonability of the system model has a key influence on the accuracy of the following thermodynamic analysis. Thus, it is very necessary to validate the Cryo-TEG model first before carrying out the thermodynamic analysis on the system.

6.3.1 Model validation for single thermoelectric module

The single thermoelectric module is validated by comparing the simulation results with Gou et al. [174]. In the simulation, hot water (313-353 K) and ambient air are used as the hot and cold

source, respectively. The comparison results are shown in Figure 6.6. It can be observed that the maximum deviation is 3.45%, illustrating that the model of the single thermoelectric module is reasonable and can be used to build the complete model of the Cryo-TEG system.

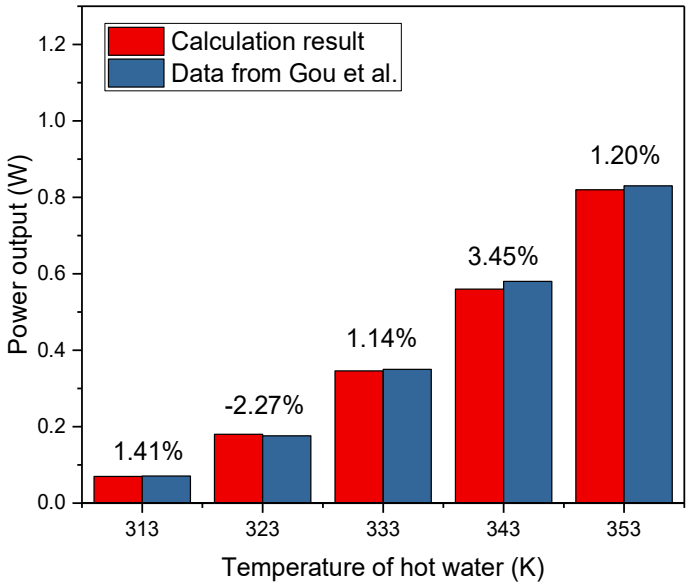

Figure 6.6 Validation result for the single thermoelectric module

6.3.2 Model validation for the Cryo-TEG system

To validate the model of the Cryo-TEG system, simulation results are compared with experimental results obtained from a prototype developed by Solid Cell Inc [162] for cryogenic energy recovery from LNG terminals . The operating conditions used in the simulation process are the same as the experimental conditions of the prototype: 40 thermoelectric modules (MT2.6-0.8-263) are installed in the heat exchanger; liquid nitrogen of 0.05 kg/s and hot water of 0.207 kg/s are selected as the cold and heat stream, respectively; the inlet temperature of liquid nitrogen and hot water are 77.15K and of 335.15K, respectively. The comparison results are illustrated in Table 6.1, indicating that the maximum error is 4.04%, which means that the model is reasonable, and the algorithm is feasible for the subsequent research and analysis.

Table 6.1 Model validation results for the Cryo-TEG system

Parameters	Simulation result	Prototype data [162]	Relative error
Outlet temperature of the hot water (K)	323.72	324.15	-0.13%
Heat flow (W)	9895.5	9540	3.73%
Output power (W)	878.1	844	4.04%
Thermal efficiency	8.87%	8.85%	0.23%

6.4 Results and discussion

The default operating parameters of the Cryo-TEG are listed in Table 6.2. The properties of the TEG module with the type of TEC-12708 are collected from its manufacturer (Hebei I.T. (Shanghai) Co., Ltd) [175]. The heat source is assumed to be from industrial waste heat with thermal oil as the heat transfer fluid; the cold source is selected as the stored liquid nitrogen (LN_2) from liquid air energy storage. The mass flow rate of the thermal oil (m_h) is variable for optimization, while the liquid nitrogen (m_c) has a fixed mass flow rate of 0.05 kg/s.

Table 6.2 Default parameters of the Cryo-TEG

Parameters	Value
Seebeck coefficient, S (VK^{-1})	0.0517
Thermal conductance, K_0 (WK^{-1})	0.772
Electric resistance, R_0 (Ω)	1.411
K_1F_1 (W/K)	5.5
K_2F_2 (W/K)	5.5
M×N	5×10
Lifetime (years)	20
Hot stream	Thermal oil
Mass flow rate of thermal oil, m_h (kg/s)	0.25
Thermal oil temperature (K)	333.15
Thermal oil pressure (MPa)	0.1
Cold stream	Liquid nitrogen (LN_2)

Mass flow rate of LN_2, m_c (kg/s)	0.05
LN_2 temperature (K)	77.15
LN_2 pressure (MPa)	0.1

6.4.1 Performance optimization of the Cryo-TEG

The performance of the Cryo-TEG is mainly affected by the external load, heat/cold source and thermoelectric module numbers. Thus, to achieve the optimum performance, the key parameters of the Cryo-TEG should be carefully selected.

6.4.1.1 Effect of the external load on the Cryo-TEG

The external load (R_{load}) is the electrical resistance of devices from end-users which consume the electricity generated by the Cryo-TEG. Its value will affect the power generation per unit mass flow of liquid nitrogen ($w_{TE,c}$) and the thermal efficiency (η_{TE}) of the Cryo-TEG. As shown in Figure 6.7 (a), the highest $w_{TE,c}$ always occurs when the external load (R_{load}) is equal to the internal resistance (R_0) of the Cryo-TEG ($R_{load}/R_0=1$) with a given mass flow ratio of the hot stream to cold stream (m_h/m_c). Besides, a larger m_h/m_c contributes to a higher $w_{TE,c}$ and the maximum of 17 kJ/kg is achieved as the heat source is infinite ($m_h/m_c=\infty$).

The highest power generation does not represent the highest thermal efficiency. As shown in Figure 6.7 (b), when the external load (R_{load}) is ~1.3 times of the internal resistance (R_0), the Cryo-TEG achieves the highest thermal efficiency of 9% with an infinite heat source ($m_h/m_c=\infty$). Therefore, to achieve the maximum power generation, the external load should be equal to the internal resistance of the Cryo-TEG ($R_{load}=R_0$), while R_{load} should be selected as $1.3R_0$ to obtain the highest thermal efficiency ($R_{load}=1.3R_0$).

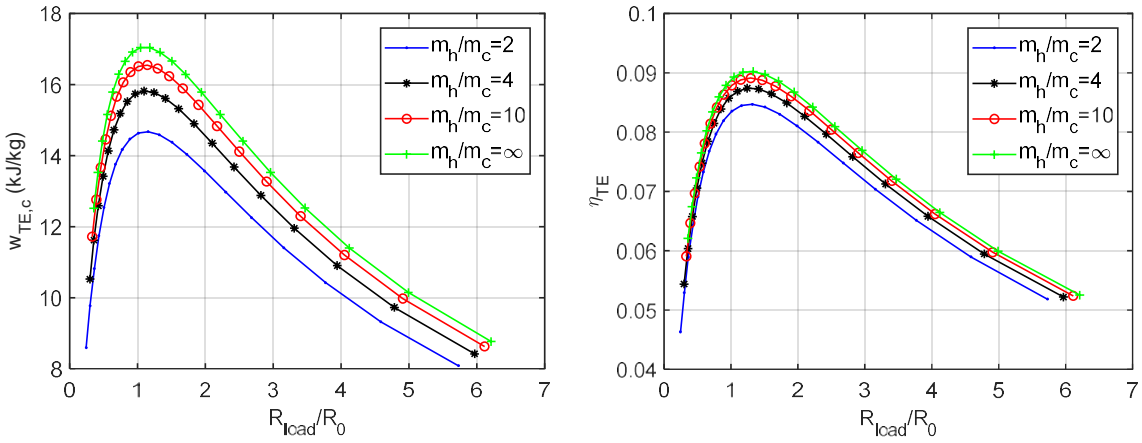

(a) (b)

Figure 6.7 Effect of the external load on the (a) specific power generation and (b) thermal efficiency of the Cryo-TEG

The external load (R_{load}) is closely related to the working electric current (I_0), and a higher external load leads to a lower electric current with a given working condition. Figure 6.8 shows how the working electric current (I_0) affects the power generation per unit mass flow of liquid nitrogen ($w_{TE,c}$) and the thermal efficiency (η_{TE}) of the Cryo-TEG. As shown in Figure 6.8 (a), the optimum working electric current is at 3.2A to achieve the maximum $w_{TE,c}$ of 17 kJ/kg, which corresponds to the $R_{load}=R_0$ in Figure 6.7 (a). However, to obtain the maximum thermal efficiency of 9%, the optimum working electric current is found at 3.0A (see Figure 6.8 (b)), which corresponds to the $R_{load}=1.3R_0$ in Figure 6.7 (b).

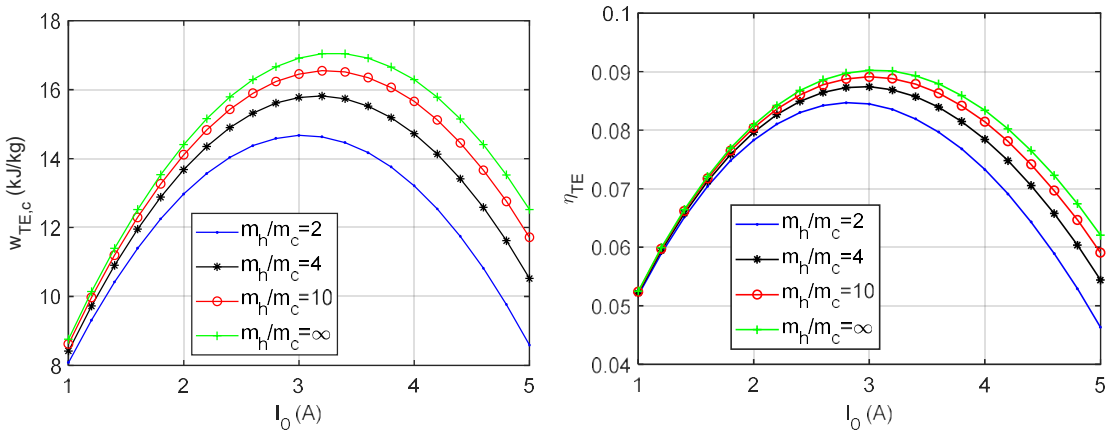

(a) (b)

Figure 6.8 Effect of the working electric current on the (a) specific power generation and (b) thermal efficiency of the Cryo-TEG

6.4.1.2 Effect of the heat source on the Cryo-TEG performance

The mass flow rate and temperature of the hot stream (thermal oil) will affect the performance of the Cryo-TEG, including the thermal efficiency (η_{TE}) and the power generation per unit mass flow of liquid nitrogen ($w_{TE,c}$) and thermal oil ($w_{TE,h}$). In Figure 6.9, the mass flow rate of liquid nitrogen (m_c) is fixed at 0.05kg/s and the external load (R_{load}) is selected to be equal to internal resistance (R_0). It can be seen that with the increase of the mass flow ratio of thermal oil to liquid nitrogen (m_h/m_c), $w_{TE,c}$ and η_{TE} gradually increase and then remains stable, while $w_{TE,h}$ decreases significantly and finally approaches zero. This is because the increase of m_h contributes to a higher average temperature on the hot side of the Cryo-TEG, which results in larger power generation (W_{TE}). Accordingly, $w_{TE,c}$ will increase as m_c is fixed, while $w_{TE,h}$ decreases as the increase of W_{TE} is less significant than that of m_h. Similarly, the thermal efficiency (η_{TE}) increases as a result of the increase of W_{TE} when heat input is only slightly increased. The increase of m_h/m_c from 2 to 22 leads to a general increase of $w_{TE,c}$ and η_{TE} by 15.0% and 7.2%, respectively, but a dramatic decrease of $w_{TE,h}$ by 89.6%. Thus, m_h/m_c is selected as 5 in the following calculation, which gives relatively high $w_{TE,c}$ of 16 kJ/kg and η_{TE} of 8.75% as well as reasonable $w_{TE,h}$ of 3 kJ/kg.

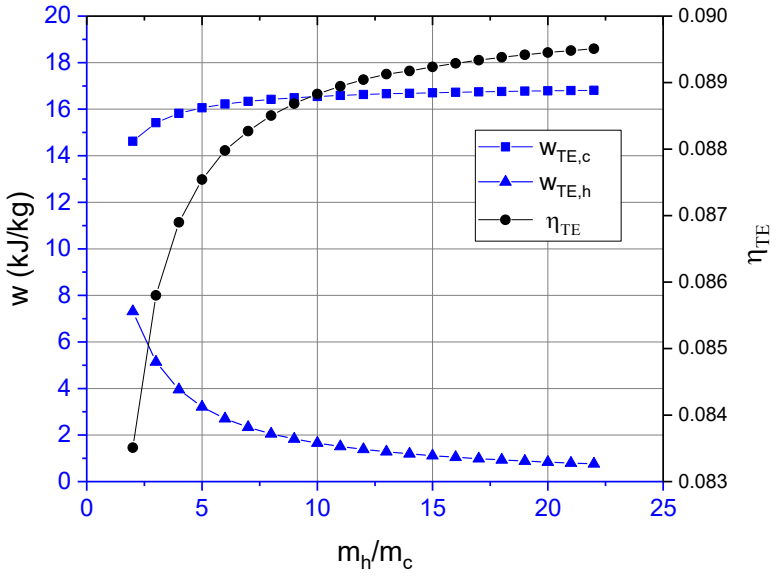

Figure 6.9 Effect of the mass flow rate of hot stream on the performance of the Cryo-TEG.

According to the results from Figure 6.7 in Section 6.4.1.1, the Cryo-TEG achieves the maximum power generation and maximum thermal efficiency as $R_{load}=R_0$ and $R_{load}=1.3R_0$, respectively. Hence, the effect of inlet temperature (T_h) of hot stream on the power generation ($w_{TE,c}$ and $w_{TE,h}$) and thermal efficiency (η_{TE}) is considered as $R_{load}=R_0$ and $R_{load}=1.3R_0$, respectively, which contributes to the optimum performance. As shown in Figure 6.10, with the increase of T_h from 333 K to 413 K, both $w_{TE,c}$ and $w_{TE,h}$ increase significantly by 67.5%, while η_{TE} increases gradually by 24.0%. Hence, a higher temperature of external heat source is recommended for the Cryo-TEG.

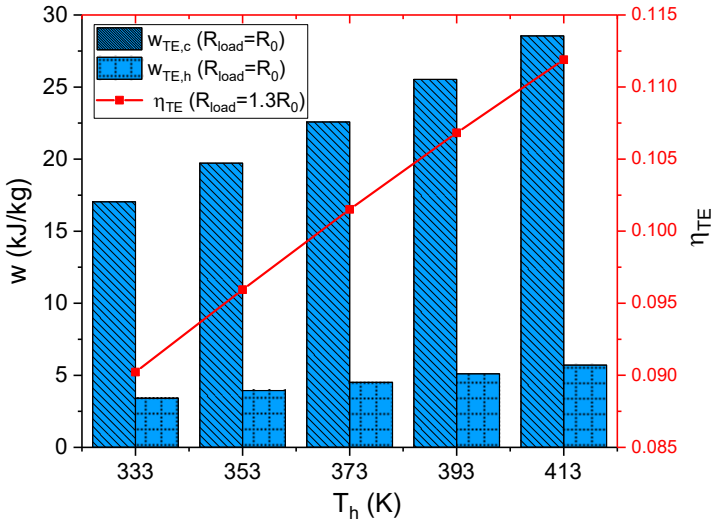

Figure 6.10 The power generation and thermal efficiency of the Cryo-TEG versus inlet temperature of hot stream.

6.4.1.3 Effect of the number of thermoelectric modules on the Cryo-TEG

The number of thermoelectric modules will affect the temperature distribution of hot (thermal oil) and cold (liquid nitrogen) streams inside the modules and thus influence the performance of the Cryo-TEG. In this section, the row of modules (M) is fixed at 5, while the column (N) is variable to investigate its effect on the Cryo-TEG.

Figure 6.11 shows a representative temperature distribution of thermal oil and liquid nitrogen along their flow direction with counter flow, where module N is set as 20 and the external load (R_{load}) is equal to the internal resistance (R_0) with the optimum working electric current of 2.8A. The temperature of thermal oil decreases gradually along its flow direction from module 1 to module 20, while the temperature of liquid nitrogen keeps stable as module is between 9 and 20, and then increases gradually, as shown in Figure 6.11 (a). This is because the liquid nitrogen flows from module 20 to module 1, which first releases latent heat with a constant temperature, completes the phase change process at module 9, and then starts to release sensible heat with a significant temperature increase. The temperature difference between thermal oil and liquid nitrogen increases significantly and then decreases slightly; the maximum value of 244 K is

obtained as N is at 9, as shown in Figure 6.11 (b). This leads to similar changes of the power generation per unit mass flow of liquid nitrogen in each module.

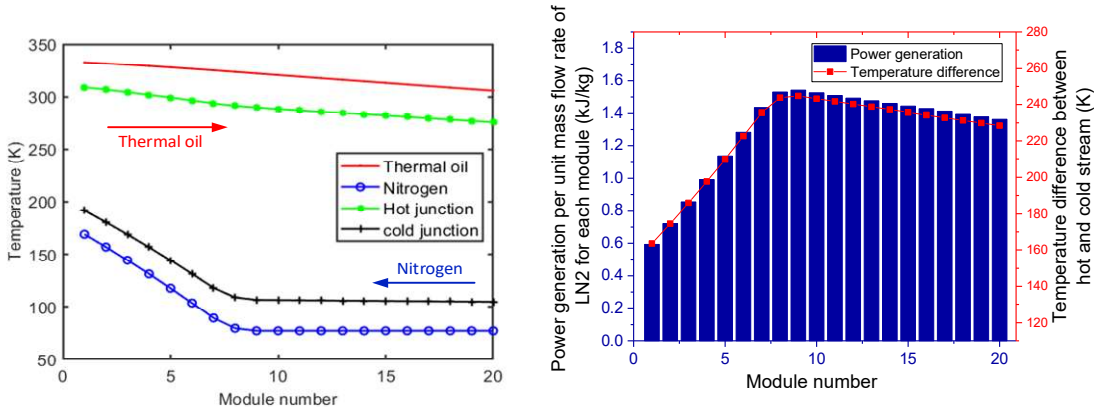

(a) (b)

Figure 6.11 Temperature (a) and power generation (b) profiles in the Cryo-TEG with column of thermoelectric modules N=20.

Figure 6.12 shows the effect of column of thermoelectric modules (N) on the maximum performance of the Cryo-TEG, including the maximum power generation per unit mass flow of liquid nitrogen ($w_{TE,c}$), thermal efficiency (η_{TE}), and the maximum exergy efficiency ($\eta_{TE,ex}$). With N increasing from 5 to 40, the optimal working electric current falls from 3.5A to 1A. When N is less than 10, the outlet temperature of liquid nitrogen ($T_{c,out}$) remains stable as only latent heat is utilized, which leads to a stable η_{TE}; as N is over 10, the $T_{c,out}$ increases significantly, resulting in a gradual decrease of the η_{TE}. The value of N has a little effect on the $\eta_{TE,ex}$ until N is over 30. For the $w_{TE,c}$, the increase of N from 5 to 40 leads to an increase first and then a decrease later; the maximum $w_{TE,c}$ of 27 kJ/kg is achieved as N is 25. This is because of the balance between the increase of module number N and the decrease of average power generation of each module affected by the increase of $T_{c,out}$. As N is larger than 25, the increase of N is less significant than the decrease of average power generation of each module, leading to a decrease of power generation of all modules ($w_{TE,c}$). Besides, the increase of N from 20 to 25 contributes to a slight growth of $w_{TE,c}$, but leads to a significant decrease of η_{TE}. Therefore, the

column of the thermoelectric modules is suggested at 20 to make effective and economical use of the cryogenic energy of liquid nitrogen for power generation.

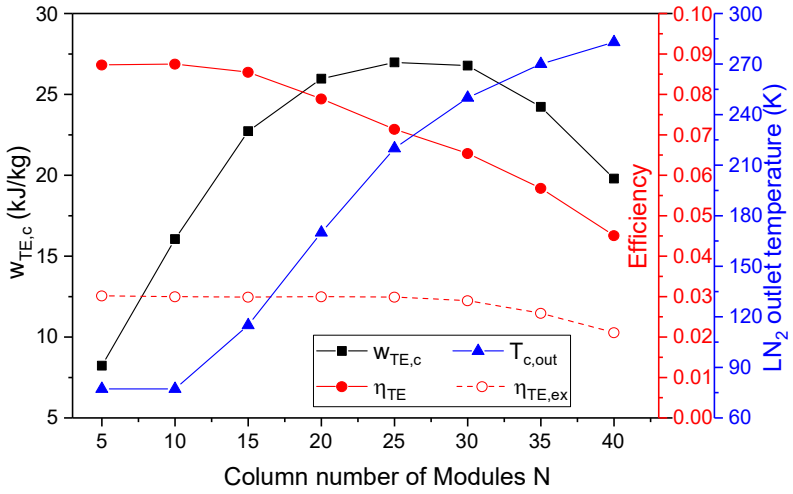

Figure 6.12 Effect of the column number of thermoelectric modules (N) on the maximum performance of the Cryo-TEG.

6.4.2 Comparisons between the Cryo-TEG and the Cryo-RC systems

Besides the Cryo-TEG, Rankine cycle is another possible way to recover the cryogenic energy from liquid nitrogen for power generation (denoted as Cryo-RC). Thus, to identify which is better, the Cryo-RC is compared with the Cryo-TEG based on the following conditions: (1) the Cryo-RC and the Cryo-TEG use the same cold source (liquid nitrogen) and heat source (thermal oil at 333.15K); (2) the mass flow rate of liquid nitrogen in the Cryo-RC and the Cryo-TEG is always the same; (2) the mass flow rate of the working fluid and heat source (thermal oil) of the Cryo-RC are optimised to maximise its thermal efficiency. To evaluate the thermodynamic and economic performance of the Cryo-RC, the following assumptions are made:

(1) The turbine efficiency and pump efficiency are selected as 80% and 70%, respectively;

(2) The pinch points of the condenser and evaporator are set as 5K;

(3) The turbine inlet and outlet pressure of the working fluid are selected as 6 MPa and 0.1 MPa, respectively;

(4) Both single-stage and double-stage Rankine cycles are considered, where argon and methane are selected as the working fluids for the first stage, and methane, ethane, propane and R23 for the second stage;

(5) The cost functions for all the components in the Cryo-RC system are calculated according to the literature [144];

(6) The O&M cost is assumed to account for 1.5% of the capital cost per annum [140];

(7) The discount rate is set as 5%;

(8) The operation hours per year and expected lifetime of the Cryo-RC system are selected as 8000 hours and 20 years, respectively;

6.4.2.1 Thermodynamic performance comparisons

Figure 6.13 shows the thermodynamic performance of the Cryo-RC and Cryo-TEG systems with the fixed mass flow rate of liquid nitrogen at 1kg/s. By optimising the mass flow rate of working fluids and heat source (thermal oil), the highest thermal efficiency of 39.5% is obtained in the one-stage Cryo-RC system with Argon as the working fluid, while the maximum power generation per unit mass flow of liquid nitrogen (174.4 kJ/kg) is achieved in the two-stage Cryo-RC system with Argon and Ethane as the working fluid for first-stage and second-stage, respectively. For the Cryo-TEG, it has the highest thermal efficiency of ~9% (M×N=100×10 at m_c=1 kg/s) and the maximum power generation per unit mass flow of liquid nitrogen of ~26 kJ/kg (M×N=100×20 at m_c=1 kg/s), which are much lower than both the one-stage and two-stage Cryo-RC systems. Thus, the Cryo-RC performs much better than the Cryo-TEG in the perspective of thermodynamics.

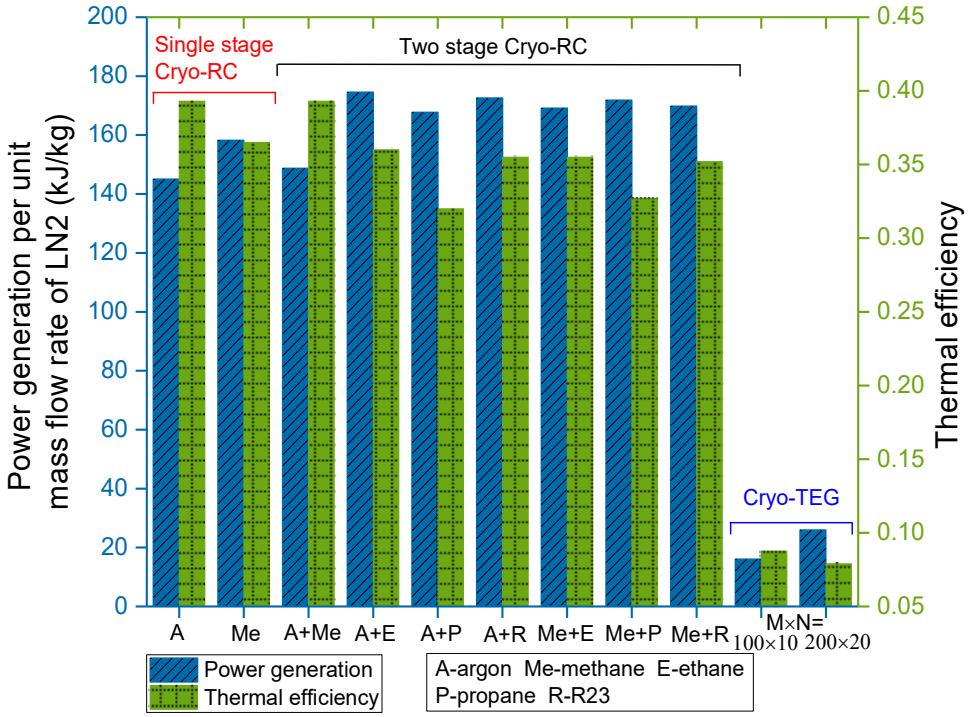

Figure 6.13 Thermodynamic performance comparison between the Cryo-RC and Cryo-TEG

6.4.2.2 Economic performance comparisons

Besides thermodynamic performances, the economic performance is also important for real application. The Cryo-RC system is compared with the Cryo-TEG in terms of the specific investment cost and LCOE (free waste heat is assumed to be available). With the mass flow rate of liquid nitrogen at 1 kg/s, the investment costs of the Cryo-RC and Cryo-TEG systems are summarised in Table 6.3. It could be seen that the Cryo-TEG system with 1000 and 2000 thermoelectric modules have a much lower investment cost than the Cryo-RC system. The specific investment cost of the Cryo-TEG system is as low as 24% of that of the Cryo-RC system.

Furthermore, the LCOE of the Cryo-RC and Cryo-TEG systems are shown in Figure 6.14. As the mass flow rate of liquid nitrogen is below 20 kg/s (i.e., 8.6 MW cooling capacity), the Cryo-TEG system shows a better LCOE than the Cryo-RC system. The LCOE of the Cryo-TEG could be as low as 0.0218-0.0245 $/kWh, while that of the Cryo-RC system is as high as 0.08-0.09

$/kWh. However, as the mass flow rate of liquid nitrogen is over 20 kg/s, the Cryo-RC system has a lower LCOE than the Cryo-TEG system. These results indicate that the Cryo-TEG system is much more applicable for waste cryogenic energy recovery in small-scale application scenarios to get lower investment and higher rates of return on investment.

Table 6.3 Investment cost comparison between the Cryo-RC and Cryo-TEG（m_c=1 kg/s）

Systems	Thermal efficiency	Rated Power (kW)	Investment cost ($)	Specific investment cost ($/kW)
Single-stage Cryo-RC (Argon)	0.395	145.0	1,016,990	7014
Single-stage Cryo-RC (Methane)	0.365	158.2	1,045,870	6611
Two-stage Cryo-RC (Argon+Ethane)	0.360	174.4	1,340,683	7687
Cryo-TEG (M×N=100×10)	0.0875	16.05	29,410	1832
Cryo-TEG (M×N=100×20)	0.077	26.00	53,499	2058

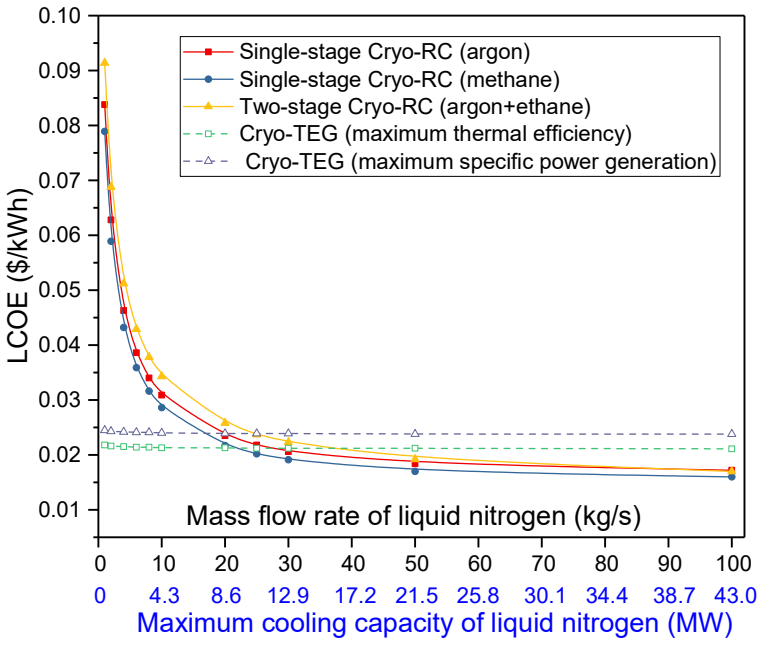

Figure 6.14 LCOE of the Cryo-RC and Cryo-TEG

6.4.3 System performance of the decoupled LAES system with Cryo-TEG

According to the comparison results between the Cryo-TEG and Cryo-RC, the Cryo-TEG is suggested to recover the cryogenic energy from the small-scale decoupled LAES system, as shown in Figure 6.1. The proposed system could provide both electricity and cooling for decentralized energy network. Waste heat (60 ˚C) is assumed to be available as the heat source and the discharging pressure of liquid nitrogen is selected as 8 MPa. The simulation data at each point is shown in Table 6.4 under the given working condition.

Table 6.4 Stream data for the decoupled LAES system integrated with Cryo-TEG

State	*T* (K)	*P* (MPa)	*h* (kJ/kg)	m (kg/s)
1	77.24	0.10	-122.25	1.0
2	80.90	8.00	-109.27	1.0
3	241.46	8.00	224.37	1.0
4	283.15	8.00	275.52	1.0
5	333.15	8.00	333.48	1.0
6	227.52	1.86	228.93	1.0
7	283.15	1.86	289.32	1.0
8	333.15	1.86	342.74	1.0
9	229.95	0.43	236.99	1.0
10	283.15	0.43	292.83	1.0
11	333.15	0.43	345.15	1.0
12	230.68	0.10	238.99	1.0
13	283.15	0.10	293.65	1.0

6.4.3.1 Effect of discharging pressure on the proposed system performance

Figure 6.15 shows how the discharging pressure of liquid nitrogen (state 2 in Figure 6.1) affects the power and cooling capacity of the decoupled LAES system. With the increase of the discharging pressure from 8 to 12 MPa, the specific power generation by the Cryo-TEG

decreases slightly from 19.2 to 17.8 kJ/kg, as shown in Figure 6.15 (a). That is because the inlet temperature of liquid nitrogen in the Cryo-TEG goes up and less cold energy could be utilized for power generation. However, the increase of the discharging pressure contributes to an increase of both the total power (air turbines + Cryo-TEG) and cooling capacities, as shown in Figure 6.15 (b). This mainly results from the increase of power generation by the air turbines.

Figure 6.15 (c) illustrates the effect of the discharging pressure on the electrical round trip efficiency (eRTE) and combined cooling and power (CCP) efficiency of the proposed decoupled LAES system. The increase of discharging pressure contributes to an increase of both eRTE and CCP efficiency. The proposed system achieves an eRTE of 25% and a CCP efficiency of 43.1% as the discharging pressure is at 12 MPa. Compared with the case without Cryo-TEG for power generation, the proposed system improves the eRTE by 6%. Thus, a larger discharging pressure is suggested for the proposed system.

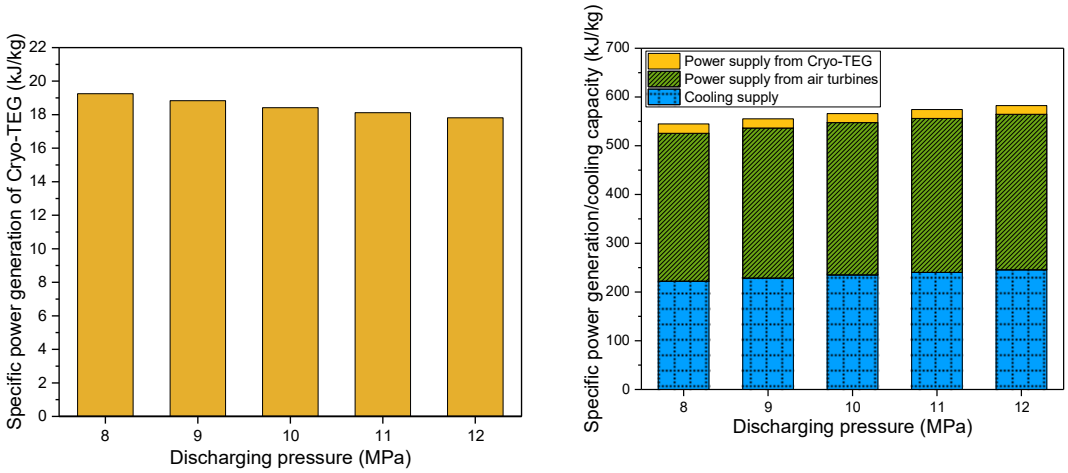

(a) (b)

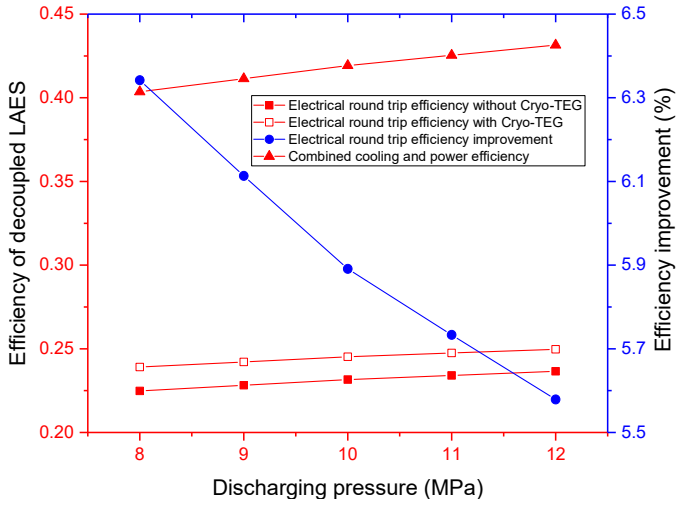

(c)

Figure 6.15 Effect of discharging pressure on the proposed decoupled LAES system

6.4.3.2 Effect of waste heat temperature on the proposed system

Figure 6.16 shows the influence of the waste heat temperature on the performance of the proposed decoupled LAES system, where discharging pressure is set as 12 MPa. With the waste heat temperature increasing from 293 to 373 K, the power capacity increases gradually, while cooling capacity decreases significantly, as shown in Figure 6.16 (a). This leads to a gradual increase of the electrical round trip efficiency from 21% to 29% and a dramatic decrease of the combined cooling and power efficiency from 50% to 37%. Thus, the waste heat should be carefully selected based on the different demands of cooling and power.

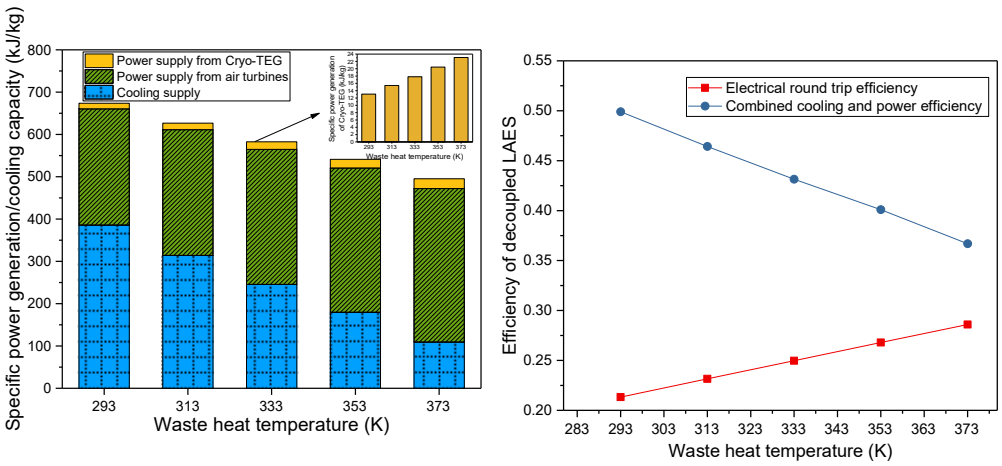

(a) (b)

Figure 6.16 Effect of waste heat temperature on the proposed decoupled LAES system

6.4.3.3 Economic performance of the Cryo-TEG in a decoupled LAES system

Figure 6.17 shows the economic performance of investing the Cryo-TEG into different power capacities of decoupled LAES system, in which the free waste heat is assumed to be available to be used as the heat source for Cryo-TEG. The following operation parameters are selected: (1) the waste heat temperature is 60 ˚C; (2) discharging pressure of liquid nitrogen is 12 MPa; (3) operation hour per year is 5000. The results indicate that investing a Cryo-TEG in the decoupled LAES system has a LCOE of 0.0343-0.0327 $/kWh with the increase of power capacity of the decoupled LAES from 0.32 to 6.4 MW. The payback period of investing the Cryo-TEG in the decoupled LAES varies between 2.2 and 4.8 years with different on-grid electricity tariffs. Thus, it is economically feasible for investing the Cryo-TEG into the decoupled LAES system.

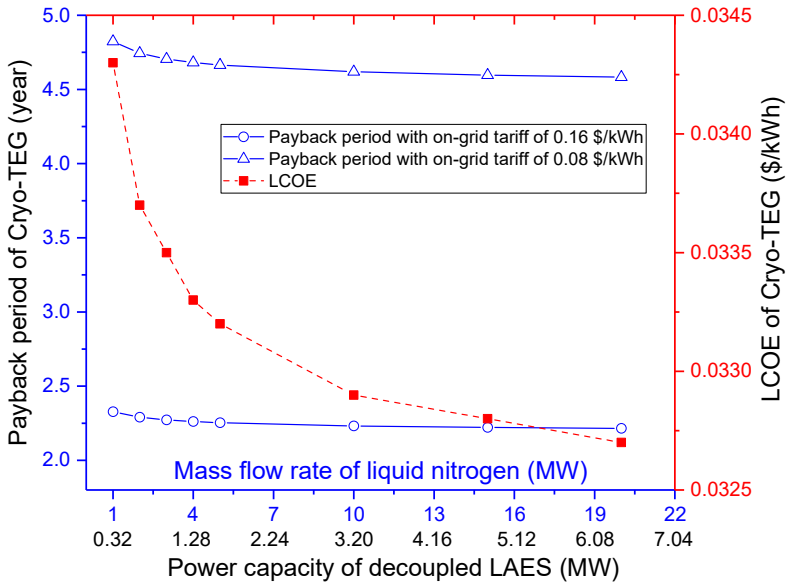

Figure 6.17 LCOE and payback period of investing the Cryo-TEG in the decoupled LAES system with different power capacities (operation hour per year=5000 hours)

Besides, the effect of the operation hour per year on the economic performance of investing the Cryo-TEG the decouple LAES system is also analysed, as shown in Figure 6.18. The results indicate that investing a Cryo-TEG in the decoupled LAES system has a LCOE of 0.0685-0.0343 $/kWh with the increase of operating hours from 2500 to 5000 hours per year. As for the payback period of the investment of a Cryo-TEG in the decoupled LAES, longer operating hours and higher on-grid electricity tariff could shorten the payback period very obviously. If the on-grid electricity tariff could be as high as 0.16 $/kWh, the payback period of the Cryo-TEG can be less than 5 years even if the decouple LAES system could only work 2500 hours per year. Given the operating hours of 3500 hours per year, the investment of a Cryo-TEG has a payback period of 3.4 -7.1 years corresponding to the electricity tariff of 0.16-0.08 $/kWh.

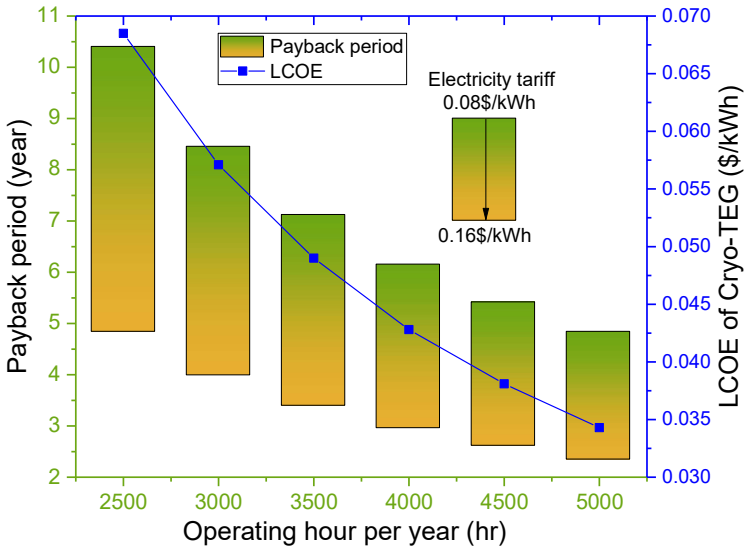

Figure 6.18 LCOE and payback period of installing Cryo-TEG in the decouple LAES system with different operation hour per year (0.32 MW LAES plant)

Furthermore, economic performance of the Cryo-TEG is compared with free waste heat and solar energy as heat sources in Figure 6.19, where the mass flow rate of liquid nitrogen is 1kg/s in the decoupled LAES system. It could be found that the additional investment on the solar collector increases the LCOE of the Cryo-TEG remarkably, which varies between 0.748 and 0.636 with the heat source temperature at 313-373 K. Thus, it is recommended to use available waste heat for the Cryo-TEG.

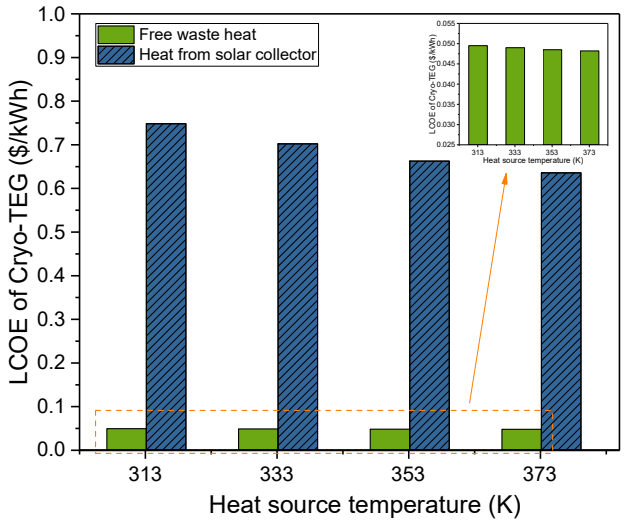

Figure 6.19 LCOE of Cryo-TEG with and without free waste heat (operation hour per year=3500 hours)

6.5 Conclusions of Chapter 6

A cryogenic thermoelectric generator (Cryo-TEG) is proposed and analysed systematically for cost-effective recovery of cryogenic energy in a decoupled LAES system. Both thermodynamic and economic analyses are conducted on the Cryo-TEG to optimize the operating parameters. Comparisons are made between the Cryo-TEG and cryogenic Rankine cycles (Cryo-RC) in terms of thermodynamic and economic performances. The system performance and economic benefits of the integrated Cryo-TEG with a decoupled LAES system are analysed. The key findings are given as follows:

- The Cryo-TEG shows a lower thermal efficiency of ~9%, compared with the Cryo-RC (~39.5%). However, the Cryo-TEG has a much lower capital cost, contributing to a LCOE as low as 0.0218-0.0245 $/kWh compared with that of the Cryo-RC at 0.08-0.09 $/kWh as the cooling capacity of liquid nitrogen is below 8.6 MW. Thus, the Cryo-TEG is much more applicable for the small-scale cryogenic energy recovery.
- The optimization of the Cryo-TEG shows that the maximum power generation and thermal efficiency are obtained when the external load is equal to 1 or 1.3 times of the internal resistance, respectively. Besides, given working conditions, the optimum column of the thermoelectric modules is suggested at 20 for maximizing power generation.
- The system performance of integrating the Cryo-TEG with the decoupled LAES system is evaluated. The proposed system shows an electrical round trip efficiency of ~29% and a combined cooling and power efficiency of ~50%. With the power contribution of the Cryo-TEG, the electrical round trip efficiency is improved by 6%.
- The economic benefits of investing the Cryo-TEG into the decoupled LAES system is investigated. The results show that the payback period could be as short as 2.2 years and the LCOE is as low as 0.0327 $/kWh as the power capacity of the decoupled LAES system is below 6.4 MW. Thus, it is economically favourable to invest the Cryo-TEG into the small-scale LAES system.

Chapter 7 Integration of liquid air energy storage with ammonia synthesis process

7.1 Introduction

The storage medium of LAES can be air or nitrogen, which is stored at a very low temperature (~78 K). This can lead to an unavoidable cold energy loss during the storage period. As a result, LAES is mainly used for short and medium duration energy storage, and the release of the stored energy often occurs within days and weeks. A longer term storage requires a medium that gives much lower energy loss during storage. Ammonia is regarded as a potential candidate for such long term energy storage. Liquid ammonia can be stored at ambient temperature under a pressure of ~1.6 MPa, which is not harsh, thus making it more attractive as a potential energy reserve for use in electricity, transport, and heating sectors [176].

Currently, ammonia is the second most-produced industrial chemical [177], and the current global production of ammonia is about 200 Mtonne/year and is projected to reach about 270 Mtonne/year by 2050 due to population growth [178]. Ammonia is mainly synthesized by a mature process called Haber–Bosch process, in which nitrogen and hydrogen are the two key component raw materials. Hydrogen is currently supplied mainly through steam reforming of methane, with a small amount from electrolysis of water; nitrogen is produced through Air Separation Unit (ASU). Thus, LAES has the potential to be integrated with the ammonia synthesis system through nitrogen flow to shift the peak time electricity consumption of ASU to off-peak time, or even to reduce the total electricity consumption of the whole ammonia synthesis system. Furthermore, this is also a promising method to convert a medium-term energy storage (liquid nitrogen in LAES) to a long-term energy strategic reserve (liquid ammonia either at ambient temperature under high pressure or at -33°C under atmospheric pressure [179,180]).

In this work, two configurations are proposed for the integration of the LAES with the ammonia synthesis system, denoted respectively as LAES-NH_3 system and LAES-AS-NH_3 system for two different application scenarios. The details are given in Section 7.2. Thermodynamic performance and economic performance of these two integrated systems are analysed and compared with the standalone LAES and the standalone ammonia synthesis system.

7.2 The two proposed LAES-NH_3 and LAES-AS-NH_3 systems

7.2.1 The LAES-NH_3 system

7.2.1.1 Working principle and configuration of the LAES-NH_3 system

The basic working principle for the LAES-NH_3 system is shown schematically in Figure 7.1, which consists of a LAES sub-system and an ammonia synthesis sub-system integrated through a nitrogen flow.

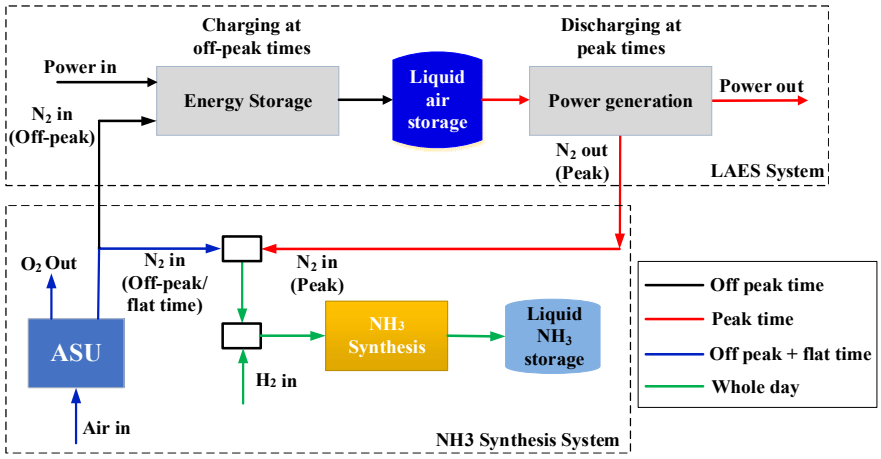

Figure 7.1 The basic working principle for the LAES-NH_3 system

Figure 7.2 shows the flow diagram of the proposed LAES-NH_3 system. The working process of the LAES-NH_3 system is outlined in the following below:

- At flat hours: the ASU operates at a low production rate to produce nitrogen for the ammonia synthesis process only. The LAES system does not operate.

- At off-peak hours: the ASU operates at a high production rate to produce nitrogen, serving two purposes: meeting the demand of nitrogen for ammonia synthesis, and meeting the demand of nitrogen for the charging process of the LAES. Meanwhile, the charging process of the LAES works to produce liquid nitrogen.
- At peak hours: The discharging process of LAES works to generate electricity. The gaseous nitrogen out of turbines (state 22) is introduced to the ammonia synthesis sub-system as the feed gas. The ASU can be off at peak hours if the nitrogen amount from the LAES is sufficient for the ammonia synthesis.

For this system, the ammonia synthesis sub-system can work 24 hours a day, with the nitrogen supplied from the ASU at flat/off-peak hours and LAES at peak hours: the feed nitrogen and hydrogen are mixed and cooled down to the ambient temperature (state N2) before fed to the multi-stage compressors, where the feed gas is compressed to 15 MPa by a three-stage compressor unit (state N9), where two streams of unreacted recycled gas (state N23 and N21) are mixed with the feed gas after the second-stage compression (state N6) and the third-stage compression (state N8), respectively; then the fully-mixed gas (state N9) is pre-heated to 400 °C (state N10) by the gas product out of the reactor#3 (state N16) before fed to the three-stage reactors. Because the ammonia synthesis is an exothermic reaction, waste heat boilers (WHB#1-3) are used to recover the excess heat of the gas product after each stage of the reactors and generate steam for power generation, maintaining the optimal reaction temperature of the reactor at 400-500 °C [181]. After the three-stage reaction and intercooling processes, the ammonia product is condensed by the feed gas in condenser #1 (state N17) and cooling water in condenser #2 (state N18), separated from the unreacted nitrogen and hydrogen in the separator, flash evaporated to a relative low pressure by passing through a throttling valve, and stored in a liquid ammonia tank (state N25). To avoid the concentration of argon in the synthesis loop building up, a certain amount of unreacted gas is purged (state N22) and the rest of the gas (state N21) is recycled to the synthesis loop. As the

purge gas contains valuable hydrogen, a membrane separator is used to recover it from the purge gas and then recycle it (state N23).

According to the system configuration and the working process of the LAES-NH_3 system, One can see that there is no change for the basic configuration of the original ammonia synthesis system, nor the baseline LAES system in this integrated system. The only change occurs in the ASU part, which needs to increase the production to meet the nitrogen demand in the LAES sub-system.

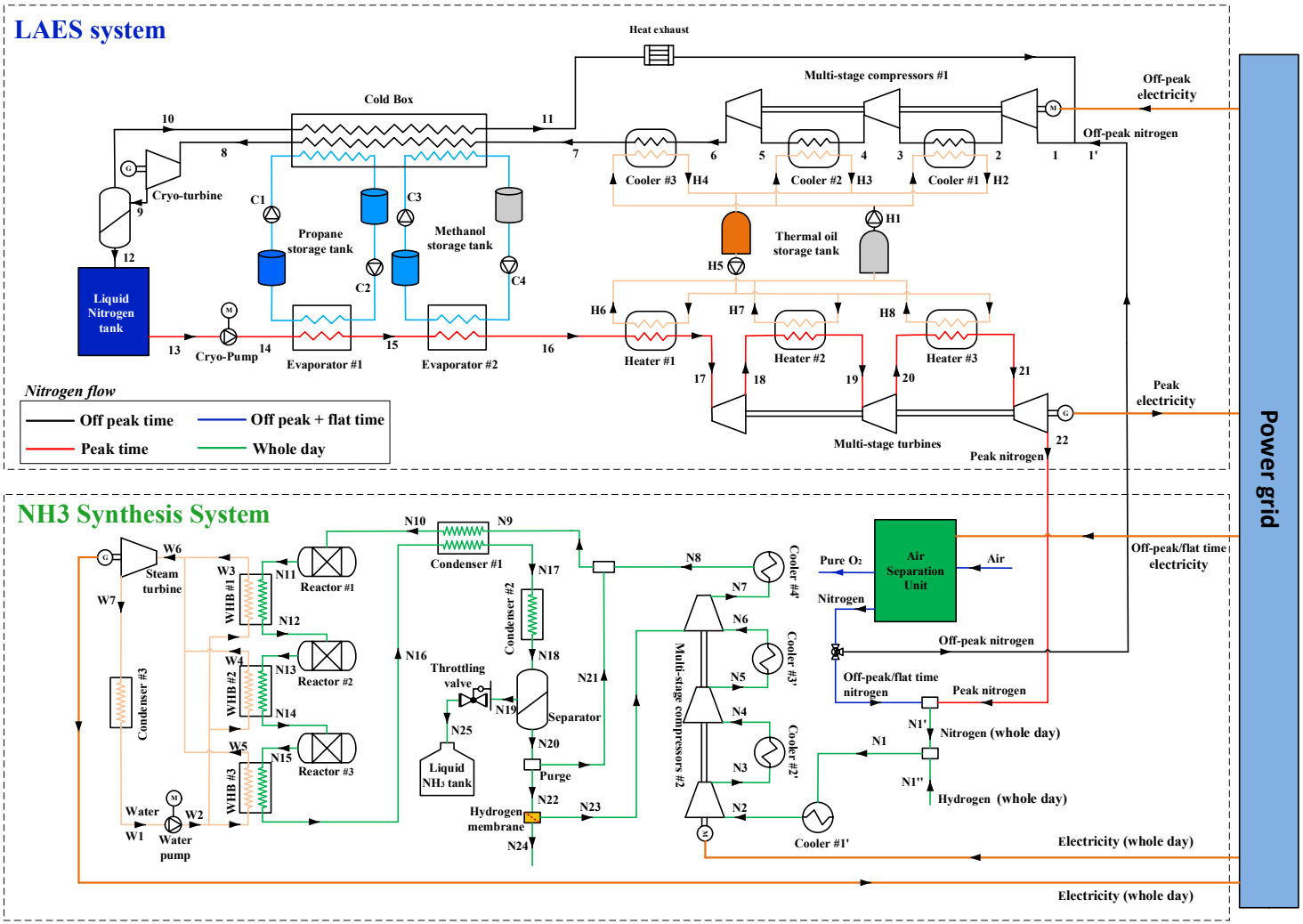

Figure 7.2 The flow diagram of the LAES-NH_3 system.

7.2.1.2 Thermodynamic model

The LAES in the LAES-NH3 system During the charging process of the LAES, the nitrogen (with a very small amount of residual argon) produced by ASU is compressed by the multi-stage compressors, consuming the off-peak electricity. The power consumption of the charging process is calculated by:

$$W_{LAES,com} = \frac{m_{LAES,ch} \cdot ((h_{2,s} - h_1) + (h_{4,s} - h_3) + (h_{6,s} - h_5))}{\eta_{com}} \tag{7.1}$$

$$m_{LAES,ch} = m_1 \tag{7.2}$$

where $m_{LAES,ch}$ is the nitrogen mass flow rate in the multi-stage air compressors in the charging process; h_i is the specific enthalpy with i corresponding to state i shown in Figure 7.2; η_{com} is the isentropic efficiency of air compressors; the subscript s represents an isentropic process.

The compressed nitrogen then goes through the cold box to be cooled down further, where the pinch point limitation is followed strictly in heat exchange calculation. The nitrogen then expands in the cryo-turbine, producing the liquid nitrogen. The power output of the cryo-turbine is expressed as follows:

$$W_{LAES,cryo-tur} = m_{LAES,ch} \cdot \eta_{cryo-tur} \cdot (h_8 - h_{9,s}) \tag{7.3}$$

where $\eta_{cryo\text{-}tur}$ is the isentropic efficiency of the cryo-turbine.

The net power consumption ($W_{LAES,ch}$) and liquid yield (Y_{LAES}), of the LAES charging process can therefore be calculated by:

$$W_{LAES,ch} = W_{LAES,com} - W_{LAES,cryo-tur} \tag{7.4}$$

$$Y = \frac{m_{LAES,ch} - m_{10}}{m_{LAES,ch}} \tag{7.5}$$

During the discharging process of the LAES, the liquid nitrogen stored in the tank is pumped up to a high-pressure state by the cryo-pump, consuming electricity ($W_{LAES,cryo\text{-}pump}$) given by:

$$W_{LAES,cryo-pump} = \frac{m_{LAES,dis} \cdot (h_{14,s} - h_{13})}{\eta_{cryo-pump}} \tag{7.6}$$

$$m_{LAES,dis} = m_{13} \tag{7.7}$$

where $m_{LAES,dis}$ is the liquid nitrogen mass flow rate in the discharging process; $\eta_{cryo\text{-}pump}$ is the isentropic efficiency of the cryo-pump.

The high-pressure liquid nitrogen exchanges heat with propane and methanol (cold energy storage medium) in evaporators #1 and #2 for pre-heating nitrogen, where the pinch point limitations are also observed. Nitrogen is further heated by the thermal oil (heat storage medium) before expanding in the three-stage turbine set. The power generation of the turbines ($W_{LAES,turb}$) is given by:

$$W_{LAES,turb} = m_{LAES,dis} \cdot \eta_{turb} \cdot ((h_{17} - h_{18,s}) + (h_{19} - h_{20,s}) + (h_{21} - h_{22,s})) \tag{7.8}$$

where η_{turb} is the isentropic efficiency of the three-stage turbine set.

Thus, the net power generation ($W_{LAES,dis}$) of the LAES discharging process is obtained by:

$$W_{LAES,dis} = W_{LAES,turb} - W_{LAES,cryo-pump} \tag{7.9}$$

The round trip efficiency, η_{LAES,E_RTE}, of the LAES sub-system can be then given by:

$$\eta_{LAES,E\_RTE} = \frac{W_{LAES,dis} \cdot t_{dis}}{W_{LAES,ch} \cdot t_{ch}} \tag{7.10}$$

The ammonia synthesis process in the LAES-NH_3 system The ammonia synthesis loop could work 24 hours a day, only changing the nitrogen supply from the ASU to the LAES at peak hours. The feed nitrogen and hydrogen need to be compressed to 15 MPa by the set of multi-stage compressor, where a stream of recycled gas from the hydrogen membrane is mixed with the feed gas before entering the third stage of the compressor unit. The gross power consumption of the set of multi-stage compressor, $W_{HB,com}$, is calculated by:

$$W_{HB,com} = \frac{m_{HB,in} \cdot ((h_{N3} - h_{N2}) + (h_{N5} - h_{N4})) + (m_{HB,in} + m_{N23}) \cdot (h_{N7} - h_{N6})}{\eta_{com}} \tag{7.11}$$

$$m_{HB,in} = m_{HB,in,N_2} + m_{HB,in,H_2} = m_{N1'} + m_{N1''} = m_{N1} \tag{7.12}$$

where $m_{HB,in}$ is the mass flow rate of the input feed gas (state N1) in the ammonia synthesis process; m_{Ni} is the total mass flow rate at the state *Ni* in Figure 7.2; η_{com} is the isentropic efficiency of the compressors.

The heat recovered from the waste heat boiler (WHB#1-3 in Figure 7.2) is used to generate steam, driving the steam turbine for power generation ($W_{HB,steam}$):

$$W_{HB,steam} = m_{steam} \left[(h_{W6} - h_{W7,s}) \cdot \eta_{steam-tur} - \frac{(h_{W2,s} - h_{W1})}{\eta_{steam-pump}} \right] \tag{7.13}$$

where $\eta_{steam\text{-}tur}$ and $\eta_{steam\text{-}pump}$ is the isentropic efficiency of the steam turbine and water pump, respectively.

The total power consumption of the ammonia synthesis loop could be calculated as:

$$W_{HB} = W_{HB,com} - W_{HB,steam} \tag{7.14}$$

The thermodynamic model for the complete ammonia synthesis process is given in Appendix A of this thesis.

7.2.1.3 Evaluation index

Operation cost of ASU At flat hours (t_{flat}), ASU works for ammonia synthesis sub-system only. At off-peak hours (t_{off}), ASU needs to produce nitrogen for both the ammonia synthesis sub-system and the LAES charging process. At peak hours (t_{peak}), the ammonia synthesis sub-system uses preferably the nitrogen released from the LAES discharging process. However, the ASU still needs to work for a period of time ($t_{peak,ASU}$) if the nitrogen released from the LAES discharging cycle cannot meet the nitrogen demand for the ammonia synthesis during peak time. Thus, the electricity consumption of the ASU in one day, Q_{ASU}, and the operation cost of the ASU in one day, $Cost_{ASU}$, can be calculated as follows:

$$Q_{ASU} = Q_{ASU}^{flat} + Q_{ASU}^{off} + Q_{ASU}^{peak} = [m_{HB,in,N_2} \cdot t_{flat} + (m_{HB,in,N_2} + m_{LAES,ch,N_2} \cdot Y_{LAES}) \cdot t_{off} + m_{HB,in,N_2} \cdot t_{peak,ASU}] \cdot q_{ASU}^{N_2} \quad (7.15)$$

$$Cost_{ASU} = \frac{(Q_{ASU}^{flat} \cdot tariff_{flat} + Q_{ASU}^{off} \cdot tariff_{off} + Q_{ASU}^{peak} \cdot tariff_{peak})}{Y_{NH_3}} \quad (7.16)$$

$$\begin{cases} \dfrac{m_{LAES,ch,N_2} \cdot Y_{LAES} \cdot t_{off}}{m_{HB,in,N_2}} \geq t_{peak}, t_{peak,ASU} = 0 \\ \dfrac{m_{LAES,ch,N_2} \cdot Y_{LAES} \cdot t_{off}}{m_{HB,in,N_2}} < t_{peak}, t_{peak,ASU} = t_{peak} - \dfrac{m_{LAES,ch,N_2} \cdot Y_{LAES} \cdot t_{off}}{m_{HB,in,N_2}} \end{cases} \quad (7.17)$$

In Equation (7.15), q_{ASU}^{N2} is the electricity consumption of ASU to produce 1kg pure nitrogen. In Equation (7.16), *tariff* represents electricity price; Y_{NH3} is the product yield of ammonia in one day. In Equation (7.17), it can be seen that when the nitrogen discharged from the LAES sub-system is more than enough for the peak time nitrogen demand of the ammonia synthesis sub-system, the ASU can be off during the peak time ($t_{peak,ASU}$ =0). Otherwise, the ASU needs to operate for a period of time during peak time ($t_{peak,ASU}$>0).

The electricity consumption, $Q_{ASU}^{'}$, and the operating cost, $Cost_{ASU}^{'}$, of the ASU in the standalone ammonia synthesis system can be calculated for comparison:

$$Q_{ASU}^{'} = Q_{ASU}^{flat'} + Q_{ASU}^{off'} + Q_{ASU}^{peak'} = m_{HB,in,N_2} \cdot (t_{flat} + t_{off} + t_{peak}) \cdot q_{ASU}^{N_2} \quad (7.18)$$

$$Cost_{ASU}^{'} = \frac{(Q_{ASU}^{flat'} \cdot tariff_{flat} + Q_{ASU}^{off'} \cdot tariff_{off} + Q_{ASU}^{peak'} \cdot tariff_{peak})}{Y_{NH_3}} \quad (7.19)$$

Overall ammonia synthesis cost The operation cost of the hydrogen production ($Cost_{H2}$), ASU ($Cost_{ASU}$), and the ammonia synthesis process (Haber–Bosch process, $Cost_{HB}$) need to be considered together to calculate the overall ammonia synthesis cost ($Cost_{overall}$ for LAES-NH_3 system and $Cost_{overall}^{'}$ for standalone ammonia synthesis system):

$$Cost_{overall} = Cost_{ASU} + Cost_{H_2} + Cost_{HB} \quad (7.20)$$

$$Cost_{overall}^{'} = Cost_{ASU}^{'} + Cost_{H_2} + Cost_{HB} \quad (7.21)$$

$$Cost_{H_2} = \frac{m_{HB,in,H_2} \cdot (t_{flat} + t_{off} + t_{peak}) \cdot cost^{0}_{H_2}}{Y_{NH_3}} \tag{7.22}$$

$$Cost_{HB} = \frac{W_{HB} \cdot t_{flat} \cdot tariff_{flat} + W_{HB} \cdot t_{off} \cdot tariff_{off} + W_{HB} \cdot t_{peak} \cdot tariff_{peak}}{Y_{NH_3}} \tag{7.23}$$

in which the cost to produce 1kg hydrogen ($Cost^{0}_{H2}$) depends on the hydrogen production method. If the traditional method (steam methane reforming), it is about 0.828 £/kg [182].

Economic performance of the LAES-NH₃ system The application scenario of this proposed LAES-NH_3 system is that there has been already an ammonia production plant, and an LAES power plant will be established nearby. This LAES plant can provide energy storage service to the power grid as a standard energy storage plant, obtaining revenues through electricity price arbitrage (other revenues are possible but not considered). Meanwhile, the LAES can also supply nitrogen shift service to the ammonia production plant, saving the operation cost of ASU. Furthermore, since the ASU in the ammonia production plant supplies pure nitrogen to LAES, the initial investment of the LAES is reduced due to the removal of the pre-purification unit of the charging process.

(1) Benefit for LAES side

The capital cost of a standalone LAES plant (C'_{LAES}) is divided into three parts: liquefaction unit (C_L), liquid nitrogen storage unit (C_S), and power generation unit (C_P), given below:

$$C'_{LAES} = C_L + C_S + C_P \tag{7.24}$$

According to the Highview Power Storage Technology and Performance Review 2012, and the average exchange rate for the GPB against the USD in 2012 [183] and the inflation rate over 2012-2020 [184], the capital cost (thousand GPB) of each unit can be estimated as follows:

$$C_L = \left(\frac{P_L}{4}\right)^{0.6} \times 11406 / 1.46 \tag{7.25}$$

$$C_S = \left(\frac{V_s}{85.7}\right)^{0.6} \times 1778 / 1.46 \tag{7.26}$$

$$C_P = \left(\frac{P_P}{10}\right)^{0.6} \times 5653 / 1.46 \tag{7.27}$$

where P_L, V_S and P_P represent the rated charging power, storage capacity and rated discharging power; 11406, 1778 and 5653 are the capital cost (thousand USD) of the liquefaction unit, liquid nitrogen storage unit, and power generation unit for a baseline LAES system (P_L=4MW, V_S =85.7MWh and P_P=10MW), respectively; 1.46 is a correction factor in view of both the exchange rate and inflation rate.

If the LAES is constructed next to an ammonia production plant, the capital cost of the pre-purification unit for air liquefication (C_{pre}) can be saved:

$$C_{LAES} = (C_L - C_{Pre}) + C_S + C_P \tag{7.28}$$

$$C_{LAES}^{save} = C'_{LAES} - C_{LAES} = C_{Pre} \tag{7.29}$$

The capital cost of the pre-purification unit is highly related to its inlet mass flow rate of air. Given that the average exchange rate for the GPB against the USD in 2018 [183] and the inflation rate over 2018-2020 [184], the capital cost of the pre-purification unit (million GPB, C_{Pre}) is estimated as follows [185]:

$$C_{Pre} = \left(\frac{m_{LAES,N_2} / hour}{394}\right)^{0.6} \times 9 / 1.30 \tag{7.30}$$

where $m_{LAES,N2}$/hour is the nitrogen demand of the LAES charging process per hour; 9 is the rough capital cost (million USD) for a standard pre-purification unit with the inlet air flow rate of 394 ton/hour; 1.30 is a correction factor in view of both the exchange rate and inflation rate.

(2) Benefit for ammonia synthesis side

Through the integration with a LAES plant, there will be a undercapacity issue for the current ASU of the ammonia production plant. The capacity of the ASU therefore needs to be increased to meet the higher nitrogen demand, which would lead to an additional cost (C_{ASU_extra}) to the ammonia production plant. The C_{ASU_extra} is defined as the difference between the capital cost of the newly expanded ASU (C_{ASU}) and the capital cost of the original ASU in the standalone ammonia production plant (C'_{ASU}):

$$C_{ASU\_extra} = C_{ASU} - C'_{ASU} \tag{7.31}$$

The capital cost of the ASU is highly related to its maximum potential production per day. Given the average exchange rate for the GPB against the USD in 2014 [183] and the inflation rate over 2014-2020 [184], the capital cost of the ASU (million GPB) can be calculated as follows [186]

$$C_{ASU} = (0.0103 \times Y_{ASU\_N_2} + 14.44) / 1.44 \tag{7.32}$$

where Y_{ASU_N2} is the nitrogen yield of the ASU plant per day and 1.44 is a correction factor in view of both the exchange rate and inflation rate.

To evaluate if the investment to expand the ASU capacity is economically feasible to the ammonia production plant side, the saving to investment ratio (*SIR*) needs to be investigated, which can be calculated by dividing the present value of revenue by the present value of cost. *SIR* >1 indicates that the expansion of the ASU has a potential economic benefit, otherwise, it suggests an economic loss.

$$SIR = \frac{\sum_{i=1}^{lifetime} \frac{C_{NCI}}{(1+r)^i}}{C_{ASU\_extra}} \tag{7.33}$$

The net cash inflow, C_{NCI}, is calculated as the difference of the cash inflow and outflow:

$$C_{NCI} = C_{ASU}^{\text{save}} - C_{O\&M} \tag{7.34}$$

where $C_{O\&M}$ is the operating and maintenance cost, which is typically about 1.5%-3% of the capital cost of the plant per year [140] with 1.5% selected for this study; C_{ASU}^{save} is the operation cost saving of ASU per year.

The payback period is also an important index to evaluate the economic value of an investment, which is defined as below:

$$payback\_period = \frac{C_{ASU\_extra}}{C_{NCI}} \tag{7.35}$$

Furthermore, the electricity tariff data used in the calculation is from the industrial tariff in Jiangsu province, China [187].

7.2.2 LAES-AS-NH_3 system

7.2.2.1 Working principle and configuration of the LAES-AS-NH_3 system

The basic working principle for the LAES-AS-NH_3 system is shown in Figure 7.3, which consists of the LAES sub-system with air separation function (termed as LAES-AS system) and the ammonia synthesis sub-system connected through nitrogen flow and high-temperature heat storage. The ASU is removed from the LAES-AS-NH_3 system since its air separation function is now realized by the LAES-AS system.

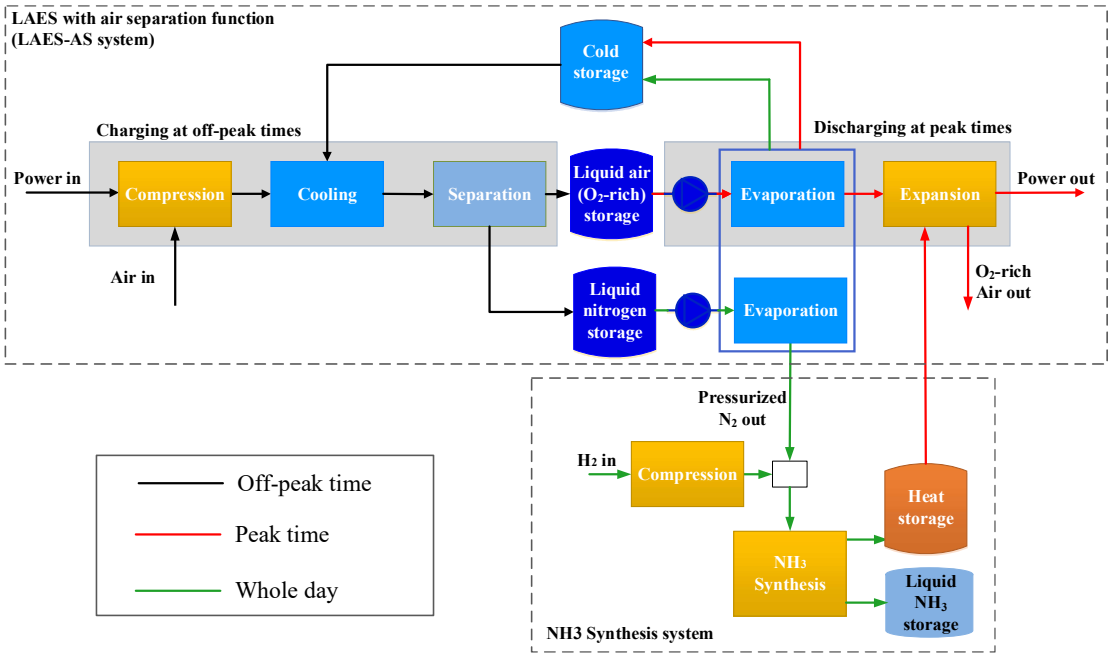

Figure 7.3 The basic working principle for the LAES-AS-NH_3 system

Figure 7.4 shows a schematic flow diagram of the proposed LAES-AS-NH_3 system. The working process of the LAES-AS-NH_3 system is explained as follows:

- At off-peak hours: The charging process of the LAES-AS system is on. The purified air is compressed to a high pressure by a set of multi-stage compressor with interstage cooling (State 7). The pressurized air then enters the cold box, where it is cooled down to state 8 by a cold storage medium (methanol, state C6) from the methanol storage tank, the second stream of cold storage medium (propane, state C4) from the propane storage tank #2, and the third stream of cold storage medium (also propane, state C2) from the propane storage tank #1 in turn. The low-temperature air (state 8) expands in a cryo-turbine to 0.5 MPa, with a portion of the air liquified (state 9). After that, the liquid air and gaseous air enter the distillation column via the medium stage (state 10) and bottom stage (state 11), respectively. The distillation column separates the air to pressurized high-purity nitrogen in the liquid phase (state 16) and ambient-pressure oxygen-enriched air (state 12). The oxygen-enriched air enters a

separator to obtain liquid air for storage (state 15) and gaseous air for exhaust (state 13) after recovery the cold energy in the cold box (state 14).

- At peak hours: The discharging process of LAES-AS system is on. The stored liquid oxygen-enriched air (state 21) is pumped to a high pressure (state 22), transferring the cold energy to the two streams of propane (state C7 and C9) and the one stream of methanol (state C11) in turn, with cold energy stored in the two cold storage mediums in the three tanks. Air is now at around the room temperature (state 25), which is heated to state 26 by the exhaust air from state 32 first, and then further heated to a high temperature by a heat storage medium (molten salt is considered in this case) from the molten salt storage tank, before entering the multi-stage air turbine to generate electricity.

The ammonia synthesis sub-system works continuous 24 hours a day, with the nitrogen supplied from the liquid nitrogen tank in the LAES-AS system. The process is: the stored pressurized liquid nitrogen (state 17) is pumped to the working pressure for the ammonia synthesis (state 18), transferring cold energy to propane (state C13) and methanol (state C15) in turn. The nitrogen is close to ambient temperature at state 20, which is mixed with other feed gas at the outlet of the multi-stage compressors (state N9) in the ammonia synthesis sub-system. From this onwards, the working process of this ammonia synthesis sub-system is almost the same as that of the normal ammonia synthesis system (see Section 7.2.1.1), except for one difference: in the normal ammonia synthesis system, the waste heat released by the synthesis reaction is usually used to generate steam for power generation. In the ammonia synthesis process of this LAES-AS-NH_3 system, this part of waste heat is recovered by the molten salt and used for air superheating in the discharging process of the LAES-AS sub-system. While the ammonia synthesis sub-system operating (24 hours per day), to maintain the optimal reaction temperature of reactors at 400-500 °C, the reaction gas needs to get through cooler#4-6 for being cooled down after getting out from the three reactors, where the low-temperature molten salt (state H1, 390°C) is used to recovery this part of reaction heat.

The high-temperature molten salt can be obtained (state H2-H4, ~500℃) and stored in the high-temperature thermal storage tank. During the discharging process of the LAES-AS sub-system, the molten salt from the high-temperature thermal storage tank (state H5) is used to heat the air in heater#1-3. After releasing the reaction heat, the low-temperature molten salt (state H6-H8) will flow back to the low-temperature thermal storage tank.

Compared with the LAES-NH_3 system, one can find that the ammonia synthesis sub-system and the LAES-AS sub-system are much more highly integrated in the LAES-AS-NH_3 system. Thus, the original configurations of the ammonia synthesis system and the LAES system need more modifications. As mentioned in Section 7.2.1, the LAES-NH_3 system is more suitable for an existing ammonia synthesis plant because there is almost no requirement to modify the current layouts and facilities except for expanding the ASU capacity. On the contrary, the LAES-AS-NH_3 system is more suitable for a new ammonia synthesis plant, employing the newly proposed configuration for construction directly. In this way, the initial investment of the ASU part could be saved.

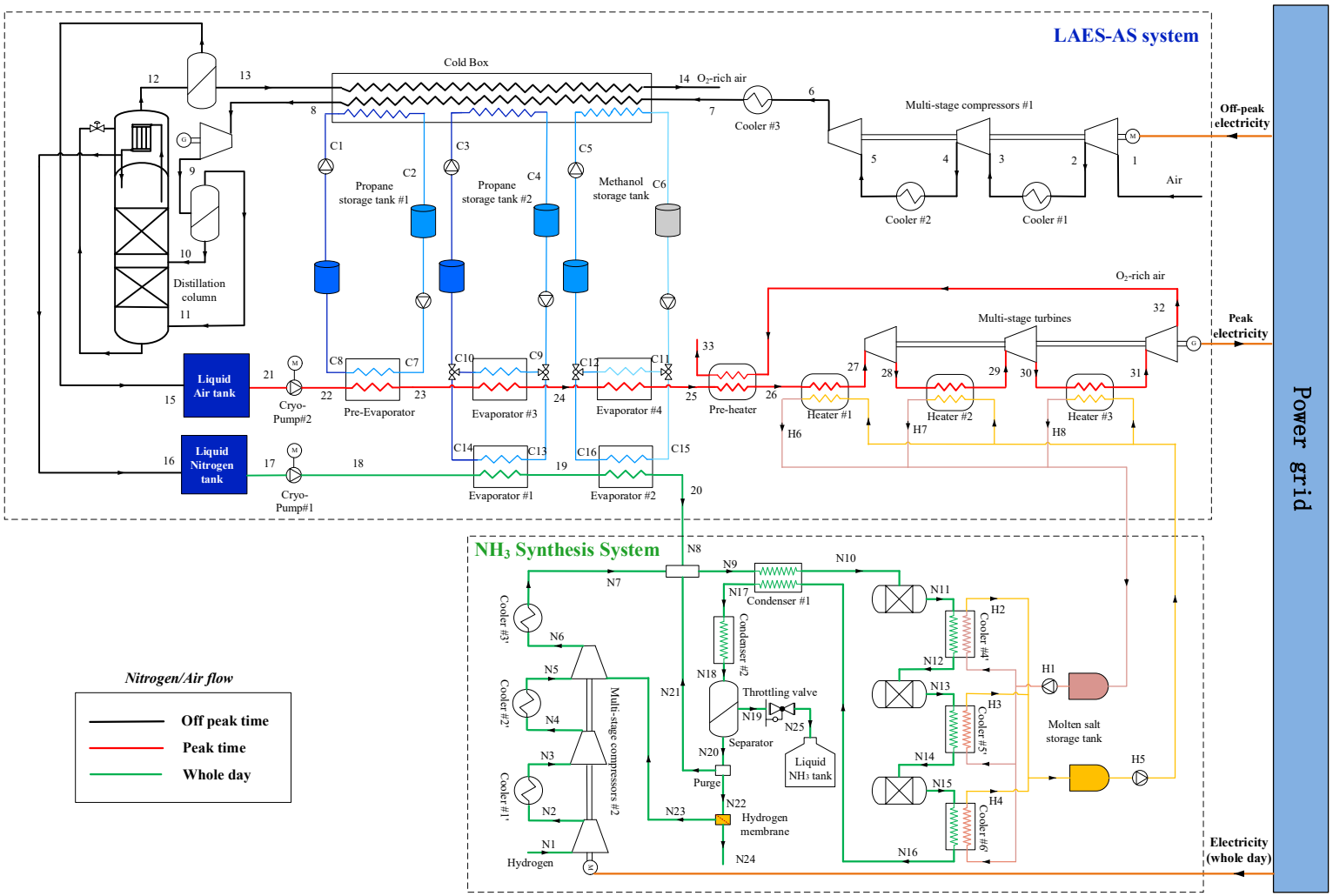

Figure 7.4 The flow diagram of the LAES-AS-NH_3 system.

7.2.2.2 Thermodynamic model

The LAES-AS in the LAES-AS-NH3 system The net power consumption ($W_{LAES\text{-}AS,ch}$) of the LAES-AS charging process is calculated by:

$$W_{LAES\text{-}AS,ch} = W_{LAES\text{-}AS,com} - W_{LAES-AS,cryo-tur} \tag{7.36}$$

$$W_{LAES\text{-}AS,com} = \frac{m_{LAES\text{-}AS,ch} \cdot ((h_{2,s} - h_1) + (h_{4,s} - h_3) + (h_{6,s} - h_5))}{\eta_{com}} \tag{7.37}$$

$$W_{LAES\text{-}AS,cryo-tur} = m_{LAES-AS,ch} \cdot \eta_{cryo-tur} \cdot (h_8 - h_{9,s}) \tag{7.38}$$

$$m_{LAES\text{-}AS,ch} = m_1 \tag{7.39}$$

Three liquid yields defined for the charging process of the LAES-AS system: liquid nitrogen yield ($Y_{LAES\text{-}AS,N2}$), liquid air (oxygen-enriched air) yield ($Y_{LAES\text{-}AS,air}$), and total liquid yield ($Y_{LAES\text{-}AS}$), which are expressed by:

$$Y_{LAES-AS,N_2} = \frac{m_{16}}{m_{LAES\text{-}AS,ch}} \tag{7.40}$$

$$Y_{LAES-AS,air} = \frac{m_{15}}{m_{LAES\text{-}AS,ch}} \tag{7.41}$$

$$Y_{LAES-AS} = \frac{m_{15} + m_{16}}{m_{LAES\text{-}AS,ch}} \tag{7.42}$$

The net power generation ($W_{LAES\text{-}AS,dis}$) of the LAES-AS discharging process can be obtained by:

$$W_{LAES\text{-}AS,dis} = W_{LAES\text{-}AS,turb} - W_{LAES\text{-}AS,cryo-pump\#2} \tag{7.43}$$

with

$$W_{LAES\text{-}AS,cryo-pump\#2} = \frac{m_{LAES-AS,dis} \cdot (h_{22,s} - h_{21})}{\eta_{cryo-pump}} \tag{7.44}$$

$$W_{LAES\text{-}AS,turb} = m_{LAES\text{-}AS,dis} \cdot \eta_{tur} \cdot ((h_{27} - h_{28,s}) + (h_{29} - h_{30,s}) + (h_{31} - h_{32,s})) \tag{7.45}$$

$$m_{LAES\text{-}AS,dis} = m_{21} \tag{7.46}$$

Thus, the electrical round trip efficiency, $\eta_{LAES\text{-}AS,E\_RTE}$, of the LAES-AS system can be given by:

$$\eta_{LAES\text{-}AS,E\_RTE} = \frac{W_{LAES-AS,dis} \cdot t_{dis}}{W_{LAES-AS,ch} \cdot t_{ch}} \tag{7.47}$$

The single distillation column used in the LAES-AS system has a specific configuration as illustrated in Figure 7.5 (a). It consists of several stages. Feed liquid and feed gas are fed into the distillation column respectively from the medium stage (state 10 in Figure 7.4) and the bottom stage (state 11 in Figure 7.4). Liquid air (oxygen-enriched) is obtained at the outlet of stage N (state U_N). The liquid air then goes through a throttle valve to reduce pressure to ambient pressure, reaching a lower temperature. The ambient-pressure air is then introduced to stage 1 to liquify the pure nitrogen product from stage 2. Thus, the heat exchanger in stage 1 works as a reboiler for the liquid air and a condenser for the gaseous nitrogen. Here, a portion of the liquid nitrogen out of stage 1 needs to return stage 2 as the reflux liquid (state L_1), and the rest of the liquid nitrogen (state U_1) is stored in the liquid nitrogen tank (state 16 in Figure 7.4). A schematic diagram of a generic stage in the single distillation column is summarized in Figure 7.5 (b). Some assumptions are made for modelling of the single distillation column [188,189]:

- Steady state.
- Ideal vapour phase behaviour.
- Each stage is a perfectly mixed stage, i.e., the vapour and liquid phases are homogeneous in each of these stages.
- The vapour and liquid leaving any stage are in thermodynamic equilibrium.
- Heat transfer only occurs in the condenser/reboiler (i.e., stage 1).
- No reaction occurs in the column.
- Effects due to column internals, e.g., pressure drops, are not considered.

- The air assumed to be made up of 78.12% of nitrogen, 20.96% of oxygen, and 0.92% of argon by volume.

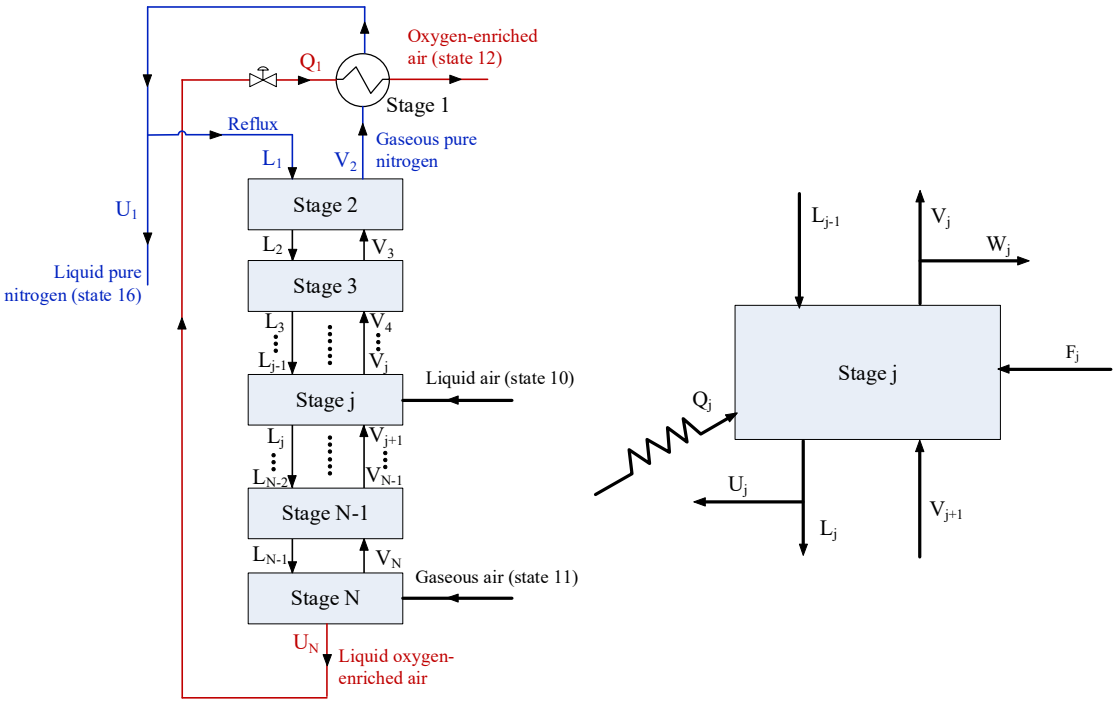

Figure 7.5 (a) Schematic representation of the single distillation column, and (b) schematic representation of input and output streams in a generic stage.

The general model for the separation stage j is given as follows:

(1) Mass balance for components

$$F_j z_{i,j} + L_{j-1} x_{i,j-1} + V_{j+1} y_{i,j+1} - (L_j + U_j) x_{i,j} - (V_j + W_j) y_{i,j} = 0 \tag{7.48}$$

where F_j is the molar flow rate of the feed stream to stage j, L_j is the liquid molar flow rate outputting stage j and and inputting stage $j+1$, V_j is the vapor molar flow rate outputting stage j and inputting stage $j-1$, U_j is the liquid side molar flow rate outputting stage j and W_j is the vapor side molar flow rate outputting stage j; $x_{i,j}$ is the mole fraction of component i in the liquid phase of stage j, $y_{i,j}$ is the mole fraction of component i in the vapor phase of stage j and $z_{i,j}$ is the mole fraction of component i in the feed stream of stage j; The components in the stream include nitrogen, oxygen and argon, i.e., $i = N_2$, O_2, Ar.

(2) Equilibrium relationship

The compositions of the streams leaving a stage are in equilibrium. Therefore, the mole fractions of component *i* in the liquid and vapour streams leaving stage *j* are related by the equilibrium relationships given below:

$$y_{i,j} = K_{i,j} x_{i,j} \tag{7.49}$$

$$K_{i,j} = K(T_j, P_j, x_{i,j}) \tag{7.50}$$

where $K_{i,j}$ is the ideal temperature-dependent vapour–liquid equilibrium constant, which is determined by the temperature (T_j), pressure (P_j) and mole fraction of component *i* in the liquid phase ($x_{i,j}$) of stage *j* [190,191].

(3) Total mass balance

The mole fractions of all the components, either in vapour or liquid phase, must sum to unity:

$$\sum_{i=1}^{3} x_{i,j} = 1 \qquad \sum_{i=1}^{3} y_{i,j} = 1 \tag{7.51}$$

(4) Heat balance

The heat balance is given by:

$$F_j h_{F,j} + L_{j-1} h_{L,j-1} + V_{j+1} h_{V,j+1} - (L_j + U_j) h_{L,j} - (V_j + W_j) h_{V,j} + Q_j = 0 \tag{7.52}$$

where *h* represents the specific enthalpy of feed stream (subscript *F*), liquid (subscript *L*), gas (subscript *V*), side liquid (subscript *U*) and side gas (subscript *W*) at stage *j*; and Q_j represents heat input or output for the stage *j*.

The above model equations for the distillation process are simple algebraic equations developed by applying mass and energy balances in the column. These equations can be solved by using the so-called ‘fsolve’ function in MATLAB, which is designed to find the root of a set of nonlinear equations.

The ammonia synthesis process in the LAES-AS-NH3 system The total power consumption of the ammonia synthesis loop is calculated by:

$$W_{HB} = W_{HB,com} + W_{LAES\text{-}AS,cryo-pump\#1} \tag{7.53}$$

where

$$W_{HB,com} = \frac{m_{HB,in,H_2} \cdot ((h_{N2} - h_{N1}) + (h_{N4} - h_{N3})) + (m_{HB,in,H_2} + m_{N23}) \cdot (h_{N6} - h_{N5})}{\eta_{com}} \tag{7.54}$$

$$m_{HB,in,H_2} = m_{N1} \tag{7.55}$$

$$W_{LAES\text{-}AS,cryo-pump\#1} = \frac{m_{HB,in,N_2} \cdot (h_{18,s} - h_{17})}{\eta_{cryo-pump}} \tag{7.56}$$

$$m_{HB,in,N_2} = m_{17} = m_{N8} \tag{7.57}$$

7.2.2.3 Evaluation index

Nominal electrical round trip efficiency With the LAES-AS, the ammonia synthesis process could save some electricity consumption for its daily operation (Q_{save}), including the electricity consumption of ASU and the electricity consumption of the multistage compressors. Thus, the nominal round trip efficiency ($\eta_{LAES\text{-}AS,NE\_RTE}$) of the LAES-AS system is defined as:

$$\eta_{LAES\text{-}AS,NE\_RTE} = \frac{W_{LAES-AS,dis} \cdot t_{dis} + Q_{save}}{W_{LAES-AS,ch} \cdot t_{ch}} \tag{7.58}$$

Power-to-Ammonia-to-Power (P2A2P) efficiency

To evaluate the overall energy conversion efficiency of the LAES-AS-NH_3 system, the Power-to-Ammonia-to-Power (*P2A2P*) efficiency is introduced.

The *P2A2P* efficiency of a standalone ammonia synthesis system ($P2A2P_{Standalone\text{-}NH3}$) is defined as the ratio of the available output power from combustion to the energy required for its production [192]:

$$P2A2P_{Standalone\text{-}NH_3} = \frac{\left(HHV_{NH_3} \cdot Y_{NH_3} \cdot \eta_{combustion}\right)}{Q_{H_2} + Q_{Standalone\text{-}HB} + Q_{ASU}} \tag{7.59}$$

where HHV_{NH3} is the higher heating value of ammonia and $\eta_{combustion}$ is the combustion efficiency of ammonia (the fraction of the heating value of that is converted to power); Q is the electricity consumption of every key process for standalone ammonia synthesis system to produce Y_{NH3} -kg ammonia; subscribe H_2, *standalone-HB* and *ASU* represent hydrogen production process, the Haber–Bosch process, and the nitrogen production process by ASU, respectively. Because the *P2A2P* is a kind of round trip efficiency, assuming that ammonia is a storage medium for electricity, Q_{ASU}, Q_{H2}, and $Q_{Standalone\text{-}HB}$ must be electricity consumptions to make this efficiency index valid. Thus, in the calculation of the *P2A2P*, hydrogen is assumed to be produced by water electrolysis, which consumes about 53.15 kWh to produce 1kg hydrogen [181].

In the LAES-AS-NH_3 system, the electricity consumption ($Q_{LAES\text{-}AS,ch}$) and generation ($Q_{LAES\text{-}AS,dis}$) of the LAES-AS system during one day are considered in the calculation of the *P2A2P* efficiency, which is given below:

$$P2A2P_{LAES-AS-NH_3} = \frac{\left(HHV_{NH_3} \cdot Y_{NH_3} \cdot \eta_{combustion}\right) + Q_{LAES\text{-}AS,dis}}{Q_{H_2} + Q_{HB} + Q_{LAES\text{-}AS,ch}} \tag{7.60}$$

7.3 Results and discussion

7.3.1 Results and discussion for the LAES-NH_3 system

Some additional assumptions were made in the process of simulation and performance analyses, which are summarized as follows:

- Pure propane and methanol are used both as the cold storage media and cold energy transfer fluids;
- Dowtherm G is used both as the heat transfer and storage medium of the compression heat;

- Nitrogen produced by ASU contains some residual argon (assuming a mass ratio of nitrogen to argon at 100:1).

Table 7.1 gives the default parameters of the LAES-NH_3 system, whereas Table 7.2 (a) and (b) list the calculated stream parameters of the LAES-NH_3 system under the default working conditions given in Table 7.1, with the charging pressure and discharging pressure at 15 MPa and 8 MPa, respectively. Figure 7.6 shows the temperature profiles of the key heat exchange components in the LAES-NH_3 system, illustrating that the temperature gradients of the working fluids match well with the constraints at the pinch point. Figure 7.7 shows the temperature and ammonia profiles along the three reactor beds, indicating that the reaction temperature in the three beds is strictly controlled between 400 and 500 ˚C. Ammonia synthesis is an exothermic reaction, and hence the temperature along each bed increases. The ammonia production rate and the temperature rising rate are much higher in reaction bed 1 than beds 2 and 3 because of the higher content of the nitrogen and hydrogen and lower content of the ammonia in bed 1.

Table 7.1 Default parameters of the LAES-NH_3 system

	Parameter	Value	Unit
	Ambient temperature	293	K
	Ambient pressure	100	kPa
	Thermal oil temperature	293	K
	Propane temperature	214	K
	Methanol temperature	293	K
	Minimum Approach Temperature in heater	5	K
	Minimum Approach Temperature in cooler	2	K
LAES	Minimum Approach Temperature in cold box	5	K
	Minimum Approach Temperature in evaporator	2	K
	Relative pressure drop in heat exchangers	1%	
	Isentropic efficiency of compressor	85%	
	Isentropic efficiency of turbine	90%	
	Isentropic efficiency of cryo-turbine	75%	
	Isentropic efficiency of cryo-pump	75%	
	Nitrogen mass flow rate at inlet of compressor	14	kg/s

ASU	Mass fraction of argon in 1kg nitrogen product	0.01	kg
	Energy consumption for N_2 production [193]	0.11	kWh/kg
NH_3 synthesis process	Nitrogen mass flow rate at inlet of compressor	10.25	kg/s
	Hydrogen mass flow rate at inlet of compressor	1.25	kg/s
	Product yield of Ammonia	500	ton/day
	Reaction pressure	15	MPa
	Reaction temperature range	673.15-773.15	K
	Purge fraction	50%	
	Hydrogen membrane recovery	85%	
	Other gas membrane recovery	10%	
	Ammonia recovery	92%	
	Minimum Approach Temperature in Condenser#1	2	K
	Minimum Approach Temperature in waste heat boiler	2	K
	Isentropic efficiency of compressor	85%	
	Isentropic efficiency of steam turbine	90%	
	Cost of Hydrogen from methane reforming [182]	0.828	£/kg
Electricity market/ Economic calculation	Electricity price of peak time	0.12	£/kWh
	Electricity price of off-peak time	0.034	£/kWh
	Electricity price of flat time	0.07	£/kWh
	Peak time during one day	8	hours
	Off-peak time during one day	8	hours
	Flat time during one day	8	hours
	Discount rate	4%	

Table 7.2 (a) Stream data for the LAES-NH_3 system

State	Pressure (MPa)	Temperature (K)	Nitrogen (kg/s)	Hydrogen (kg/s)	Ammonia (kg/s)	Argon (kg/s)	Total (kg/s)
1	0.100	293.00	14.000	0.000	0.000	0.140	14.140
2	0.531	503.06	14.000	0.000	0.000	0.140	14.140
3	0.526	303.00	14.000	0.000	0.000	0.140	14.140
4	2.795	520.61	14.000	0.000	0.000	0.140	14.140
5	2.767	303.00	14.000	0.000	0.000	0.140	14.140
6	14.702	523.18	14.000	0.000	0.000	0.140	14.140
7	14.554	303.00	14.000	0.000	0.000	0.140	14.140
8	14.409	92.78	14.000	0.000	0.000	0.140	14.140
9	0.110	78.10	14.000	0.000	0.000	0.140	14.140
10	0.110	78.16	1.652	0.000	0.000	0.017	1.669
11	0.109	272.70	1.652	0.000	0.000	0.017	1.669
12	0.110	78.10	12.348	0.000	0.000	0.123	12.471
13	0.110	78.10	12.348	0.000	0.000	0.123	12.471

14	8.000	81.81	12.348	0.000	0.000	0.123	12.471
15	7.920	211.90	12.348	0.000	0.000	0.123	12.471
16	7.841	291.00	12.348	0.000	0.000	0.123	12.471
17	7.762	492.36	12.348	0.000	0.000	0.123	12.471
18	1.801	340.02	12.348	0.000	0.000	0.123	12.471
19	1.783	492.36	12.348	0.000	0.000	0.123	12.471
20	0.414	341.29	12.348	0.000	0.000	0.123	12.471
21	0.410	492.36	12.348	0.000	0.000	0.123	12.471
22	0.095	341.65	12.348	0.000	0.000	0.123	12.471
N1	0.100	295.00	10.250	1.254	0.000	0.102	11.606
N2	0.100	295.00	10.250	1.254	0.000	0.102	11.606
N3	0.531	506.86	10.250	1.254	0.000	0.102	11.606
N4	0.531	295.00	10.250	1.254	0.000	0.102	11.606
N5	2.823	507.21	10.250	1.254	0.000	0.102	11.606
N6	2.823	295.00	10.250	1.254	0.000	0.102	11.606
N7	15.000	507.86	10.837	2.322	0.025	0.114	13.298
N8	15.000	295.00	10.837	2.322	0.025	0.114	13.298
N9	15.000	295.00	16.702	3.579	0.266	0.228	20.774
N10	15.000	673.15	16.702	3.579	0.266	0.228	20.774
N11	15.000	772.19	14.839	3.180	2.528	0.228	20.774
N12	15.000	673.15	14.839	3.180	2.528	0.228	20.774
N13	15.000	773.14	12.967	2.779	4.801	0.228	20.774
N14	15.000	673.15	12.967	2.779	4.801	0.228	20.774
N15	15.000	739.49	11.731	2.514	6.302	0.228	20.774
N16	15.000	676.99	11.731	2.514	6.302	0.228	20.774
N17	15.000	352.02	11.731	2.514	6.302	0.228	20.774
N18	15.000	295.00	11.731	2.514	6.302	0.228	20.774
N19	15.000	295.00	0.000	0.000	5.798	0.000	5.798
N20	15.000	295.00	11.731	2.514	0.504	0.228	14.976
N21	15.000	295.00	5.865	1.257	0.252	0.114	7.488
N22	15.000	295.00	5.865	1.257	0.252	0.114	7.488
N23	2.823	295.00	0.587	1.068	0.025	0.011	1.691
N24	15.000	295.00	5.279	0.189	0.227	0.102	5.797
N25	1.600	296.43	0.000	0.000	5.798	0.000	5.798

(b) Stream data for thermal oil, propane, methanol, and water steam

State	Pressure (MPa)	Temperature (K)	Mass flow rate (kg/s)	Fluid
H1	0.1	293.00	27.869	Thermal oil
H2	0.1	489.75	8.792	Thermal oil
H3	0.1	502.90	9.017	Thermal oil
H4	0.1	499.00	10.059	Thermal oil
H5	0.1	497.36	23.053	Thermal oil
H6	0.1	301.00	8.180	Thermal oil

H7	0.1	350.02	7.480	Thermal oil
H8	0.1	351.29	7.398	Thermal oil
C1	0.1	85.60	14.042	Propane
C2	0.1	214.00	14.042	Propane
C3	0.1	213.90	6.712	Methanol
C4	0.1	293.00	6.712	Methanol
W1	0.4	293.00	5.651	Water
W2	6	293.32	5.651	Water
W3	6	770.10	2.141	Water
W4	6	771.05	2.145	Water
W5	6	737.40	1.365	Water
W6	6	762.52	5.651	Water
W7	0.4	438.44	5.651	Water

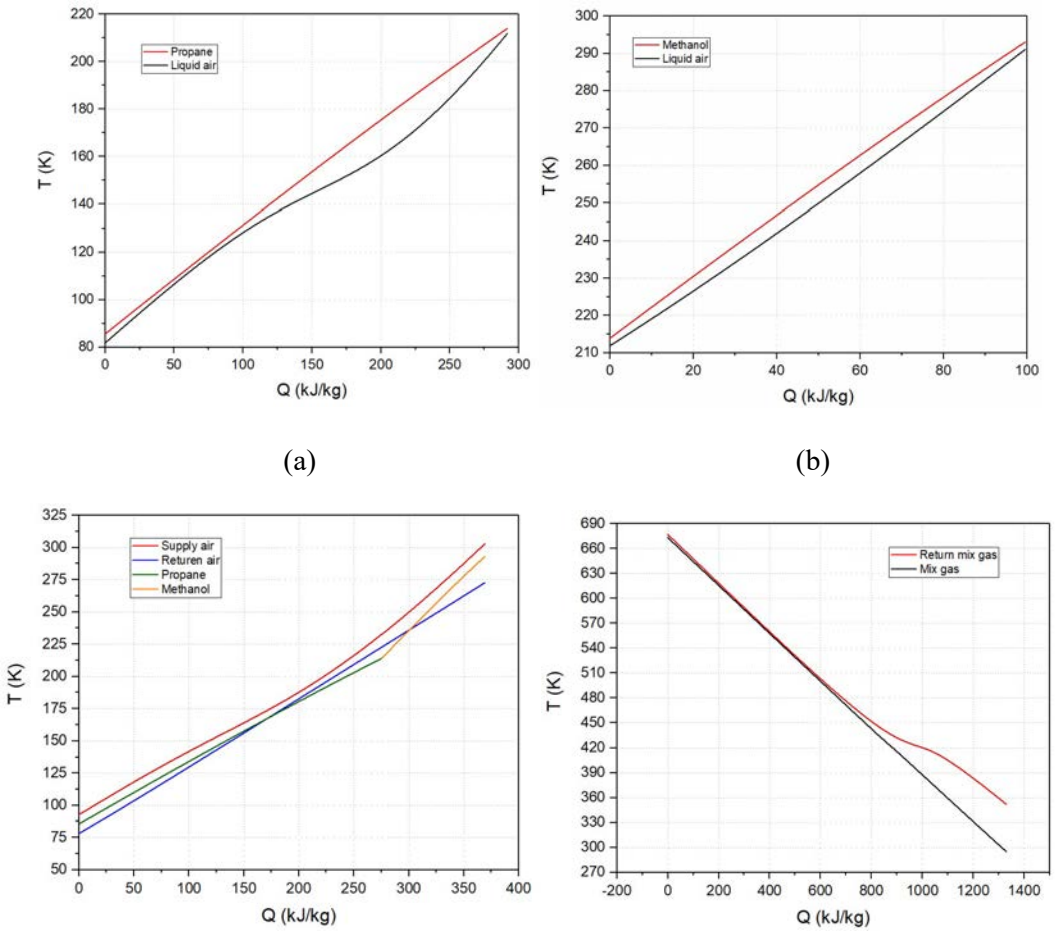

(a) (b)

(c) (d)

Figure 7.6 Temperature profiles of heat exchangers in LAES-NH_3 system: (a) Evaporator #1, (b) Evaporator #2, (c) Cold box and (d) Condenser #1.

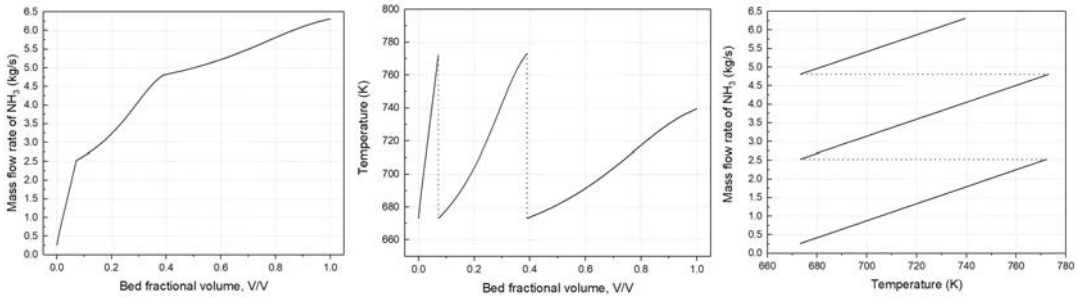

(a) (b) (c)

Figure 7.7 Temperature and ammonia profiles along the three reactor beds: (a) ammonia profile, (b) temperature profile and (c) temperature-ammonia profile.

7.3.1.1 Operation modes of the LAES-NH_3 system

Prior to the thermodynamic and economic analyses of the LAES-NH_3 system, the operation modes of this integrated system need to be determined. Three basic operation modes are considered as shown in Figure 7.8, which are sorted by the matching degree between the nitrogen output of the LAES discharging process and the nitrogen demand of the ammonia synthesis sub-system. The operation mode does not affect the ammonia synthesis process, so that the nitrogen consumption of the ammonia synthesis is constant. At flat hours, the ASU works in a low capacity to provide nitrogen to the ammonia synthesis sub-system only, which is the same in all the three working modes. At off-peak hours, the ASU produces nitrogen for both the ammonia synthesis sub-system and LAES charging process. The feed nitrogen of the LAES system is finally liquefied and stored as the energy storage medium. At peak hours, the LAES discharging process is on. The stored liquid nitrogen is used for power generation first, which can then be used as the feed gas for the ammonia synthesis sub-system. If the liquid nitrogen from the LAES system is insufficient to meet the peak-time nitrogen demand of the ammonia synthesis sub-system, the LAES-NH_3 system works in mode (a), with the ASU on for a period at peak times to make up the deficit of the nitrogen. If the amount of liquid nitrogen from the LAES system can match the peak-time nitrogen consumption of the ammonia synthesis sub-system, the LAES-NH_3 system works in mode (b), with the ASU off during the whole peak hours, and no excess nitrogen released to ambient from this integrated system.

When the amount of liquid nitrogen from the LAES system exceeds the peak-time nitrogen demand of the ammonia synthesis sub-system, the LAES-NH_3 system works in mode (c), with the ASU off during the whole peak hours and the excess nitrogen to be released to ambient after power generation.

Figure 7.8 Three operation modes of the LAES-NH_3 system: mode (a), (b) and (c).

7.3.1.2 Effect of the charging pressure of the LAES on the LAES-NH_3 system

The charging pressure of LAES is an important influence factor on the performance of the standalone LAES system. This parameter, in turn, could affect the working performance of the LAES-NH_3 system. To study the effect of the charging pressure on the LAES-NH3 system,

both the discharging pressure of the LAES and the inlet nitrogen mass flow rate of the multi-stage compressors in the charging process are fixed. Figure 7.9 (a) shows the liquid nitrogen yield of the LAES sub-system as a function of the nitrogen charging pressure. A clear increasing trend is observed. The maximum liquid yield, ~0.90, occurs at a charging pressure of ~16 MPa, beyond which the LN_2 yield remains unchanged. Figure 7.9 (a) also shows a similar increasing trend of the round trip efficiency first with charging pressure, peaks at 61.8% with a charging pressure of ~16 MPa, but falls with a further increase in the charging pressure. This is mainly because that the liquid yield remains almost unchanged when the charging pressure is higher than 16 MPa, while the power consumption of the multi-stage compressor keeps increasing.

The change in liquid nitrogen yield affects the nitrogen output of the LAES discharging process. An excessively low liquid nitrogen yield can lead to the deficit of nitrogen in the ammonia synthesis sub-system if the LAES is the only nitrogen supplier at peak hours. Thus, in this case, the ASU has to be on for a period of peak time to make up for nitrogen short fall. Figure 7.9 (b) shows the effect of the charging pressure on the operation time allocation of LAES and ASU. One can see that the running time of the ASU at peak times decreases gradually with increasing nitrogen charging pressure. When the charging pressure reaches 11 MPa, and the liquid nitrogen yield is improved to ~ 0.74, the nitrogen output of the LAES discharging process is able to support the ammonia synthesis at peak hours, indicating that the LAES-NH_3 system starts to work in mode (b) or (c).

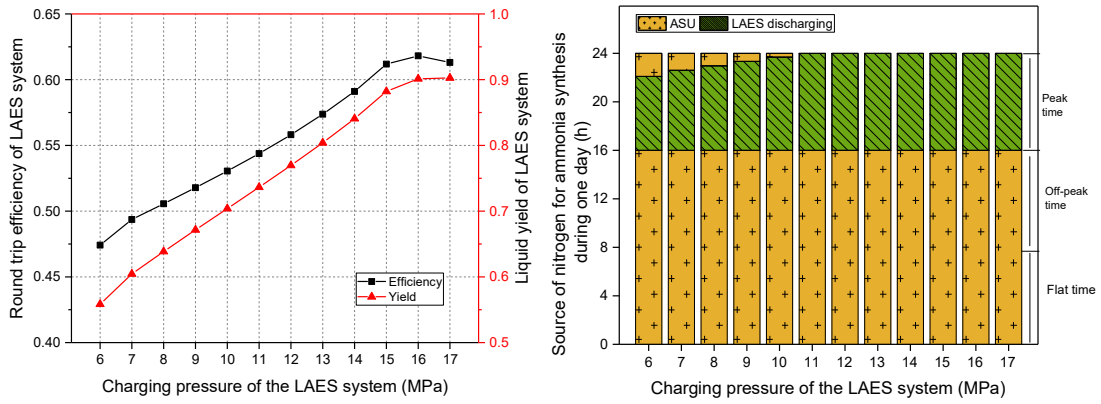

(a) (b)

Figure 7.9 The effect of charging pressure on (a) the LAES performance and (b) the operation time of the LAES and ASU (discharging pressure at 8 MPa).

To find out the nitrogen flow direction at off-peak and peak times separately, the effect of the charging pressure on the nitrogen consumption profile at off-peak times and nitrogen production profile at peak times are studied, and are shown in Figure 7.10 (a) and (b), respectively. From Figure 7.10 (a), one can see that the total nitrogen yield of the ASU at off-peak times depends on the total nitrogen consumption of the LAES and ammonia synthesis. An increase of the charging pressure of the LAES gives an increased total nitrogen yield of the ASU due to the increasing nitrogen demand of the LAES sub-system, given the nitrogen demand of the ammonia synthesis. The reason that the LAES consumes more nitrogen at a high charging pressure is because of the incresed liquid nitrogen yield of the LAES sub-system with an increased charging pressure. The amount of the return nitrogen therefore reduces and fresh nitrogen from the ASU is needed to maintain a constant inlet nitrogen flow rate of the multi-stage compressor.

The decomposition of the nitrogen supply at peak times is shown in Figure 7.10 (b), which illustrates that the nitrogen consumption of the ammonia synthesis sub-system is constant. However, with the increasing charging pressure, the LAES sub-system releases more nitrogen for the ammonia synthesis sub-system during the discharging process, leading to a reduced nitrogen yield of the ASU at peak times. This is because that when the charging pressure

increases, more liquid nitrogen can be produced and stored during the LAES charging process, implying more nitrogen is released during the LAES discharging process. When the charging pressure reaches 11 MPa, the nitrogen output of the LAES discharging process can match with the nitrogen demand of the ammonia synthesis, indicating that the LAES-NH_3 system is almost working in mode (b). If the charging pressure continues increasing, the LAES-NH3 system will shift to the working mode (c). In such a scenario, overproduction of liquid nitrogen occurs during the LAES charging process. The nitrogen output of the LAES discharging process exceeds the actual nitrogen demand of the ammonia synthesis sub-system, resulting in nitrogen waste.

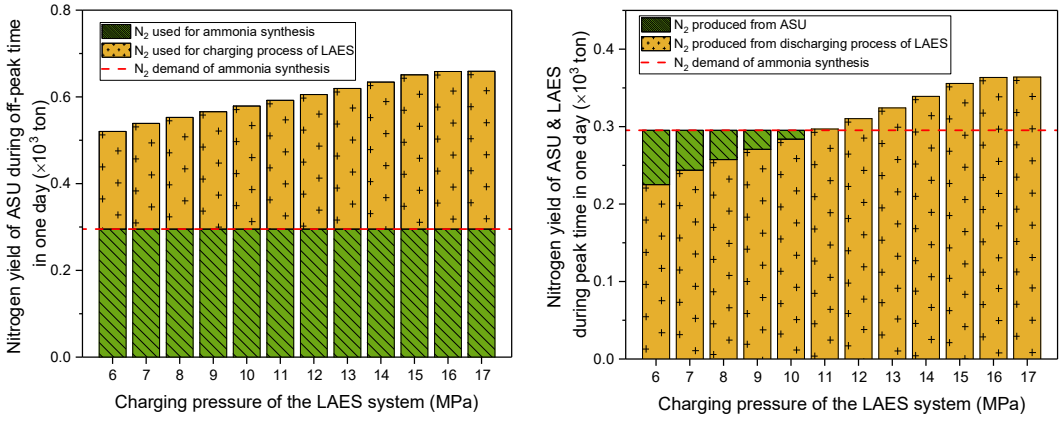

(a) (b)

Figure 7.10 The effect of charging pressure on (a) the nitrogen consumption by the LAES and ammonia synthesis at off-peak times and (b) the nitrogen production by the LAES and ASU at peak times (discharging pressure at 8 MPa).

Since the charging pressure affects the operating duration and the total nitrogen yield of the ASU, the electricity consumption and the operation cost of the ASU are also influenced, as shown in Figure 7.11 (a) and (b). From Figure 7.11 (a), the electricity consumption of the ASU is seen to remain the same at a charging pressure below 11 MPa. However, when the charging pressure increases to above 11 MPa, the electricity consumption of the ASU starts to increase, reaches to a peak at a charging pressure of 16 MPa, beyond which the electricity consumption becomes constant. The ASU electricity consumption only depends on the total nitrogen yield

of the ASU over the whole day. Because the LASE sub-system only acts as a nitrogen buffer for the LAES-NH_3 system, all the nitrogen output of the LASE discharging process is essentially produced by the ASU. When the charging pressure is lower than 11 MPa, the LAES-NH_3 system works under mode (a), and the nitrogen production is used in the ammonia synthesis sub-system, indicating that the total nitrogen yield of the ASU is equal to the nitrogen consumption of the ammonia synthesis sub-system (which is constant). However, when the charging pressure is over 11 MPa, overproduction of nitrogen occurs, implying excess nitrogen to be released to the ambient directly during the LAES discharging process. This means that the total nitrogen yield of the ASU exceeds the nitrogen consumption of the ammonia synthesis sub-system, and hence an increased ASU electricity consumption. Figure 7.11 (b) compares the ASU operation cost between the LAES-NH_3 system and the standalone ammonia synthesis system. The results illustrate that, with the LAES system integrated, the operating cost of the ASU is much lower than that without the LAES. Although, when the charging pressure is higher than 11 MPa, more electricity is consumed by the ASU in the LAES-NH_3 system than the standalone ammonia synthesis system, the LAES-NH_3 system still has a lower ASU operation cost. That is because all the over-consumed electricity of the ASU is off-peak electricity which is much lower than the peak-time electricity. The maximum decrease of the ASU operation cost is ~38.3%, which occurs at a charging pressure of 11 MPa, with the LAES-NH_3 system operating in mode (b): the ASU only works at off-peak times and no waste nitrogen is released to the ambient during the LAES discharging process.

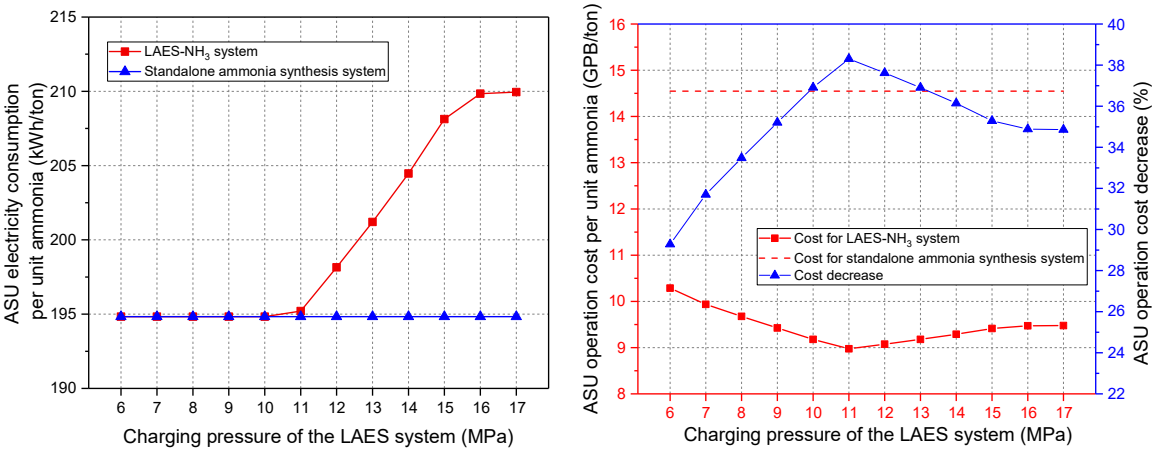

(a) (b)

Figure 7.11 The effect of charging pressure on the benefits of adding LAES in the ammonia synthesis system: (a) ASU electricity consumption and (b) ASU operation cost (discharging pressure at 8 MPa).

The operation cost of the whole ammonia synthesis process is also analysed, and the results are shown in Figure 7.12. The overall ammonia synthesis cost of the LAES-NH_3 system has a minimum value at the charging pressure of 11 MPa, which is the same as that of the ASU operation cost (Figure 7.11 (b)).

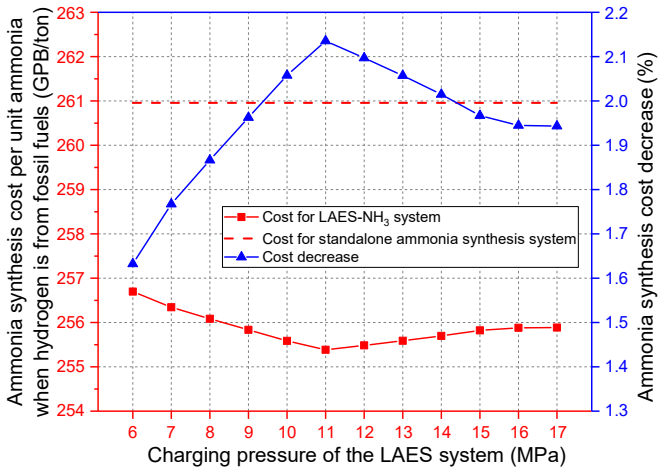

Figure 7.12 The effect of charging pressure on the overall ammonia synthesis cost (discharging pressure at 8 MPa).

7.3.1.3 Effect of the discharging pressure of the LAES on the LAES-NH_3 system

To study the effect of the discharging pressure on the LAES-NH_3 system, both the LAES charging pressure and the inlet nitrogen mass flow rate of the multi-stage compressor in the charging process are fixed. Figure 7.13 (a) shows the round trip efficiency and liquid nitrogen yield of the LAES system as a function of the discharging pressure over a range from 6 to 14 MPa. It can be seen that both the round trip efficiency and the liquid yield decrease with increasing discharging pressure. This is due to the cold recovery from the liquid nitrogen by propane and methanol during the discharging process, which decreases with increasing discharging pressure due to the increased nitrogen specific heat capacity. This, in turn, leads to a lower liquid nitrogen yield, making more specific power consumption of the multi-compressor during the charging process. Although a higher discharging pressure can contribute to a higher specific output of the multi-stage turbine, the decrease of the liquid yield plays a major role in determining the round trip efficiency. Figure 7.13 (b) shows the source of feed nitrogen of the ammonia synthesis loop. One can see that when the discharging pressure is lower than 10 MPa, the ASU does not need to operate during peak time to produce nitrogen for ammonia synthesis, indicating that the LAES-NH_3 system is operating under mode (b) or (c). When the discharging pressure is over 10 MPa, the LAES-NH_3 system enters to the mode (a). A longer working period of ASU at peak times is required to make up for the shortfall for nitrogen for the ammonia synthesis loop with a higher discharging pressure.

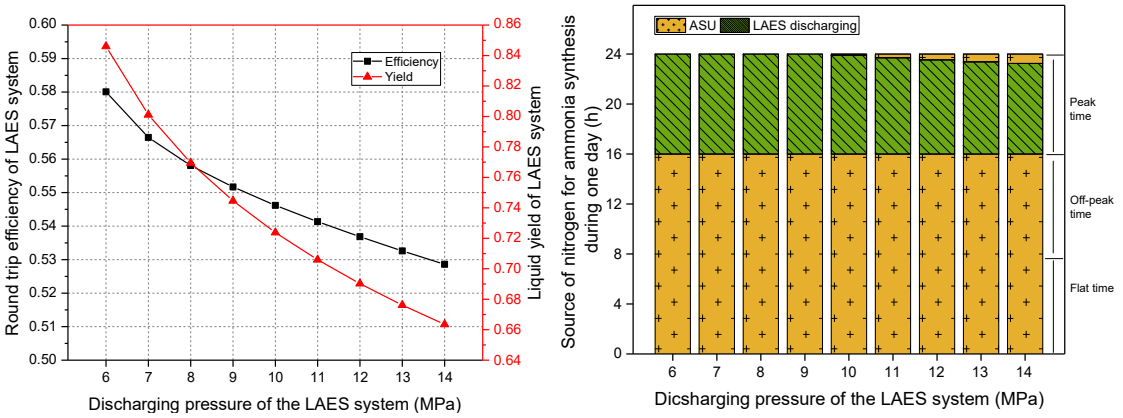

(a) (b)

Figure 7.13 The effect of discharging pressure on (a) the LAES performance and (b) the operation time of the LAES and ASU (charging pressure at 12 MPa).

Figure 7.14 (a) and (b) illustrate the effect of the discharging pressure on the nitrogen yield of ASU at off-peak times, and the nitrogen yield of ASU and LAES at peak times, respectively. An increased discharging pressure gives a less nitrogen production from ASU at off-peak times due to decreased nitrogen demand of the LAES charging process, as shown in Figure 7.14 (a). At peak times, with the increasing discharging pressure, the LAES discharging process provides less nitrogen due to the less liquid nitrogen yield of the charging process at off-peak times, as shown in Figure 7.14 (b). Besides, it can also be seen in Figure 7.14 (b) that when the discharging pressure is within the range of 6 to 9 MPa, the LAES-NH3 system operates under mode (c) because some of the nitrogen released by the LAES during the discharging process is exhausted to the ambient.

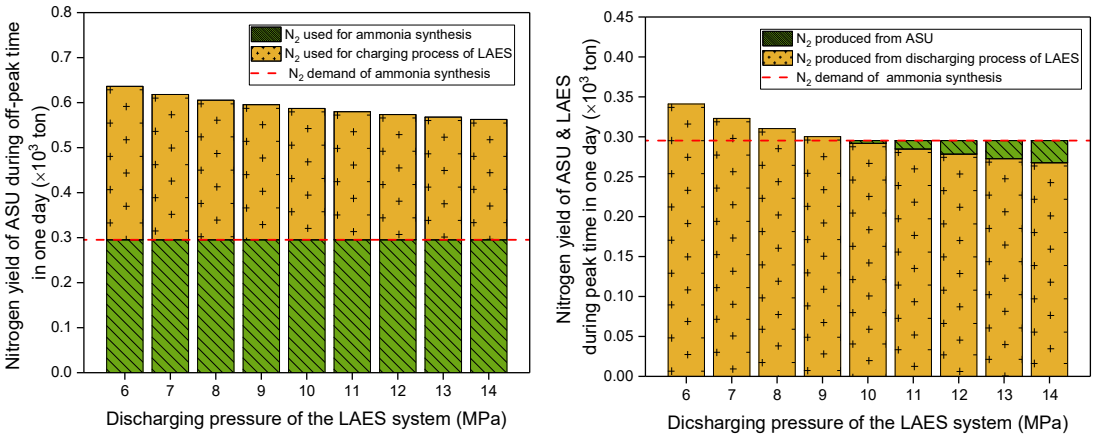

(a) (b)

Figure 7.14 The effect of discharging pressure on (a) the nitrogen consumption by the LAES and NH_3 at off-peak times and (b) the nitrogen production by the LAES and ASU at peak times (charging pressure at 12 MPa).

Figure 7.15 (a) and (b) show the influence of the discharging pressure on the electricity consumption and operation cost of the ASU, respectively. One can see that when the LAES-NH_3 system works under mode (c) (at the discharging pressure of 6-9 MPa), the electricity consumption of the ASU is more than that in the standalone ammonia synthesis system, see Figure 7.15 (a). When the discharging pressure is within the range of 10 to 14 MPa, the LAES-NH3 system works under mode (a), in which the ASU only produces the same amount of nitrogen as the nitrogen demand of the ammonia synthesis loop. Thus, the electricity consumption of the LAES-NH_3 system is the same as that of the standalone ammonia synthesis system. As for the AUS operation cost, the LAES-NH_3 system has a lower ASU operation cost than the standalone ammonia synthesis system within the full range of the researched discharging pressure, as shown in Figure 7.15 (b). The minimum ASU operation cost occurs at the discharging pressure of 9 MPa with a decrease of 38.1%. According to the discussion above, it could be found that the operation mode of the LAES-NH_3 system at the discharging pressure of 9 MPa is the closest to the mode (b), suggesting that the closer the LAES-NH_3 system working mode is to mode (b), the more the ASU operation cost saving could be

obtained. The same result is also observed in the overall ammonia synthesis cost, as shown in Figure 7.16.

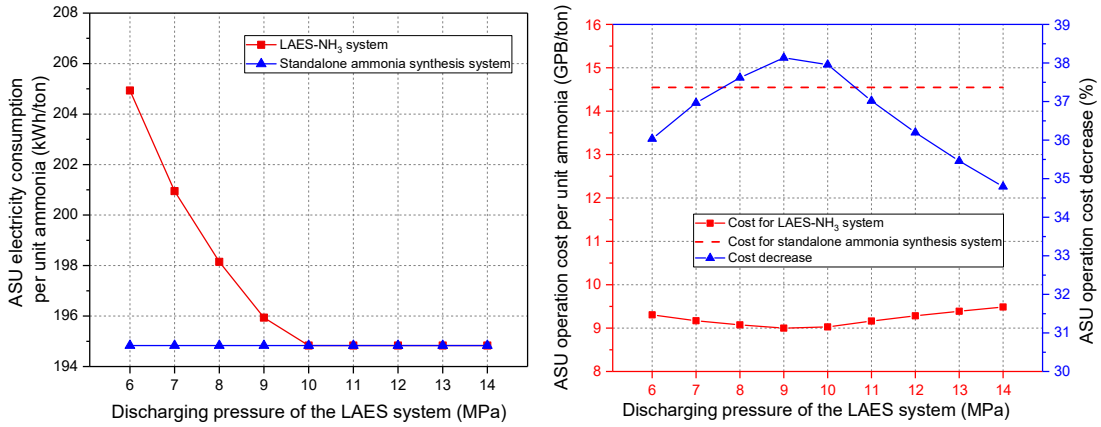

(a) (b)

Figure 7.15 The effect of discharging pressure on the benefits of adding LAES in the ammonia synthesis system: (a) ASU electricity consumption and (b) ASU operation cost (charging pressure at 12 MPa).

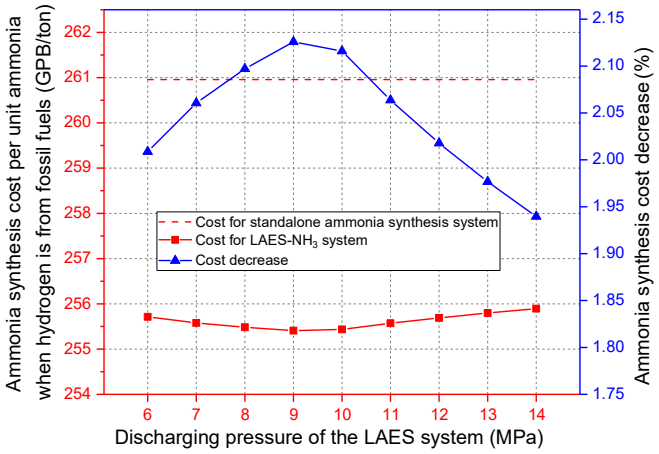

Figure 7.16 The effect of discharging pressure on the overall ammonia synthesis cost (charging pressure at 12 MPa).

7.3.1.4 Effect of the capacity of the LAES on the LAES-NH_3 system

According to the results and discussions above, when the capacity of the LAES is fixed (the inlet nitrogen mass flow rate of the multi-stage compressor is fixed), both the charging and discharging pressure can affect the performance of the LASE-NH_3 system. In this section, a

LAES system with fixed charging pressure and discharging pressure but varying capacity is coupled with the ammonia synthesis sub-system to study the capacity match aspects. 15 MPa and 8 MPa are selected as the charging and discharging pressure of the LAES system, respectively, which leads to a liquid nitrogen yield of 0.882 and a round trip efficiency of 61.18%. Based on these parameters, the inlet nitrogen mass flow rate of the multi-stage compressor is adjusted, making the capacity of this LAES system vary from 5 MWh to 85 MWh.

The effect of the capacity of the LAES on the ASU operation cost is studied, as shown in Figure 7.17. The results indicate that the ASU operation cost of the LAES-NH_3 system decreases first, reaches the minimum value, and then increases with the increasing capacity of the LAES. The LAES-NH_3 system is working under mode (a) when the capacity of the LAES is smaller than 38 MWh. Within this range, increasing the capacity of the LAES can make the nitrogen released from the LAES sub-system approach the peak-time nitrogen demand of the ammonia synthesis sub-system gradually. This means that the working mode of the LAES-NH_3 system is approaching mode (b) gradually, resulting in a decreased ASU operation cost. The LAES-NH_3 system finally reaches mode (b) and obtains the lowest ASU operation cost at the capacity of 38 MWh, at which the nitrogen output of the LAES sub-system during the discharging process can match the peak-time nitrogen demand of the ammonia synthesis sub-system. Then, the LAES-NH_3 enters to mode (c) with further increasing the capacity of the LAES system, which implying more nitrogen from ASU released to the ambient instead of the ammonia synthesis system. Hence, the ASU operation cost increases when the capacity of the LAES is beyond 38 MWh.

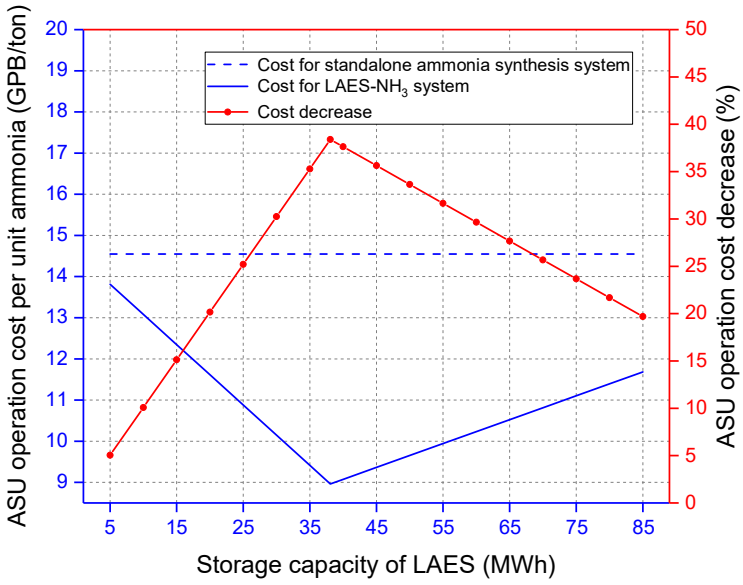

Figure 7.17 The effect of the storage capacity of the LAES on the ASU operation cost.

7.3.1.5 Economic analysis

LAES plant If the investor of the LAES can build a LAES power plant next to an existing ammonia production plant with the proposed configuration, the main benefit is that the initial investment of the LAES power plant can be reduced due to saving the cost of the air pre-purification unit. Figure 7.18 shows the initial investment cost decrease of the LAES power plant co-located with an ammonia synthesis plant with different daily ammonia production yields. One can see that, with the increase of the storage capacity of the LAES, the initial investment cost saving increases and reaches a maximum value of 11.3% at a certain storage capacity, beyond which the initial investment cost decrease ratio keeps constant. The maximum value occurs when the LAES storage capacity and the ammonia synthesis plant size can perfectly match to make the LAES-NH_3 system work under mode (b). Once the maximum value occurs, if the storage capacity of LAES still keeps increasing, the LAES-NH_3 system enters to mode (c), which will not contribute to the initial investment cost decrease ratio any longer. Besides, it can also be found in Figure 7.18 that an ammonia synthesis plant with a larger daily ammonia production needs to match with a LAES power plant with a larger storage capacity to reach working mode (b).

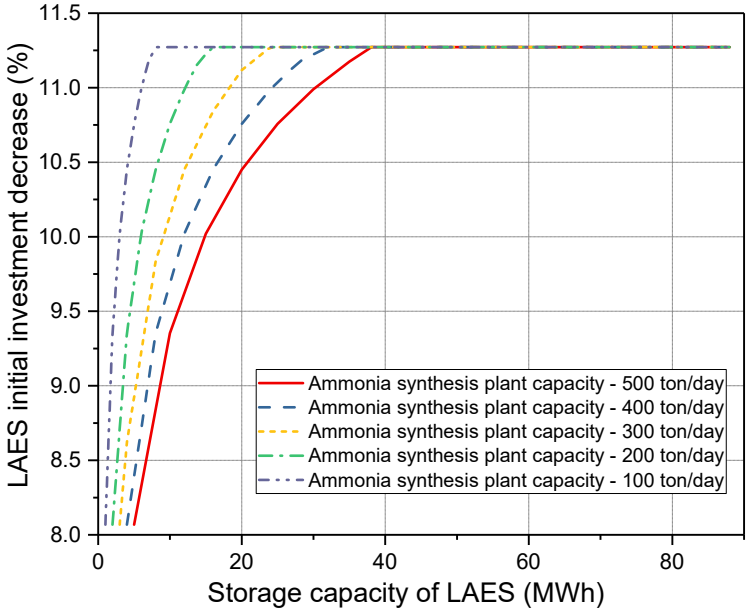

Figure 7.18 Initial investment savings of LAES with different storage capacities integrated with different sizes of ammonia synthesis plants.

Ammonia synthesis plant If an existing ammonia synthesis plant would operate with a LAES power plant together, the capacity of the original ASU unit needs to be increased, which can save the operation cost for the ammonia synthesis plant. The economic analysis needs to be carried out to evaluate if the investment for this ASU expansion can generate effective benefit to the ammonia synthesis plant. Figure 7.19 (a) illustrates the payback period and saving to investment ratio (SIR) of the ASU expansion project for an ammonia synthesis plant with a production capacity of 500 ton/day. One can see that, when the storage capacity of the co-located LAES is equal to or smaller than 38MWh, the LAES-NH_3 system can work under mode (b) or mode (a), which can make the payback period and SIR of the ASU expansion project stabilize at 6.9 years and 2.52, respectively. When the storage capacity of the co-located LAES is larger than 38MWh, the LAES-NH_3 system works under mode (c), indicating that part of the capacity expansion of the ASU will be used to produce nitrogen for the LAES only, which will not be reused in the ammonia synthesis plant. In this scenario, this additional investment cannot benefit the ammonia synthesis plant, leading to an increased payback period and a decreased SIR. When the storage capacity of the co-located LAES is larger than

~60MWh, the value of SIR will be smaller than 1, indicating that the maximal storage capacity of the co-located LAES is 60MWh, beyond which the ASU expansion project will cause an economic loss for the ammonia synthesis plant. Thus, for an ammonia synthesis plant with a 500 ton/day production capacity, a 38MWh LAES power plant is suggested to maximise the benefit for both the LAES and ammonia plant. Figure 7.19 (b) shows the recommended LAES storage capacity and the maximal LAES storage capacity for operating under mode (b) and making SIR equal to 1 respectively, for ammonia synthesis plants with different daily production capacities.

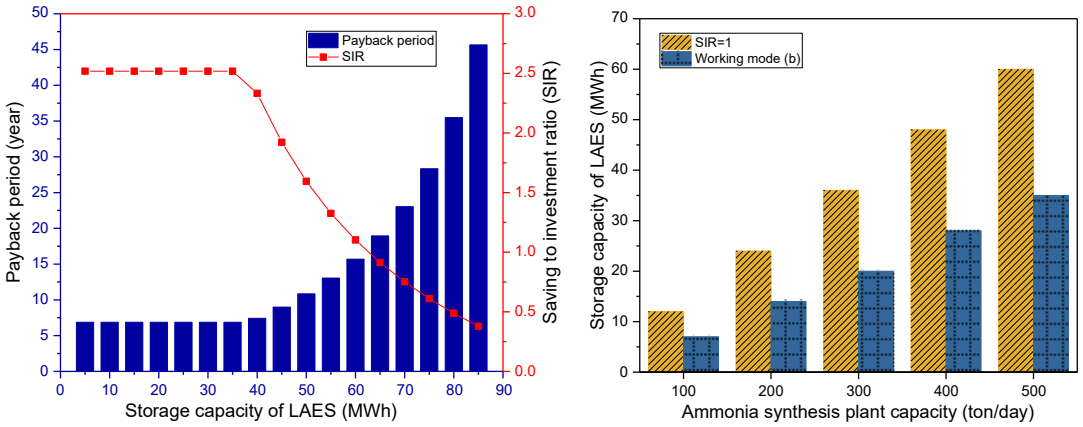

(a) (b)

Figure 7.19 The economic benefits of the ASU scale-up project for ammonia synthesis plant (500 ton/day) (a), and the best LAES storage capacities and the largest LAES storage capacities suggested for different sizes of ammonia synthesis plants (b).

7.3.2 Results and discussion for LAES-AS-NH_3 system

Additional assumptions were made for the simulation and performance analyses, which are summarized as follows:

- Pure propane and methanol are used as the cold storage mediums;
- Dynalene MS-1 is used as the heat transfer and storage medium of the reaction heat;
- Air consists of nitrogen (78.12%), oxygen (20.96%) and argon (0.92%) by volume.

Table 7.3 shows the default parameters of the LAES-AS-NH_3 system. Table 7.4, Table 7.5 and Table 7.6 show the calculated stream parameters of the LAES-AS-NH_3 system under the default working condition shown in Table 7.3, where the charging pressure and discharging pressure are 8 MPa and 10 MPa, respectively.

Table 7.3 Default parameters of the LAES-AS-NH_3 system

	Parameter	Value	Unit
LAES-AS System	Ambient temperature	293	K
	Ambient pressure	100	kPa
	Propane#1 temperature	105.59	K
	Propane#2 temperature	214	K
	Methanol temperature	293	K
	Minimum Approach Temperature in heater	5	K
	Minimum Approach Temperature in cooler	2	K
	Minimum Approach Temperature in cold box	5	K
	Minimum Approach Temperature in evaporator	2	K
	Number of stages in distillation column	46	
	Working pressure of the distillation column	0.5	MPa
	Relative pressure drop of heat exchangers	1%	
	Isentropic efficiency of compressor	85%	
	Isentropic efficiency of turbine	90%	
	Isentropic efficiency of cryo-turbine	75%	
	Isentropic efficiency of cryo-pump	75%	
	Working hours of charging and discharging per day	8	hour/day
Ammonia synthesis process	Product yield of Ammonia	50	ton/day
	Reaction pressure	15	MPa
	Oxygen volume concentration requirement in nitrogen [194]	10	ppm
	Reaction temperature range	673.15-773.15	K
	Purge fraction	50%	
	Hydrogen membrane recovery	85%	
	Other gas membrane recovery	10%	
	Ammonia recovery	92%	
	Minimum Approach Temperature in Condenser#1	2	K
	Molten salt temperature	663	K
	Isentropic efficiency of compressor	85%	
	Isentropic efficiency of steam turbine	90%	
	Energy consumption of hydrogen [181]	53.15	kWh/kg

Higher heating value of ammonia	$22.5 \cdot 10^6$	kJ/ton
Combustion efficiency of ammonia [192]	53%	

Table 7.4 Stream data for the LAES-AS system

State	Pressure (MPa)	Temperature (K)	Mass flow rate (kg/s)	Working fluid	Oxygen content (vol%)	Working hours per day (hour)
1	0.10	293.15	14.87	Air	20.9600%	8
2	0.43	470.45	14.87	Air	20.9600%	8
3	0.43	303.15	14.87	Air	20.9600%	8
4	1.84	486.59	14.87	Air	20.9600%	8
5	1.82	303.15	14.87	Air	20.9600%	8
6	7.84	488.04	14.87	Air	20.9600%	8
7	7.76	303.15	14.87	Air	20.9600%	8
8	7.68	138.49	14.87	Air	20.9600%	8
9	0.50	96.84	14.87	Air	20.9600%	8
10	0.50	96.13	8.37	Air	20.9600%	8
11	0.50	98.39	6.50	Air	20.9600%	8
12	0.10	81.02	11.79	Air	26.6844%	8
13	0.10	82.56	7.72	Air	26.6844%	8
14	0.10	288.48	7.72	Air	26.6844%	8
15	0.10	79.29	4.08	Air	26.6844%	8
16	0.50	94.00	3.07	Nitrogen	0.00096%	8
17	0.50	94.00	1.02	Nitrogen	0.00096%	24
18	15.31	103.49	1.02	Nitrogen	0.00096%	24
19	15.15	212.00	1.02	Nitrogen	0.00096%	24
20	15.00	291.15	1.02	Nitrogen	0.00096%	24
21	0.10	79.29	4.08	Air	26.6844%	8
22	10.00	83.51	4.08	Air	26.6844%	8
23	9.90	103.50	4.08	Air	26.6844%	8
24	9.80	200.00	4.08	Air	26.6844%	8
25	9.70	291.15	4.08	Air	26.6844%	8
26	9.61	502.41	4.08	Air	26.6844%	8
27	9.51	755.22	4.08	Air	26.6844%	8
28	2.05	523.55	4.08	Air	26.6844%	8
29	2.03	755.22	4.08	Air	26.6844%	8
30	0.44	524.24	4.08	Air	26.6844%	8
31	0.43	755.22	4.08	Air	26.6844%	8
32	0.09	524.42	4.08	Air	26.6844%	8
33	0.09	296.25	4.08	Air	26.6844%	8

Table 7.5 Stream data for the ammonia synthesis system

State	Pressure (MPa)	Temperature (K)	Nitrogen (kg/s)	Hydrogen (kg/s)	Ammonia (kg/s)	Argon (kg/s)	Total (kg/s)	Working hours per day (hour)
N1	0.10	293.15	0.00	0.13	0.00	0.00E+00	0.13	24
N2	0.53	503.96	0.00	0.13	0.00	0.00E+00	0.13	24
N3	0.53	303.15	0.00	0.13	0.00	0.00E+00	0.13	24
N4	2.82	521.03	0.00	0.13	0.00	0.00E+00	0.13	24
N5	2.82	303.15	0.00	0.13	0.00	0.00E+00	0.13	24
N6	15.00	520.97	0.06	0.23	0.00	9.13E-06	0.29	24
N7	15.00	303.15	0.06	0.23	0.00	9.13E-06	0.29	24
N8	15.00	291.15	1.02	0.00	0.00	8.22E-05	1.03	24
N9	15.00	297.17	1.67	0.36	0.03	1.83E-04	2.06	24
N10	15.00	673.15	1.67	0.36	0.03	1.83E-04	2.06	24
N11	15.00	771.85	1.49	0.32	0.25	1.83E-04	2.06	24
N12	15.00	673.15	1.49	0.32	0.25	1.83E-04	2.06	24
N13	15.00	772.83	1.30	0.28	0.48	1.83E-04	2.06	24
N14	15.00	673.15	1.30	0.28	0.48	1.83E-04	2.06	24
N15	15.00	739.94	1.17	0.25	0.63	1.83E-04	2.06	24
N16	15.00	676.99	1.17	0.25	0.63	1.83E-04	2.06	24
N17	15.00	353.95	1.17	0.25	0.63	1.83E-04	2.06	24
N18	15.00	293.15	1.17	0.25	0.63	1.83E-04	2.06	24
N19	15.00	293.15	0.00	0.00	0.58	0.00E+00	0.58	24
N20	15.00	293.15	1.17	0.25	0.05	1.83E-04	1.48	24
N21	15.00	293.15	0.59	0.13	0.03	9.13E-05	0.74	24
N22	15.00	293.15	0.59	0.13	0.03	9.13E-05	0.74	24
N23	2.82	293.15	0.06	0.11	0.00	9.13E-06	0.17	24
N24	15.00	293.15	0.53	0.02	0.02	8.22E-05	0.57	24
N25	1.60	294.64	0.00	0.00	0.58	0.00E+00	0.58	24

Table 7.6 Stream data for molten salt, propane, and methanol

	State	Pressure (MPa)	Temperature (K)	Mass flow rate (kg/s)	Working fluid	Working hours per day (hour)
Heat storage	H1	0.1	663.00	12.96	Molten salt	24
	H2	0.1	769.79	4.48	Molten salt	24
	H3	0.1	770.77	4.45	Molten salt	24
	H4	0.1	737.88	4.03	Molten salt	24
Heat utilization	H5	0.1	760.22	22.09	Molten salt	8
	H6	0.1	663.00	7.90	Molten salt	8

	H7	0.1	663.00	7.12	Molten salt	8
	H8	0.1	663.00	7.07	Molten salt	8
Cold storage	C7	0.1	105.59	3.98	Propane	8
	C8	0.1	85.60	3.98	Propane	8
	C9	0.1	214.00	4.11	Propane	8
	C10	0.1	105.60	4.11	Propane	8
	C11	0.1	293.15	2.32	Methanol	8
	C12	0.1	202.10	2.32	Methanol	8
	C13	0.1	214.00	1.03	Propane	24
	C14	0.1	105.59	1.03	Propane	24
	C15	0.1	293.15	0.62	Methanol	24
	C16	0.1	214.10	0.62	Methanol	24
Cold utilization	C1	0.1	85.60	3.98	Propane	8
	C2	0.1	105.59	3.98	Propane	8
	C3	0.1	105.60	7.19	Propane	8
	C4	0.1	214.00	7.19	Propane	8
	C5	0.1	207.48	4.19	Methanol	8
	C6	0.1	293.15	4.19	Methanol	8

7.3.2.1 Working performance of the distillation column

The distillation column is the most important part of the proposed LAES-AS sub-system, which determines the amount and the purity of the liquid nitrogen. Thus, the working performance of the distillation column is studied first.

The liquid fraction of the feedstock (m_{10}/m_9) impacts the performance of the distillation column strongly. As shown in Figure 7.20, with more liquid fed into the distillation column, the total cooling capacity inside the distillation column increases, leading to an increased total liquid yield (the sum of liquid air and liquid nitrogen). For the liquid nitrogen yield, it reaches a peak when the liquid fraction of the feedstock equals to 0.3 (m_{10}/m_9=0.3). This is because when the m_{10}/m_9 is small, more gaseous air is fed into the distillation column from the bottom stage, which is good for the yield of the high-purity nitrogen at the top stage. One can see from the Figure 7.21 that, with decreasing m_{10}/m_9, more liquid nitrogen (yellow bar + green bar) can be obtained, and less residual oxygen is left in the nitrogen. However, the decreasing m_{10}/m_9 also

leads to the shortage of the cooling capacity in the distillation column, making more liquid nitrogen have to return to the distillation column as the liquid reflux. Thus, the highest liquid nitrogen yield is a balance between the purity and the cooling capacity.

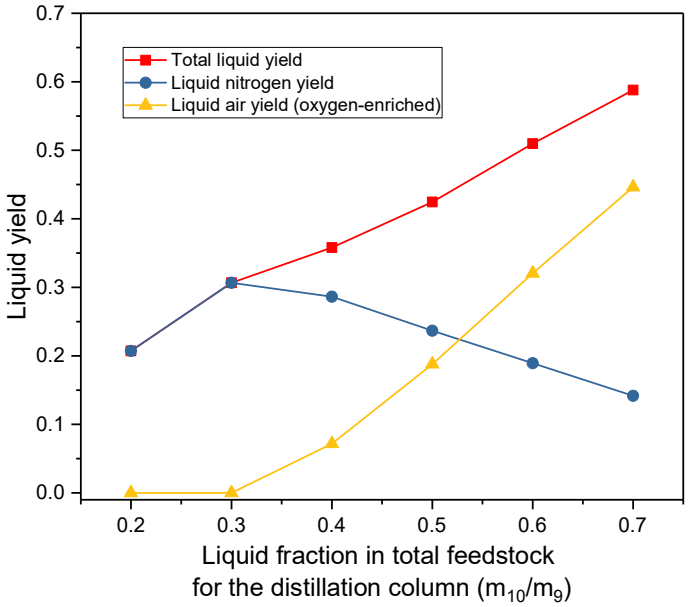

Figure 7.20 The effect of liquid fraction in total feedstock for the distillation on liquid yield

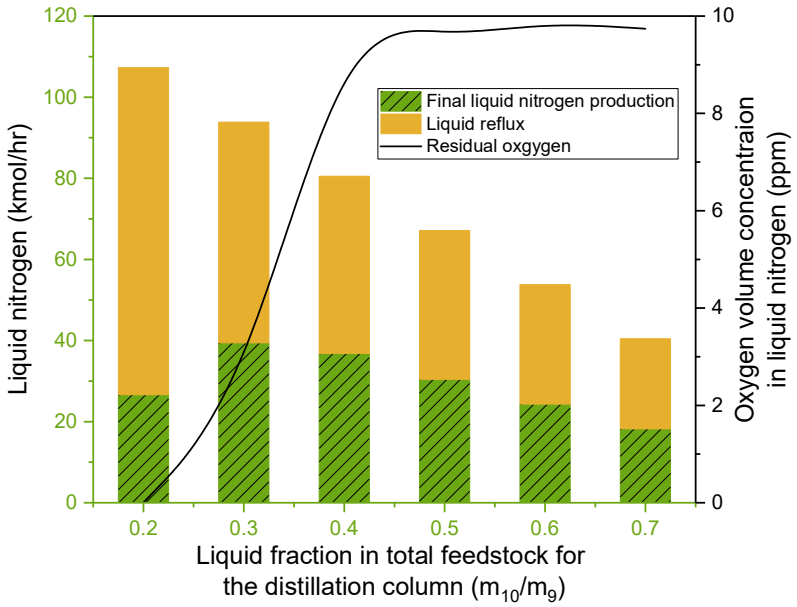

Figure 7.21 The effect of liquid fraction in total feedstock for the distillation on nitrogen purity and nitrogen production (total feedstock=1kg/s).

7.3.2.2 Effect of the charging pressure of the LAES-AS-NH_3 system

The charging pressure of the LAES-AS sub-system is a very important parameter, which can affect the overall performance of the LAES-AS sub-system. Thus, in this section, the discharging pressure is fixed at 10 MPa to study the effect of the charging pressure.

The increasing charging pressure of the LAES-AS sub-system can increase the liquid fraction of the feedstock (m_{10}/m_9) for the distillation column, as shown in Figure 7.22. Thus, with the increasing charging pressure, the total liquid yield of the LAES-AS sub-system is enhanced. When the charging pressure is at 4 MPa, the liquid fraction of the feedstock is very close to 0.3 (m_{10}/m_9=0.3), at which the liquid nitrogen yield of the LAES-AS sub-system can reach the peak value of 0.322. However, due to the insufficient cooling capacity of the distillation column, there is no liquid air can be obtained when the charging pressure is lower than 4 MPa (Noted: two-stage compression is employed when the charging pressure is lower than 4 MPa).

The effect of the charging pressure on the specific power consumption of the charging process is also studied, as shown in Figure 7.23. With the increasing charging pressure, both the specific power consumptions to produce 1kg liquid product and 1kg liquid air show a declining trend.

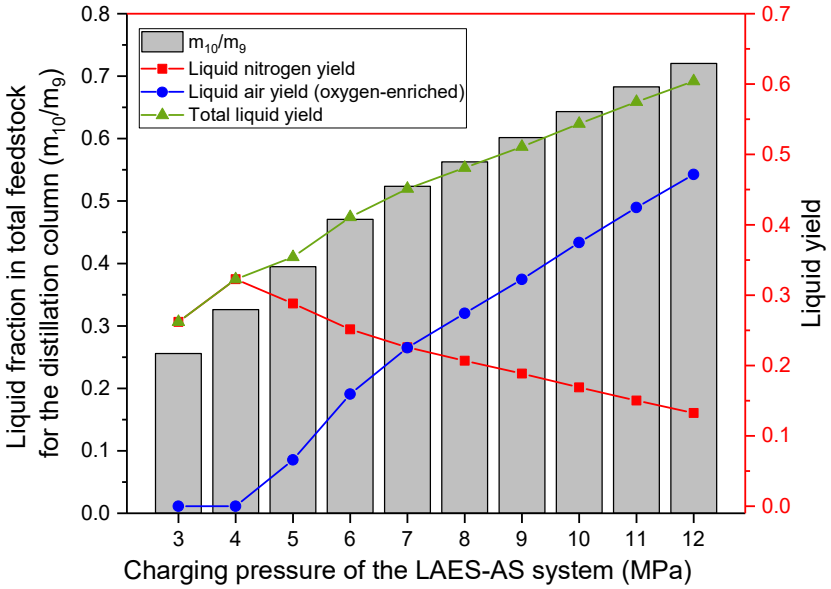

Figure 7.22 The effect of charging pressure on the liquid yield of the LAES-AS sub-system (discharging pressure at 10 MPa).

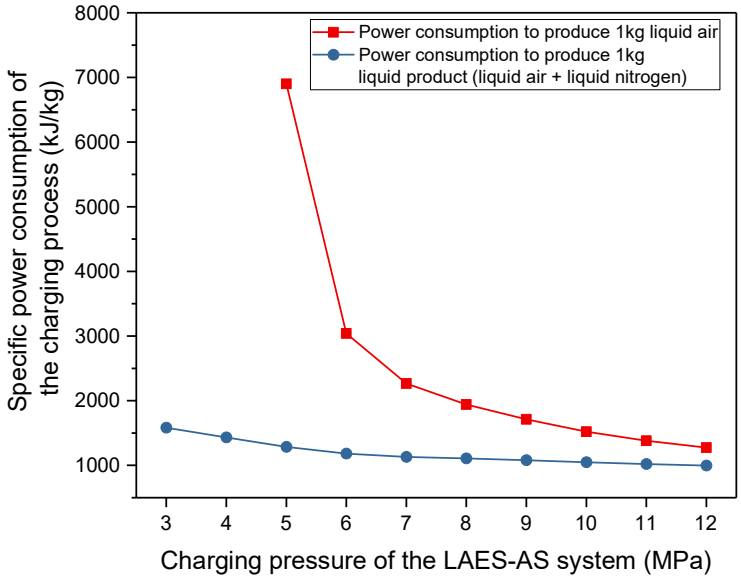

Figure 7.23 The effect of charging pressure on the specific power consumption of the LAES-AS charging process (discharging pressure at 10 MPa).

In the baseline LAES system, the charging pressure usually has very limited influence on the specific power generation of the discharging process. However, the LAES-AS sub-system shows a different result. As presented in Figure 7.24 (a), when the charging pressure is lower than 4 MPa, the specific power generation is zero because there is no stored liquid air used for

power generation in the LAES-AS sub-system. When the charging pressure is in the range of 5 to 10 MPa, the specific power generation keeps constant, beyond which the specific power generation starts to decrease significantly. This is because when the charging pressure is within the range of 5-10 MPa, the waste reaction heat stored in the molten salt is more than the heat demand of the discharging process of the LAES-AS sub-system for air superheating use. In this way, the air temperature at the inlet of turbines during the discharging process can always be heated to the highest temperature of 755 K (see Figure 7.24 (b)). Thus, the change of the charging pressure within 5-10 MPa does not affect the specific power generation of the discharging process. However, when the charging pressure is higher than 10 MPa, the reaction heat released from the ammonia synthesis process is insufficient for the discharging process, leading to a decreased air temperature at the inlet of turbines during the discharging process (see Figure 7.24 (b)), hence a decreased specific power generation.

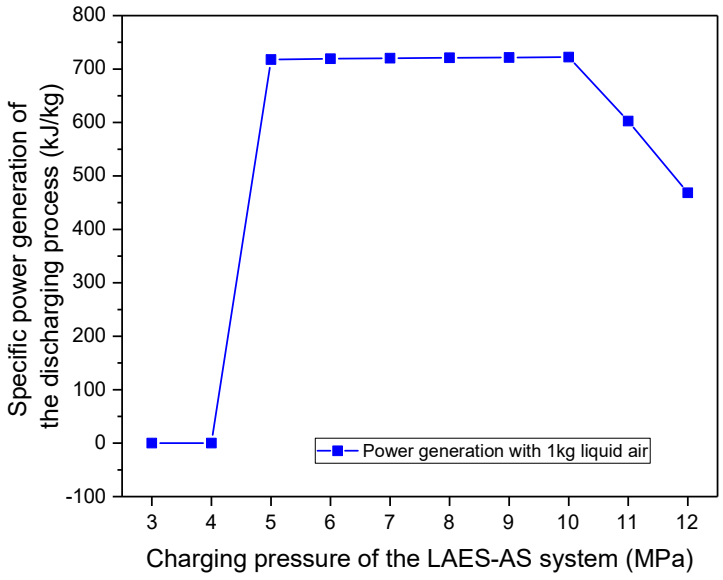

(a)

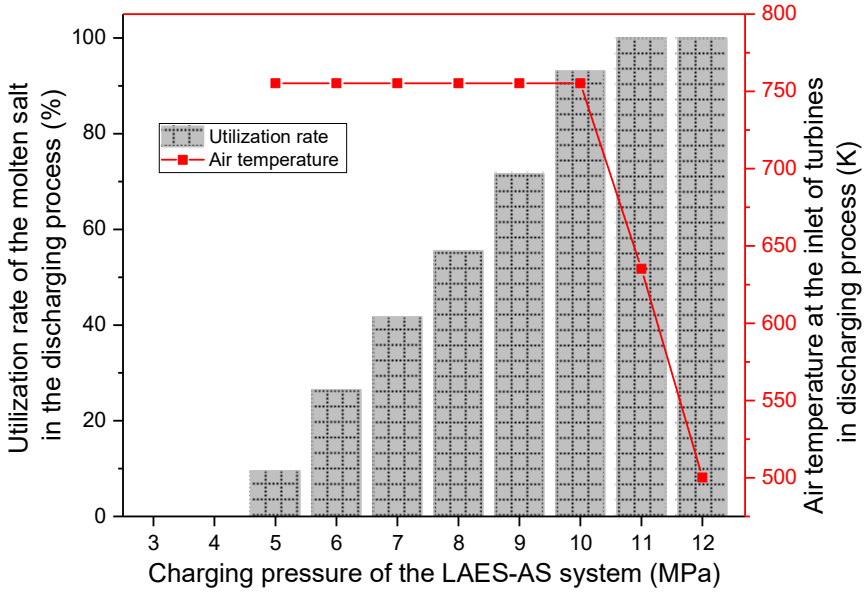

(b)

Figure 7.24 Effects of charging pressure on (a) the specific power generation of the LAES-AS discharging process, and (b) the molten salt utilization rate and the air superheating temperature (discharging pressure at 10 MPa).

The maximum round trip efficiency (47.51%) of the LAES-AS sub-system occurs at the charging pressure of 10 MPa due to the variations of the specific power consumption of the charging process and the specific power generation of the discharging process, as shown in Figure 7.25. One can see that the nominal round trip efficiency of the LAES-AS sub-system is much higher than the round trip efficiency due to the electricity saving of the ammonia synthesis process. The electricity consumption of the ammonia synthesis process can be reduced by 31.6%, i.e., 713 kJ when 1kg nitrogen fed into the ammonia synthesis process (see Figure 7.26). As a result, the maximum nominal round trip efficiency is 68.63%, which also occurs at the charging pressure of 10 MPa.

The *P2A2P* efficiency of the whole LAES-AS-NH_3 system is studied, which is shown in Figure 7.27. It can be seen that the highest *P2A2P* efficiency (29.5%) occurs at the charging pressure of 10 MPa, which is 12.2% higher than the *P2A2P* efficiency of the standalone ammonia synthesis system (26.27%).

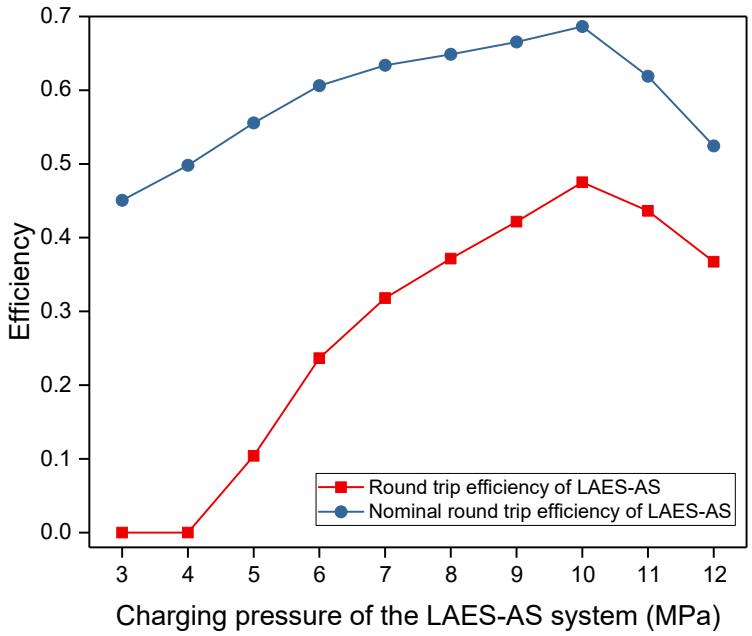

Figure 7.25 Effects of charging pressure on the round trip efficiency and the nominal round trip efficiency of the LAES-AS system (discharging pressure at 10 MPa).

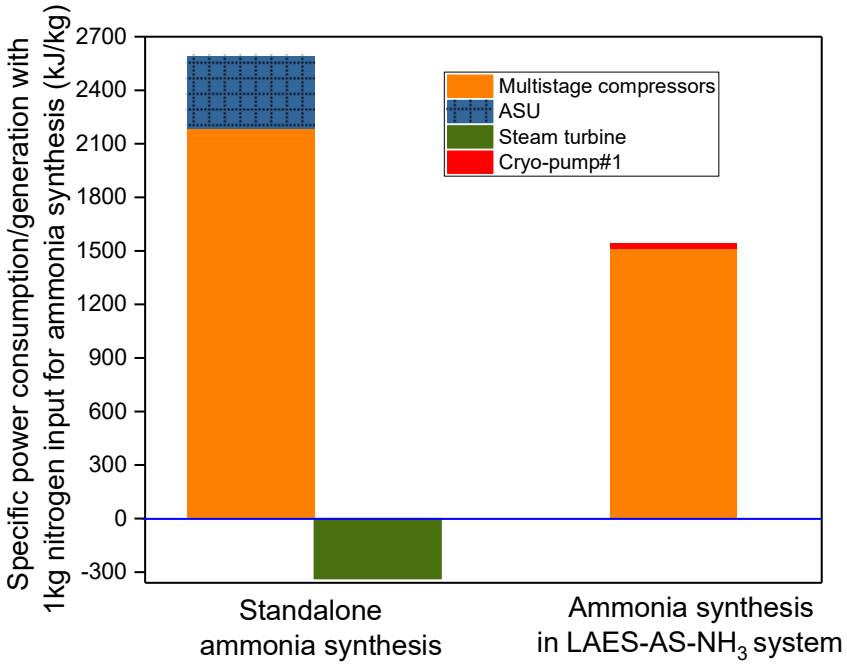

Figure 7.26 Electricity consumptions of the standalone ammonia synthesis system and the ammonia synthesis system in the LAES-AS-NH_3 (negative value implies power generation; the energy consumption of the hydrogen production is excluded).

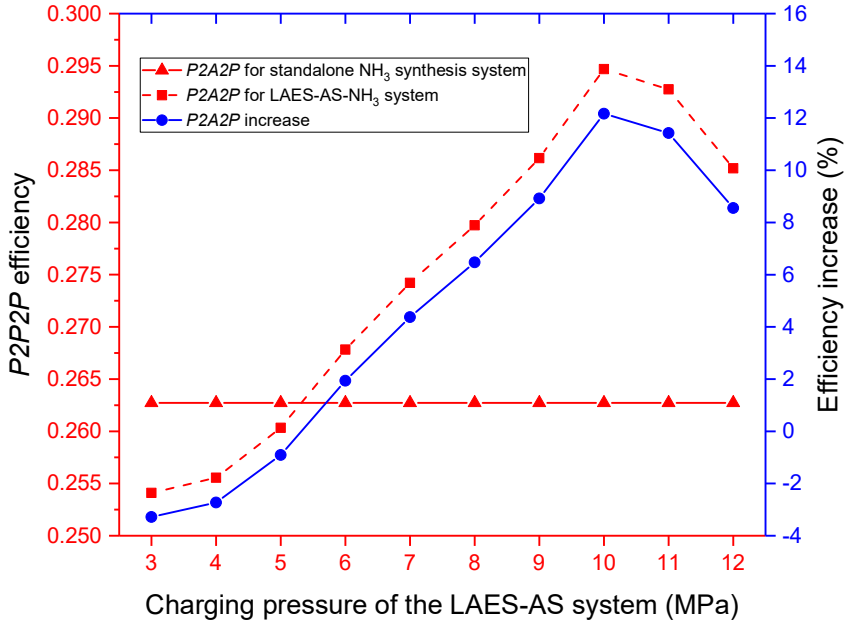

Figure 7.27 The effect of charging pressure on the *P2A2P* efficiency of the LAES-AS-NH_3 system (discharging pressure at 10 MPa).

7.3.2.3 Effect of the discharging pressure of the LAES-AS-NH_3 system

In this section, the charging pressure is fixed at 10 MPa to study the influence of the discharging pressure. The increase of the discharging pressure can result in the decrease of the stored cryogenic energy, which would reduce the liquid fraction of the feedstock (m_{10}/m_9) for the distillation column (see Figure 7.28). Therefore, with the increasing discharging pressure, the total liquid yield of the LAES-AS sub-system decreases, while the liquid nitrogen yield increases. As a result, both the specific power consumptions to produce 1kg liquid product and 1kg liquid air show increasing trends as the discharging pressure increases, as shown in Figure 7.29.

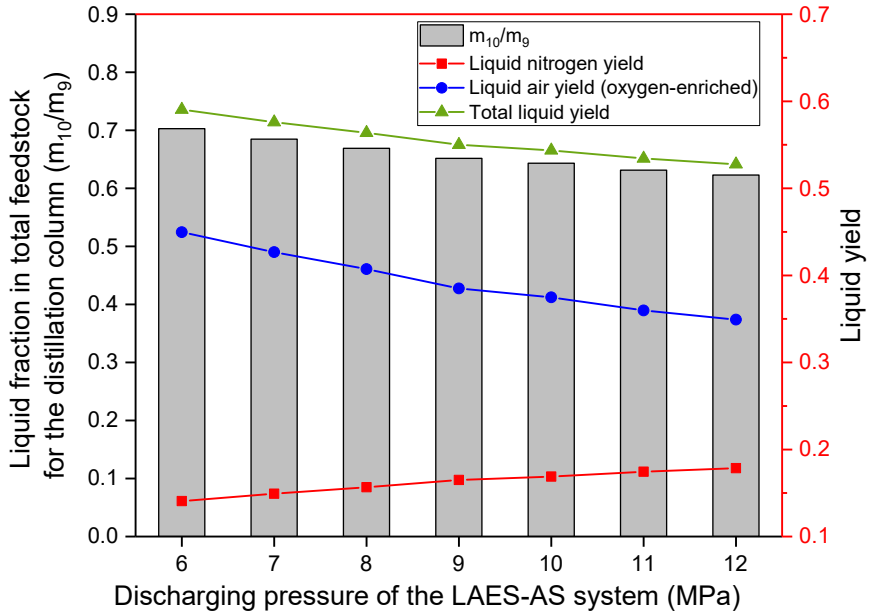

Figure 7.28 The effect of discharging pressure on the liquid yield of the LAES-AS sub-system (charging pressure at 10 MPa).

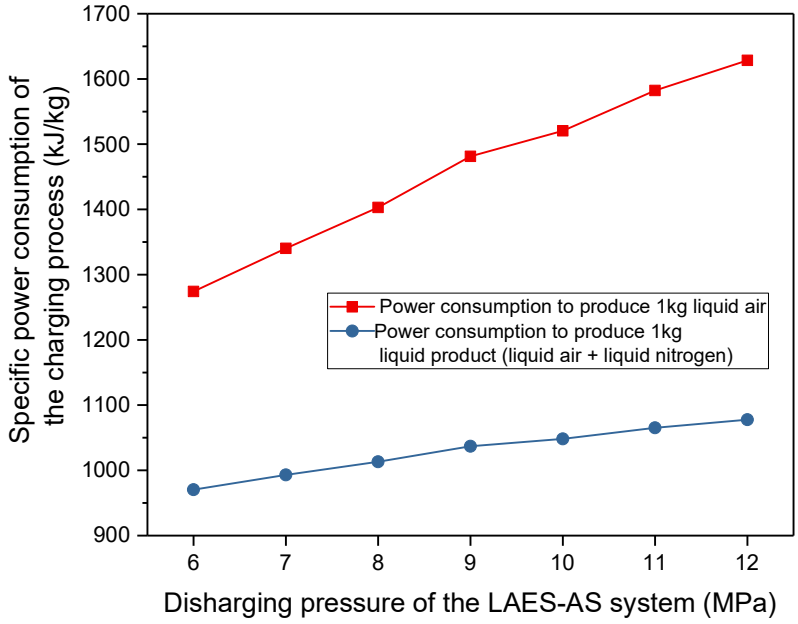

Figure 7.29 The effect of discharging pressure on the specific power consumption of the LAES-AS charging process (charging pressure at 10 MPa).

It is certain that the increase of the discharging pressure can improve the specific power generation of the LAES-AS discharging process, as shown in Figure 7.30 (a). However, it can

also be seen that when the discharging pressure is increased from 6 to 9 MPa, the increase in the specific power generation is more significant than that when the discharging pressure is increased from 9 to 12 MPa. The reason is that when the discharging pressure is lower than 9 MPa, the waste reaction heat from the ammonia synthesis process is not sufficient for the discharging process of the LAES-AS sub-system. With the increase of the discharging pressure from 6-9 MPa, the air temperature before expansion in turbines increases because of the increase of the molten salt (waste heat), as shown in Figure 7.30 (b). Thus, both the air pressure and air temperature before expansion is improved when the discharging pressure is increased from 6 to 9 MPa, leading to a very significant increase in the specific power generation of the LAES-AS sub-system. However, when the discharging pressure is higher than 9 MPa, the waste reaction heat is more than enough to superheat the air temperature before expansion to the highest value (755 K), as shown in Figure 7.30 (b). Thus, when the discharging pressure is increased from 9 to 12 MPa, only the increased air pressure contributes to the enhancement of the specific power generation of the LAES-AS sub-system, resulting in a lower increasing rate.

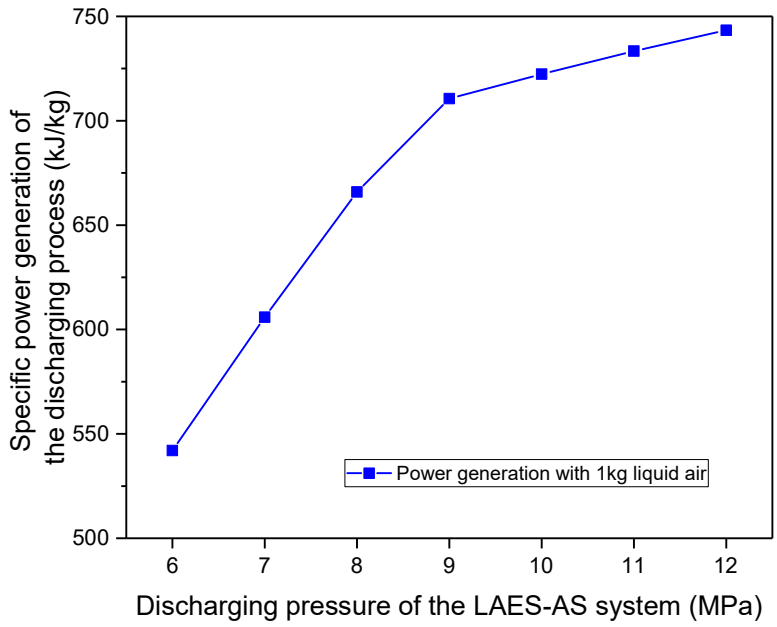

(a)

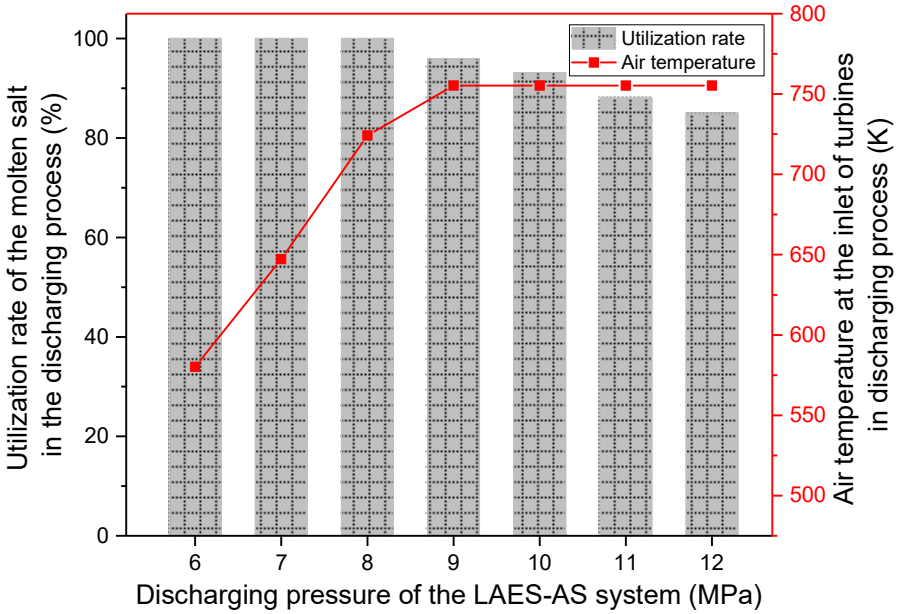

(b)

Figure 7.30 Effects of discharging pressure on (a) the specific power generation of the LAES-AS discharging process, and (b) the molten salt utilization rate and the air superheating temperature (charging pressure at 10 MPa).

The highest round trip efficiency (47.97%) and the highest nominal round trip efficiency (68.63%) of the LAES-AS system can be realized when the discharging pressure is 9 MPa and 10 MPa, respectively, as presented in Figure 7.31. Figure 7.32 shows the comparison of the *P2A2P* efficiency between the standalone ammonia synthesis system and the LAES-AS-NH_3 system. It can be found that the *P2A2P* efficiency of the LAES-AS-NH_3 system is always higher than that of the standalone ammonia synthesis system within the discharging pressure of 6-12 MPa, with a maximum value of 29.63% occurred at 8 MPa.

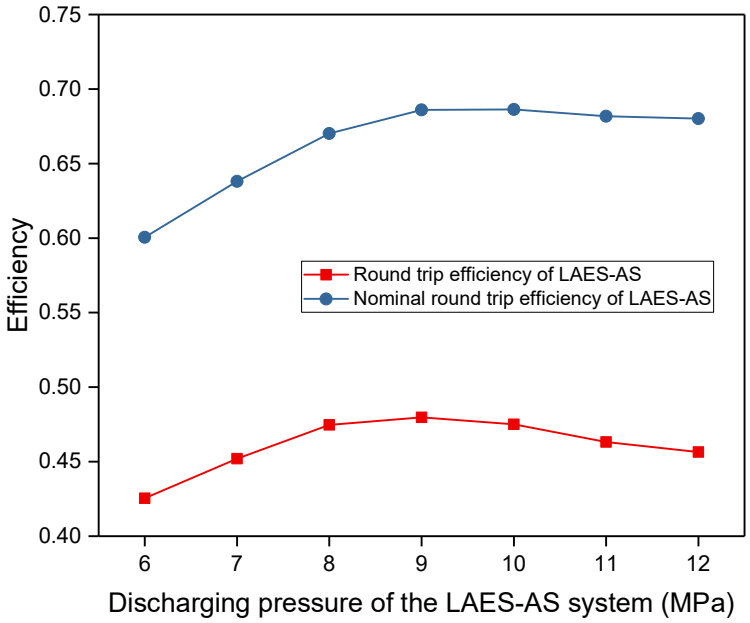

Figure 7.31 Effects of discharging pressure on the round trip efficiency and the nominal round trip efficiency of the LAES-AS system (charging pressure at 10 MPa).

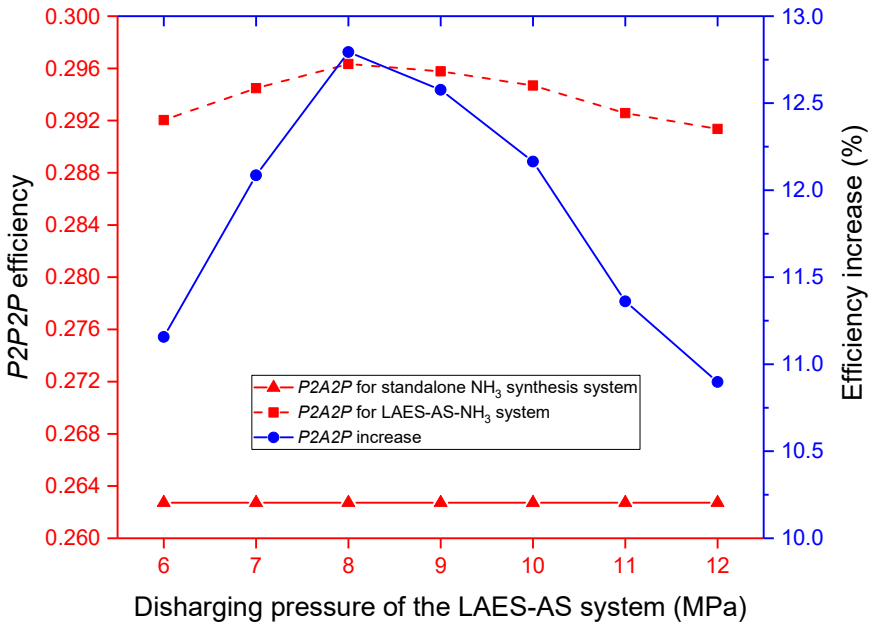

Figure 7.32 The effect of discharging pressure on the *P2A2P* efficiency of the LAES-AS-NH_3 system (charging pressure at 10 MPa).

7.4 Concussions of Chapter 7

This chapter investigates the integration of the LAES system with the ammonia synthesis system. Two integrated systems, LAES-NH_3 and LAES-AS-NH_3, are proposed and investigated. The main conclusions are as follows:

7.4.1 LAES-NH_3 system

- The LAES-NH_3 system is proposed for the existing ammonia production plant due to little modifications needed for the ammonia synthesis sub-system.
- Three working modes are identified for this LAES-NH_3 system, distinguished by the nitrogen amount matching between the LAES sub-system and the ammonia synthesis sub-system. Among them, working mode (b), in which the LAES system as the nitrogen buffer for the ammonia synthesis process, can store and release the same amount of nitrogen to meet the peak-time nitrogen demand of the ammonia synthesis sub-system, has the highest operation cost saving for the ammonia synthesis process.
- The charging pressure, discharging pressure and the storage capacity of the LAES sub-system are optimized to make the LAES-NH_3 system works under mode (b). In this way, the LAES-NH_3 system can work with the lowest ASU operation cost, which is ~38% lower than that of the standalone ammonia synthesis system.
- For an ammonia synthesis plant with 500 ton/day ammonia production, a LAES system with 38MWh storage capacity is suggested, providing the best match to make the LAES-NH_3 system operate under mode (b). This also helps to reduce the LAES initial investment cost by 11.3% and shorten the payback period of the ASU capacity expansion project to 6.9 years. There is also a maximal storage capacity of the LAES of ~60MWh in the LAES-NH_3 system, beyond which, ammonia synthesis plant side will show an economic loss.

7.4.2 LAES-AS-NH_3 system

- The LAES-AS-NH_3 system is proposed for new ammonia production plants because the conventional ammonia synthesis process needs to be modified for integration with the

LAES-AS sub-system. Besides, the operation of the ammonia synthesis sub-system and the LAES-AS sub-system are highly coupled with each other, which implies either of them cannot work alone.

- The liquid nitrogen yield of the LAES-AS sub-system has a maximum value of ~0.3 when the liquid fraction of the feedstock for the distillation column is 0.3. However, the total liquid yield (liquid nitrogen and liquid air) can keep increasing with the increasing liquid fraction of the feedstock for the distillation column. Both the increase of the charging pressure and the decrease of the discharging pressure can improve the liquid fraction of the feedstock for the distillation column, improving the total liquid yield of the LAES-AS sub-system.
- The LAES-AS sub-system shows a maximum round trip efficiency of ~48%. Besides, the LAES-AS sub-system can help the ammonia synthesis sub-system to save the electricity consumption of 713 kJ (with 1kg liquid nitrogen input), which accounts for 31.6% of the total electricity consumption. In this way, the nominal round trip efficiency of the LAES-AS sub-system can reach ~69%.
- The highest Power-to-Ammonia-to-Power (*P2A2P*) efficiency (i.e., the round trip efficiency of the overall LAES-AS-NH_3 system) can be as high as ~30%, which is almost 13% higher than that of the standalone ammonia synthesis system.

Chapter 8 Conclusions and Recommendations for Further Research

This chapter summarized the main conclusions of this Ph.D. study, based on which, recommendations for future work are proposed.

8.1 Summary of the main conclusions

This work focuses on three technical aspects of the liquid air energy storage technology:

(1) The development of flexible and effective methods to utilize the excess compression heat of the LAES system.
(2) The development of a cost-effective method for the recovery of the cryogenic energy in the discharging process of a decoupled LAES system.
(3) The integration of the LAES with industrial processes, including LNG regasification process and the ammonia synthesis process.

The main conclusions are as follows:

(1) The power plant based on the waste energy recovery from both the LAES and LNG can achieve the maximum thermal efficiencies of 27% and 28% and exergy efficiencies of 40% and 32% for nitrogen and argon, respectively. Here, with the nitrogen as working fluid undergoes a complete Brayton Cycle, while the argon based power plant goes through a combined Brayton and Rankine Cycle. The payback period of this proposed power plant which is co-located with a 5MW/40MWh LAES system is as short as ~2.2 years. The findings suggest that a waste energy based power plant can be co-located with a LNG terminal and a LAES plant to provide additional power output and reduce energy waste.
(2) A standalone LAES for electricity supply only (baseline LAES) can achieve an electrical round trip efficiency above 60% at a high charging pressure of 19 MPa. However, if the excess heat is considered, the performance of the baseline LAES can give a high exergy

efficiency (i.e., maximum electrical round trip efficiency) even at a low charging pressure, with the local maximum of 62% achieved at ~4 MPa.

(3) The proposed standalone LAES system for combined cooling, heating, hot water, and electricity supply can achieve a high nominal electrical round trip efficiency between 52% and 76%, with the maximum at a charging pressure of ~5 MPa. For a given size of a LAES system (8MWh), the primary energy savings and avoided carbon dioxide emissions are up to 12.1 MWh and 2.3 ton per day, respectively. These new findings suggest, for the first time, that small-scale LAES systems can be best operated at lower charging pressures and the technologies have a great potential for applications in local decentralized micro energy grids.

(4) The proposed Cryo-TEG has a thermal efficiency of ~9%, which is much lower than the Cryo-RC (~39.5%). However, the Cryo-TEG gives a much better economic performance, especially as the cooling capacity of liquid nitrogen is below 8.6 MW: the levelized cost of electricity (LCOE) of the Cryo-TEG is as low as 0.0218 $/kWh, ~4 times cheaper than that of the Cryo-RC. This indicates that the Cryo-TEG is more favourable for cryogenic energy recovery in the small-scale decoupled LAES. With the Cryo-TEG, the decoupled LAES systems can achieve an electrical round trip efficiency of ~29% and a combined cooling and power efficiency of ~50%.

(5) In the proposed LAES-NH_3 system, there is no requirement to change the original configuration of the ammonia synthesis process except for increasing the capacity of the ASU. Thus, this integration of the LAES with the ammonia synthesis system is more suitable for an existing ammonia production plant. To save the operation cost of the ammonia synthesis process to the maximum extent, the nitrogen released from the LAES discharging process needs to be the same as the peak-time nitrogen demand of the ammonia synthesis sub-system (i.e., working mode (b)). In this way, the operation cost of the ASU can be saved by ~38%.

(6) For an ammonia synthesis system with 500 ton/day ammonia production, a LAES system with a storage capacity of 38 MWh can make the LAES-NH_3 system operate under mode

(b). As a result, the capital cost of the LAES is reduced by ~11.3% and the payback period of the ASU capacity expansion of the ammonia plant is ~6.9 years.

(7) The proposed LAES-AS-NH_3 system is more suitable for a new ammonia production plant. In this way, the LAES-AS sub-system acts as an energy storage system with the air separation function to produce pure nitrogen for the ammonia synthesis sub-system. The maximum nominal round trip efficiency of the LAES-AS sub-system is as high as ~69%. The electricity consumption of the ammonia synthesis sub-system can be decreased by ~31.6%. The LAES-AS-NH_3 system can achieve the highest overall round trip efficiency (i.e., *P2A2P*) of ~30%, which is 13% higher than that of the standalone ammonia synthesis system.

8.2 Recommendations for the future research

Based on the results of this Ph.D. study, the following are recommended:

(1) Dynamic modelling of the LAES system is suggested, especially for the study on the integration of the LAES with power grids (national transmission grids and local distribution), renewable and conventional (thermal and nuclear) power plants and local energy networks.

(2) The decoupled LAES work only scratches the surface. A more comprehensive study on a complete system including the charging process, storage, transport process, and discharging process is recommended.

(3) The integration of the LAES with different industrial processes is mostly in the theoretical research stage. Small-scale experimental studies and large-scale demonstrations are recommended.

(4) To extend the application scope of the LAES, more services that the LAES can provide to the grid (e.g., black start) and more integrations of the LAES with conventional power generation methods (e.g., gas turbine) are recommended to be studied both theoretically and experimentally.

Appendix A Thermodynamic model for the ammonia synthesis system

The feed nitrogen and hydrogen for the ammonia synthesis process need to be compressed to 15 MPa by the multi-stage compressors, where a stream of recycle gas from the hydrogen membrane is mixed with the feed gas before entering the third-stage compressor. The gross power consumption of the multi-stage compressors, $W_{HB,com}$, could be calculated as follows:

$$W_{HB,com} = m_{HB,in} \cdot ((h_{N3} - h_{N2}) + (h_{N5} - h_{N4})) + (m_{HB,in} + m_{N23}) \cdot (h_{N7} - h_{N6}) \quad \text{(A.1)}$$

$$m_{HB,in} = m_{HB,in,N_2} + m_{HB,in,H_2} = m_{N1'} + m_{N1''} = m_{N1} \quad \text{(A.2)}$$

$$h_{N(i+1)} = h_{Ni} + \frac{h_{N(i+1),s} - h_{Ni}}{\eta_{com}} \; i \in [2,4,6] \quad \text{(A.3)}$$

where $m_{HB,in}$ is the total inlet mass flow rate of the multi-stage compressor; m_{N23} is the mass flow rate of the recycle gas flowing out of the membrane.

Then, another stream of recycle gas, which recovers from the purge process, joins the feed gas after the compression process, forming the final feed gas for the ammonia synthesis reaction (m_{HB}):

$$m_{HB} = m_{HB,in} + m_{N23} + m_{N21} \quad \text{(A.4)}$$

The feed gas is pre-heated to 400 ˚C by the gas product out of Reactor#3 before entering Reactor#1. The three-stage reactors are connected by waste heat boilers for intercooling. In every reactor, the reaction rate R_{reac} at pressure P and temperature T is calculated by the modified form of the Temkin equation, developed by Dyson and Simon [195]:

$$R_{reac} = 3K_r \left[{K_c}^2 a_{N_2} \left(\frac{a_{H_2}^3}{a_{NH_3}^2} \right)^{\alpha} - \left(\frac{a_{NH_3}^2}{a_{H_2}^3} \right)^{1-\alpha} \right] \Phi\Omega / 3600 \quad \text{(A.5)}$$

with

$$\log\left(K_c\right)=\frac{2250.322}{T}-0.85430-1.51049\log_{10}T \\ -2.58987\times10^{-4}T+1.48961\times10^{-7}T^2 \tag{A.6}$$

$$K_r=8.849\cdot10^{14}e^{-\left(\frac{40765}{1.987T}\right)} \tag{A.7}$$

$$a_j=y_j\gamma_jP,\ j\in\left[H_2,N_2,NH_3\right] \tag{A.8}$$

$$y_j=\frac{F_j}{\sum_{j\in[H_2,N_2,NH_3]}F_j},\ F_j=\frac{m_j}{M\mathrm{r}_j} \tag{A.9}$$

$$\gamma_{H_2}=\exp(e^{-3.8402T^{0.125}+0.541}P-e^{-0.1263T^{0.5}-15.98}P^2+300(e^{-0.011901T-5.941})(e^{-\frac{P}{300}}-1)) \tag{A.10}$$

$$\gamma_{N_2}=0.93431737+0.3101804\cdot10^{-3}T+0.295896\cdot10^{-3}P \\ -0.2707279\cdot10^{-6}T^2+0.4775207\cdot10^{-6}P^2 \tag{A.11}$$

$$\gamma_{NH_3}=0.1438996+0.2028538\cdot10^{-2}T-0.4487672\cdot10^{-3}P \\ -0.1142945\cdot10^{-5}T^2+0.2761216\cdot10^{-6}P^2 \tag{A.12}$$

$$\alpha=0.5,\ \Omega=1 \tag{A.13}$$

$$\Phi=b_0+b_1T+b_2\eta+b_3T^2+b_4\eta^2+b_5T^3+b_6\eta^3,\eta_c=\frac{F_{H_2}^0-F_{H_2}}{F_{H_2}^0} \tag{A.14}$$

where K_c is equilibrium constant; K_r is the rate constant; a_j is the activity of the component j; α is the kinetic parameter which is 0.5 [177]; Φ is the effectiveness factor and the coefficients for Φ is shown in Table A.1; Ω is the catalytic activity which is usually equal to 1 [196]; m_j and F_j represent the mass and molar flow rate of the component j, respectively; $M\mathrm{r}_j$ represents the molecular weight of the component j; F_j^0 represents the reactor inlet molar flow rate of the component j; η_c represents the conversion rate of the reaction.

Table A.1 Coefficients for Equation (A.14)

P (atm)	b_0	b_1	b_2	b_3	b_4	b_5	b_6
150	-17.539096	0.07697849	6.900548	-1.082790e-04	-26.42469	4.927648e-08	38.93727

According to the mass balance, the new conversion rate, η_c, could be obtained, and the molar flow rates of every component in the next step could be updated as follows:

$$\frac{\mathrm{d}\eta_c}{\mathrm{d}z} = \frac{R_{reac} A_t}{F_{H_2}^0} \tag{A.15}$$

$$\eta_c = \eta_c + \mathrm{d}\eta_c \tag{A.16}$$

$$F_{H_2} = F_{H_2}^0 (1 - \eta_c) \tag{A.17}$$

$$F_{N_2} = F_{N_2}^0 (1 - \eta_c) \tag{A.18}$$

$$F_{NH_3} = F_{NH_3}^0 (1 + \eta_c) \tag{A.19}$$

The heat transfer of every step in the reactor is divided into three parts, reaction heat of ammonia synthesis $\mathrm{d}Q_{reac}$, heat transfer with external $\mathrm{d}Q_{ext}$, and energy flow of the gas $\mathrm{d}Q_{flow}$:

$$\mathrm{d}Q_{reac} = \frac{2}{3} \left| \Delta H_{NH_3} \right| F_{H_2}^0 \mathrm{d}\eta_c \tag{A.20}$$

$$\begin{aligned} \Delta H_{NH_3} = 4.184 \Big[& -\left(0.54526 + 846.609 T^{-1} + 459.734 \times 10^6 T^{-3}\right) P \\ & -5.34685 T - 0.2525 \times 10^{-3} T^2 + 1.69197 \times 10^{-6} T^3 - 9157.09 \Big] \end{aligned} \tag{A.21}$$

$$\mathrm{d}Q_{ext} = \frac{k_{bed} \mathrm{L} \mathrm{d}z (T - T_{ext})}{\delta} \tag{A.22}$$

$$\mathrm{d}Q_{flow} = m_{HB} C_p \mathrm{d}T \tag{A.23}$$

where ΔH_{NH_3} is the reaction heat to synthesize 1 mol ammonia.

Thus, the temperature of the gas in the next step could be updated as follows based on the total heat balance of every step:

$$\mathrm{d}Q_{flow} + \mathrm{d}Q_{reac} + \mathrm{d}Q_{ext} = 0 \tag{A.24}$$

$$T = T + \mathrm{d}T \tag{A.25}$$

There are two constraint conditions, which are needed to be checked in every step, to obtain the reaction endpoint of every reactor precisely:

(1) The temperature T of every step in the reactor needs to be checked. Once T≥500˚C, the gas needs to come out from the reactor and to be cooled down to 400˚C in the waste heat boiler before entering the next reactor.

(2) The equilibrium constant K_c of every step in the reactor needs to be checked as well. Once $K_c \le K_c^{'}$ occurs, which means equilibrium conversion is reached, the forward and reverse rates of the reaction will be equal, and no more ammonia could be obtained.

$$K_c^{'} = \frac{P_{NH_3}}{P_{N_2}^{0.5} \cdot P_{H_2}^{1.5}} = \frac{\frac{F_{NH_3}}{F_{mix}} P}{\left(\frac{F_{N_2}}{F_{mix}} P\right)^{0.5} \left(\frac{F_{H_2}}{F_{mix}} P\right)^{1.5}} = \frac{F_{mix}}{P} \frac{F_{NH_3}}{F_{N_2}^{0.5} \cdot F_{H_2}^{1.5}} \tag{A.26}$$

$$F_{mix} = F_{N_2} + F_{H_2} + F_{NH_3} \tag{A.27}$$

The final gas product out of the Reactor#3 goes through the waste heat boiler (WHB#3) and condenser#1 and 2 to condense the ammonia product. The liquid ammonia is separated in the separator with an ammonia recovery rate ($X_{NH_3,recovery}$=92%), reduces pressure to 1.6 MPa through a throttling valve and stored in the liquid ammonia tank finally. The rest of the unreacted gas (nitrogen, argon, and hydrogen) and the unrecovered ammonia need to go through a purge valve with a purge fraction of 50% ($X_{HB,purge}$=50%) before returning to the synthesis loop. Then 85% ($X_{membrane,H_2}$=85%) of the hydrogen and 10% ($X_{membrane,other}$=10%) of other gases in the purge gas are recovered by a hydrogen membrane and return to the synthesis loop as well.

$$m_{N25} = m_{N19} = X_{NH_3,recovery} m_{N18}^{NH_3} \tag{A.28}$$

$$m_{N20} = m_{N18} - m_{N19} \tag{A.29}$$

$$m_{N21} = (1 - X_{HB,purge}) \cdot m_{N20} \tag{A.30}$$

$$m_{N22} = m_{N20} - m_{N21} = X_{HB,purge} \cdot m_{N20} \tag{A.31}$$

$$m_{N23} = X_{membrane,H_2} \cdot m_{N22}^{H_2} + X_{membrane,other} \cdot (m_{N22} - m_{N22}^{H_2}) \tag{A.32}$$

where m_{Ni}^{j} represents the mass flow rate of the component *j* at the status *Ni* in the ammonia synthesis loop.

Besides, the heat recovered from the waste heat boiler is used to generate steam to drive the turbine for power generation:

$$W_{HB,steam} = m_{steam}\left[(h_{W6} - h_{W7}) - (h_{W2} - h_{W1})\right] \tag{A.33}$$

Thus, the total power consumption of the ammonia synthesis loop could be calculated as:

$$W_{HB} = W_{HB,com} - W_{HB,steam} \tag{A.34}$$

Appendix B Publications

Journal paper:

(1) Zhang T, She X, You Z, Zhao Y, Fan H, Ding Y. Cryogenic thermoelectric generation using cold energy from a decoupled liquid air energy storage system for decentralised energy networks. Appl Energy 2022;305:117749.

(2) Zhang T, She X, Ding Y. A power plant for integrated waste energy recovery from liquid air energy storage and liquefied natural gas. Chinese J Chem Eng 2021;34:242–57.

(3) She X, Zhang T, Peng X, Wang L, Tong L, Luo Y, et al. Liquid Air Energy Storage for Decentralized Micro Energy Networks with Combined Cooling, Heating, Hot Water and Power Supply. J Therm Sci 2020;29:1–17.

(4) She X, Zhang T, Cong L, Peng X, Li C, Luo Y, et al. Flexible integration of liquid air energy storage with liquefied natural gas regasification for power generation enhancement. Appl Energy 2019;251.

Chapter:

(1) Yu Q, Zhang T, Peng X, Cong L, Tong L, Wang L, et al. Cryogenic Energy Storage and Its Integration With Nuclear Power Generation for Load Shift. Storage Hybrid. Nucl. Energy, Elsevier; 2019, p. 249–73.

(2) She X, Zhang T, Meng Y, Liang T, Peng X, Tong L, et al. Cryogenic Energy Storage. Ref Modul Earth Syst Environ Sci 2021.

(3) Liang T, Zhang T, Li Y, Tong L, Wang L, Ding Y. Thermodynamic Analysis of Liquid Air Energy Storage (LAES) System. Ref Modul Earth Syst Environ Sci 2021.

Patent:

(1) Yulong Ding, Tongtong Zhang. Power generation system based on liquid air and method, China Patent No. CN112392599A, Feb 2021.

(2) Yulong Ding, Xiaohui She, Tongtong Zhang. An integrated device and method of liquid air energy storage and ammonia synthesis, China Patent No. CN112179046A, Jan 2021.

(3) Yulong Ding, Xiaohui She, Tongtong Zhang, Xiaodong Peng, Li Wang, Lige Tong. Cold-heat-electricity combined supply system based on liquid air energy storage, China Patent No. CN109373703A, Sep 2019.

(4) Yulong Ding, Abudukade Aihamaide, Yanqi Zhao, Tongtong Zhang. Energy efficiency improving device of low-pressure operating liquid air energy storage system, China Patent No. CN112282881A, Jan 2021.

Bibliography

[1] International Renewable Energy Agency (IRENA). Reaching zero with renewables: Eliminating CO2 emissions from industry and transport in line with the 1.5°C climate goal. 2020.

[2] Renewable Energy Network Policy for the 21st Century (REN21). Renewables 2020 Global Status Report. 2020.

[3] U.S.Energy Information Administration (EIA). International Energy Outlook 2017. 2017.

[4] Weisser D, Garcia RS. Instantaneous wind energy penetration in isolated electricity grids: Concepts and review. Renew Energy 2005;30:1299–308. doi:10.1016/j.renene.2004.10.002.

[5] Denholm P, Hand M. Grid flexibility and storage required to achieve very high penetration of variable renewable electricity. Energy Policy 2011;39:1817–30. doi:10.1016/j.enpol.2011.01.019.

[6] Palizban O, Kauhaniemi K. Energy storage systems in modern grids—Matrix of technologies and applications. J Energy Storage 2016;6:248–59. doi:10.1016/j.est.2016.02.001.

[7] Chen H, Cong TN, Yang W, Tan C, Li Y, Ding Y. Progress in electrical energy storage system: A critical review. Prog Nat Sci 2009;19:291–312. doi:10.1016/j.pnsc.2008.07.014.

[8] Greenblatt JB, Succar S, Denkenberger DC, Williams RH, Socolow RH. Baseload wind energy: modeling the competition between gas turbines and compressed air energy storage for supplemental generation. Energy Policy 2007;35:1474–92. doi:10.1016/j.enpol.2006.03.023.

[9] Hill CA, Such MC, Chen D, Gonzalez J, Grady WMK. Battery energy storage for enabling integration of distributed solar power generation. IEEE Trans Smart Grid 2012;3:850–7. doi:10.1109/TSG.2012.2190113.

[10] Renewable Energy Network Policy for the 21st Century (REN21). Renewables in Cities 2021 Global Status Report. 2021.

[11] International Renewable Energy Agency (IRENA). Innovation Outlook: Thermal Energy Storage. 2020.

[12] Kousksou T, Bruel P, Jamil A, El Rhafiki T, Zeraouli Y. Energy storage: Applications and challenges. Sol Energy Mater Sol Cells 2014;120:59–80. doi:10.1016/j.solmat.2013.08.015.

[13] Argyrou MC, Christodoulides P, Kalogirou SA. Energy storage for electricity generation and related processes: Technologies appraisal and grid scale applications. Renew Sustain Energy Rev 2018;94:804–21. doi:10.1016/j.rser.2018.06.044.

[14] Argyrou MC, Christodoulides P, Marouchos CC, Kalogirou SA, Florides GA, Lazari L. Overview of energy storage technologies and a short-term storage application for wind turbines. Proc. Int. Offshore Polar Eng. Conf., vol. 2016- Janua, 2016, p. 444–52.

[15] Haisheng Chen, Yulong Ding, T Peters, F Berger. Energy storage and generation. US Patent US20090282840, 2009.

[16] Liquid air in the energy and transport systems. Cent Low Carbon Futur 2013. http://liquidair.org.uk/files/full-report.

[17] Robert Giglio, Nygard Stefan. The pathway to renewables and the role of liquid air. Mod Power Syst Mag 2020:16–20.

[18] Smith EM. STORAGE OF ELECTRICAL ENERGY USING SUPERCRITICAL

LIQUID AIR. Inst Mech Eng Proc 1977;191. doi:10.1243/pime_proc_1977_191_035_02.

[19] Tanaka T, Ishikawa A, Aoyama K, Kishimoto K, Yoshida Y, Toda K, et al. Gas turbine inlet air cooling system with liquid air. Mitsubishi Heavy Ind Ltd Tech Rev 1997;34:91–5.

[20] Araki H, Nakabaru M, Chino K. Simulation of heat transfer in the cool storage unit of a liquid–air energy storage system. Heat Transf Res 2002;31:284–96.

[21] Brett G, Barnett M. The application of liquid air energy storage for large scale long duration solutions to grid balancing. EPJ Web Conf 2014;79:03002. doi:10.1051/EPJCONF/20137903002.

[22] Coyne B. 15MWh liquid air energy storage plant opens, owners plot world domination. The Energyst 2018. https://theenergyst.com/15mwh-liquid-air-energy-storage-plant-opens/.

[23] EMILY HOLBROOK. World's Largest Liquid-Air Energy Storage Construction to Begin. Environ Energy Lead 2021. https://www.environmentalleader.com/2021/04/construction-to-begin-on-worlds-largest-liquid-air-energy-storage-project/ (accessed 2 January 2022).

[24] Li Y, Chen H, Zhang X, Tan C, Ding Y. Renewable energy carriers: Hydrogen or liquid air/nitrogen? Appl Therm Eng 2010;30:1985–90. doi:10.1016/j.applthermaleng.2010.04.033.

[25] Charters D. A comparison of energy vectors in powering hybrid buses. Renew Energy Focus 2016;17:73–4. doi:10.1016/j.ref.2016.02.011.

[26] Li QY, Ju YL. Design and analysis of liquefaction process for offshore associated gas resources. Appl Therm Eng 2010;30:2518–25.

doi:10.1016/j.applthermaleng.2010.07.001.

[27] Chang HM, Chung MJ, Kim MJ, Park SB. Thermodynamic design of methane liquefaction system based on reversed-Brayton cycle. Cryogenics (Guildf) 2009;49:226–34. doi:10.1016/j.cryogenics.2008.08.006.

[28] Remeljej CW, Hoadley AFA. An exergy analysis of small-scale liquefied natural gas (LNG) liquefaction processes. Energy 2006;31:2005–19. doi:10.1016/j.energy.2005.09.005.

[29] Li Y. Cryogen Based Energy Storage : Process Modelling and Optimisation. PhD Thesis Univ Leeds 2011.

[30] Peng X. Liquid air energy storage: process optimization and performance enhancement 2018.

[31] Hamdy S, Moser F, Morosuk T, Tsatsaronis G. Exergy-based and economic evaluation of liquefaction processes for cryogenics energy storage. Energies 2019;12. doi:10.3390/en12030493.

[32] K SK, Jacob Thomas R. Exergy Based Analysis of Gas Liquefaction Cycles. Int J Innov Res Electr 2020;8.

[33] Maytal BZ. Maximizing production rates of the Linde-Hampson machine. Cryogenics (Guildf) 2006;46:49–54. doi:10.1016/j.cryogenics.2005.11.004.

[34] Yilmaz C, Cetin TH, Ozturkmen B, Kanoglu M. Thermodynamic perfor mance analysis of gas liquefaction cycles for cryogenic applications. J Therm Eng 2019;5:62–75. doi:10.18186/thermal.513038.

[35] Abdo RF, Pedro HTC, Koury RNN, Machado L, Coimbra CFM, Porto MP. Performance evaluation of various cryogenic energy storage systems. Energy

2015;90:1024–32. doi:10.1016/j.energy.2015.08.008.

[36] Aneke M, Wang M. Energy storage technologies and real life applications – A state of the art review. Appl Energy 2016;179:350–77. doi:10.1016/j.apenergy.2016.06.097.

[37] Ding Y, Tong L, Zhang P, Li Y, Radcliffe J, Wang L. Liquid Air Energy Storage. Storing Energy With Spec. Ref. to Renew. Energy Sources, Elsevier Inc.; 2016, p. 167–81. doi:10.1016/B978-0-12-803440-8.00009-9.

[38] Sciacovelli A, Smith D, Navarro ME, Vecchi A, Peng X, Li Y, et al. Performance Analysis and Detailed Experimental Results of the First Liquid Air Energy Storage Plant in the World. Proc Inst Civ Eng 2018;140. doi:10.1115/1.4038378.

[39] Morgan R, Nelmes S, Gibson E, Brett G. Liquid air energy storage - Analysis and first results from a pilot scale demonstration plant. Appl Energy 2015;137:845–53. doi:10.1016/j.apenergy.2014.07.109.

[40] Sabihuddin S, Kiprakis AE, Mueller M. A numerical and graphical review of energy storage technologies. Energies 2015;8:172–216. doi:10.3390/en8010172.

[41] International Electrotechnical Commission (IEC). IEC White Paper: Electrical Energy Storage. 2011.

[42] Olabi AG, Onumaegbu C, Wilberforce T, Ramadan M, Abdelkareem MA, Al – Alami AH. Critical review of energy storage systems. Energy 2021;214:118987. doi:10.1016/j.energy.2020.118987.

[43] Díaz-González F, Sumper A, Gomis-Bellmunt O, Villafáfila-Robles R. A review of energy storage technologies for wind power applications. Renew Sustain Energy Rev 2012;16:2154–71. doi:10.1016/j.rser.2012.01.029.

[44] China builds the world's largest lithium-free battery. En:Former 2021.

https://www.en-former.com/en/china-builds-the-worlds-largest-lithium-free-battery/ (accessed 10 September 2021).

[45] Fernandes D, Pitié F, Cáceres G, Baeyens J. Thermal energy storage: 'How previous findings determine current research priorities'. Energy 2012;39:246–57. doi:10.1016/j.energy.2012.01.024.

[46] Koohi-Fayegh S, Rosen MA. A review of energy storage types, applications and recent developments. J Energy Storage 2020;27:101047. doi:10.1016/j.est.2019.101047.

[47] Borri E, Tafone A, Romagnoli A, Comodi G. A preliminary study on the optimal configuration and operating range of a "microgrid scale" air liquefaction plant for Liquid Air Energy Storage. Energy Convers Manag 2017;143:275–85. doi:10.1016/j.enconman.2017.03.079.

[48] Morgan R, Gibson E, Brett Bsc G. An analysis of a large-scale liquid air energy storage system. Proc Inst Civ Eng 2015;168:135–44. doi:10.1680/ener.14.00038.

[49] Hamdy S, Morosuk T, Tsatsaronis G. Cryogenics-based energy storage: Evaluation of cold exergy recovery cycles. Energy 2017;138:1069–80. doi:10.1016/j.energy.2017.07.118.

[50] Antonelli M, Barsali S, Desideri U, Giglioli R, Paganucci F, Pasini G. Liquid air energy storage: Potential and challenges of hybrid power plants. Appl Energy 2017;194:522–9. doi:10.1016/j.apenergy.2016.11.091.

[51] Chino K, Araki H. Evaluation of energy storage method using liquid air. Heat Transf - Asian Res 2000;29:347–57. doi:10.1002/1523-1496(200007)29:5<347::AID-HTJ1>3.0.CO;2-A.

[52] Guizzi GL, Manno M, Tolomei LM, Vitali RM. Thermodynamic analysis of a liquid

air energy storage system. Energy 2015;93:1639–47. doi:10.1016/j.energy.2015.10.030.

[53] Sciacovelli A, Vecchi A, Ding Y. Liquid air energy storage (LAES) with packed bed cold thermal storage – From component to system level performance through dynamic modelling. Appl Energy 2017;190:84–98. doi:10.1016/j.apenergy.2016.12.118.

[54] She X, Peng X, Nie B, Leng G, Zhang X, Weng L, et al. Enhancement of round trip efficiency of liquid air energy storage through effective utilization of heat of compression. Appl Energy 2017;206:1632–42. doi:10.1016/j.apenergy.2017.09.102.

[55] Peng X, She X, Cong L, Zhang T, Li C, Li Y, et al. Thermodynamic study on the effect of cold and heat recovery on performance of liquid air energy storage. Appl Energy 2018;221:86–99. doi:10.1016/j.apenergy.2018.03.151.

[56] Xue XD, Wang SX, Zhang XL, Cui C, Chen LB, Zhou Y, et al. Thermodynamic analysis of a novel liquid air energy storage system. Phys. Procedia, vol. 67, Elsevier B.V.; 2015, p. 733–8. doi:10.1016/j.phpro.2015.06.124.

[57] Tafone A, Romagnoli A, Borri E, Comodi G. New parametric performance maps for a novel sizing and selection methodology of a Liquid Air Energy Storage system. Appl Energy 2019;250:1641–56. doi:10.1016/j.apenergy.2019.04.171.

[58] Lin X, Wang L, Xie N, Li G, Chen H. Thermodynamic analysis of the cascaded packed bed cryogenic storage based supercritical air energy storage system. Energy Procedia, vol. 158, Elsevier Ltd; 2019, p. 5079–85. doi:10.1016/j.egypro.2019.01.639.

[59] Kim J, Chang D. Pressurized cryogenic air energy storage for efficiency improvement of liquid air energy storage. Energy Procedia, vol. 158, Elsevier Ltd; 2019, p. 5086–91. doi:10.1016/j.egypro.2019.01.638.

[60] Peng H, Shan X, Yang Y, Ling X. A study on performance of a liquid air energy

storage system with packed bed units. Appl Energy 2018;211:126–35. doi:10.1016/j.apenergy.2017.11.045.

[61] Vecchi A, Li Y, Mancarella P, Sciacovelli A. Integrated techno-economic assessment of Liquid Air Energy Storage (LAES) under off-design conditions: Links between provision of market services and thermodynamic performance. Appl Energy 2020;262:114589. doi:10.1016/j.apenergy.2020.114589.

[62] Guo L, Gao Z, Ji W, Xu H, Chen L, Wang J. Thermodynamics and Economics of Different Asymmetric Cold Energy Transfer in a Liquid Air Energy Storage System. Energy Technol 2020;8. doi:10.1002/ente.201901487.

[63] She X, Li Y, Peng X, Ding Y. Theoretical analysis on performance enhancement of stand-alone liquid air energy storage from perspective of energy storage and heat transfer. Energy Procedia, vol. 142, Elsevier Ltd; 2017, p. 3498–504. doi:10.1016/j.egypro.2017.12.236.

[64] Bindra H, Bueno P, Morris JF, Shinnar R. Thermal analysis and exergy evaluation of packed bed thermal storage systems. Appl Therm Eng 2013;52:255–63. doi:10.1016/j.applthermaleng.2012.12.007.

[65] Mertens N, Alobaid F, Frigge L, Epple B. Dynamic simulation of integrated rock-bed thermocline storage for concentrated solar power. Sol Energy 2014;110:830–42. doi:10.1016/j.solener.2014.10.021.

[66] Legrand M, Rodríguez-Antón LM, Martinez-Arevalo C, Gutiérrez-Martín F. Integration of liquid air energy storage into the spanish power grid. Energy 2019;187. doi:10.1016/j.energy.2019.115965.

[67] Hüttermann L, Span R. Influence of the heat capacity of the storage material on the efficiency of thermal regenerators in liquid air energy storage systems. Energy

2019;174:236–45. doi:10.1016/j.energy.2019.02.149.

[68] Zhang T, Zhang XL, He YL, Xue XD, Mei SW. Thermodynamic analysis of hybrid liquid air energy storage systems based on cascaded storage and effective utilization of compression heat. Appl Therm Eng 2020;164. doi:10.1016/j.applthermaleng.2019.114526.

[69] Zhang T, Zhang X, Xue X, Wang G, Mei S. Thermodynamic analysis of a hybrid power system combining Kalina cycle with liquid air energy storage. Entropy 2019;21:220. doi:10.3390/e21030220.

[70] Liu Q, He Z, Liu Y, He Y. Thermodynamic and parametric analyses of a thermoelectric generator in a liquid air energy storage system. Energy Convers Manag 2021;237:114117. doi:10.1016/j.enconman.2021.114117.

[71] She X, Zhang T, Peng X, Wang L, Tong L, Luo Y, et al. Liquid Air Energy Storage for Decentralized Micro Energy Networks with Combined Cooling, Heating, Hot Water and Power Supply. J Therm Sci 2020;29:1–17. doi:10.1007/s11630-020-1396-x.

[72] Tafone A, Borri E, Comodi G, Van Den Broek M, Romagnoli A. Preliminary assessment of waste heat recovery solution (ORC) to enhance the performance of Liquid Air Energy Storage system. Energy Procedia, vol. 142, Elsevier Ltd; 2017, p. 3609–16. doi:10.1016/j.egypro.2017.12.252.

[73] Tafone A, Romagnoli A, Li Y, Borri E, Comodi G. Techno-economic Analysis of a Liquid Air Energy Storage (LAES) for Cooling Application in Hot Climates. Energy Procedia, vol. 105, Elsevier Ltd; 2017, p. 4450–7. doi:10.1016/j.egypro.2017.03.944.

[74] Tafone A, Ding Y, Li Y, Xie C, Romagnoli A. Levelised Cost of Storage (LCOS) analysis of liquid air energy storage system integrated with Organic Rankine Cycle. Energy 2020;198. doi:10.1016/j.energy.2020.117275.

[75] Tafone A, Borri E, Comodi G, van den Broek M, Romagnoli A. Liquid Air Energy Storage performance enhancement by means of Organic Rankine Cycle and Absorption Chiller. Appl Energy 2018;228:1810–21. doi:10.1016/j.apenergy.2018.06.133.

[76] Al-Zareer M, Dincer I, Rosen MA. Analysis and assessment of novel liquid air energy storage system with district heating and cooling capabilities. Energy 2017;141:792–802. doi:10.1016/j.energy.2017.09.094.

[77] Gao Z, Guo L, Ji W, Xu H, An B, Wang J. Thermodynamic and economic analysis of a trigeneration system based on liquid air energy storage under different operating modes. Energy Convers Manag 2020;221:113184. doi:10.1016/j.enconman.2020.113184.

[78] Karimi IA, Khan MS. Special Issue on PSE Advances in Natural Gas Value Chain: Editorial. Ind Eng Chem Res 2018;57:5733–5. doi:10.1021/acs.iecr.8b01543.

[79] Zhang T, Chen L, Zhang X, Mei S, Xue X, Zhou Y. Thermodynamic analysis of a novel hybrid liquid air energy storage system based on the utilization of LNG cold energy. Energy 2018;155:641–50. doi:10.1016/j.energy.2018.05.041.

[80] Luyao L, Sixian W, Zhang D, Luwei Y, Yuan Z, Junjie W. Performance analysis of liquid air energy storage utilizing LNG cold energy. IOP Conf. Ser. Mater. Sci. Eng., 2017. doi:10.1088/1757-899X/171/1/012032.

[81] Peng X, She X, Li C, Luo Y, Zhang T, Li Y, et al. Liquid air energy storage flexibly coupled with LNG regasification for improving air liquefaction. Appl Energy 2019;250:1190–201. doi:10.1016/j.apenergy.2019.05.040.

[82] Kim J, Noh Y, Chang D. Storage system for distributed-energy generation using liquid air combined with liquefied natural gas. Appl Energy 2018;212:1417–32.

doi:10.1016/j.apenergy.2017.12.092.

[83] Park J, You F, Cho H, Lee I, Moon I. Novel massive thermal energy storage system for liquefied natural gas cold energy recovery. Energy 2020;195. doi:10.1016/j.energy.2020.117022.

[84] Park J, Lee I, Yoon H, Kim J, Moon I. Application of Cryogenic Energy Storage to Liquefied Natural Gas Regasification Power Plant. Comput. Aided Chem. Eng., vol. 40, Elsevier B.V.; 2017, p. 2557–62. doi:10.1016/B978-0-444-63965-3.50428-1.

[85] Park J, Lee I, Moon I. A Novel Design of Liquefied Natural Gas (LNG) Regasification Power Plant Integrated with Cryogenic Energy Storage System. Ind Eng Chem Res 2017;56:1288–96. doi:10.1021/acs.iecr.6b04157.

[86] Park J, Cho S, Qi M, Noh W, Lee I, Moon I. Liquid Air Energy Storage Coupled with Liquefied Natural Gas Cold Energy: Focus on Efficiency, Energy Capacity, and Flexibility. Energy 2020:119308. doi:10.1016/j.energy.2020.119308.

[87] Qi M, Park J, Kim J, Lee I, Moon I. Advanced integration of LNG regasification power plant with liquid air energy storage: Enhancements in flexibility, safety, and power generation. Appl Energy 2020;269. doi:10.1016/j.apenergy.2020.115049.

[88] Lee I, Park J, Moon I. Conceptual design and exergy analysis of combined cryogenic energy storage and LNG regasification processes: Cold and power integration. Energy 2017;140:106–15. doi:10.1016/j.energy.2017.08.054.

[89] Kanbur BB, Xiang L, Dubey S, Choo FH, Duan F. Cold utilization systems of LNG: A review. Renew Sustain Energy Rev 2017;79:1171–88. doi:10.1016/J.RSER.2017.05.161.

[90] Lee I, You F. Systems design and analysis of liquid air energy storage from liquefied natural gas cold energy. Appl Energy 2019;242:168–80.

doi:10.1016/j.apenergy.2019.03.087.

[91] Lee I, Park J, You F, Moon I. A novel cryogenic energy storage system with LNG direct expansion regasification: Design, energy optimization, and exergy analysis. Energy 2019;173:691–705. doi:10.1016/j.energy.2019.02.047.

[92] He T, Lv H, Shao Z, Zhang J, Xing X, Ma H. Cascade utilization of LNG cold energy by integrating cryogenic energy storage, organic Rankine cycle and direct cooling. Appl Energy 2020;277. doi:10.1016/j.apenergy.2020.115570.

[93] She X, Zhang T, Cong L, Peng X, Li C, Luo Y, et al. Flexible integration of liquid air energy storage with liquefied natural gas regasification for power generation enhancement. Appl Energy 2019;251. doi:10.1016/j.apenergy.2019.113355.

[94] Li Y, Cao H, Wang S, Jin Y, Li D, Wang X, et al. Load shifting of nuclear power plants using cryogenic energy storage technology. Appl Energy 2014;113:1710–6. doi:10.1016/j.apenergy.2013.08.077.

[95] Cetin TH, Kanoglu M, Yanikomer N. Cryogenic energy storage powered by geothermal energy. Geothermics 2019;77:34–40. doi:10.1016/j.geothermics.2018.08.005.

[96] Cetin TH, Kanoglu M, Bedir F. Integration of cryogenic energy storage and cryogenic organic cycle to geothermal power plants. Geothermics 2020;87:101830. doi:10.1016/j.geothermics.2020.101830.

[97] Ji W, Zhou Y, Sun Y, Zhang W, Pan CZ, Wang JJ. Thermodynamic characteristics of a novel wind-solar-liquid air energy storage system. IOP Conf. Ser. Mater. Sci. Eng., vol. 278, Institute of Physics Publishing; 2017, p. 012070. doi:10.1088/1757-899X/278/1/012070.

[98] Ebrahimi A, Ghorbani B, Skandarzadeh F, Ziabasharhagh M. Introducing a novel

liquid air cryogenic energy storage system using phase change material, solar parabolic trough collectors, and Kalina power cycle (process integration, pinch, and exergy analyses). Energy Convers Manag 2021;228:113653. doi:10.1016/j.enconman.2020.113653.

[99] Nabat MH, Zeynalian M, Razmi AR, Arabkoohsar A, Soltani M. Energy, exergy, and economic analyses of an innovative energy storage system; liquid air energy storage (LAES) combined with high-temperature thermal energy storage (HTES). Energy Convers Manag 2020;226:113486. doi:10.1016/j.enconman.2020.113486.

[100] Wu S, Zhou C, Doroodchi E, Moghtaderi B. Techno-economic analysis of an integrated liquid air and thermochemical energy storage system. Energy Convers Manag 2020;205. doi:10.1016/j.enconman.2019.112341.

[101] Li Y, Jin Y, Chen H, Tan C, Ding Y. An integrated system for thermal power generation, electrical energy storage and CO2 capture. Int J Energy Res 2011;35:1158–67. doi:10.1002/er.1753.

[102] Li Y, Wang X, Ding Y. A cryogen-based peak-shaving technology: Systematic approach and techno-economic analysis. Int J Energy Res 2013;37:547–57. doi:10.1002/er.1942.

[103] Pacheco KA, Li Y, Wang M. Study of integration of cryogenic air energy storage and coal oxy-fuel combustion through modelling and simulation. Comput. Aided Chem. Eng., vol. 33, Elsevier B.V.; 2014, p. 1537–42. doi:10.1016/B978-0-444-63455-9.50091-X.

[104] Wang C, Akkurt N, Zhang X, Luo Y, She X. Techno-economic analyses of multi-functional liquid air energy storage for power generation, oxygen production and heating. Appl Energy 2020;275:115392. doi:10.1016/j.apenergy.2020.115392.

[105] He X, Liu Y, Rehman A, Wang L. A novel air separation unit with energy storage and generation and its energy efficiency and economy analysis. Appl Energy 2021;281:115976. doi:10.1016/j.apenergy.2020.115976.

[106] Kantharaj B, Garvey S, Pimm A. Compressed air energy storage with liquid air capacity extension. Appl Energy 2015;157:152–64. doi:10.1016/j.apenergy.2015.07.076.

[107] Kantharaj B, Garvey S, Pimm A. Thermodynamic analysis of a hybrid energy storage system based on compressed air and liquid air. Sustain Energy Technol Assessments 2015;11:159–64. doi:10.1016/j.seta.2014.11.002.

[108] Farres-Antunez P, Xue H, White AJ. Thermodynamic analysis and optimisation of a combined liquid air and pumped thermal energy storage cycle. J Energy Storage 2018;18:90–102. doi:10.1016/j.est.2018.04.016.

[109] Osorio JD, Panwar M, Rivera-Alvarez A, Chryssostomidis C, Hovsapian R, Mohanpurkar M, et al. Enabling thermal efficiency improvement and waste heat recovery using liquid air harnessed from offshore renewable energy sources. Appl Energy 2020;275:115351. doi:10.1016/j.apenergy.2020.115351.

[110] Ahmad A, Al-Dadah R, Mahmoud S. Liquid air utilization in air conditioning and power generating in a commercial building. J Clean Prod 2017;149:773–83. doi:10.1016/j.jclepro.2017.02.143.

[111] Navarro ME, Ahmad A, Luo Y, She X. Integrated Cryogenic and Thermal Energy Storage for Decarbonizing Energy Consumption: Development and Challenges. ES Energy Environ 2019. doi:10.30919/esee8c300.

[112] Parker ME, Plummer MC, Ordonez CA, Parker ME, Plummer MC, Ordonez CA. CooLN2Car: An Experimental Car Which Uses Liquid Nitrogen as Its Fuel. APS

1997:BE.03.

[113] Wen DS, Chen HS, Ding YL, Dearman P. Liquid nitrogen injection into water: Pressure build-up and heat transfer. Cryogenics (Guildf) 2006;46:740–8. doi:10.1016/J.CRYOGENICS.2006.06.007.

[114] Wen D, Ding Y, Dearman P. PHASE CHANGE HEAT TRANSFER OF LIQUID NITROGEN INJECTION INSIDE A HEAT TRANSFER FLUID. Int Heat Transf Conf 13 2006. doi:10.1615/IHTC13.P12.430.

[115] Ding Y, Wen D, Dearman P. Cryogenic engines. US 2009/0320476A1, 2009.

[116] Owen N. The Dearman engine–liquid air for transport cooling 2016.

[117] Tafone A, Dal Magro F, Romagnoli A. Integrating an oxygen enriched waste to energy plant with cryogenic engines and Air Separation Unit: Technical, economic and environmental analysis. Appl Energy 2018;231:423–32. doi:10.1016/j.apenergy.2018.09.024.

[118] Che S, Kim J, Chang D. Liquid Air as an Energy Carrier for Liquefied Natural Gas Cold Energy Distribution in Cold Storage Systems. Energies 2021;14:272. doi:10.3390/en14020272.

[119] Ahmad A, Al-Dadah R, Mahmoud S. Air conditioning and power generation for residential applications using liquid nitrogen. Appl Energy 2016;184:630–40. doi:10.1016/j.apenergy.2016.11.022.

[120] Li Y, Wang X, Jin Y, Ding Y. An integrated solar-cryogen hybrid power system. Renew Energy 2012;37:76–81. doi:10.1016/j.renene.2011.05.038.

[121] Park J, You F, Mun H, Lee I. Liquefied natural gas supply chain using liquid air as a cold carrier: Novel method for energy recovery. Energy Convers Manag

2021;227:113611. doi:10.1016/j.enconman.2020.113611.

[122] Rehman A, Qyyum MA, Qadeer K, Zakir F, Ding Y, Lee M, et al. Integrated biomethane liquefaction using exergy from the discharging end of a liquid air energy storage system. Appl Energy 2020;260. doi:10.1016/j.apenergy.2019.114260.

[123] REFPROP Graphical User Interface — REFPROP 10.0 documentation 2018. https://refprop-docs.readthedocs.io/en/latest/GUI/index.html (accessed 22 June 2021).

[124] NIST REFPROP Database in TDE n.d. https://trc.nist.gov/TDE/TDE_Help/NIST REFPROP Database.htm (accessed 22 June 2021).

[125] Reference Fluid Thermodynamic and Transport Properties Database (REFPROP) | NIST n.d. https://www.nist.gov/programs-projects/reference-fluid-thermodynamic-and-transport-properties-database-refprop (accessed 22 June 2021).

[126] Winterbone DE, Turan A. Pinch Technology. Adv. Thermodyn. Eng., Elsevier; 2015, p. 447–65. doi:10.1016/b978-0-444-63373-6.00019-8.

[127] Linnhoff B, Flower JR. Synthesis of heat exchanger networks: I. Systematic generation of energy optimal networks. AIChE J 1978;24:633–42. doi:10.1002/aic.690240411.

[128] Linnhoff B, Flower JR. Synthesis of heat exchanger networks: II. Evolutionary generation of networks with various criteria of optimality. AIChE J 1978;24:642–54. doi:10.1002/aic.690240412.

[129] Flower JR, Linnhoff B. Thermodynamic analysis in the design of process networks. Comput Chem Eng 1979;3:283–91. doi:10.1016/0098-1354(79)80047-2.

[130] Linnhoff B, Hindmarsh E. The pinch design method for heat exchanger networks. Chem Eng Sci 1983;38:745–63. doi:10.1016/0009-2509(83)80185-7.

[131] Aspelund A, Berstad DO, Gundersen T. An Extended Pinch Analysis and Design procedure utilizing pressure based exergy for subambient cooling. Appl Therm Eng 2007;27:2633–49. doi:10.1016/j.applthermaleng.2007.04.017.

[132] March L. Introduction to Pinch Technology. 1998.

[133] Kemp IC. Pinch Analysis and Process Integration 2nd Edition - A User Guide on Process Integration for the Efficient Use of Energy. Elsevier Ltd; 2006. doi:10.1016/B978-0-7506-8260-2.X5001-9.

[134] Kanbur BB, Xiang L, Dubey S, Choo FH, Duan F. Cold utilization systems of LNG: A review. Renew Sustain Energy Rev 2017;79:1171–88. doi:10.1016/j.rser.2017.05.161.

[135] Marmolejo-Correa D, Gundersen T. A comparison of exergy efficiency definitions with focus on low temperature processes. Energy 2012;44:477–89. doi:10.1016/j.energy.2012.06.001.

[136] Kotas TJ. EXERGY CRITERIA OF PERFORMANCE FOR THERMAL PLANT. Int J Heat Fluid Flow 1980;2:147–63. doi:10.1016/0142-727X(80)90010-7.

[137] Bao J, Lin Y, Zhang R, Zhang N, He G. Strengthening power generation efficiency utilizing liquefied natural gas cold energy by a novel two-stage condensation Rankine cycle (TCRC) system. Energy Convers Manag 2017;143:312–25. doi:10.1016/j.enconman.2017.04.018.

[138] Li C, Liu J, Zheng S, Chen X, Li J, Zeng Z. Performance analysis of an improved power generation system utilizing the cold energy of LNG and solar energy. Appl Therm Eng 2019;159. doi:10.1016/j.applthermaleng.2019.113937.

[139] Tsougranis EL, Wu D. A feasibility study of Organic Rankine Cycle (ORC) power generation using thermal and cryogenic waste energy on board an LNG passenger vessel. Int. J. Energy Res., vol. 42, 2018, p. 3121–42. doi:10.1002/er.4047.

[140] Xie C, Hong Y, Ding Y, Li Y, Radcliffe J. An economic feasibility assessment of decoupled energy storage in the UK: With liquid air energy storage as a case study. Appl Energy 2018;225:244–57. doi:10.1016/j.apenergy.2018.04.074.

[141] Function Team M. Compressor Selection Guidelines. 2013.

[142] Li Y, Chen H, Ding Y. Fundamentals and applications of cryogen as a thermal energy carrier: A critical assessment. Int J Therm Sci 2010;49:941–9. doi:10.1016/j.ijthermalsci.2009.12.012.

[143] Ozen DN, Uçar İ. Energy, exergy, and exergo-economic analysis of a novel combined power system using the cold energy of liquified natural gas (LNG). Environ Prog Sustain Energy 2020;39. doi:10.1002/ep.13377.

[144] Le S, Lee JY, Chen CL. Waste cold energy recovery from liquefied natural gas (LNG) regasification including pressure and thermal energy. Energy 2018;152:770–87. doi:10.1016/j.energy.2018.03.076.

[145] Zare V, Mahmoudi SMS, Yari M. An exergoeconomic investigation of waste heat recovery from the Gas Turbine-Modular Helium Reactor (GT-MHR) employing an ammonia-water power/cooling cycle. Energy 2013;61:397–409. doi:10.1016/j.energy.2013.09.038.

[146] Mirmasoumi S, Khoshbakhti Saray R, Ebrahimi S. Evaluation of thermal pretreatment and digestion temperature rise in a biogas fueled combined cooling, heat, and power system using exergo-economic analysis. Energy Convers Manag 2018;163:219–38. doi:10.1016/j.enconman.2018.02.069.

[147] 2019 Chemical Engineering Plant Cost Index Annual Average - Chemical Engineering | Page 1 n.d. https://www.chemengonline.com/2019-chemical-engineering-plant-cost-index-annual-average/ (accessed 16 February 2021).

[148] Chen JJJ. Comments on improvements on a replacement for the logarithmic mean. Chem Eng Sci 1987;42:2488–9. doi:10.1016/0009-2509(87)80128-8.

[149] Wang ZQ, Zhou NJ, Guo J, Wang XY. Fluid selection and parametric optimization of organic Rankine cycle using low temperature waste heat. Energy 2012;40:107–15. doi:10.1016/j.energy.2012.02.022.

[150] https://www.atlascopco.com/en-uk/compressors n.d. https://www.atlascopco.com/en-uk/compressors (accessed 5 July 2021).

[151] PIP REEC001 07 REEC001 - Compressor Selection Guidelines. 2013.

[152] Zheng J, Zhou Z, Zhao J, Wang J. Integrated heat and power dispatch truly utilizing thermal inertia of district heating network for wind power integration. Appl Energy 2018;211:865–74. doi:10.1016/j.apenergy.2017.11.080.

[153] How efficient is my boiler? - British Gas n.d. https://www.britishgas.co.uk/home-services/boilers-and-heating/guides/boiler-efficiency.html (accessed 5 July 2021).

[154] Kurzke J, Halliwell I. Propulsion and Power: An Exploration of Gas Turbine Performance Modeling. 2018. doi:10.1007/978-3-319-75979-1.

[155] G.F. H. Refrigeration, Air Conditioning and Heat Pumps. MDPI; 2021. doi:10.3390/books978-3-03943-824-2.

[156] Atienza-Márquez A, Bruno JC, Akisawa A, Nakayama M, Coronas A. Fluids selection and performance analysis of a polygeneration plant with exergy recovery from LNG-regasification. Energy 2019;176:1020–36. doi:10.1016/j.energy.2019.04.060.

[157] Pátek J, Klomfar J. A computationally effective formulation of the thermodynamic properties of LiBr-H2O solutions from 273 to 500 K over full composition range. Int J Refrig 2006;29:566–78. doi:10.1016/j.ijrefrig.2005.10.007.

[158] Talbi MM, Agnew B. Exergy analysis: An absorption refrigerator using lithium bromide and water as the working fluids. Appl Therm Eng 2000;20:619–30. doi:10.1016/S1359-4311(99)00052-6.

[159] Khalil KM, Ahmad A, Mahmoud S, Al-Dadah RK. Liquid air/nitrogen energy storage and power generation system for micro-grid applications. J Clean Prod 2017;164:606–17. doi:10.1016/j.jclepro.2017.06.236.

[160] Kalavani F, Mohammadi-Ivatloo B, Zare K. Optimal stochastic scheduling of cryogenic energy storage with wind power in the presence of a demand response program. Renew Energy 2019;130:268–80. doi:10.1016/j.renene.2018.06.070.

[161] Chen LG, Meng FK, Sun FR. Thermodynamic analyses and optimization for thermoelectric devices: The state of the arts. Sci China Technol Sci 2016;59:442–55. doi:10.1007/s11431-015-5970-5.

[162] Lobunets Y. Thermoelectric Generator for Utilizing Cold Energy of Cryogen Liquids. J Electron Mater 2019;48:5491–6. doi:10.1007/s11664-019-07392-3.

[163] Yu J, Zhao H. A numerical model for thermoelectric generator with the parallel-plate heat exchanger. J Power Sources 2007;172:428–34. doi:10.1016/J.JPOWSOUR.2007.07.045.

[164] He W, Wang S, Lu C, Zhang X, Li Y. Influence of different cooling methods on thermoelectric performance of an engine exhaust gas waste heat recovery system. Appl Energy 2016;162:1251–8. doi:10.1016/j.apenergy.2015.03.036.

[165] He W, Wang S, Li Y, Zhao Y. Structural size optimization on an exhaust exchanger based on the fluid heat transfer and flow resistance characteristics applied to an automotive thermoelectric generator. Energy Convers Manag 2016;129:240–9. doi:10.1016/J.ENCONMAN.2016.10.032.

[166] Esarte J, Min G, Rowe DM. Modelling heat exchangers for thermoelectric generators. J Power Sources 2001;93:72–6. doi:10.1016/S0378-7753(00)00566-8.

[167] Kosky P, Balmer R, Keat W, Wise G. Mechanical Engineering. Explor. Eng., Elsevier; 2013, p. 259–81. doi:10.1016/b978-0-12-415891-7.00012-1.

[168] Steiner D, Schlünder EU. Heat transfer and pressure drop for boiling nitrogen flowing in a horizontal tube. Cryogenics (Guildf) 1976;16:387–98. doi:10.1016/0011-2275(76)90050-3.

[169] Rowe DM, editor. CRC Handbook of Thermoelectrics. 2018. doi:10.1201/9781420049718.

[170] Hsiao YY, Chang WC, Chen SL. A mathematic model of thermoelectric module with applications on waste heat recovery from automobile engine. Energy 2010;35:1447–54. doi:10.1016/j.energy.2009.11.030.

[171] Amatya R, Ram RJ. Solar thermoelectric generator for micropower applications. J Electron Mater 2010;39:1735–40. doi:10.1007/s11664-010-1190-8.

[172] Tschopp D, Tian Z, Berberich M, Fan J, Perers B, Furbo S. Large-scale solar thermal systems in leading countries: A review and comparative study of Denmark, China, Germany and Austria. Appl Energy 2020;270:114997. doi:10.1016/j.apenergy.2020.114997.

[173] Karki S, Haapala KR, Fronk BM. Technical and economic feasibility of solar flat-plate collector thermal energy systems for small and medium manufacturers. Appl Energy 2019;254:113649. doi:10.1016/j.apenergy.2019.113649.

[174] Gou X, Xiao H, Yang S. Modeling, experimental study and optimization on low-temperature waste heat thermoelectric generator system. Appl Energy 2010;87:3131–6. doi:10.1016/j.apenergy.2010.02.013.

[175] Hebei I.T. (Shanghai) Co., Ltd:Product catalogue - Peltier Modules n.d. https://peltiermodules.com/?p=product (accessed 1 July 2021).

[176] Nayak-Luke R, Bañares-Alcántara R, Wilkinson I. 'green' Ammonia: Impact of Renewable Energy Intermittency on Plant Sizing and Levelized Cost of Ammonia. Ind Eng Chem Res 2018;57:14607–16. doi:10.1021/acs.iecr.8b02447.

[177] Cheema II, Krewer U. Operating envelope of Haber–Bosch process design for power-to-ammonia. RSC Adv 2018;8:34926–36. doi:10.1039/C8RA06821F.

[178] World fertilizer trends and outlook to 2020: Summary report - Food and Agriculture Organization of the United Nations - Google Books n.d. https://books.google.co.uk/books?id=6kttDwAAQBAJ&pg=PR1&lpg=PR1&dq=World+fertilizer+trends+and+outlook+to+2020;+Food+and+Agriculture+Organization+of+the+United+Nations:+Rome,+2017&source=bl&ots=6QkLElyB8H&sig=ACfU3U1M46LANTrYMDgRkBwz-GsuB9YAfQ&hl=en&sa=X&ved=2ahUKEwjf57Pa1I_oAhVSTsAKHX9BCScQ6AEwAnoECAgQAQ#v=onepage&q=World fertilizer trends and outlook to 2020%3B Food and Agriculture Organization of the United Nations%3A Rome%2C 2017&f=false (accessed 10 March 2020).

[179] Mannan MS. Lees' Loss Prevention in the Process Industries: Hazard Identification, Assessment and Control: Third Edition. Lees' Loss Prev Process Ind Hazard Identification, Assess Control Third Ed 2004;9780750675550:1–3567. doi:10.1016/B978-0-7506-7555-0.X5081-6.

[180] Fertilizers Europe. GUIDANCE FOR INSPECTION OF ATMOSPHERIC, REFRIGERATED AMMONIA STORAGE TANKS GUIDANCE FOR INSPECTION OF ATMOSPHERIC, REFRIGERATED AMMONIA STORAGE TANKS, 2008 Edition,Issue 2014. 2008.

[181] Sánchez A, Martín M. Optimal renewable production of ammonia from water and air. J Clean Prod 2018;178:325–42. doi:10.1016/j.jclepro.2017.12.279.

[182] Dagdougui H, Sacile R, Bersani C, Ouammi A. Hydrogen Production and Current Technologies. Hydrog. Infrastruct. Energy Appl., Elsevier; 2018, p. 7–21. doi:10.1016/b978-0-12-812036-1.00002-0.

[183] HMRC yearly average and spot rates n.d.:https://www.gov.uk/government/publications/exchang.

[184] Consumer price inflation time series n.d.:https://www.ons.gov.uk/economy/inflationandpricein.

[185] Brigagão GV, Arinelli L de O, de Medeiros JL, Araújo O de QF. A new concept of air pre-purification unit for cryogenic separation: Low-pressure supersonic separator coupled to finishing adsorption. Sep Purif Technol 2019;215:173–89. doi:10.1016/j.seppur.2019.01.015.

[186] Dry M. Technical & Cost Comparison of Laterite Treatment Processes Part 3. Proc. ALTA 2015 Nickel-Cobalt-Copper Sess., 2015.

[187] Industrial electricity tariff in China n.d.:https://www.sohu.com/a/248700878_296300.

[188] Steffen V, Silva EA da. Steady-State Modeling of Equilibrium Distillation. Distill. - Innov. Appl. Model., InTech; 2017. doi:10.5772/66833.

[189] Sohail Rasool Lone SAA. Modelling and Simulation of a Distillation Column using Matlab. Int J Eng Res Sci Technol 2013;2(4):1–4. doi:10.1007/978-981-15-8704-7_10.

[190] Bian S, Khowinij S, Henson MA, Belanger P, Megan L. Compartmental modeling of high purity air separation columns. Comput Chem Eng 2005;29:2096–109. doi:10.1016/j.compchemeng.2005.06.002.

[191] Huang R, Zavala VM, Biegler LT. Advanced step nonlinear model predictive control for air separation units. J Process Control 2009;19:678–85. doi:10.1016/j.jprocont.2008.07.006.

[192] Grinberg Dana A, Elishav O, Bardow A, Shter GE, Grader GS. Nitrogen-Based Fuels: A Power-to-Fuel-to-Power Analysis. Angew Chemie - Int Ed 2016;55:8798–805. doi:10.1002/anie.201510618.

[193] Bañares-Alcántara R, Dericks G, Fiaschetti M, Grünewald P, Masa Lopez J, Tsang E, et al. Analysis of Islanded NH3-based Energy Storage Systems Analysis of Islanded Ammonia-based Energy Storage Systems. 2015.

[194] Moghaddam AA, Krewer U. Poisoning of ammonia synthesis catalyst considering off-design feed compositions. Catalysts 2020;10:1–16. doi:10.3390/catal10111225.

[195] Ashmore PG, King C V. Catalysis and Inhibition of Chemical Reactions. J Electrochem Soc 1965;112:13C. doi:10.1149/1.2423453.

[196] Appl M. Ammonia, 2. Production Processes. Ullmann's Encycl Ind Chem 2011. doi:10.1002/14356007.O02_O11.